AERODYNAMIC OPTIMIZATION BY VARIABLE-RESOLUTION MODELING AND SPACE MAPPING

May 2012

Eiríkur Jónsson

Master of Science in Mechanical Engineering

AERODYNAMIC OPTIMIZATION BY VARIABLE-RESOLUTION MODELING AND SPACE MAPPING

Eiríkur Jónsson
Master of Science
Mechanical Engineering
May 2012
School of Science and Engineering
Reykjavík University

M.Sc. RESEARCH THESIS

ISSN 1670-8539

Aerodynamic Optimization by Variable-Resolution Modeling and Space Mapping

by

Eiríkur Jónsson

Research thesis submitted to the School of Science and Engineering
at Reykjavík University in partial fulfillment of
the requirements for the degree of
Master of Science in **Mechanical Engineering**

May 2012

Research Thesis Committee:

Leifur Þór Leifsson, Supervisor
Assistant Professor, School of Science and Engineering

Slawomir Koziel, Supervisor
Professor, School of Science and Engineering

Copyright
Eiríkur Jónsson
May 2012

The undersigned hereby certify that they recommend to the School of Science and Engineering at Reykjavík University for acceptance this research thesis entitled **Aerodynamic Optimization by Variable-Resolution Modeling and Space Mapping** submitted by **Eiríkur Jónsson** in partial fulfillment of the requirements for the degree of **Master of Science** in **Mechanical Engineering**.

Date

Leifur Þór Leifsson, Supervisor
Assistant Professor, School of Science and Engineering

Slawomir Koziel, Supervisor
Professor, School of Science and Engineering

The undersigned hereby grants permission to the Reykjavík University Library to reproduce single copies of this research thesis entitled **Aerodynamic Optimization by Variable-Resolution Modeling and Space Mapping** and to lend or sell such copies for private, scholarly or scientific research purposes only.

The author reserves all other publication and other rights in association with the copyright in the research thesis, and except as herein before provided, neither the research thesis nor any substantial portion thereof may be printed or otherwise reproduced in any material form whatsoever without the author's prior written permission.

Date

Eiríkur Jónsson
Master of Science

Aerodynamic Optimization by Variable-Resolution Modeling and Space Mapping

Eiríkur Jónsson

May 2012

Abstract

Computational fluid dynamics (CFD) simulations are an important part of modern design. High-fidelity CFD simulations are accurate and reliable, but yet computationally expensive. The main objective of this work is to develop a computationally, efficient and robust methodology for aerodynamic shape optimization. We use surrogate-based optimization (SBO) in which direct optimization is replaced by iterative updating and re-optimization of a computationally cheap surrogate. The surrogate is constructed using a low-fidelity model based on the same governing fluid flow equations as the high-fidelity model, but with a coarser discretization and relaxed convergence criteria. The low-fidelity model is then corrected using spaces mapping methodology where it becomes a reliable representation of the high-fidelity model. The corrected model is then used to find an approximate optimum design of the high-fidelity model. Due to noise in the low-fidelity model we introduce polynomial approximation models based on sampled low-fidelity model data. To our knowledge this is one of the first applications of space mapping using such methods in aerodynamic shape optimization. This methodology is applied to two cases; (1) A constrained low-speed high-lift airfoil drag minimization in two-dimensional viscous flow. Here the algorithm requires less than 31 high-fidelity model evaluations compared to 180 high-fidelity model evaluations using direct optimization, and (2) a constrained transonic wing, lift maximization case in three-dimensional viscous flow. Optimized designs are obtained with less than 10 high-fidelity function evaluations.

Loftalffræðileg bestun með reiknilegum straumfræðilíkönum og rýmisvörpun

Eiríkur Jónsson

Maí 2012

Útdráttur

Tölulegar straumfræðihermanir eru mikilvægar þegar kemur að verkfræðilegri hönnun. Hágæða straumfræðilíkön eru nákvæm og áreiðanleg en einnig reikniþung. Höfuðmarkmið þessa verkefnis er að þróa reiknifræðilega hraðvirka og skilvirka bestunaraðferð fyrir loftaflfræðilega bestun. Aðferðin sem er lögð til í þessu verkefni byggir á bestunaraðferð þar sem notuð eru leiðrétt lággæða straumfræðilíkön í staðinn fyrir hágæðalíkön. Lággæða líkönin eru byggð á sömu straumfræðijöfnum og hágæðalíkönin en með mun grófara reiknineti og slakari samleitni skilyrðum. Lággæðalíkanið er síðan leiðrétt með rýmisvörpun (space mapping) og það notað sem nálgun við hágæðalíkanið. Leiðrétta lággæðalíkanið er því næst notað til að finna bestu lausn. Lággæðalíkönin innihalda mikið tölulegt suð og er því búið til margliðu nálgunarlíkan úr gögnum frá lággæðalíkönum. Aðferðarfræðin kynnt hér hefur ekki verið notuð áður í hönnun á loftaflfræðilegum yfirborðum. Sýnt er fram á hraðvirkni og áreiðanleika aðferðarinnar með tvenns konar hönnunardæmum; (1) Fyrra dæmið er vængprófíll í lághraða tvíviðu seigu flæði þar sem markmiðið er að hámarka lyftikraft. Aðferðin sem kynnt er hér þarf eingöngu 31 ítrun með hágæðalíkaninu borið saman við 180 ef bestunin er framkvæmd eingöngu með hágæðalíkaninu, (2) Seinna dæmið er þrívíður vængur í seigu flæði nálægt hljóðhraða. Aðferðin sem kynnt er hér þarf eingöngu 10 ítranir með hágæðalíkaninu til að finna bestu lausn.

Acknowledgements

I would like to thank all the people who have supported me through my thesis and studies. I consider myself very fortunate to have had the opportunity to work with Leifur Þór Leifsson and Slawomir Koziel and have them as my supervisors. I have been inspired by them time and time again and I am very thankful for all their support and the time they have given me. Furthermore, I would like to express my gratitude to Reykjavik University faculty. This work was part funded by RANNIS, The Icelandic Research Fund for Graduate Students, fund ID: 110395-0061. Finally I would like to thank my spouse and family for believing in me and for their invaluable support.

Contents

List of Figures x

List of Tables xxi

List of Abbreviations xxiii

List of Symbols xxv

1 Introduction 1

2 Variable-resolution Shape Optimization 5

2.1 General Optimization Formulation 5

2.2 Optimization Methods 6

2.2.1 Gradient-Based Methods 7

2.2.2 Derivative-Free Methods 8

2.3 Surrogate-Based Optimization (SBO) 8

2.3.1 SBO Concept 9

2.3.2 Surrogate Modeling and Correction 10

2.4 Optimization using Space Mapping 13

2.4.1 Space Mapping Basics 14

2.4.2 Low-Fidelity CFD Model 15

2.4.3 Surrogate Model Construction 16

2.4.4 Optimization Algorithm 18

3 Low-Speed High-Lift Airfoil Optimization 19

3.1 Problem Definition 19

3.2 High-Fidelity CFD Model 21

3.2.1 Governing Equations 21

3.2.2 Trawldoor Geometry 22

3.2.3 Computational Grid 25

3.2.4 Boundary Conditions and Solver Setup 26
3.2.5 Grid Convergence Study - NACA 0012 29
3.2.6 CFD Model Validation - NACA 0012 30
3.3 Performance Analysis of the F11 Trawl-Door 38
3.3.1 Results 38
3.3.2 Numerical noise 56
3.3.3 Conclusion 57
3.4 Design Optimization of the Trawl-door 59
3.4.1 Formulation 59
3.4.2 Low-Fidelity CFD Model 61
3.4.3 Direct Optimization Results 62
3.4.4 Space Mapping Optimization Results 65
3.5 Summary 72

4 Transonic Wing Optimization **75**
4.1 Problem Definition 75
4.2 High-Fidelity CFD Model 77
4.2.1 Governing Equations 78
4.2.2 Wing Geometry 78
4.2.3 Computational Grid 82
4.2.4 Boundary Conditions and Solver Setup 86
4.2.5 Grid Convergence Study - ONERA M6 86
4.2.6 CFD Model Validation - ONERA M6 88
4.3 Wing Design Optimization at Transonic Flow Conditions 96
4.3.1 Formulation 96
4.3.2 Low-Fidelity CFD Model 97
4.3.3 Space Mapping Optimization Results 98
4.4 Summary 121

5 Conclusion and Future Work **123**

A Computational Fluid Dynamic Modeling **129**
A.1 Governing Equations 129
A.1.1 Navier Stokes Equations 129
A.1.2 RANS equations 132
A.1.3 Turbulence Models 133
A.2 Numerical Modeling 135
A.2.1 Geometry 135

A.2.2 Computational Grid 136
A.2.3 Flow solution 139

B Aerodynamics **141**
B.1 Airfoil geometry 141
B.2 Wing geometry 142
B.3 Aerodynamic forces 143
B.4 Lift Coefficient 145
B.4.1 Subsonic Lift-Curve slope 146
B.5 Drag Coefficient 147
B.5.1 Parasite Drag 147
B.5.2 Induced drag 148
B.5.3 Total drag 149
B.6 Flow Separation and Stall 150
B.7 High-Lift Devices 151
B.7.1 Flap Effect 151
B.7.2 Slats Effect 152
B.8 Types of flow 153
B.8.1 Incompressible versus Compressible Flow 153
B.8.2 Mach Number and Flow Regimes 153
B.8.3 Subsonic Flow 153
B.8.4 Transonic Flow 154

List of Figures

2.1 Flowchart of the direct optimization approach. 7
2.2 Flowchart of the surrogate-based optimization 10
2.3 Flowchart of the key stages of the functional surrogate construction. If quality of the model is insufficient, procedure can be iterated by adding more sample points. 12

3.1 Trawl gear drag decomposition diagram [1]. Approximately 30% of the assembly is due to the trawl-doors. 20
3.2 Typical trawl-doors. Source http://www.hlerar.is. 21
3.3 CAD drawing of the F11 trawl-door elements. Main element (ME), Slat 1 and Slat 2. The span is $b = 5.8m$ and the extended chord length is $c' = 2.4m$. This is a low aspect ratio wing with $AR = 2.4$ 23
3.4 Shift (x_{S1}, y_{S1}) relative to $(0, 0)$ and orientation θ_{S1} of one slat. The second slat is omitted for simplicity. The chord length c of each element is defined from its leading edge to trailing edge and c' is the extended chord length for the assembly. Thickness t_{ME} and radius R_{ME} for the ME are shown but omitted for slat. 24
3.5 Cross-section of the normalized F11 trawl-door with three elements, main element (ME), slat 1 and slat 2. 24
3.6 Farfield configured as a box topology. The leading edge of the trawl-door airfoil is placed at $(x/c_{ME}, y/c_{ME}) = (0, 0)$. 25
3.7 High-fidelity mesh for the angle of attack $\alpha = 50$ degrees. Starting form the domain boundaries figure a), increasing zoom in at trawl-door at each image ending with figure f) a close up of the boundary layer. 27
3.8 Boundary types used. Cross-section of the normalized F11 trawl-door with three elements, main element (ME), slat 1 and slat 2. 28

3.9 Grid convergence study using the NACA 0012 airfoil at $V_\infty = 2m/s, Re = 2 \times 10^6$ and angle of attack $\alpha = 3°$. a) Lift (C_l) and drag (C_d) coefficient versus number of grid elements, b) simulation time versus number of grid elements. 31

3.10 NACA 0012 computational grid for the angle of attack $\alpha = 10$ degrees. As shown in Fig. 3.10c the trailing edge (TE) is sharp. 32

3.11 Lift coefficient (C_l) versus angle of attack (α) of the NACA 0012 validation case, shown with solid line (-o-). Experimental data from Ladson [2] show with squares. Agreement is excellent up to the stall region. 34

3.12 Drag coefficient (C_d) versus angle of attack (α) of the NACA 0012 validation case, shown with solid line (-o-). Experimental data from Ladson [2] show with squares. Agreement is excellent for lower $\alpha < 10°$, but not as good for higher angle of attack close to the stall region 34

3.13 Drag coefficient (C_d) versus Lift coefficient (C_l) of the NACA 0012 validation case, shown with solid line (-o-). Experimental data from Ladson [2] show with squares. Agreement is excellent for low $(C_l < 1)$ 35

3.14 Lift to Drag coefficient ratio C_l/C_d versus angle of attack (α) of the NACA 0012 validation case, shown with solid line (-o-). Experimental data from Ladson [2] show with squares. Agreement is excellent up to $\alpha < 5°$ 35

3.15 Pressure coefficient (C_p) of upper NACA 0012 surface for angle of attack $\alpha = 0°$, shown with solid line (-). $C_l \approxeq 0$. Gregory experimental data [3] shown with square markers and Ladson data [4] with circles. 36

3.16 Pressure coefficient (C_p) of upper NACA 0012 surface for angle of attack $\alpha = 10°$, shown with solid line (-). $C_l \approxeq 1.1$. Gregory experimental data [3] shown with square markers and Ladson data [4] with circles. 36

3.17 Pressure coefficient (C_p) of upper NACA 0012 surface for angle of attack $\alpha = 15°$, shown with solid line (-). $C_l \approxeq 1.5$. Gregory experimental data [3] shown with square markers and Ladson data [4] with circles. 37

3.18 Lift coefficient (C_l) versus angle of attack (α) at $V_\infty = 2m/s, Re_c = 2 \times 10^6$. Computational results are shown with dotted dash line (.-.), dashed line (- -) and solid line (–) for Main Element only (ME), ME + 1 slat and ME + 2 (the F11 trawl-door design) respectively. 40

3.19 Drag coefficient (C_d) versus angle of attack (α) at $V_\infty = 2m/s, Re_c = 2 \times 10^6$. Computational results are shown with dotted dash line (.-.), dashed line (- -) and solid line (–) for Main Element only (ME), ME + 1 slat and ME + 2 (the F11 trawl-door design) respectively. 40

3.20 Drag coefficient (C_d) versus Lift coefficient (C_l) at $V_\infty = 2m/s, Re_c = 2 \times 10^6$. Computational results are shown with dotted dash line (.-.), dashed line (- -) and solid line (–) for Main Element only (ME), ME + 1 slat and ME + 2 (the F11 trawl-door design) respectively. 41

3.21 Lift to Drag ratio C_l/C_d versus angle of attack (α) at $V_\infty = 2m/s, Re_c = 2 \times 10^6$. Computational results are shown with dotted dash line (.-.), dashed line (- -) and solid line (–) for Main Element only (ME), ME + 1 slat and ME + 2 (the F11 trawl-door design) respectively. 41

3.22 F11 trawl-door characteristics at $V_\infty = 2m/s, Re_c = 2 \times 10^6$, angle of attack $\alpha = -5°$. a) Velocity contour, b) Skin friction coefficient (C_f), c) Pressure coefficient (C_p) 42

3.23 F11 trawl-door characteristics at $V_\infty = 2m/s, Re_c = 2 \times 10^6$, angle of attack $\alpha = 0°$. a) Velocity contour, b) Skin friction coefficient (C_f), c) Pressure coefficient (C_p) 43

3.24 F11 trawl-door characteristics at $V_\infty = 2m/s, Re_c = 2 \times 10^6$, angle of attack $\alpha = 5°$. a) Velocity contour, b) Skin friction coefficient (C_f), c) Pressure coefficient (C_p) 44

3.25 F11 trawl-door characteristics at $V_\infty = 2m/s, Re_c = 2 \times 10^6$, angle of attack $\alpha = 10°$. a) Velocity contour, b) Skin friction coefficient (C_f), c) Pressure coefficient (C_p) 45

3.26 F11 trawl-door characteristics at $V_\infty = 2m/s, Re_c = 2 \times 10^6$, angle of attack $\alpha = 15°$. a) Velocity contour, b) Skin friction coefficient (C_f), c) Pressure coefficient (C_p) 46

3.27 F11 trawl-door characteristics at $V_\infty = 2m/s, Re_c = 2 \times 10^6$, angle of attack $\alpha = 20°$. a) Velocity contour, b) Skin friction coefficient (C_f), c) Pressure coefficient (C_p) 47

3.28 F11 trawl-door characteristics at $V_\infty = 2m/s, Re_c = 2 \times 10^6$, angle of attack $\alpha = 25°$. a) Velocity contour, b) Skin friction coefficient (C_f), c) Pressure coefficient (C_p) 48

3.29 F11 trawl-door characteristics at $V_\infty = 2m/s, Re_c = 2 \times 10^6$, angle of attack $\alpha = 30°$. a) Velocity contour, b) Skin friction coefficient (C_f), c) Pressure coefficient (C_p) 49

3.30 F11 trawl-door characteristics at $V_\infty = 2m/s, Re_c = 2 \times 10^6$, angle of attack $\alpha = 35°$. a) Velocity contour, b) Skin friction coefficient (C_f), c) Pressure coefficient (C_p) 50

3.31 F11 trawl-door characteristics at $V_\infty = 2m/s, Re_c = 2 \times 10^6$, angle of attack $\alpha = 40°$. a) Velocity contour, b) Skin friction coefficient (C_f), c) Pressure coefficient (C_p) 51
3.32 F11 trawl-door characteristics at $V_\infty = 2m/s, Re_c = 2 \times 10^6$, angle of attack $\alpha = 45°$. a) Velocity contour, b) Skin friction coefficient (C_f), c) Pressure coefficient (C_p) 52
3.33 F11 trawl-door characteristics at $V_\infty = 2m/s, Re_c = 2 \times 10^6$, angle of attack $\alpha = 50°$. a) Velocity contour, b) Skin friction coefficient (C_f), c) Pressure coefficient (C_p) 53
3.34 F11 trawl-door characteristics at $V_\infty = 2m/s, Re_c = 2 \times 10^6$, angle of attack $\alpha = 55°$. a) Velocity contour, b) Skin friction coefficient (C_f), c) Pressure coefficient (C_p) 54
3.35 F11 trawl-door characteristics at $V_\infty = 2m/s, Re_c = 2 \times 10^6$, angle of attack $\alpha = 60°$. a) Velocity contour, b) Skin friction coefficient (C_f), c) Pressure coefficient (C_p) 55
3.36 Linear validation between two designs $\mathbf{x}_1 = [-0.2515, -0.0299, 22.3649, 2.8059]$ and $\mathbf{x}_2 = [-0.2495, -0.0289, 22.3649, 2.8059]$. Validation is done at $V_\infty = 2m/s, Re = 2 \times 10^6$ at angle of attack $\alpha = 2.8059°$ a) Low-fidelity model response. Noise due to transient flow effects or the solver not able to converge are visible for the low-fidelity model. Obvious oscillation of lift and drag, (squares and circles, respectively) around mean response values for lift (- -) and drag (.-.). b) High-fidelity model response. Model shows consistency in lift and drag except for one design. 58
3.37 Modified design of the F11 trawl-door where two element assembly, main element and one slat, is considered as an initial design for optimization process. 60
3.38 Definitions of gap and overlap. 60
3.39 Lift and Drag coefficient convergence plot for low-fidelity model obtained in grid convergence study simulation for NACA 0012 at Reynolds number $Re = 2 \times 10^6$ and angle of attack $\alpha = 3°$. 62
3.40 High-fidelity optimum design geometry obtained using direct optimization with the initial design shown as well. 64
3.41 Direct optimization results $V_\infty = 2m/s, Re_c = 2 \times 10^6$. Optimized design characteristics at angle of attack $\alpha = 2.8058°$. a) Velocity contour, b) Skin friction coefficient (C_f), c) Pressure coefficient (C_p) 66
3.42 Optimum design geometry obtained using space mapping with the initial design shown as well. 68

3.43 Optimization history using the proposed SM methodology. a) Evolution of the objective function; b) convergence Plot; c) evolution of lift coefficient where dash line (- -) is the lift constrain and; d) evolution of drag coefficient 70
3.44 Space Mapping optimization results $V_\infty = 2m/s, Re_c = 2 \times 10^6$. Optimized design characteristics at angle of attack $\alpha = 2°$. a) Velocity contour, b) Skin friction coefficient (C_f), c) Pressure coefficient (C_p) 71

4.1 Planform view of a trapezoidal wing of a semi-span $b/2$ and quarter chord sweep angle Λ. Spanstations are marked 1 through 7 and freestream velocity is V_∞. Leading edge and trailing edge angles are ϕ and ψ is also shown. Other design parameters are not shown. 76
4.2 Airfoil wing cross-section (solid line) of thickness t and chord length c. V_∞ is the freestream velocity and is at an angle of attack α relative to the x-axis. F is the resulting aerodynamic force where l is the lift force, perpendicular to V_∞ and d is the drag force, parallel to V_∞. p is the pressure acting normal to a surface element ds. τ is the viscous wall shear stress acting parallel to the surface element. θ is the angle that p and τ make relative to the z and x-axis, respectively where positive angle is clockwise. 77
4.3 Examples of two airfoils sections generated with the NACA four digit method. NACA 0012 $m = 0, p = 0, t/c = 0.12$ is shown by solid line (–) and is a symmetric airfoil. NACA 0012 $m = 0.04, p = 0.6, t/c = 0.08$ is shown by dash line (- -). 80
4.4 Planform view of a constant chord wing used in this work. The rectangular wing consisting of two NACA airfoils, shown at spanstations 1 the wing root and 2 wing tip. Each airfoil has its own set of design parameters, $m, c, t/c$, describing the airfoil cross-section. 81
4.5 Planform view of a conventional transport wing consisting of 3 NACA 4 digit airfoils where sweep has been introduced. Each spanstation $1 - 3$ is an airfoil which has its own set of design parameters $m, c, t/c$. 81
4.6 Farfield configured as a box topology. The leading edge of the wing root airfoil is placed at $(x, y, z) = (0, 0, 0)$. 82
4.7 Shell grid shown for all surfaces. a) wing shell grid; b-c) symmetry plane where the wing placed; d) prism layer applied close to the wing surface to capture the viscous boundary layer; e) farfield volume 84

4.8 Volume grid a) looking in span-wise direction y-axis; b) looking in stream-wise direction x-axis; c) looking from below along z-axis. We note how the elements are dense close to the surface and gradually grow into the volume. 85
4.9 Breakout of the boundary types used. All boundaries are set as pressure-farfield (PF) except one the wing penetrates which is a symmetry boundary. 87
4.10 Grid convergence study using the ONERA M6 wing at $M_\infty = 0.8395$ and angle of attack $\alpha = 3.06°$. a) Lift (C_L) and drag (C_D) coefficient versus number of grid elements, b) simulation time versus number of grid elements. 89
4.11 Pressure coefficient (C_p) at $y/(b/2) = 0.2$ of ONERA M6 wing at $M_\infty = 0.8395$ and angle of attack $\alpha = 3.06°$. CFD results shown with solid line (-). Wind tunnel experiment 2308 conducted by Schmitt, V. and F. Charpin [5] shown with square markers. 92
4.12 Pressure coefficient (C_p) at $y/(b/2) = 0.44$ of ONERA M6 wing at $M_\infty = 0.8395$ and angle of attack $\alpha = 3.06°$. CFD results shown with solid line (-). Wind tunnel experiment 2308 conducted by Schmitt, V. and F. Charpin [5] shown with square markers. 92
4.13 Pressure coefficient (C_p) at $y/(b/2) = 0.65$ of ONERA M6 wing at $M_\infty = 0.8395$ and angle of attack $\alpha = 3.06°$. CFD results shown with solid line (-). Wind tunnel experiment 2308 conducted by Schmitt, V. and F. Charpin [5] shown with square markers. 93
4.14 Pressure coefficient (C_p) at $y/(b/2) = 0.8$ of ONERA M6 wing at $M_\infty = 0.8395$ and angle of attack $\alpha = 3.06°$. CFD results shown with solid line (-). Wind tunnel experiment 2308 conducted by Schmitt, V. and F. Charpin [5] shown with square markers. 93
4.15 Pressure coefficient (C_p) at $y/(b/2) = 0.9$ of ONERA M6 wing at $M_\infty = 0.8395$ and angle of attack $\alpha = 3.06°$. CFD results shown with solid line (-). Wind tunnel experiment 2308 conducted by Schmitt, V. and F. Charpin [5] shown with square markers. 94
4.16 Pressure coefficient (C_p) at $y/(b/2) = 0.95$ of ONERA M6 wing at $M_\infty = 0.8395$ and angle of attack $\alpha = 3.06°$. CFD results shown with solid line (-). Wind tunnel experiment 2308 conducted by Schmitt, V. and F. Charpin [5] shown with square markers. 94

4.17 Pressure coefficient (C_p) at $y/(b/2) = 0.99$ of ONERA M6 wing at $M_\infty = 0.8395$ and angle of attack $\alpha = 3.06°$. CFD results shown with solid line (-). Wind tunnel experiment 2308 conducted by Schmitt, V. and F. Charpin [5] shown with square markers. 95
4.18 Upper surface, pressure coefficient (C_p) contour plot of ONERA M6 wing at $M_\infty = 0.8395$ and angle of attack $\alpha = 3.06°$. Note the double shock on the surface, one at the leading edge and one at mid wing, where they then merge close to the wing tip. 95
4.19 Rectangular wing planform view. $b/2$ is the normalized wingspan and c is the normalized wing chord length. 96
4.20 Lift and Drag coefficient convergence plot for low-fidelity model obtained in grid convergence study simulation using ONERA M6 wing at Mach number $M_\infty = 0.8395$ and angle of attack $\alpha = 3.06°$. 98
4.21 Run 1 optimum design geometry of the NACA airfoil obtained using space mapping algorithm shown with dashed line (- -). Initial design shown with solid line (–). 101
4.22 Optimization history using the proposed SM methodology. a) Evolution of the objective function; b) convergence Plot; c) evolution of lift coefficient and; d) evolution of drag coefficient where dash line (- -) is the drag constraint. At iteration 3 flow solver crashes due to grid error. 102
4.23 Run 1 pressure coefficient (C_p) at $y/(b/2) = 0.2$ where $M_\infty = 0.8395$ and angle of attack $\alpha = 0°$. Initial design shown with solid line (–). Optimum design shown with dashed line (- -). 103
4.24 Run 1 pressure coefficient (C_p) at $y/(b/2) = 0.44$ where $M_\infty = 0.8395$ and angle of attack $\alpha = 0°$. Initial design shown with solid line (–). Optimum design shown with dashed line (- -). 103
4.25 Run 1 pressure coefficient (C_p) at $y/(b/2) = 0.65$ where $M_\infty = 0.8395$ and angle of attack $\alpha = 0°$. Initial design shown with solid line (–). Optimum design shown with dashed line (- -). Notice the shock close to the trailing edge. 104
4.26 Run 1 pressure coefficient (C_p) at $y/(b/2) = 0.8$ where $M_\infty = 0.8395$ and angle of attack $\alpha = 0°$. Initial design shown with solid line (–). Optimum design shown with dashed line (- -). Notice the shock close to the trailing edge. 104

4.27 Run 1 pressure coefficient (C_p) at $y/(b/2) = 0.9$ where $M_\infty = 0.8395$ and angle of attack $\alpha = 0°$. Initial design shown with solid line (–). Optimum design shown with dashed line (- -). Notice the shock close to the trailing edge. 105

4.28 Run 1 pressure coefficient (C_p) at $y/(b/2) = 0.95$ where $M_\infty = 0.8395$ and angle of attack $\alpha = 0°$. Initial design shown with solid line (–). Optimum design shown with dashed line (- -). Notice the shock close to the trailing edge. 105

4.29 Run 1 pressure coefficient (C_p) at $y/(b/2) = 0.99$ where $M_\infty = 0.8395$ and angle of attack $\alpha = 0°$. Initial design shown with solid line (–). Optimum design shown with dashed line (- -). Notice the shock close to the trailing edge. 106

4.30 Run 1 planform pressure coefficient contour plots of the initial design geometry. a) The upper surface shows a shocks at mid section of the wing. b) The lower surface shows one shock at the leading edge. 107

4.31 Run 1 planform pressure coefficient contour plots of the optimized design geometry. a) The upper surface shows two shocks, one at mid section of the wing and one close to the wing tip at the trailing edge. b) The lower surface shows one shock at the leading edge. 107

4.32 Run 1 Mach number contour plot (M) at $y/(b/2) = 0.2$ where $M_\infty = 0.8395$ and angle of attack $\alpha = 0°$. a) Shows the initial design; b) Shows the optimized design. 108

4.33 Run 1 Mach number contour plot (M) at $y/(b/2) = 0.44$ where $M_\infty = 0.8395$ and angle of attack $\alpha = 0°$. a) Shows the initial design; b) Shows the optimized design. 109

4.34 Run 1 Mach number contour plot (M) at $y/(b/2) = 0.65$ where $M_\infty = 0.8395$ and angle of attack $\alpha = 0°$. a) Shows the initial design; b) Shows the optimized design. 110

4.35 Run 1 Mach number contour plot (M) at $y/(b/2) = 0.8$ where $M_\infty = 0.8395$ and angle of attack $\alpha = 0°$. a) Shows the initial design; b) Shows the optimized design. Notice the shock at the trailing edge. 111

4.36 Run 1 Mach number contour plot (M) at $y/(b/2) = 0.9$ where $M_\infty = 0.8395$ and angle of attack $\alpha = 0°$. a) Shows the initial design; b) Shows the optimized design. Notice the shock at the trailing edge. 112

4.37 Run 1 Mach number contour plot (M) at $y/(b/2) = 0.95$ where $M_\infty = 0.8395$ and angle of attack $\alpha = 0°$. a) Shows the initial design; b) Shows the optimized design. Notice the shock at the trailing edge. 113

4.38 Run 1 Mach number contour plot (M) at $y/(b/2) = 0.99$ where $M_\infty = 0.8395$ and angle of attack $\alpha = 0°$. a) Shows the initial design; b) Shows the optimized design. 114

4.39 Run 2 optimum design geometry of the NACA airfoil obtained using space mapping algorithm shown with dashed line (- -). Initial design shown with solid line (- -). 116

4.40 Optimization history using the proposed SM methodology. a) Evolution of the objective function; b) convergence Plot; c) evolution of lift coefficient and; d) evolution of drag coefficient where dash line (- -) is the lift constraint. At iteration 6 the flow solver crashes due to grid error. 117

4.41 Run 2 pressure contour plot of the optimum design geometry obtained using space mapping. Left) The upper surface shows two shocks one at mid section of the wing and another close to the wing tip at the trailing edge. Right) The lower surface shows one shock between the leading edge and mid section of the wing. 118

4.42 Graphical comparison of Run 1 and Run 2, initial and optimized designs. a) Initial design comparison b) Optimized comparison. Run 1 is shown with a solid lines (–), and Run 2 with dashed lines (- -) 120

A.1 A hierarchy of the governing equation along with approximations and associated assumptions 132

A.2 Basic flow diagram of a single CFD simulation in numerical wing shape optimization 135

A.3 Convergence history of a typical simulation. a) Residual convergence history b) lift and drag history 140

B.1 Airfoil a wing cross-section (solid line) of thickness t and chord length c. V_∞ is the freestream velocity and is at an angle of attack α relative to the x-axis. F is the resulting aerodynamic force where L is the lift force, perpendicular to $\mathbf{V}_\infty$ and D is the drag force, parallel to V_∞. p is the pressure acting normal to a surface element ds. τ is the viscous wall shear stress acting parallel to the surface element. θ is the angle that p and τ make relative to the z and x-axis, respectively where positive angle is clockwise. 141

B.2 Schematic of a wing planform of a semi-span $b/2$ and quarter chord sweep angle Λ. Spanstations are marked 1 through 7 and freestream velocity is V_∞. Leading edge and trailing edge angles are ϕ and ψ is also shown. Other design parameters are not shown. 143

B.3 Typical airfoil or wing pressure distribution 144
B.4 Aerodynamic forces on an element of the body surface. 145
B.5 Effects on lift coefficient by varying angle of attack and camber. 146
B.6 Various sources of drag and the drag terminology 147
B.7 Finite wing. Streamlines over the top and bottom surface shows that there exists a component of flow in spanwise direction. 148
B.8 Effect of downwash on the local flow over local airfoil section of wing. . 149
B.9 Types of stall 150
B.10 High lift devices nomenclature 151
B.11 The effects of high lift devices. Adding slat extends the lift slope hence increases $C_{l\,\max}$ and stall is experienced ad higher angle of attack (α_{stall}). Adding flap shifts the lift curve up and aft, increasing $C_{l\,\max}$ but stall occurs at lower angle of attack (α_{stall}). 152
B.12 Different regimes of flow 154

List of Tables

2.1 Problem formulation for two-dimensional airfoil shape optimization. Constraints on minimum allowable area are also included in the design. Three dimensional wing shape optimization is almost identical where the subscript on the coefficient would change to capital letters. 6

3.1 Normalized design parameters of the F11 trawl-door extracted from CAD drawings Fig. 3.3 23
3.2 Water properties used for CFD simulation and boundary conditions for the velocity-inlet and pressure-outlet. 29
3.3 Numerical results of direct optimization, using random-search and pattern-search optimizing the low-fidelity model and pattern-search optimizing high-fidelity model. Shown are initial design, low-fidelity model optimum design (coarse) and the high-fidelity optimum design parameters (fine). 63
3.4 High-fidelity optimum design compared to interpolated results obtained from Fig. 3.18 to Fig. 3.21 for the F11 trawl-door design at lift $C_l = 1.5634$. 65
3.5 Numerical results initial, direct and surrogate based optimization using space mapping. The ratio of the high-fidelity model evaluation time to the low-fidelity is 10. 68
3.6 Space mapping optimum design compared to interpolated results obtained from Fig. 3.18 to Fig. 3.21 for the F11 trawl-door design at lift $C_l = 1.4382$. 69

4.1 Air properties and boundary conditions for pressure-farfield. 87
4.2 Geometry properties of the ONERA M6 wing. 90
4.3 Flow condition of the ONERA M6 experiment 2308 conducted by Schmitt, V. and F. Charpin [5]. 90

4.4 Optimum numerical results for Run 1 compared to initial design $\mathbf{x}^{(0)} = [0.0200, 0.7000, 0.0628]$. The ratio of the high-fidelity model evaluation time to the low-fidelity is 34. 101
4.5 Optimum numerical results for Run 2 compared to initial design $\mathbf{x}^{(0)} = [0.0232, 0.8550, 0.0600]$. The ratio of the high-fidelity model evaluation time to the low-fidelity is 34. 116
4.6 Numerical comparison of Run 1 and Run 2, initial and optimized designs. The ratio of the high-fidelity model evaluation time to the low-fidelity is 34. 119

List of Abbreviations

2D	Two Dimensional
3D	Three Dimensional
AMMO	Approximation Model Management Algorithm
ASO	Aerodynamics Shape Optimization
CAD	Computer Aided Design
CFD	Computational Fluid Dynamics
DoE	Design of Experiment
EOMC	Engineering Optimization & Modeling Center
LE	Leading Edge
LHS	Latin Hypercube Sampling
ME	Main Element
NACA	National Advisory Committee for Aeronautics
NURBS	Non-Uniform Rational B-Spline
PE	Parameter Extraction
PF	Pressure farfield
RANS	Reynolds Average Navier-Stokes
S-A	Spalart-Almaras
SBO	Surrogate-Based Optimization
SM	Space Mapping
SPRP	Shape Preserving Response Prediction
TE	Trailing Edge

List of Symbols

AR	Aspect Ratio
b	Wing span
c	Chord
c'	Extended chord length when flaps of slats are extended
c'_{mac}	Mean aerodynamic chord length
C_d	Airfoil drag coefficient $= \frac{d}{q_\infty c}$
$C_{d,f}$	High-fidelity model airfoil drag coefficient
$C_{d,s}$	Surrogate model airfoil drag coefficient
$C_{d,\max}$	Airfoil maximum drag coefficient constraint
C_D	Wing drag coefficient $= \frac{D}{q_\infty S}$
$C_{D,f}$	High-fidelity model wing drag coefficient
$C_{D,s}$	Surrogate model wing drag coefficient
$C_{D,\max}$	Wing maximum drag coefficient constraint
C_l	Airfoil lift coefficient $= \frac{l}{q_\infty c}$
$C_{l,\max}$	Airfoil maximum lift coefficient
$C_{l,\min}$	Airfoil minimum lift coefficient constraint
$C_{l,f}$	High-fidelity model airfoil lift coefficient
$C_{l,s}$	Surrogate model airfoil lift coefficient
C_L	Wing lift coefficient $= \frac{L}{q_\infty S}$
$C_{L,\max}$	Wing maximum lift coefficient
$C_{L,\min}$	Wing minimum lift coefficient constraint
$C_{L,f}$	High-fidelity model wing lift coefficient
$C_{L,s}$	Surrogate model wing lift coefficient
C_f	Skin friction coefficient $= \frac{\tau}{q_\infty}$
C_p	Pressure coefficient $= \frac{p-p_\infty}{q_\infty}$

$\mathbf{x}$	Design vector
$\mathbf{x}^*$	Optimum design vector
$\mathbf{A}$	Output SM scaling parameters
$\mathbf{D}$	Output SM shifting parameters
$\mathbf{q}$	SM parameters additive parameter
$f(\mathbf{x})$	High-fidelity model
$H(f(\mathbf{x}))$	Objective function
$A(\mathbf{x})$	Normalized airfoil cross-sectional area of given design $\mathbf{x}$
A_{min}	Minimum area constraint
$s(\mathbf{x})$	Surrogate model
$\mathbf{p}$	SM parameters extracted through parameter extraction
R/c_{ME}	Radius of trawl-door elements, slats or main element
t/c_{ME}	Thickness of trawl-door elements, slats or main element
x/c_{ME}	Location of trawl-door slats relative to main element in x direction.
y/c_{ME}	Location of trawl-door slats relative to main element in y direction.
q_∞	Dynamic pressure $1/2\rho V^2$
δ_{ij}	Kronecker delta
ρ_∞	Free-stream fluid density
μ_∞	Free-stream dynamic viscosity
μ_t	Turbulent viscosity
θ	Orientation of slats relative to x-axis, positive ccw
y^+	A non-dimensional wall distance for a wall-bounded flow
$Re_{c_{ME}}$	Reynolds number for trawl-door $= \frac{\rho_\infty V_\infty c_{ME}}{\mu_\infty}$
$Re_{\infty,S}$	Reynolds number for wing based in reference area $= \frac{\rho_\infty V_\infty S}{\mu_\infty}$
$Re_{\infty,c_{mac}}$	Reynolds number for wing based on mean aerodynamic chord $= \frac{\rho_\infty V_\infty S}{\mu_\infty}$
α	Angle of attack
α_{stall}	Stall angle of attack
$Overlap$	Distance the slat overlaps the main element on x-axis
Gap	Distance from any point on main element to any point on slat
m	Airfoil camber
p	Airfoil maximum camber location
t/c	Airfoil thickness to chord ratio
S	Reference area of wing, chosen here as planform area
Λ	Wing Quarter chord sweep angel
ϕ	Wing leading edge sweep angel
ψ	Wing trailing edge sweep angel
λ	Wing taper ratio
γ_θ	Wing twist

l	Airfoil lift force
d	Airfoil drag force
L	Wing lift force
D	Wing drag force
p	Pressure force
τ	Shear stress
M_∞	Freestream Mach number
a_∞	Freestream speed of sound
T_∞	Freestream temperature
c_p	Specific heat capacity
k	Thermal conductivity
γ	Specific heat ratio
R	The gas constants for dry air
N_c	Number of coarse model evaluations
N_f	Number of fine model evaluations

Chapter 1

Introduction

Aerodynamic and hydrodynamic shape optimization is of primary importance in many engineering disciplines such as aircraft design [6] and turbomachinery [7]. In aircraft design the wing shape is designed to provide maximum performance under a variety of operating conditions such as takeoff, cruise, and landing [8] while for designing turbine blades one seeks efficiency to maximize the turbines energy output [7]. Common to all engineering disciplines is the fundamental goal of designing an aerodynamic shape such that it maximizes efficiency or performance under a given set of operating conditions but yet fulfills multiple design constraints [9, 7]. In order to optimize an aerodynamic shape one must parametrize and analyse its geometry. Describing the geometry accurately, one may need a number of parameters and constraints. As the number of parameters increases, the computational cost increases. Therefore, the selection of computational methods, both in terms of fluid flow analysis and optimization process, is imperative for a fast and efficient design process.

Numerical optimization of airfoils and wings extends back to the mid 1970s, when Hicks and Henne [8] applied gradient-based optimization techniques to airfoils and wings at subsonic and transonic conditions. Adjoint methods introduced by Jameson [10] and later extended by co-workers is an efficient gradient-based method. This method has been applied on high-lift designs both on airfoils [10] and wings [9] using the viscous Navier-Stokes equations.

The above methods directly apply the computational code in the optimization loop. More recently, the drive has been towards including higher fidelity analyses in the design process. As a result, design optimization, which requires large numbers of high-fidelity model evaluations, becomes impractical and computationally expensive even when using cheap adjoint sensitivities. Computationally efficient optimization can be performed using surrogate-based optimization (SBO). One of the objectives of using SBO methods is to reduce the number of evaluations of the high-fidelity models, hence making the optimization process more efficient. Surrogate-based optimization methods employ computationally cheap surrogates in lieu of the computationally expensive high-fidelity models [11, 12, 13].

The surrogate model can be constructed prior to using it in design and optimization by approximating sampled high-fidelity model data using, e.g., polynomial regression, Kriging interpolation, radial basis functions or neural networks [13]. Approximation methods usually require a large number of high-fidelity function evaluations to ensure a decent model accuracy since the number of samples grows exponentially with the number of design parameters. The computational cost can therefore become high. The approximation-based surrogates are referred to as functional surrogates.

Physics-based surrogate models are not as versatile as approximation models because they rely on the underlying low-fidelity models where the low-fidelity model is a simplified description of the high-fidelity model. These physics-based low-fidelity models can be constructed by using simplified physics models, or by exploiting same CFD solver as used to evaluate the high-fidelity model but with a coarser discretization and relaxed convergence criterion [14]. Physics-based surrogates seem to offer better efficiency simply because the low-fidelity model contains knowledge about the system which results in a higher quality surrogate using a limited amount of high-fidelity model evaluations.

Space mapping (SM) [15, 13] is growing as a popular surrogate-based optimization algorithm that exploits physical surrogates. Several other SBO algorithms exists such as the Approximation and Model Management Optimization (AMMO) [16] framework and the recently shape-preserving response prediction (SPRP) [17] technique.

Space mapping was developed for simulation-driven microwave engineering but is gaining popularity in other areas of engineering. Despite of its potential and popularity in microwave engineering, only few aerodynamic design optimizations studies have been performed to our knowledge where little or no computational improvements have been shown. However a recent study, optimizing an airfoil shape at transonic flow condition, was performed within our research group, the Engineering Optimization & Modeling Center (EOMC) at Reykjavik University where a simple variation of space mapping was used [18]. A significant improvement was shown where computational cost was reduced by 80% using space mapping compared to a direct optimization.

In this work we adopt the space mapping methodology and apply it to two cases, a two-dimensional low-speed, high-lift airfoil design where the objective is to minimize drag with constraints on the lift, and a three-dimensional wing design at transonic flow conditions where the objective is to maximize lift with constraints on drag and wing tip cross-sectional area. In both cases, a physics-based low-fidelity model is constructed using the same CFD solver but with a coarser grid and relaxed convergence criteria. Due to noise in the low-fidelity model we extend the method by introducing polynomial approximation models based on sampled low-fidelity model data. To our knowledge this is one of the one of the first applications of space mapping using such methods in aerodynamic shape optimization. We demonstrate that the approach yields a design improvement for both applications where the computational cost is significantly decreased.

The thesis is outlined as follows. In Chapter 2, we introduce variable resolution modelling using surrogate based optimization and space mapping. In Chapter 3, the proposed method is applied to low-speed high-lift airfoil design and in Chapter 4 to a wing at transonic conditions. Chapter 5 concludes the thesis.

Chapter 2

Variable-resolution Shape Optimization

In this chapter, we start by presenting a general optimization formulation, and available optimization techniques such as gradient-based and derivative-free methods. We then introduce surrogate-based optimization (SBO), where the SBO concept, modelling and correction techniques are presented. Space mapping methodology is then presented where we introduce space mapping basics, give a mathematical formulation of the surrogate model construction and present the optimization algorithm.

2.1 General Optimization Formulation

The computational burden increases rapidly by the increased number of design variables as well as extending the flow solution domain to a three dimensional problem. The need for a clever and computationally efficient optimization process are important in a fast design process is dominant in today's environment. Two common approaches exist when designing a wing or an airfoil. Firstly, the most common method, is the direct design where the goal is to maximize the wing performance. Design setups often include lift maximization, drag minimization and lift-to-drag maximization. The other method, the inverse design, typically targets characteristic values to be obtained, e.g., a certain pressure distribution or a flow behaviour.

Table 2.1: Problem formulation for two-dimensional airfoil shape optimization. Constraints on minimum allowable area are also included in the design. Three dimensional wing shape optimization is almost identical where the subscript on the coefficient would change to capital letters.

Case	$f(\mathbf{x})$	$g_1(\mathbf{x})$
Lift maximization	$-C_l(\mathbf{x})$	$C_d(\mathbf{x}) - C_d^{limit} \leq 0$
Drag minimization	$C_d(\mathbf{x})$	$C_l^{limit} - C_l(\mathbf{x}) \leq 0$
L/D maximization	$-C_l(\mathbf{x})/C_d(\mathbf{x})$	$C_l^{limit} - C_l(\mathbf{x}) \leq 0$
Inverse design	$1/2 \int (C_p(\mathbf{x}) - C_p^{target})^2 ds$	

Generally, aerodynamic shape optimization can be formulated as a non-linear minimization problem, i.e., for a given operating condition, solve

$$\begin{aligned} &\min_{\mathbf{x}} f(\mathbf{x}) \\ &\text{s.t.} \quad g_j(\mathbf{x}) \leq 0 \\ &\mathbf{l} \leq \mathbf{x} \leq \mathbf{u} \end{aligned} \tag{2.1.1}$$

where $f(\mathbf{x})$ is the objective function, $\mathbf{x}$ is the design variable vector, $g_j(\mathbf{x})$ is the design constraint and $\mathbf{l}$ and $\mathbf{u}$ are the lower and upper bounds for the design variables. Design variables and detailed formulation are problem specific but a typical formulation for a two-dimensional airfoil optimization is shown in Table 2.1. Similar formulation can be applied to a three dimensional wing design. Additional constraints are often introduced. Constraints concerning the physical structure of a wing one typically sets constraints for airfoil cross-sectional area. Area constraint can be formally written as $g_2(\mathbf{x}) = A_{\min} - A(\mathbf{x}) \leq 0$, where $A(\mathbf{x})$ is the cross-sectional area of the airfoil for the design vector $\mathbf{x}$ and $A_{\min}$ is the minimum allowable cross-sectional area. Other constraints such as mathematical models describing the structural weight of the wing are often included in optimization [9].

2.2 Optimization Methods

Various optimizations methods exist and methods are usually chosen based on the problem at hand. The basic flow of a direct optimization is shown in Fig. 2.1 and can be summarized in the following steps;

1. An initial design $\mathbf{x}^{(0)}$ is considered and the high-fidelity CFD model is evaluated at a given design resulting in values for the objective function and constraints.

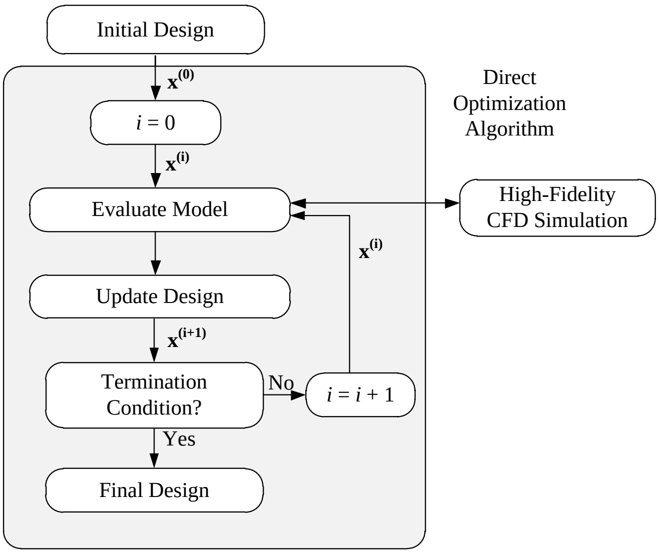
Initial Design
x(0)
i = 0
x(i)
Evaluate Model
Update Design
x(i+1)
Termination Condition?
No
i = i + 1
Yes
Final Design
x(i)
Direct Optimization Algorithm
High-Fidelity CFD Simulation

Figure 2.1: Flowchart of the direct optimization approach.

2. The optimization routine finds a new design $\mathbf{x}$, evaluating the high-fidelity model yielding new values for the objective function and constraints.
3. Based on the value of the objective function and constraints, violated, critical or fulfilled, the optimizer either
   (a) Finds another design to evaluate, or
   (b) Uses current design for the ith design iteration to yield $\mathbf{x}^{(i)}$
4. The loop is repeated until a termination condition is met.

The high-fidelity model is usually evaluated many times during one design iteration. Termination conditions can be problem specific, but usually include maximum number of allowable iterations. Termination condition can also be based on the change in shape between two consecutive design iteration $\mathbf{x}^{(i)}$ and $\mathbf{x}^{(i+1)}$ [19].

2.2.1 Gradient-Based Methods

Gradient based methods have a long history in numerical optimization and have been used for a quite some time in aerodynamic design optimization as Hicks and Henne [20] coupled gradient-based solver with CFD codes. Many different methods exist, such as Line Search, Steepest Decent and Newton-type methods. Development of new techniques such as Adjoint methods is getting popular. Adjoint methods [9, 10] is an efficient gradient based method where the calculation of the gradient is effectively independent of the number of design variables. This method have been used both with inviscid and viscous solvers in 2D and 3D [9].

Gradient based methods are robust for local search, but lack robustness in global search. Also often a large number of high-fidelity function evaluations are needed which can be prohibiting based on the total computational cost of the model. The objective function may not be continuous, hence not differentiable, and there may exist multiple local minima. Numerical noise in the model can also be a serious issue for gradient-based methods.

2.2.2 Derivative-Free Methods

All the issues with gradient-based methods mentioned in Section 2.2.1 give rise to derivative-free methods. The main advantage of using these methods is that they do not require gradient information and can be used with noisy models as well as discontinuous functions. The downside of derivative-free methods is that they usually require large number of function evaluations. Many methods exist and they can be divided into two categories, local and global ones. Popular local search methods include:

- Pattern-search algorithms [21]
- Nelder-Mead algorithm [22]

Popular global search methods include algorithms such as

- Genetic Algorithms (GAs) [23]
- Evolutionary Algorithms (EAs) [24]
- Particle Swarm Optimization [25, 26]
- Random Search

In this thesis, Pattern-Search and Random Search are considered as optimization methods of choice in Chapter 3.

2.3 Surrogate-Based Optimization (SBO)

In this section, we give a brief overview of surrogate-based optimization [12, 11]. First, the concept of the SBO will be presented, followed by a discussion on creating surrogate-based models, correction, and optimizing the models.

2.3.1 SBO Concept

There are many reasons why direct optimization may be infeasible. In CFD, this is particularly the case when the computational cost of simulating a high-fidelity model, such as a 3D wing, can take up to weeks as discussed in Appendix A.1.1. Numerical noise which is always present in CFD solvers can also be difficult to cope with. Surrogate-based optimization alleviates such problems by using auxiliary models or functions, the surrogates, which are a sufficiently accurate description of the original model. These models need to be analytically smooth and preferably computationally cheap so the cost of the entire optimization process is reduced. The surrogate-based optimization is an iterative procedure where the design obtained through optimizing the surrogate model is verified by evaluating the high-fidelity model or the original function. The high-fidelity data obtained by this verification process is then used to update the surrogate.

The flow of the genetic SBO algorithm is shown in Fig. 2.2. The computational burden is shifted from the high-fidelity model (denoted by f) to the surrogate model (denoted by s). The surrogate model is optimized giving a prediction or an approximation of the minimizer for the high-fidelity model. This prediction is then verified by evaluating the high-fidelity model, typically once at the beginning of a new design $\mathbf{x}^{(i+1)}$. The optimization process may terminate or continue after this verification depending on the results. If the process continues, the surrogate model is updated using the high-fidelity data that was obtained for the new design and re-optimized hopefully yielding a new and a better approximation of the high-fidelity model: The process described above can be summarized as follows.

1. Generate the initial surrogate model.
2. Optimize surrogate and obtain an approximate solution.
3. Evaluate high-fidelity model at the approximate solution obtained in step 2.
4. Surrogate updated using new high-fidelity data obtained in step 3.
5. Stop if termination condition is met, otherwise repeat processes from step 2.

Because of the computational efficiency of the surrogate model optimization the cost of the surrogate can usually be neglected so that the computational cost of the overall process can be estimated as the total number of high-fidelity model evaluations. The number of iterations needed by the surrogate-based algorithm described above can therefore be considerably lower than while optimizing the high-fidelity model directly using, e.g., gradient based method.

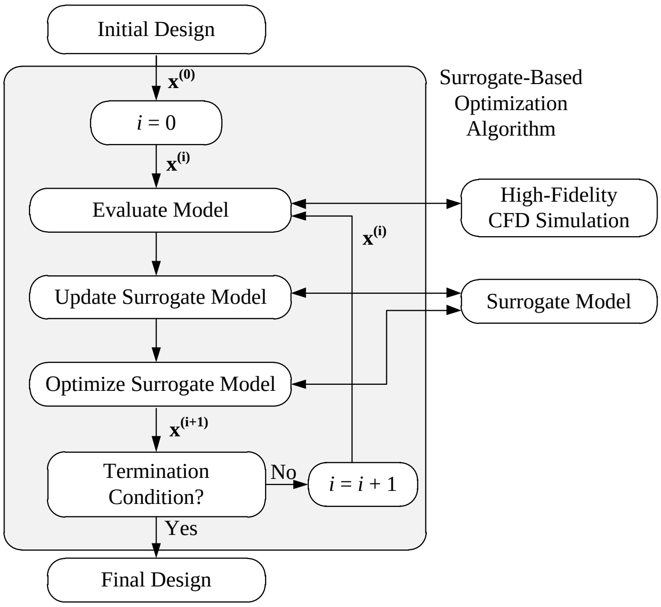
Initial Design
$\mathbf{x}^{(0)}$
Surrogate-Based Optimization Algorithm
$i = 0$
$\mathbf{x}^{(i)}$
Evaluate Model
High-Fidelity CFD Simulation
$\mathbf{x}^{(i)}$
Update Surrogate Model
Surrogate Model
Optimize Surrogate Model
$\mathbf{x}^{(i+1)}$
Termination Condition?
No
$i = i + 1$
Yes
Final Design

Figure 2.2: Flowchart of the surrogate-based optimization

2.3.2 Surrogate Modeling and Correction

Surrogate models are generally split into two categories, functional and physics based ones.

Functional Surrogates

The functional surrogates can be considered as a black-box method. The intention is to build a surrogate without using any knowledge of the physical system. A typical black-box approach involves sampling of the design space, called training data which is used to train the surrogate. It is then validated with testing data from the same design space. The construction of the surrogate consist of four steps which are design of experiments (DoE), acquire output data by evaluating training points, model selection and identification and finally model validation using test points. These steps are show in Fig. 2.3 and are summarized here below:

- **Design of Experiments (DoE):** A sampling plan in the design variable space. Sample points or training points should be selected in such way that they maximize the gained information of the design variable space with as few samples as possible because of computational cost[11]. Generally there are three types of DoE, factorial, space filling and adaptive designs.

   1. Factorial designs are classical DoE methods. Used to estimate the gross effects such as interaction between design variables. Samples are usually chosen to be as far apart as possible in order to reduce random errors. This is good in terms of physical experimental data which always include random errors [27].

   2. Space filling designs are intended to treat all regions of the design space equally and are popular choice today. Many methods exist such as, Random sampling, Stratified random sampling and Latin hypercube sampling (LHS), where LHS is the most commonly used [7]. This method will be used in this thesis and here will be given brief description of its functionality.
      LHS Divide each of n intervals into N subintervals where N is the number of samples, yielding N^n bins in the design space. Select N samples placing them randomly inside a bin so that for all one-dimensional projection, no more than one sample will be allocates in each bin [7].

   3. Adaptive designs are methods that adjust the data by refining sample resolution at a specific or an interesting location.

- **Acquire data:** Training data or sample points obtained with the DoE methods are evaluated in this step using the high-fidelity model.

- **Model Detection and Identification:** Here, the approximation model is chosen and its parameters determined. There are number of models available such as polynomial regression, radial basis functions, neural networks and Kriging, just to mention a few popular choices [13].

- **Model Validation:** The model needs to be validated with test samples from the design space. This determines the accuracy of the model and the generalization error of the model. Several methods exist. The simplest ones are split-sample method [12] where the points obtained in DoE are divided into two sets of data, the training and the test set. If the total number of sampling points is limited, one can use other methods. Probably the most popular method is the cross-validation method [12] where sample points are divided into n subsets, and the surrogate is constructed n times, where it is trained by $n - 1$ subsets and validated with the remaining subset.

Functional surrogates are computationally cheap when set up but constructing the surrogate can require a large number of sample points for it to be a reasonable approximation of the high-fidelity model. The main advantage is however that it is a generic method which can be applied to a number of problems without having any prior knowledge of the physical system.

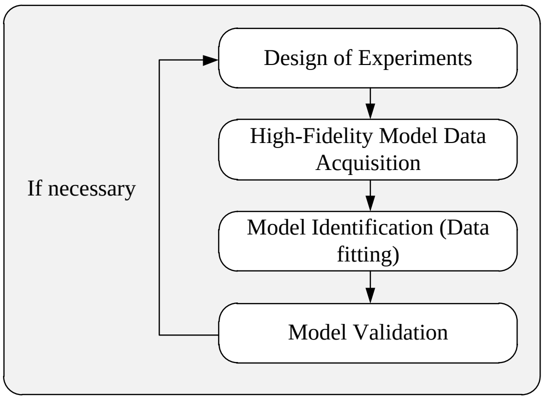
Design of Experiments
High-Fidelity Model Data Acquisition
Model Identification (Data fitting)
Model Validation
If necessary

Figure 2.3: Flowchart of the key stages of the functional surrogate construction. If quality of the model is insufficient, procedure can be iterated by adding more sample points.

Physics-Based Surrogates

Physics-based surrogates are constructed by correcting a low-fidelity model, denoted by c. The low-fidelity model is an approximate description of the high-fidelity model and can be based on one or all of the following approximations:

- **Simplified physics:** Simplifying flow physics is common where one replaces the governing equations such as the RANS equations or Euler equation by the Potential equations or even Transonic Small-Disturbance Equations [14]. This method is referred to as *variable-fidelity* physics model.
- **Coarse discretization:** For the same governing equations and fluid model the computational mesh is made coarser reducing the number of elements that need to be solved [17]. This is referred as *variable-resolution* models.
- **Relaxed convergence criteria:** The number of maximum allowable iterations is reduced. Residual may also be relaxed. This is referred as *variable-accuracy* models.

In general, physics-based models are based on particular knowledge on the system, they are problem specific and usually more expensive to evaluate than the functional based surrogates. They do, however, offer greater accuracy in a global sense than the functional-based surrogates and the main advantage is that the number of high-fidelity model data necessary to obtain an accurate response is substantially lower than for the functional-based surrogates. The low-fidelity physics-based model inherit all the underlying physics of the high-fidelity model and is therefore able to approximate globally the general response of the high-fidelity model. This response needs to be corrected to match the sampled data of the high-fidelity model to be an accurate prediction of the latter. This gives rise to methods used to correct the surrogate which is crucial within any surrogate-based optimization methodology.

Several correction techniques exist such as, General Response Correction [16], Shape-Preserving Response Prediction (SPRP) [17] and Space Mapping [13, 15]. Space mapping will be covered in Section 2.4.

Several optimization techniques that exploit surrogate models are available. To name a few, Approximation Model Management Algorithm (AMMO) [16], Surrogate Management Framework [28] and Space Mapping [15] are popular choices.

2.4 Optimization using Space Mapping

In this section, we give a mathematical formulation of Space Mapping [15, 13] optimization methodology used in this thesis. The formulation will be given for a three-dimensional wing body but it also applies to a two-dimensional airfoil problem [18].

The simulation-driven design can be generally formulated as a nonlinear minimization problem as noted before. Refining Eq. (2.1.1) and constraints we define

$$\mathbf{x}^* = \arg\min_{\mathbf{x}} H\left(f(\mathbf{x})\right), \tag{2.4.1}$$

where $\mathbf{x}$ is a vector of design parameters, f the high-fidelity model to be minimized at $\mathbf{x}$ and H is the objective function. $\mathbf{x}^*$ is the optimum design vector. The high-fidelity model will represent aerodynamic forces, lift and drag coefficient, as well as other scalar responses such as cross-sectional area A of the wing at interesting location. Area response can be of a vector form $\mathbf{A}$ if one requires multiple area cross-sectional constraints at various locations on the wing, e.g., the wing root and the wing tip. The response will have to form

$$f(\mathbf{x}) = \left[C_{L,f}(\mathbf{x}), C_{D,f}(\mathbf{x}), A_f(\mathbf{x})\right]^T, \tag{2.4.2}$$

where $C_{L,f}$ and $C_{D,f}$ are the lift and drag coefficient for a 3D wing, respectively, generated by the high-fidelity model. We are interested in the maximizing lift case and the minimizing drag case, so the objective function will take the form of

$$H\left(f(\mathbf{x})\right) = -C_L, \tag{2.4.3}$$

$$H\left(f(\mathbf{x})\right) = C_D, \tag{2.4.4}$$

with the design constraints denoted as

$$C\left(f(\mathbf{x})\right) = \left[c_1\left(f(\mathbf{x})\right), \ldots, c_k\left(f(\mathbf{x})\right)\right]^T. \tag{2.4.5}$$

Maximizing lift will yield two nonlinear design constraints for drag and area,

$$c_1\left(f(\mathbf{x})\right) = C_{D,f}(\mathbf{x}) - C_{D,\max} \leq 0, \tag{2.4.6}$$

$$c_2\left(f(\mathbf{x})\right) = -A_f(\mathbf{x}) + A_{\min} \leq 0. \tag{2.4.7}$$

Similarly, minimizing drag we have two nonlinear design constraints for lift and area,

$$c_1\left(f(\mathbf{x})\right) = -C_{L,f}(\mathbf{x}) + C_{L,\min} \leq 0, \tag{2.4.8}$$

$$c_2\left(f(\mathbf{x})\right) = -A_f(\mathbf{x}) + A_{\min} \leq 0. \tag{2.4.9}$$

2.4.1 Space Mapping Basics

Starting from a initial design $\mathbf{x}^{(0)}$ the genetic space mapping algorithm produces a sequence $\mathbf{x}^{(i)}, i = 0, 1 \ldots$ of approximate solution to Eq. (2.4.1) as

$$\mathbf{x}^{(i+1)} = \arg\min_{\mathbf{x}} H\left(s^{(i)}(\mathbf{x})\right), \tag{2.4.10}$$

where

$$s^{(i)}(\mathbf{x}) = \left[C_{L,s}^{(i)}(\mathbf{x}), C_{D,s}^{(i)}(\mathbf{x}), A_s(\mathbf{x})^{(i)}\right]^T, \tag{2.4.11}$$

is the surrogate model at iteration i. As previously described, the accurate high-fidelity CFD model f is accurate but computationally expensive. Using Space Mapping, the surrogate s is a composition of the low-fidelity CFD model c and a simple linear transformations to correct the low-fidelity model response [15]. The corrected response is denoted as $s(\mathbf{x}, \mathbf{p})$ where $\mathbf{p}$ represent a set of model parameters and at iteration i the surrogate is

$$s^{(i)}(\mathbf{x}) = s(\mathbf{x}, \mathbf{p}). \tag{2.4.12}$$

The SM parameters $\mathbf{p}$ are determined through a parameter extraction (PE) process. In general this process is a nonlinear optimization problem where the objective is to minimize the misalignment of surrogate response at some or all previous iteration high-fidelity model data points [15]. The PE optimization problem can be defined as

$$\mathbf{p}^{(i)} = \arg\min_{\mathbf{p}} \sum_{k=0}^{i} w_{i,k} \| f(\mathbf{x}^{(k)}) - s(\mathbf{x}^{(k)}, \mathbf{p}) \|^2, \tag{2.4.13}$$

where $w_{i,k}$ are weight factors that control how much impact previous iterations affect the SM parameters. Popular choices are

$$w_{i,k} = 1 \quad \forall i, k\,, \tag{2.4.14}$$

and

$$w_{i,k} = \begin{cases} 1 & k = i \\ 0 & \text{otherwise} \end{cases} . \tag{2.4.15}$$

In the first case, all previous SM iterations influence the parameters; in the second case, the parameters depend only on the most recent SM iteration.

Four different groups of SM surrogate models exist in literature, they are, Input, Output, Implicit and Frequency space mapping. Here, we give examples of SM surrogate models using input and output SM [15, 29].

Input SM where response correction based on a parameter shift and scaling,

$$s(\mathbf{x}, \mathbf{p}) = s(\mathbf{x}, \mathbf{B}, \mathbf{q}) = c(\mathbf{B}\mathbf{x} + \mathbf{q}). \tag{2.4.16}$$

For parameter shift only $\mathbf{B} = \mathbf{I}$, where I is an identity matrix.

Output SM response correction is based on multiplicative and additive response corrections and is given by

$$s(\mathbf{x}, \mathbf{p}) = s(\mathbf{x}, \mathbf{A}, \mathbf{d}) = \mathbf{A}c(\mathbf{x}) + \mathbf{d}. \tag{2.4.17}$$

Special cases, such as the multiplicative correction only, with $\mathbf{d} = 0$, or additive only, with $\mathbf{A} = \mathbf{I}$, are also common.

2.4.2 Low-Fidelity CFD Model

In this thesis, the low-fidelity CFD models are physics-based models where the same governing equations (RANS equations) as the high-fidelity one, but with a coarser grid and relaxed convergence criteria. The low-fidelity model is obtained through a grid convergence study.

Grid Convergence Study

A grid convergence study procedure consists of the following steps;

1. Generate a grid using reasonable number of elements and analyse the model.
2. Regenerate the mesh with higher element density distribution, re-analyse and compare the results to the previous mesh results.
3. Based on the result in step 2, keep increasing the mesh density and re-analysing the model until the results converge satisfactorily.

The above steps are ideal when no prior knowledge is available on how dense the grid must be to yield accurate enough results. If prior knowledge exists, one can also perform the inverse study where starting from a known fine high density mesh with accurate results make the grid as coarse as possible.

For relaxed convergence criteria, residuals and convergence history are inspected. Based on the history one simply selects the appropriate number of iterations where the solution has converged e.g. inspecting Fig. A.3b one could say that lift and drag coefficient have converged after 80-100 iterations.

In this work, the low-fidelity CFD model can be very noisy and it is relatively expensive to evaluate. To mitigate that, a Kriging model can be constructed using a clever DoE sampling plan, and the coarse low-fidelity CFD model data which is obtained through a grid convergence study.

2.4.3 Surrogate Model Construction

As mentioned above, the SM surrogate model s is a composition of the low-fidelity CFD model c and corrections or linear transformations where model parameters p are extracted using one of the PE processes described above. Parameter extraction and surrogate optimization create a certain overhead on the whole process and this overhead can be up to 80-90 % of the computational cost. This is due to the fact that the physics-based low-fidelity models are in general relatively expensive to evaluate compared to the functional-based ones. Despite this, SM may be beneficial [30].

To alleviate this problem, the output SM with both multiplicative and additive response correction is exploited here with the surrogate model parameters extracted analytically. We use the following formulation;

$$\begin{aligned} s^{(i)}(\mathbf{x}) &= \mathbf{A}^{(i)} \circ c(\mathbf{x}) + \mathbf{D}^{(i)} + \mathbf{q}^{(i)} && (2.4.18) \\ &= \left[a_L^{(i)} C_{L,c}(\mathbf{x}) + d_L^{(i)} + q_L^{(i)}, \quad a_D^{(i)} C_{D,c}(\mathbf{x}) + d_D^{(i)} + q_D^{(i)}, \quad A_c(\mathbf{x}) \right]^T, && (2.4.19) \end{aligned}$$

where $\circ$ is component wise multiplication. No mapping is needed for the area $A_c(\mathbf{x})$ where, $A_c(\mathbf{x}) = A_f(\mathbf{x}) \quad \forall\, \mathbf{x}$ since low- and high-fidelity model represent the same geometry. Parameters $\mathbf{A}^{(i)}$ and $\mathbf{D}^{(i)}$ are obtained using

$$\left[\mathbf{A}^{(i)}, \mathbf{D}^{(i)}\right] = \arg\min_{\mathbf{A},\mathbf{D}} \sum_{k=0}^{i} \| f\left(\mathbf{x}^{(k)}\right) - \mathbf{A} \circ c\left(\mathbf{x}^{(k)}\right) + \mathbf{D} \|^2, \tag{2.4.20}$$

where $w_{i,k} = 1$, i.e., all previous iteration points are used to improve globally the response of the low-fidelity model. The additive term $q^{(i)}$ is defined so as to ensure such a perfect match between the surrogate and the high-fidelity model at design $\mathbf{x}^{(i)}$, namely $f\left(\mathbf{x}^{(i)}\right) = s\left(\mathbf{x}^{(i)}\right)$ or a zero-order consistency [16]. We can write the additive term as

$$q^{(i)} = f\left(\mathbf{x}^{(i)}\right) - \left[\mathbf{A}^{(i)} \circ c(\mathbf{x}^{(i)}) + \mathbf{D}^{(i)}\right]. \tag{2.4.21}$$

Since analytical solution exists for $\mathbf{A}^{(i)}, \mathbf{D}^{(i)}$ and $\mathbf{q}^{(i)}$ there is no need for non-linear optimization solving Eq. (2.4.13) to obtain parameters. We can obtain $\mathbf{A}^{(i)}$ and $\mathbf{D}^{(i)}$ by solving

$$\begin{bmatrix} a_L^{(i)} \\ d_L^{(i)} \end{bmatrix} = \left(\mathbf{C}_L^T \mathbf{C}_L\right)^{-1} \mathbf{C}_L^T \mathbf{F}_L\,, \tag{2.4.22}$$

$$\begin{bmatrix} a_D^{(i)} \\ d_D^{(i)} \end{bmatrix} = \left(\mathbf{C}_D^T \mathbf{C}_D\right)^{-1} \mathbf{C}_D^T \mathbf{F}_D\,, \tag{2.4.23}$$

where

$$\mathbf{C}_L = \begin{bmatrix} C_{L,c}(\mathbf{x}^{(0)}) & C_{L,c}(\mathbf{x}^{(1)}) & \dots & C_{L,c}(\mathbf{x}^{(i)}) \\ 1 & 1 & \dots & 1 \end{bmatrix}^T, \tag{2.4.24}$$

$$\mathbf{F}_L = \begin{bmatrix} C_{L,f}(\mathbf{x}^{(0)}) & C_{L,f}(\mathbf{x}^{(1)}) & \dots & C_{L,f}(\mathbf{x}^{(i)}) \\ 1 & 1 & \dots & 1 \end{bmatrix}^T, \tag{2.4.25}$$

$$\mathbf{C}_D = \begin{bmatrix} C_{D,c}(\mathbf{x}^{(0)}) & C_{D,c}(\mathbf{x}^{(1)}) & \dots & C_{D,c}(\mathbf{x}^{(i)}) \\ 1 & 1 & \dots & 1 \end{bmatrix}^T, \tag{2.4.26}$$

$$\mathbf{F}_D = \begin{bmatrix} C_{D,f}(\mathbf{x}^{(0)}) & C_{D,f}(\mathbf{x}^{(1)}) & \dots & C_{D,f}(\mathbf{x}^{(i)}) \\ 1 & 1 & \dots & 1 \end{bmatrix}^T, \tag{2.4.27}$$

which are the least-square optimal solutions to the linear regression problems

$$\mathbf{C}_L a_L^{(i)} + d_L^{(i)} = \mathbf{F}_L\,, \tag{2.4.28}$$

$$\mathbf{C}_D a_D^{(i)} + d_D^{(i)} = \mathbf{F}_D\,. \tag{2.4.29}$$

Note that $\mathbf{C}_L^T\mathbf{C}_L$ and $\mathbf{C}_L^T\mathbf{C}_L$ are non-singular for $i > 1$ and assuming that $\mathbf{x}^{(k)} \neq \mathbf{x}^{(i)}$ for $k \neq i$. For $i = 1$ only the multiplicative SM correction with $\mathbf{A}^{(i)}$ is used.

2.4.4 Optimization Algorithm

Here we formulate the optimization algorithm exploiting the SM based surrogate and a trust-region convergence safeguard [11]. The trust-region parameter λ is updated after each iteration. This algorithm will be used in applications presented in this thesis.

1. Set $i = 0$; Select λ, the trust region radius; Evaluate the high-fidelity model at the initial solution, $f(\mathbf{x}^{(0)})$;
2. Using data from the low-fidelity model c, and f at $\mathbf{x}^{(k)}, k = 0, 1, \ldots, i$, setup the SM surrogate $s^{(i)}$; Perform PE;
3. Optimize $s^{(i)}$ to obtain $\mathbf{x}^{(i+1)}$;
4. Evaluate $f(\mathbf{x}^{(i+1)})$;
5. If $H(f(\mathbf{x}^{(i+1)})) < H(f(\mathbf{x}^{(i)}))$, accept $\mathbf{x}^{(i+1)}$; Otherwise set $\mathbf{x}^{(i+1)} = \mathbf{x}^{(i)}$;
6. Update λ;
7. Set $i = i + 1$;
8. If the termination condition is not satisfied, go to 2, else proceed;
9. End; Return $\mathbf{x}^{(i)}$ as the optimum solution.

The above presented algorithm will be applied to two aerodynamic shape optimization problems in the upcoming chapters. The first application is a two-dimensional high-lift trawl-door geometry low-speed flow conditions where the objective is to optimize its geometry to minimize drag and the second is a three dimensional wing at transonic flow conditions where the objective is to increase lift.

Chapter 3

Low-Speed High-Lift Airfoil Optimization

In this chapter, the proposed surrogate based optimization methodology is applied to a two dimensional high-lift trawl-door geometry at a low-speed flow condition. First, we introduce the high-fidelity model where we define the governing equations of the flow, wing geometry, computational grid, solver setup and boundary conditions. A grid convergence study is then performed in order to verify the computational grid. The high-fidelity model is validated using a NACA 0012 airfoil, where the CFD simulation data is compared to experimental data from a NACA 0012 wind tunnel experiment. Performance analysis is performed on three types of trawl-door geometry, the F11 trawl-doors and two modified versions of the F11 trawl-door where slats have been removed. The design optimization formulation is then presented defining the objective and constraints used in this optimization. The low-fidelity model is constructed followed by presenting the optimization results using the proposed method. The chapter concludes with a summary.

3.1 Problem Definition

Trawl-doors are essential equipment of the fishing gear used in today's modern fishing techniques. A typical fishing gear assembly, shown in Fig. 3.1, consists of a large net, pair of trawl-doors to keep the net open and a cable assembly extending from the trawl-doors to the boat and net. Although the trawl-doors are a small part of the fishing gear they are responsible for roughly 30% of the total drag of the equipment needed [1]. The motivation and benefit for optimizing the trawl-door shape is therefore clear. If the trawl-

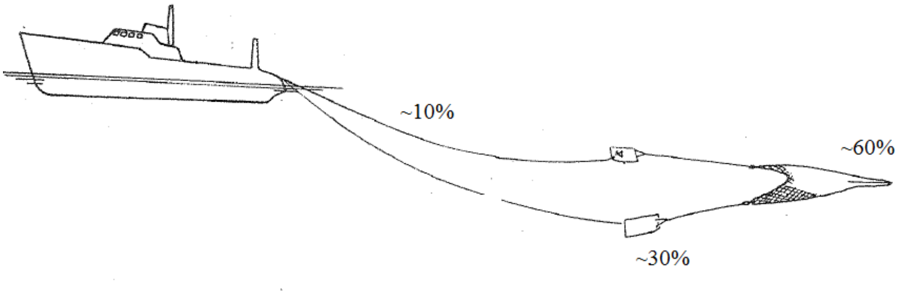

Figure 3.1: Trawl gear drag decomposition diagram [1]. Approximately 30% of the assembly is due to the trawl-doors.

door can be redesigned in such way that drag is reduced one can reduce the ship fuel consumption, hence, reduce cost.

Trawl-door designs that have been developed over the years mainly consist of a similar design where they have been designed using physical tests, where the trawl-door is built and tested. Little or no CFD analysis have been performed on trawl-doors in general. Trawl-door designs are essentially steel plates, cut down, bent with a certain radius and welded together. These designs have two key elements:

- Main element (ME) - is the largest element of the trawl-door
- Two slats - either of same size or different, located in front of the main element intended to give higher lift for increased angle of attack.

Most designs are based on these three elements and typical designs are shown in Fig. 3.2. Two dimensional cut thought any of the trawl-doors shown will yield a similar cross-section. Example of such cross-section is shown in Fig. 3.5 and will be discussed further in the following sections. Trawl-doors are normally operated at a very high angle of attack, i.e., $\alpha = 30 - 50^\circ$ or higher.

The goal of this chapter is to optimize a modern trawl-door design, namely the F11 trawl-door, with the proposed method presented in Section 2.4 in order to minimize its drag. We start by defining the high-fidelity CFD model used in the optimization process. Following that, we perform a performance analysis study on a modern trawl-door to simply set a baseline for the optimization results. Finally the optimization results are presented and discussed.

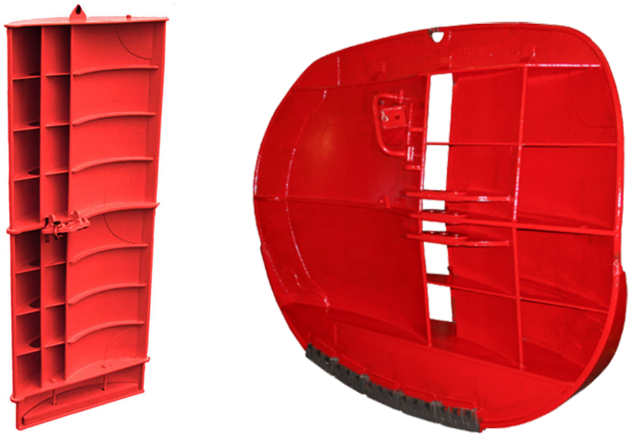

(a) (b)

Figure 3.2: Typical trawl-doors. Source http://www.hlerar.is.

3.2 High-Fidelity CFD Model

In this section, we start by describing the governing equations of the fluid flow. Following that, the trawl-door geometry, computational grid, solver setting and boundary conditions are presented. The section concludes with a grid convergence study and high-fidelity model validation study performed on a NACA 0012 airfoil.

3.2.1 Governing Equations

Trawl-doors are devices used in water, hence we can safely assume that the flow is incompressible. Further, the flow is assumed to be steady, viscous and with no body forces. In Cartesian coordinates, the continuity equation is written as

$$\frac{\partial u_i}{\partial x_i} = 0, \tag{3.2.1}$$

and the momentum equation or the Navier-Stokes Equation as

$$\rho \frac{Du_i}{Dt} = -\frac{\partial p}{\partial x_i} + \rho g_i + \mu \nabla^2 u_i, \tag{3.2.2}$$

where D/Dt is the material derivative defined as

$$\frac{Du_i}{Dt} = \frac{\partial u_i}{\partial t} + u_j \frac{\partial u_i}{\partial x_j} \tag{3.2.3}$$

and

$$\nabla^2 u_i = \frac{\partial^2 u_i}{\partial x_j \partial x_j} = \frac{\partial^2 u_i}{\partial x_1^2} + \frac{\partial^2 u_i}{\partial x_2^2}, \tag{3.2.4}$$

in two dimensions, where u_i are the velocity components in each dimension, ρ is the density, μ the dynamic viscosity and p the pressure [31]. In this work, we use the Reynolds Average Navier-Stokes (RANS) equations and since no heat transfer is included in the problem we only need to solve the averaged continuity and momentum equations. For incompressible flow:

$$\frac{\partial \bar{u}_i}{\partial x_i} = 0, \tag{3.2.5}$$

$$\frac{\partial}{\partial t}(\rho \bar{u}_i) + \frac{\partial}{\partial x_j}(\rho \bar{u}_i \bar{u}_j) = -\frac{\partial p}{\partial x_i} + \frac{\partial}{\partial x_j}\left[\mu\left(\frac{\partial \bar{u}_i}{\partial x_j} + \frac{\partial \bar{u}_j}{\partial x_i}\right) - \rho\overline{u_i' u_j'}\right], \tag{3.2.6}$$

where $\bar{u}_i$ is the mean term in Reynolds decomposition $u_i = \bar{u}_i + u_i'$ and $\bar{u_i'}$ is the fluctuating term and, $-\rho\overline{u_i' u_j'}$ is the Reynolds stress tensor [32]. To model the Reynolds stress tensor a turbulence model is needed. In this work we use the k-ω-SST turbulence model [33].

3.2.2 Trawldoor Geometry

Here we will consider a simple chord-wise cross-sectional cut of the F11 trawl-door. The CAD model geometry is shown in Fig. 3.3. The aspect ratio of this trawl-door is

$$AR = \frac{b^2}{A} = \frac{b^2}{b \times c'} = \frac{b}{c'} = \frac{5.8}{2.4} = 2.4, \tag{3.2.7}$$

which is a quite low and three dimensional flow effects may be significant. Aspect ratio $AR > 10$ is considered high. There are three elements:

1. The main element (ME), which is the largest element of the assembly.
2. Slat 1, the middle element in the assembly. The one closest the ME leading edge.
3. Slat 2, farthest element from the ME in the assembly.

In order to create a numerical model for the F11 trawl-door the geometric shape and parameters needs to be extracted from the manufacturer CAD drawings and formulated so each element is available for optimization. We consider each element with a set of design parameters. The design parameters of interest are chord length c, thickness t and the plate curvature or radius R of each element. Further we define the location of each slat (x, y), relative to the leading edge of the main element which we define as $(0, 0)$, and the orientation θ of the slats in degrees, relative to x-axis, positive being counter clock-wise.

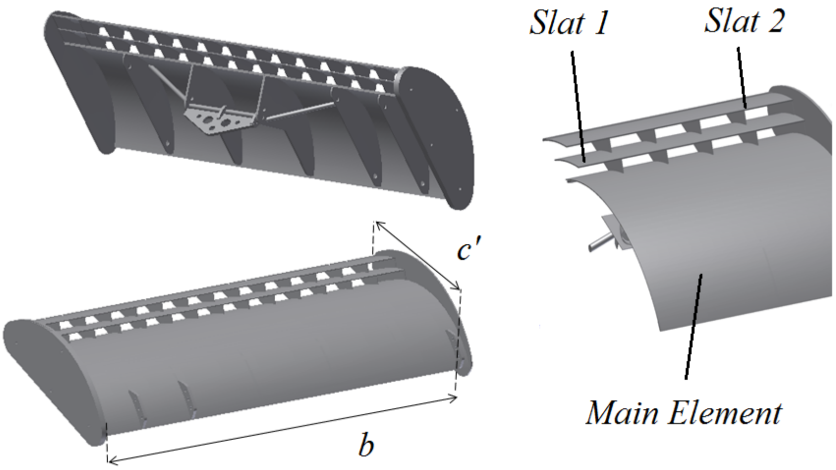

Figure 3.3: CAD drawing of the F11 trawl-door elements. Main element (ME), Slat 1 and Slat 2. The span is $b = 5.8m$ and the extended chord length is $c' = 2.4m$. This is a low aspect ratio wing with $AR = 2.4$

Table 3.1: Normalized design parameters of the F11 trawl-door extracted from CAD drawings Fig. 3.3

Variable	**Main Element**	**Slat 1**	**Slat 2**
Chord c	1	0.2531	0.2531
Thickness t/c_{ME}	0.0053	0.0063	0.0063
Radius R/c_{ME}	0.7368	0.7821	0.7821
Shift $(x/c_{ME}, y/c_{ME})$	(0,0)	(-0.1192,0.0085)	(-0.2457,0.0115)
Orientation θ [deg]	0	33.9	34.7

The following subscript notation will be used in the work to identify design parameters on the above presented design parameter are

1. Main Element parameters will be denoted with ME.
2. Slat element parameters will be denoted with $S1$ for slat 1 and $S2$ for slat 2.

The available design parameters are illustrated in Fig. 3.4 where slat 2 has been omitted for simplicity.

Parameters are extracted from CAD drawings and normalized with the chord length of the ME c_{ME} such that the main element has a chord length of unity. Normalized design parameter values are shown in Table 3.1. These values are used as an initial design for slat location in the optimization process, see Section 3.4. The normalized geometry is shown in Fig. 3.5. For the remainder of this chapter, the main element chord length c_{ME} will be denoted as c to simplify notation. If there is any possibility of ambiguity due to text context the chord length will be denoted by a subscript.

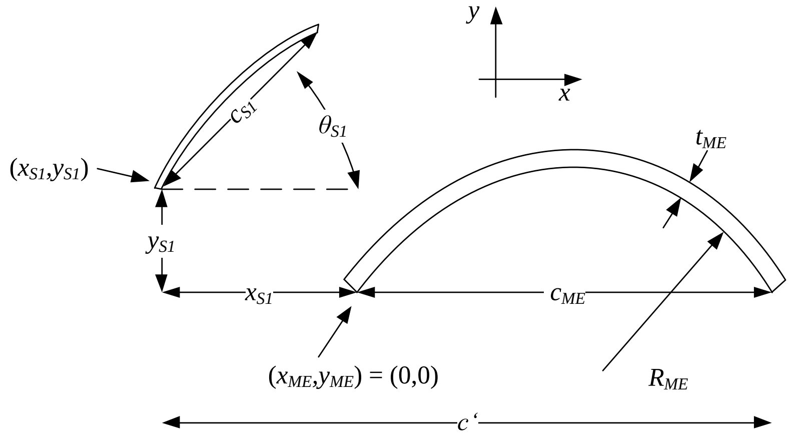

Figure 3.4: Shift (x_{S1}, y_{S1}) relative to $(0, 0)$ and orientation θ_{S1} of one slat. The second slat is omitted for simplicity. The chord length c of each element is defined from its leading edge to trailing edge and c' is the extended chord length for the assembly. Thickness t_{ME} and radius R_{ME} for the ME are shown but omitted for slat.

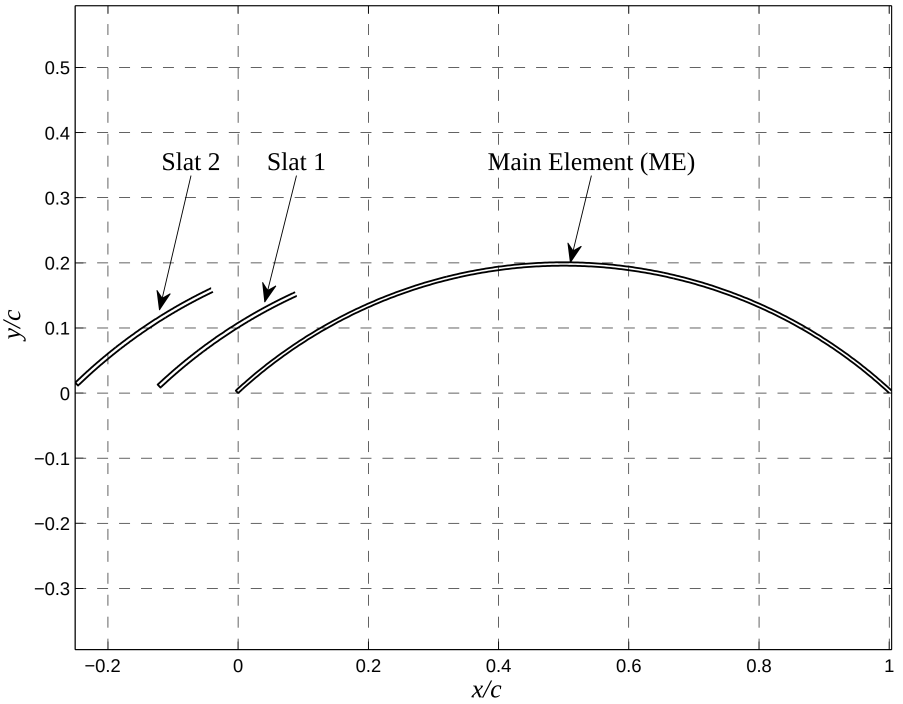

Figure 3.5: Cross-section of the normalized F11 trawl-door with three elements, main element (ME), slat 1 and slat 2.

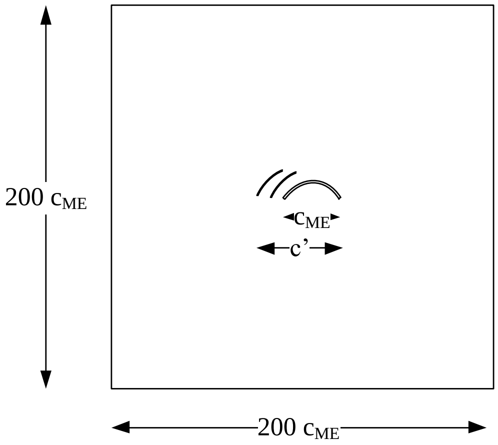

Figure 3.6: Farfield configured as a box topology. The leading edge of the trawl-door airfoil is placed at $(x/c_{ME}, y/c_{ME}) = (0, 0)$.

3.2.3 Computational Grid

Here, we describe the high-fidelity CFD grid used in this work. The density and properties of this grid is found by performing a grid convergence study. The study itself will be covered in Section 3.2.5. The parameters acquired in that study for the high-fidelity model are, however, presented here. The farfield is configured in a box-topology where the trawl-door geometry is placed in the center of the box. The main element leading edge (LE) is placed as the origin $(x/c_{ME}, y/c_{ME}) = (0, 0)$, where the farfield extends 100 main element (ME) chord lengths, $100c_{ME}$ away from the origin as shown in Fig. 3.6. The grid is a unstructured triangular grid where elements are clustered around the trawl-door geometry, growing in size as they move further away from the trawl-door. The maximum element size on geometry is set to 0.1% of the ME chord length, i.e., $0.1\%c_{ME}$. The maximum element size in domain is 10 ME chord lengths or $10c_{ME}$. In order to capture the viscous boundary layer, a prismatic inflation layer is extruded from all surfaces, i.e., the main element and slats. The inflation layer has a initial height of $5 \times 10^{-6}c_{ME}$, growing with exponential growth ratio of 1.2 extending in total 20 layer from the surface. The initial layer height is chosen so that $y^+ < 1$, defined as $y^+ = \rho u_\tau y/\mu$ (see Appendix A.1.3). In the wake region aft of the trawl-door the grid is made denser by applying a density grid with a element size of 5% of the ME chord length. It extends 20 ME chord lengths, $20c_{ME}$ aft of the trawl-door geometry. The density mesh is configured in an adaptive manner so that it changes its orientation with the angle of attack, α. An example of this is shown in Fig. 3.7b for $\alpha = 0$ degrees and $\alpha = 30$ degrees.

The grid properties are summarized here for a quick reference:

- **General Parameters**
  - Farfield extends 100 ME chord lengths, $100c_{ME}$, from the origin $(0, 0)$.
  - Maximum element size on trawl-door surface set to 0.1$\%$ of the ME chord length $0.001c_{ME}$.
  - The maximum element size in domain is 10 ME chord lengths or $10c_{ME}$.
- **Density Region**
  - Density region extends $20c_{ME}$ aft of the trawl-door.
  - Density region element maximum size is $5\%c_{ME}$.
  - Density region is adaptive, changes with angle of attack.
- **Boundary Layer**
  - Initial layer height is $5 \times 10^{-6}c_{ME}$.
  - Exponential growth ration is set 1.2.
  - Number of prism layers are 20.
  - Above properties give at any point on surface $y^+ < 1$.

The high-fidelity CFD grid is generated with the computer code ANSYS ICEM CFD [34] following the guideline given above. The mesh is shown in Fig. 3.7, where Fig. 3.7a shows the farfield domain boundaries, and Fig. 3.7b gives a close up of the density region where the trawl-door is in the lower left corner. In Fig. 3.7c to Fig. 3.7d the trawl-door is visible and Fig. 3.7e and Fig. 3.7f are close ups of the slat and the prism layer respectively. The total number of cells in the computational domain for the high-fidelity model is roughly 217000 cells.

3.2.4 Boundary Conditions and Solver Setup

Numerical fluid flow simulations are performed using the computer code ANSYS FLUENT [32]. The flow solver is set to a coupled velocity-pressure-based formulation. Spatial discretization schemes are set to second order consistency for all variables and gradient information is found using the Green-Gauss node based method. Additionally, due to the difficult flow condition at high angle of attacks, the pseudo-transient option and high-order relaxation terms are used in order to get a stable converged solution [32]. The iterative

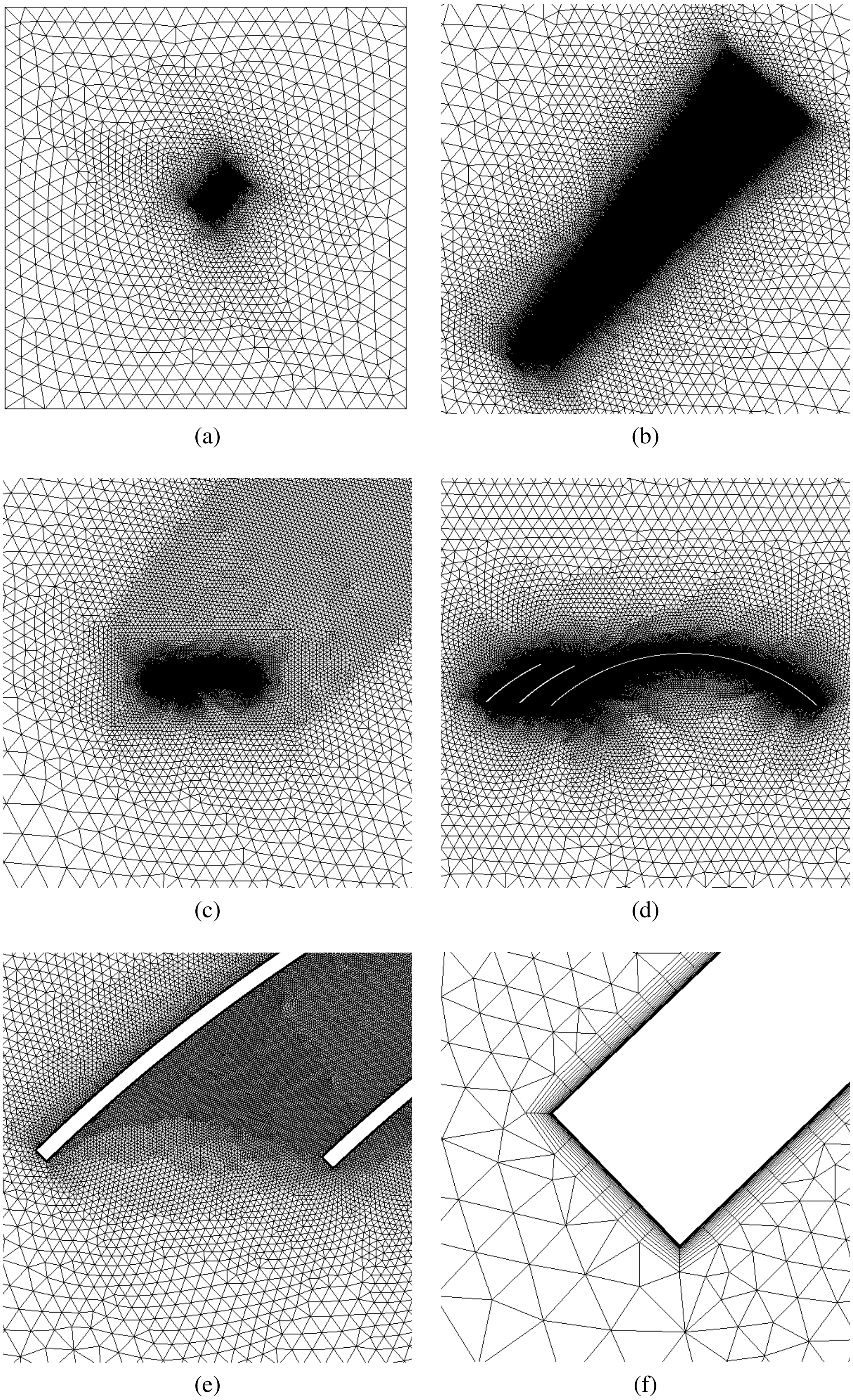

(a) (b)

(c) (d)

(e) (f)

Figure 3.7: High-fidelity mesh for the angle of attack $\alpha = 50$ degrees. Starting form the domain boundaries figure a), increasing zoom in at trawl-door at each image ending with figure f) a close up of the boundary layer.

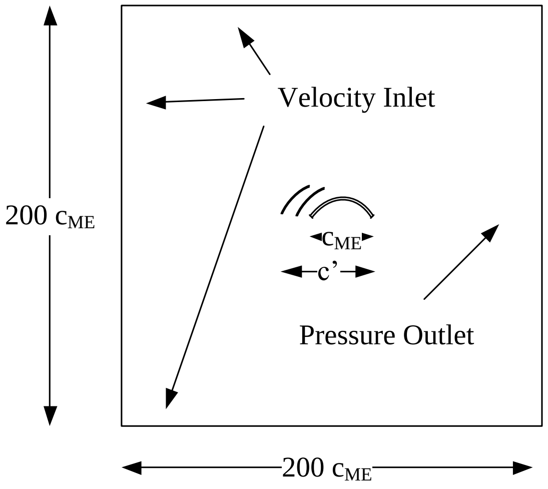

Figure 3.8: Boundary types used. Cross-section of the normalized F11 trawl-door with three elements, main element (ME), slat 1 and slat 2.

solution is performed with relaxation factors to prevent a numerical oscillation of the solution that can lead to a no solution or errors. The residuals, which are the sum of the L^2 norm of all governing equations in each cell, are monitored and checked for convergence. The convergence criterion for the high-fidelity model is such that a solution is considered to be converged if the residuals have dropped by six orders of magnitude, 10^{-6} or the total number of iterations has reached 10^3. Also the lift and drag coefficients are monitored for convergence. Here, convergence is observed in all cases where a steady-state solution is obtained.

The working fluid used is water and the inlet boundary is a velocity-inlet with a freestream velocity $V_\infty = 2m/s$, (which is typical during trawling), is split into its x and y components depending on the angle of attack α. The outlet boundary is a uniform pressure pressure-outlet as shown in Fig. 3.8. Reynolds number is found to be

$$Re_{c_{ME}} = \frac{\rho_\infty V_\infty c_{ME}}{\mu_\infty} = \frac{998.2 \times 2 \times 1}{1.003 \times 10^{-3}} \approxeq 2 \times 10^{-6}, \tag{3.2.8}$$

where $\rho_\infty = 998.2\ kg/m^3$ is the freestream water density and $\mu_\infty = 1.003 \times 10^{-3}\ Ns/m^2$ is the dynamic viscosity at 20° Celsius. We assume that the inlet flow is calm, and close to laminar conditions and turbulent intensity and viscosity ratio are set to 0.05 $\%$ and 1, respectively. The pressure is set to standard atmospheric pressure. We summarize the fluid properties and boundary conditions for quick reference in Table 3.2.

To validate whether the above presented grid is a good high-fidelity model representation and will yield an accurate lift and drag coefficient values for the geometry we validate the

Table 3.2: Water properties used for CFD simulation and boundary conditions for the velocity-inlet and pressure-outlet.

Fluid Properties	**Value**	**Units**
Freestream density ρ_∞	998.2	kg/m^3
Freestream viscosity μ_∞	1.003 $\times 10^{-3}$	Ns/m^2

Boundary Conditions	**Value**	**Units**
Freestream velocity V_∞	2	m/s
Reynolds number $Re_{c_{ME}}$	2×10^6	-
Turbulent intensity (%)	0.05	-
Turbulent viscosity ratio μ_t/μ	1	-

CFD model grid against known experimental results. In the next section, a NACA 0012 airfoil geometry will be used to validate the high-fidelity model grid.

3.2.5 Grid Convergence Study - NACA 0012

In order to find a sufficiently fine enough mesh for the high-fidelity model, a grid convergence study is carried out. This study is performed using the NACA 0012 airfoil. The formulation of the NACA 4 digit method is given in Section 4.2.2. One could argue that the trawl-door should be used as the testing geometry because of its more complex geometry, therefore yielding different flow characteristics. However, due to a lack of two-dimensional experimental and computational data of the F11 trawl-door the NACA 0012 will be used instead.

Convergence Study Setup

The idea of this study is to acquire a sufficiently fine enough grid that will capture flow physics properly and yield accurate enough aerodynamic results. The study is performed using the NACA 0012 at the same conditions as the trawl-door is operating at where, the fluid is water with freestream velocity of $V_\infty = 2m/s$, giving a Reynolds number of $Re = 2 \times 10^6$. The angle of attack is chosen as $\alpha = 3°$. Other boundary conditions and grid properties discussed in Section 3.2.4 and are the same as presented in Table 3.2.

Convergence Study Results

The convergence study shown in Fig. 3.9a revealed that 197,620 grid elements are needed for convergence using respective geometry. This grid will be used in the high-fidelity model. The grid parameter details obtained through this study where previously presented and summarized in 3.2.3 above. The overall simulation time needed for one high-fidelity CFD simulation was around 16 minutes, as shown in Fig. 3.9b, executed on four Intel-i7-2600 processors in parallel. This execution time is based on 10^3 solver iterations where the solver terminated due to the maximum number of iterations limit. The detailed grid parameters, such as grid density on the surface, farfield and density region obtained through this study where presented and summarized in 3.2.3.

3.2.6 CFD Model Validation - NACA 0012

Due to lack of two-dimensional experimental data for trawl-door shapes other geometries must therefore be used to validate the high-fidelity model. NACA 4 digit airfoils have been studied extensively, both in wind tunnels and computationally and are a popular for verification cases. We consider the NACA 0012 airfoil as the validation case for the high-fidelity CFD model presented in Section 3.2.

Validation Setup

The NACA 0012 geometry is generated with the standard NACA 4 digit method [35], with a sharp trailing edge (TE) to get a better fit of the prism layer on the upper and lower surface. A formulation of the NACA 4 digit method is given in Section 4.2.2. The high-fidelity grid with the NACA 0012 airfoil is used in the validation is shown in Fig. 3.10.

Here, the Reynolds number is $Re_c = 6 \times 10^6$ for this performance study. As before the fluid is water. The angle of attack α is varied from -5 to 19 degrees, with increments of 5 degrees up to 15 degrees and from there with one degree increments to 19 where the airfoil have stalled. Other boundary conditions and grid properties are as presented in Table 3.2.

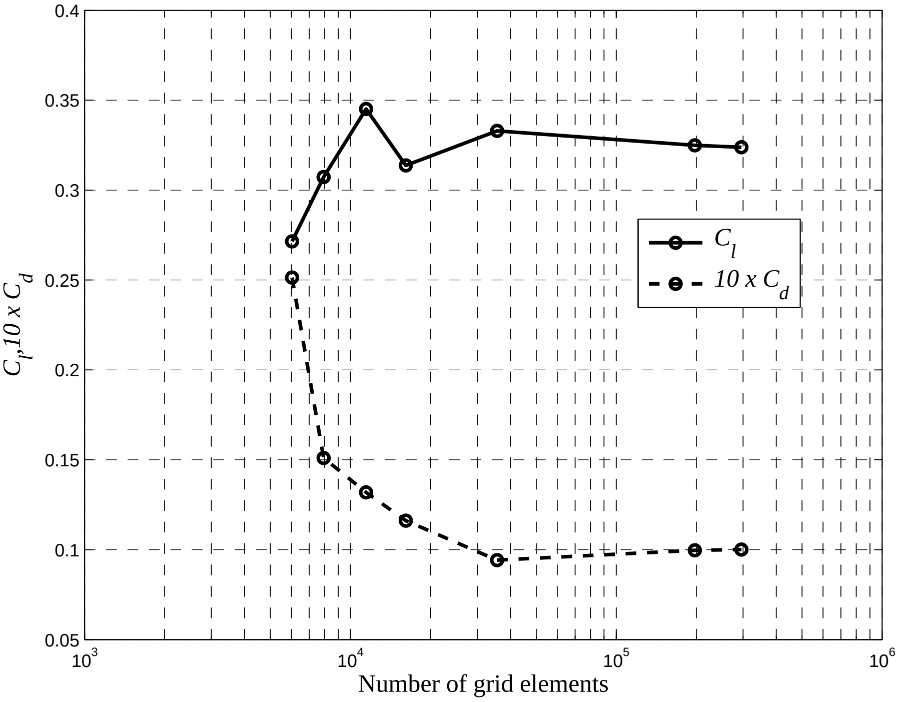

(a)

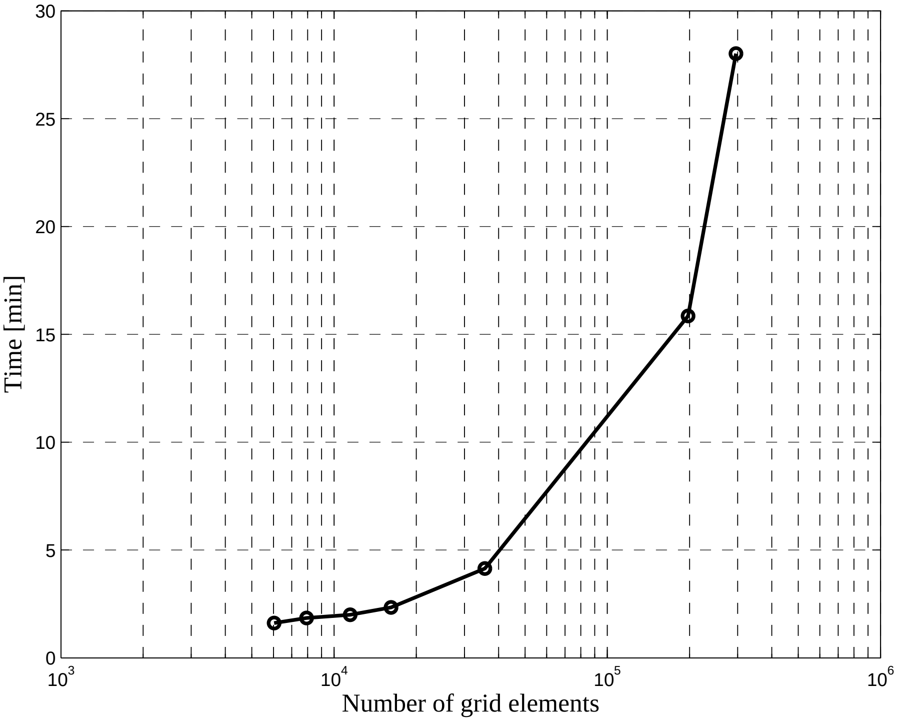

(b)

Figure 3.9: Grid convergence study using the NACA 0012 airfoil at $V_\infty = 2m/s, Re = 2 \times 10^6$ and angle of attack $\alpha = 3°$. a) Lift (C_l) and drag (C_d) coefficient versus number of grid elements, b) simulation time versus number of grid elements.

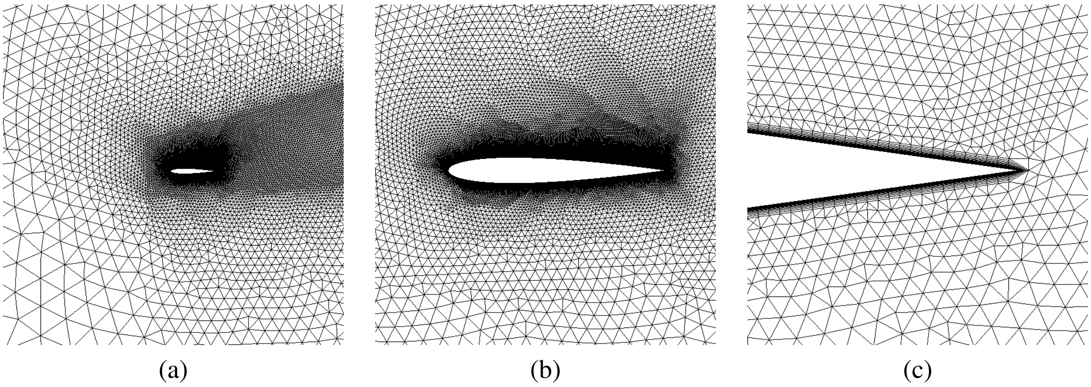
(a) (b) (c)

Figure 3.10: NACA 0012 computational grid for the angle of attack $\alpha = 10$ degrees. As shown in Fig. 3.10c the trailing edge (TE) is sharp.

Comparing Experimental Results

There exists a number of experimental results for the NACA 0012 airfoil [35, 3, 4, 2], as well as computational [36], at various Reynolds numbers. It should be recognized that two-dimensional experiments are extremely difficult to achieve, particularly at higher angles of attack approaching stall and many available experimental results differ especially near stall. It is important to note that experimental drag coefficient levels are greatly affected by tripping the boundary layer at Reynolds numbers in this range of Reynolds number [3]. For example comparing with fully turbulent CFD drag results tripped experimental data, where the transition is fixed, is more appropriate than untripped. Therefore, the experimental data is used in this work with that in mind.

Lift and Drag Coefficients

Comparing lift and drag coefficient results with experimental data the Ladson tripped data [2] appear to be the most appropriate data sets for comparison with fully turbulent boundary layer at $Re_c = 6 \times 10^6$ [36].

Inspecting the overall computational results in Fig. 3.11 to Fig. 3.14 comparing it to the Ladson experimental data [2] we see that for lift C_l versus angle of attack α in Fig. 3.11 that the agreement is excellent up to stall $C_{l,\max}$ where the airfoil stalls close to angle of attack $\alpha = 17^\circ$. Inspecting computational drag results in Fig. 3.12 we see that the agreement is excellent up to $\alpha = 10^\circ$ where separation is starting to get substantial. The error, computational versus experimental drag coefficient $C_{d,comp}/C_{d,exp}$ at $\alpha = 10^\circ$ is 11% and at $\alpha = 16^\circ$ is 33%. Similarly inspecting Fig. 3.13 and Fig. 3.14 we can see that the agreement is good but due to the discrepancy in experimental drag and computational drag the results 10-30% off for $\alpha > 10°$

As noted above, drag is difficult to predict and at a high angle of attack separation becomes massive and experimental results may not be two-dimensional. However, the overall trend is good and we can therefore assume that the high-fidelity model will yield accurate result for lift and drag coefficients.

Pressure Coefficient

For comparing surface pressure coefficients, Ladson data is not appropriate. The Ladson data [4] does not appear to resolve the leading edge upper surface pressure peak well. Here, we use the data Gregory and O'Reilly [3] pressure coefficient C_p data at $Re_c = 3 \times 10^6$ since they appear to be better resolved. Also, Gregory and O'Reilly data differ from Ladson pressure data over the front half of the airfoil at $\alpha = 10°$ and $\alpha = 15°$. Further, the Gregory data are likely more two-dimensional and hence more appropriate for CFD validation of surface pressures. However since the Gregory data is measured at $Re_c = 3 \times 10^6$ we include the Ladson C_p data as well since they are measured at $Re_c = 6 \times 10^6$.

Inspecting Fig. 3.15 to Fig. 3.17 we note that the overall agreement for both experimental dataset is excellent. The computational C_p follows the experimental Gregory data well and captures the pressure peak at the leading edge.

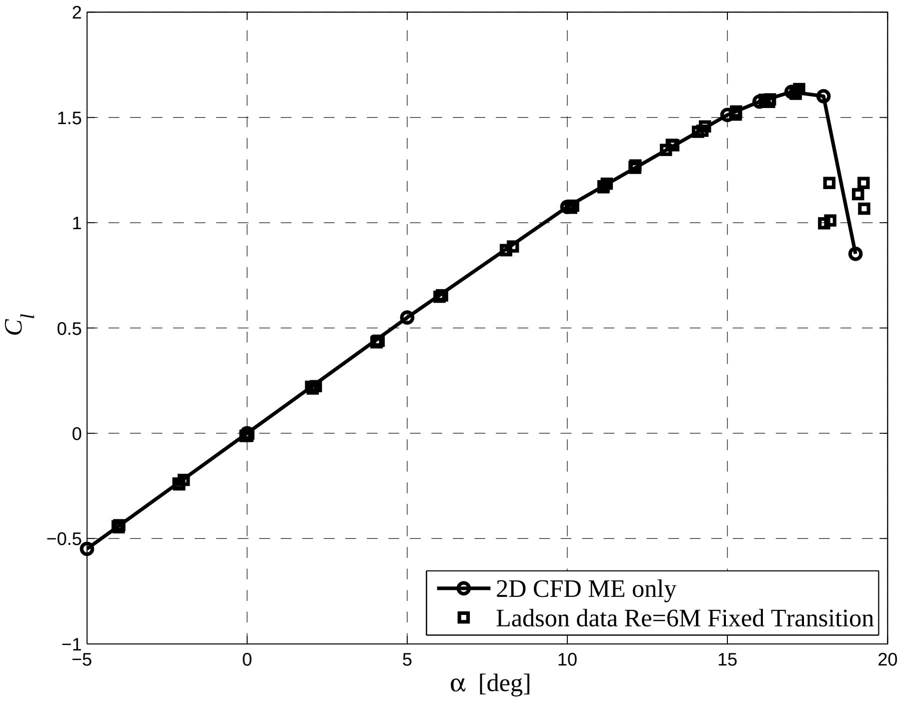

Figure 3.11: Lift coefficient (C_l) versus angle of attack (α) of the NACA 0012 validation case, shown with solid line (-o-). Experimental data from Ladson [2] show with squares. Agreement is excellent up to the stall region.

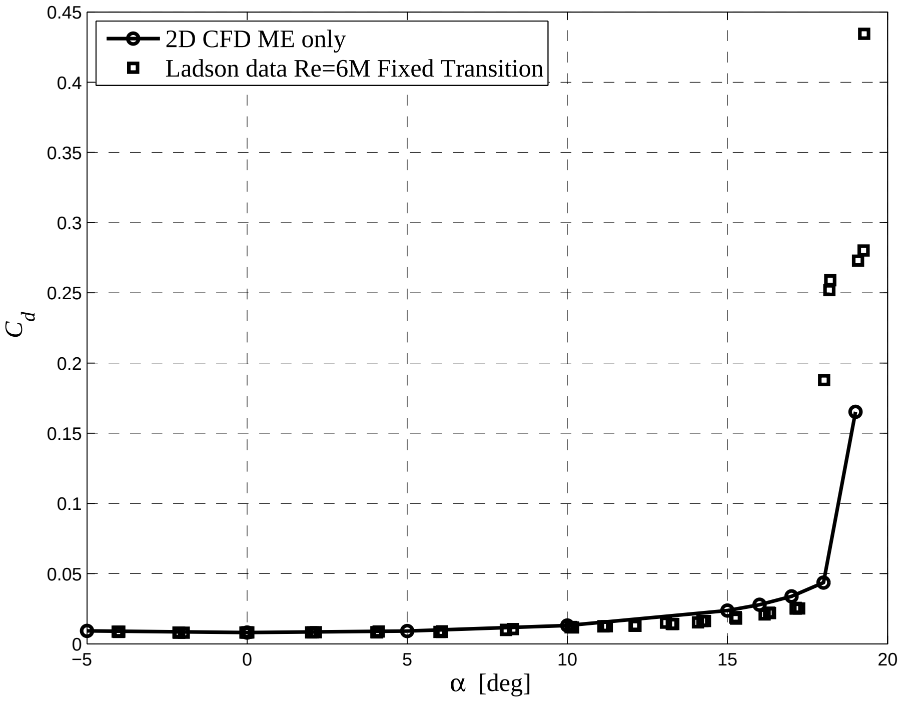

Figure 3.12: Drag coefficient (C_d) versus angle of attack (α) of the NACA 0012 validation case, shown with solid line (-o-). Experimental data from Ladson [2] show with squares. Agreement is excellent for lower $\alpha < 10°$, but not as good for higher angle of attack close to the stall region

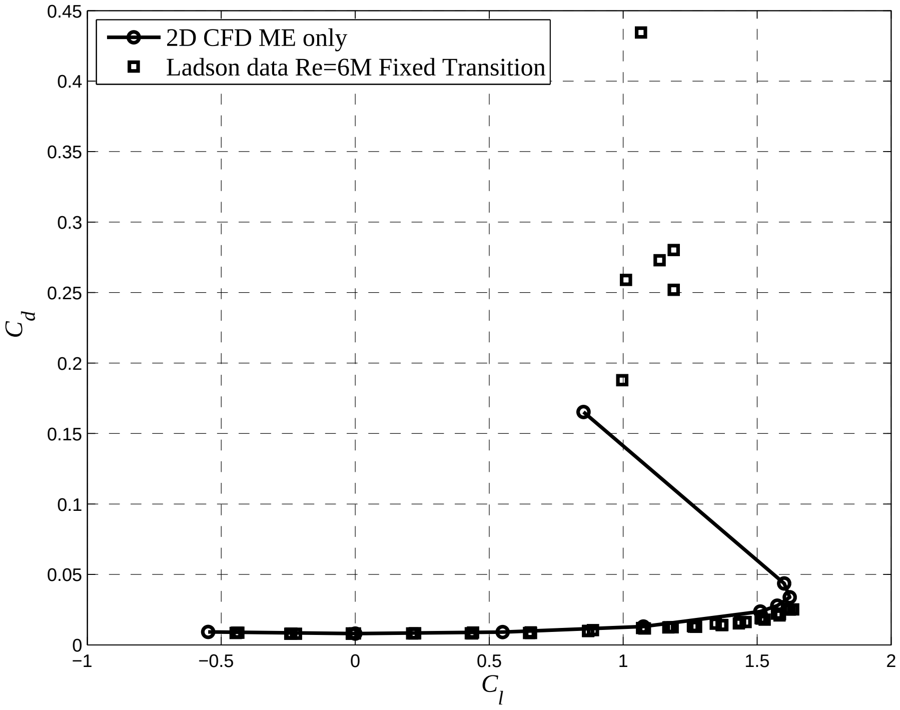

Figure 3.13: Drag coefficient (C_d) versus Lift coefficient (C_l) of the NACA 0012 validation case, shown with solid line (-o-). Experimental data from Ladson [2] show with squares. Agreement is excellent for low $(C_l < 1)$

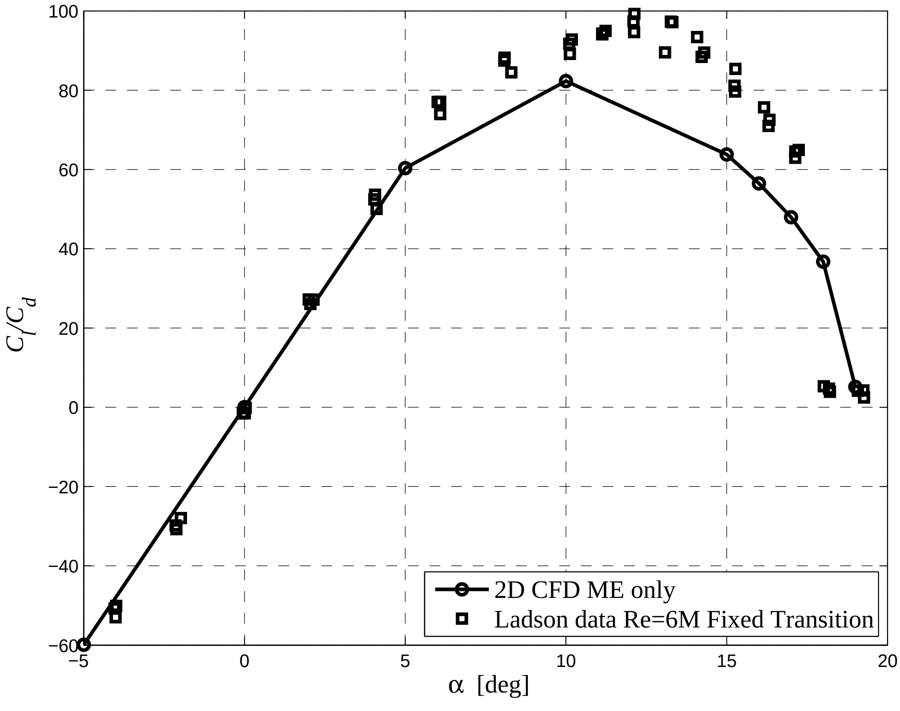

Figure 3.14: Lift to Drag coefficient ratio C_l/C_d versus angle of attack (α) of the NACA 0012 validation case, shown with solid line (-o-). Experimental data from Ladson [2] show with squares. Agreement is excellent up to $\alpha < 5^\circ$

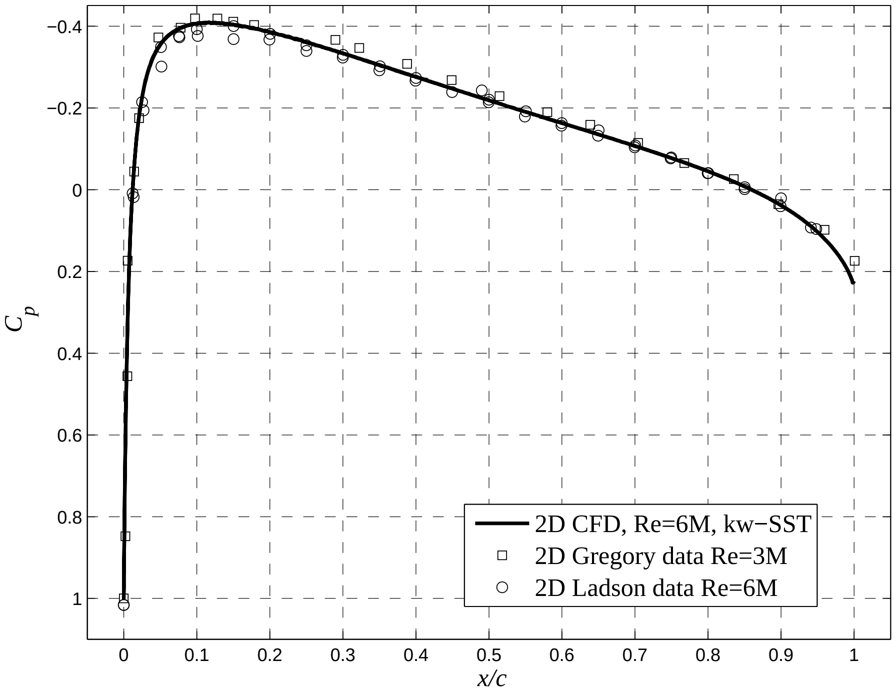

Figure 3.15: Pressure coefficient (C_p) of upper NACA 0012 surface for angle of attack $\alpha = 0°$, shown with solid line (-). $C_l \approxeq 0$. Gregory experimental data [3] shown with square markers and Ladson data [4] with circles.

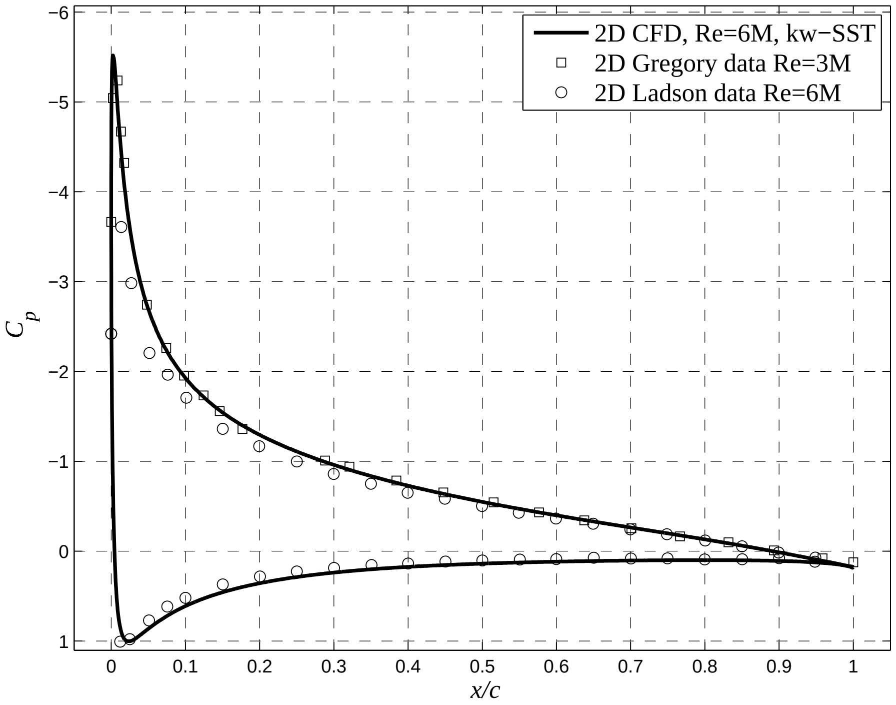

Figure 3.16: Pressure coefficient (C_p) of upper NACA 0012 surface for angle of attack $\alpha = 10°$, shown with solid line (-). $C_l \approxeq 1.1$. Gregory experimental data [3] shown with square markers and Ladson data [4] with circles.

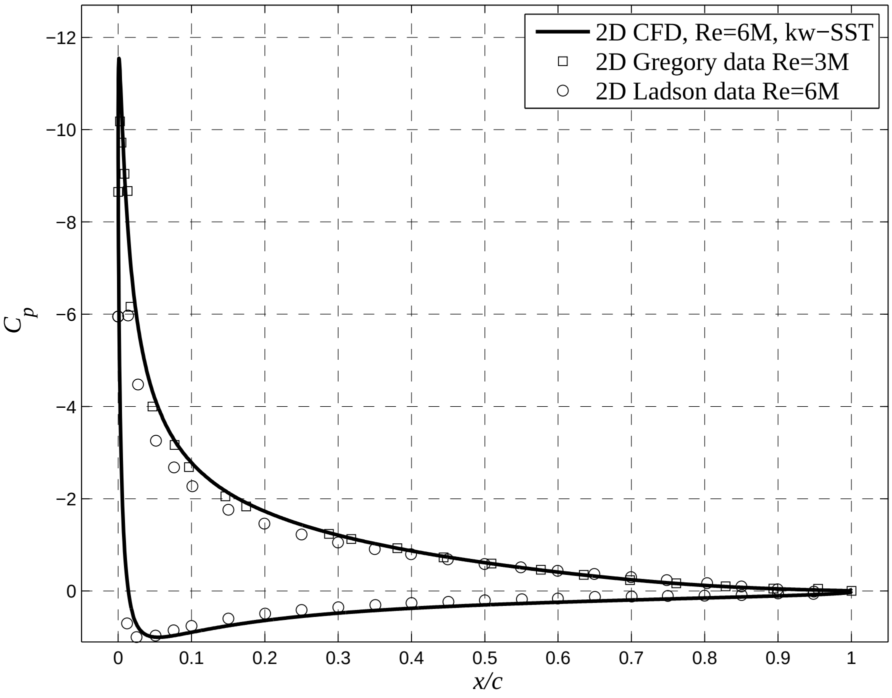

Figure 3.17: Pressure coefficient (C_p) of upper NACA 0012 surface for angle of attack $\alpha = 15°$, shown with solid line (-). $C_l \approxeq 1.5$. Gregory experimental data [3] shown with square markers and Ladson data [4] with circles.

3.3 Performance Analysis of the F11 Trawl-Door

Here, the F11 trawl-door, shown in Fig. 3.5, will be analysed in order to determine its performance. The high-fidelity CFD model proposed in Section 3.2 above and verified in Section 3.2.6 will be used as the CFD model in order to obtain results regarding its performance. The F11 trawl-door model is evaluated at number of different angle of attacks or from $\alpha = -5^\circ$ to $\alpha = 60^\circ$ with 5 degree increments. Lift, drag, skin friction and pressure coefficients are of special interest. In addition, velocity contour plots of the flow over the geometry are useful in evaluation of separation. This analysis is important step in investigating the F11 trawl-door characteristics and performance in addition to serve as a baseline or for comparison against to the optimum design obtained with the optimization process.

In addition to the analysis of the F11 trawl-door design we investigate the effects of the slats by removing them one at a time and performing the performance analysis again. In total three cases are considered:

1. Three (3) element analysis, main element and two slats. Analyse current F11 trawl-door design.
2. Two (2) element analysis, main element and one slat. Modify the F11 trawl-door geometry by removing only the slat furthest upstream. No other modification is done to the geometry.
3. One (1) element analysis, main element only. Modify the F11 trawl-door geometry by removing both slats. No other modification is done to geometry.

3.3.1 Results

Lift and drag performance analysis are presented in Fig. 3.18 to Fig. 3.21. Velocity contours, skin friction and pressure coefficient plots for the F11 trawl-door design are shown in Fig. 3.22 to Fig. 3.35. Note that main element chord length c_{ME} will be denoted as c to minimize notation.

Inspecting Fig. 3.18 reveals that flow remains attached for relatively low angles of attack when considering the main element only, and stall occurs close to $\alpha = 10^\circ$. For the main element with one slat the stall occurs at $\alpha = 20^\circ$ and for the F11 design, main element with two slats the stall occurs at $\alpha = 25^\circ$. Adding slats seems to improve the performance as expected by delaying the stall and increasing the $C_{l,\max}$ by extending the lift slope similarly as shown in Fig. B.11. Leading edge slats are intended to hinder separation from the leading edge. Therefore, they are only needed for high angle of attacks where flow separation starts to appear. They simply allow high-pressure fluid from lower surface to flow over the upper surface delaying the separation and stall. They also increase the area, which will increase lift as shown in Fig. B.11. $C_{l,\max}$ is increased as well as the stall angle of attack [37, 38].

Inspecting Fig. 3.19 we can split the plot into three regions, first where stall has not occurred where $\alpha < 20°$, after stall has occurred $20° < \alpha < 35°$ and $\alpha > 35°$. As shown in part $\alpha < 20°$ prior to stall drag increases as more slats are added to the assembly for such low angle of attacks simply because of more area that flow needs to pass. As the angle of attack is increased beyond stall $\alpha > \alpha_{stall}$ drag rises due to massive separation as shown in the region $20° < \alpha < 35°$. Effectiveness of slats are evident here where by adding slats, flow remains attached longer reducing separation and drag. In the last region $\alpha > 35°$ flow simply needs to pass more area as more slats are added increasing the drag again.

Inspecting Fig. 3.21 we note that the efficiency, lift to drag coefficient ratio C_l/C_d is highest at low angle of attack close to $\alpha = 5$. Inspecting Fig. 3.22 to Fig. 3.35 we can see that separation becomes massive close to and after stall. We can also note that at various angle of attacks, e.g., $\alpha = 20°$ that separation bubbles form at upper or lower surface on the leading edge on all elements, main element, slat 1 and slat 2. This effect can be further seen by inspecting skin friction coefficient plot where we clearly note that flow is reversed and separates at various locations where $C_f = 0$. Pressure coefficient drops where separation occurs leading to a loss in lift. It must be noted that during CFD simulation for high angles of attack that transient effects where dominant in the flow and a steady-state analysis might be inaccurate.

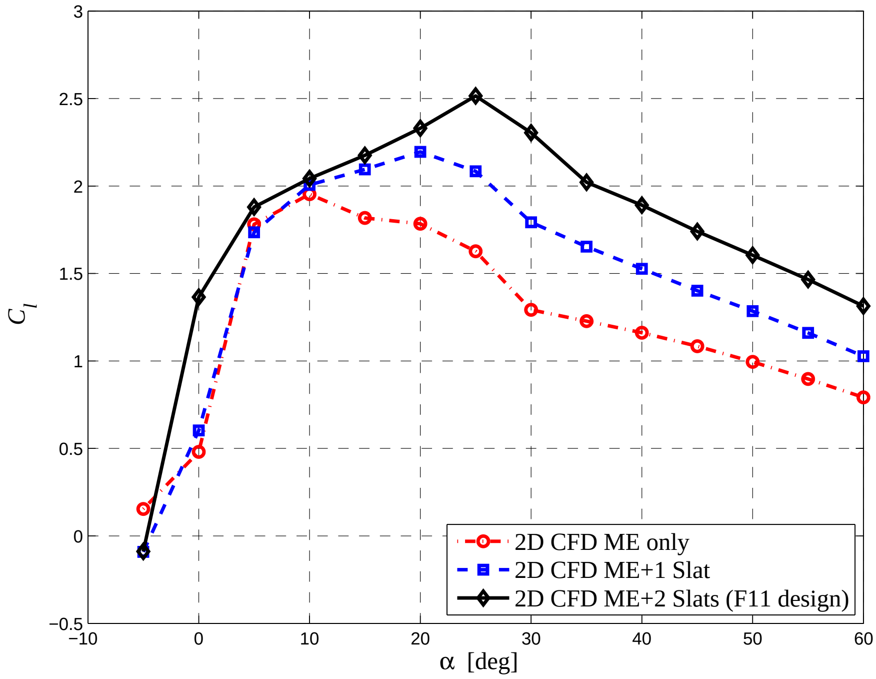

Figure 3.18: Lift coefficient (C_l) versus angle of attack (α) at $V_\infty = 2m/s, Re_c = 2\times10^6$. Computational results are shown with dotted dash line (.-.), dashed line (- -) and solid line (–) for Main Element only (ME), ME + 1 slat and ME + 2 (the F11 trawl-door design) respectively.

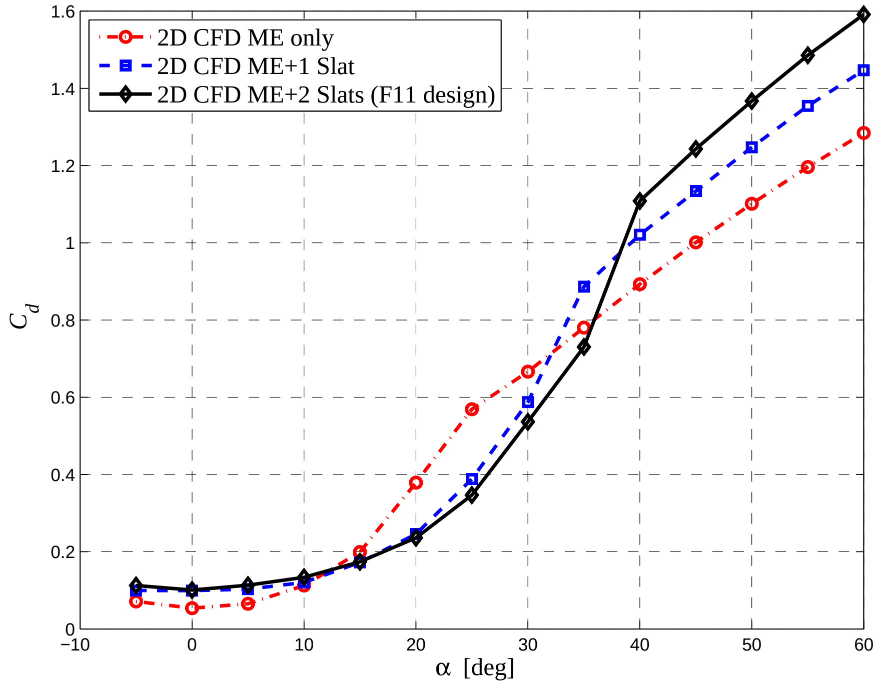

Figure 3.19: Drag coefficient (C_d) versus angle of attack (α) at $V_\infty = 2m/s, Re_c = 2\times10^6$. Computational results are shown with dotted dash line (.-.), dashed line (- -) and solid line (–) for Main Element only (ME), ME + 1 slat and ME + 2 (the F11 trawl-door design) respectively.

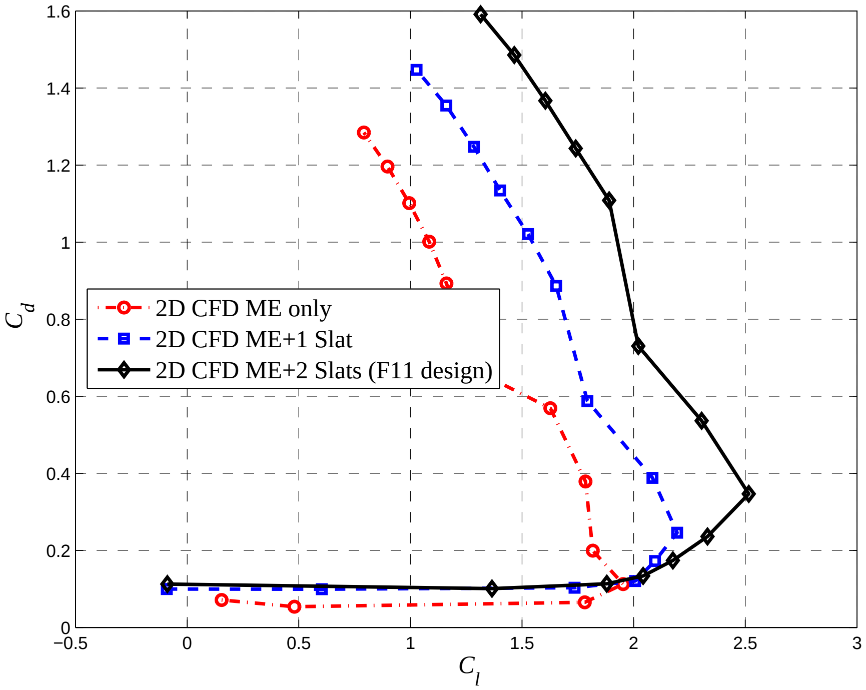

Figure 3.20: Drag coefficient (C_d) versus Lift coefficient (C_l) at $V_\infty = 2m/s, Re_c = 2 \times 10^6$. Computational results are shown with dotted dash line (.-.), dashed line (- -) and solid line (–) for Main Element only (ME), ME + 1 slat and ME + 2 (the F11 trawl-door design) respectively.

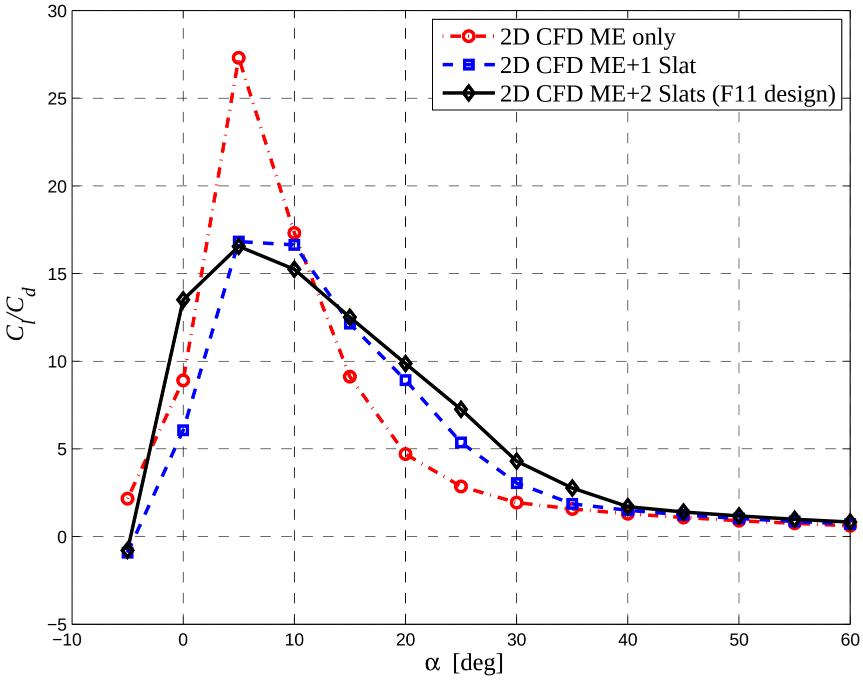

Figure 3.21: Lift to Drag ratio C_l/C_d versus angle of attack (α) at $V_\infty = 2m/s, Re_c = 2 \times 10^6$. Computational results are shown with dotted dash line (.-.), dashed line (- -) and solid line (–) for Main Element only (ME), ME + 1 slat and ME + 2 (the F11 trawl-door design) respectively.

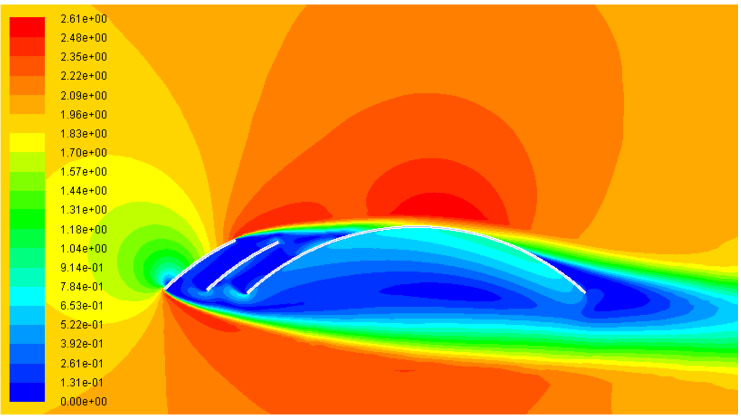

(a)

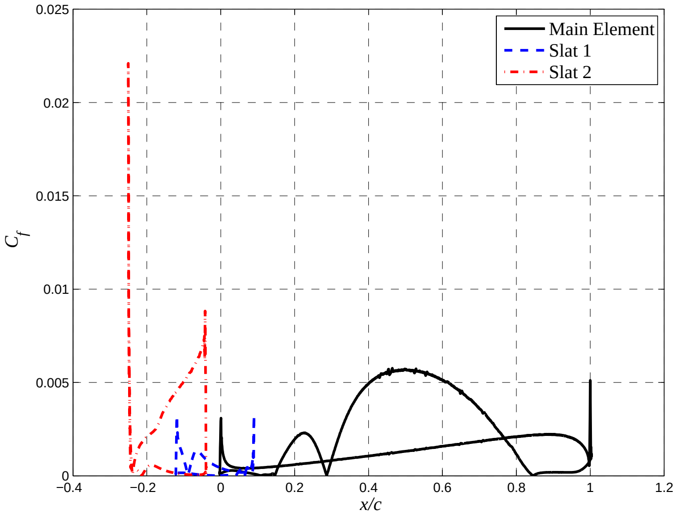

(b)

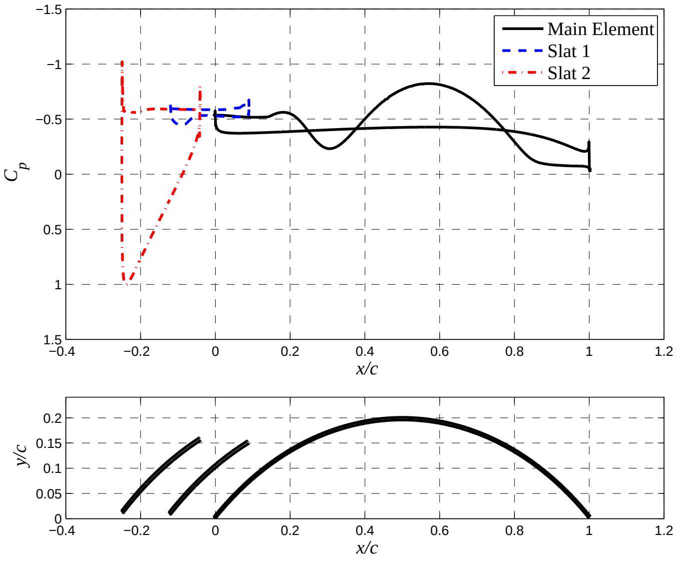

(c)

Figure 3.22: F11 trawl-door characteristics at $V_\infty = 2m/s$, $Re_c = 2\times10^6$, angle of attack $\alpha = -5°$. a) Velocity contour, b) Skin friction coefficient (C_f), c) Pressure coefficient (C_p)

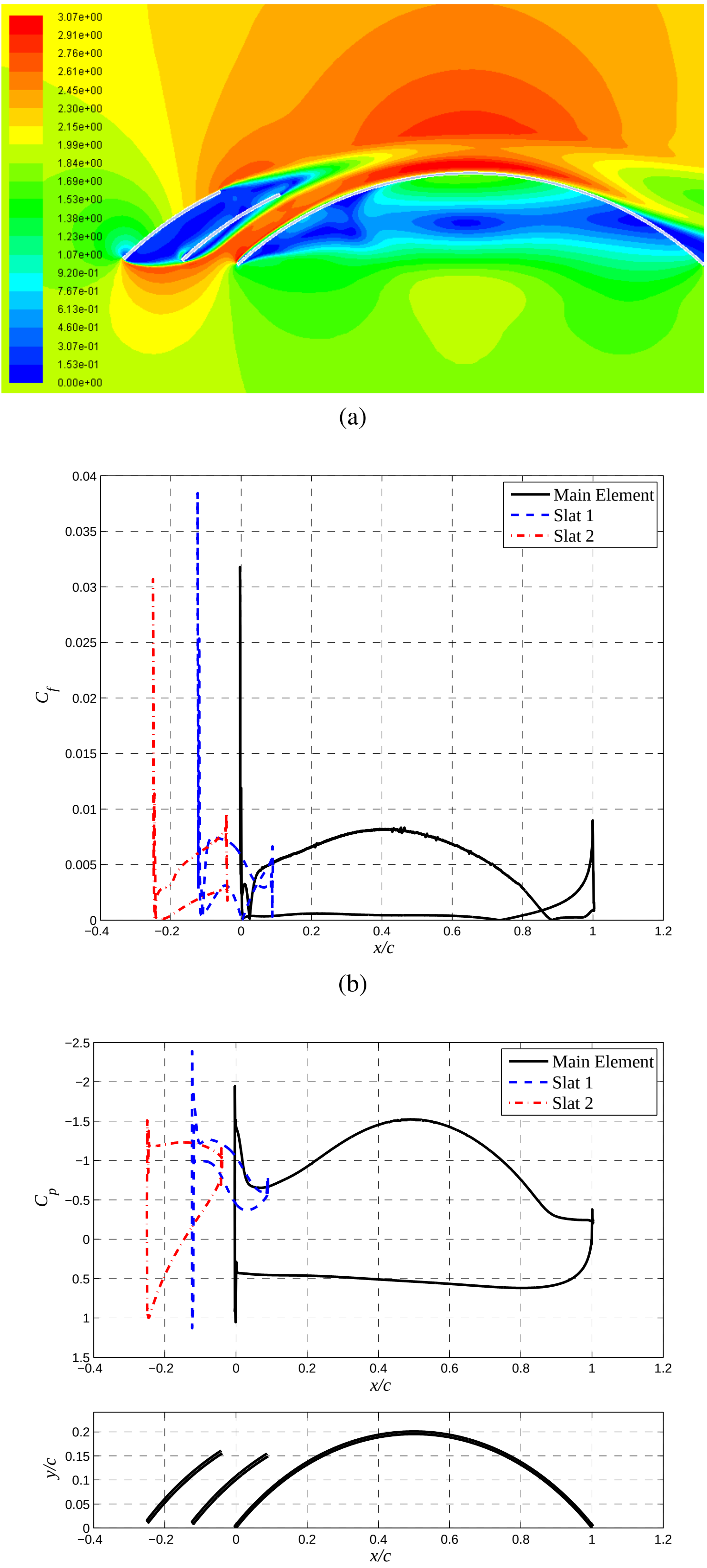

(a)

(b)

(c)

Figure 3.23: F11 trawl-door characteristics at $V_\infty = 2m/s$, $Re_c = 2 \times 10^6$, angle of attack $\alpha = 0°$. a) Velocity contour, b) Skin friction coefficient (C_f), c) Pressure coefficient (C_p)

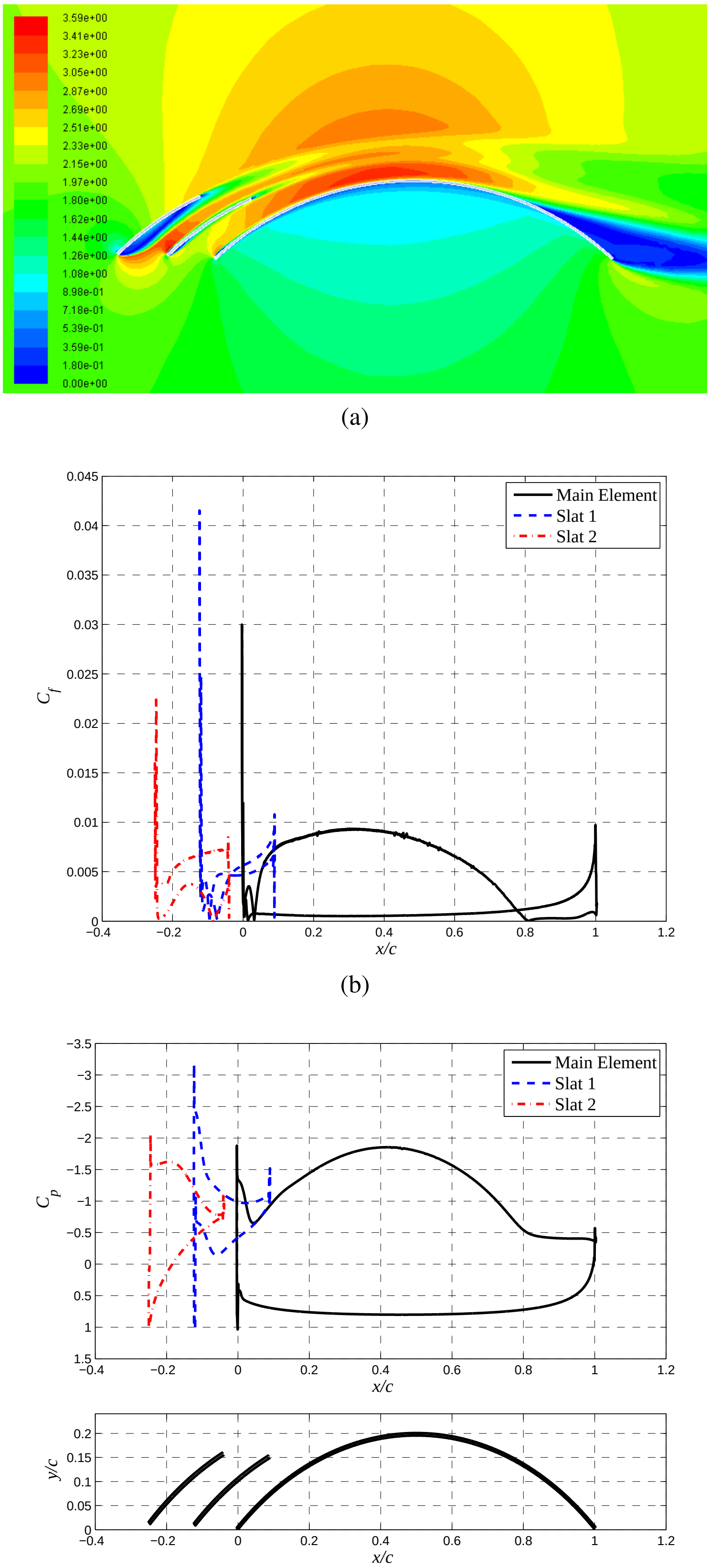

(a)

(b)

(c)

Figure 3.24: F11 trawl-door characteristics at $V_\infty = 2m/s$, $Re_c = 2 \times 10^6$, angle of attack $\alpha = 5°$. a) Velocity contour, b) Skin friction coefficient (C_f), c) Pressure coefficient (C_p)

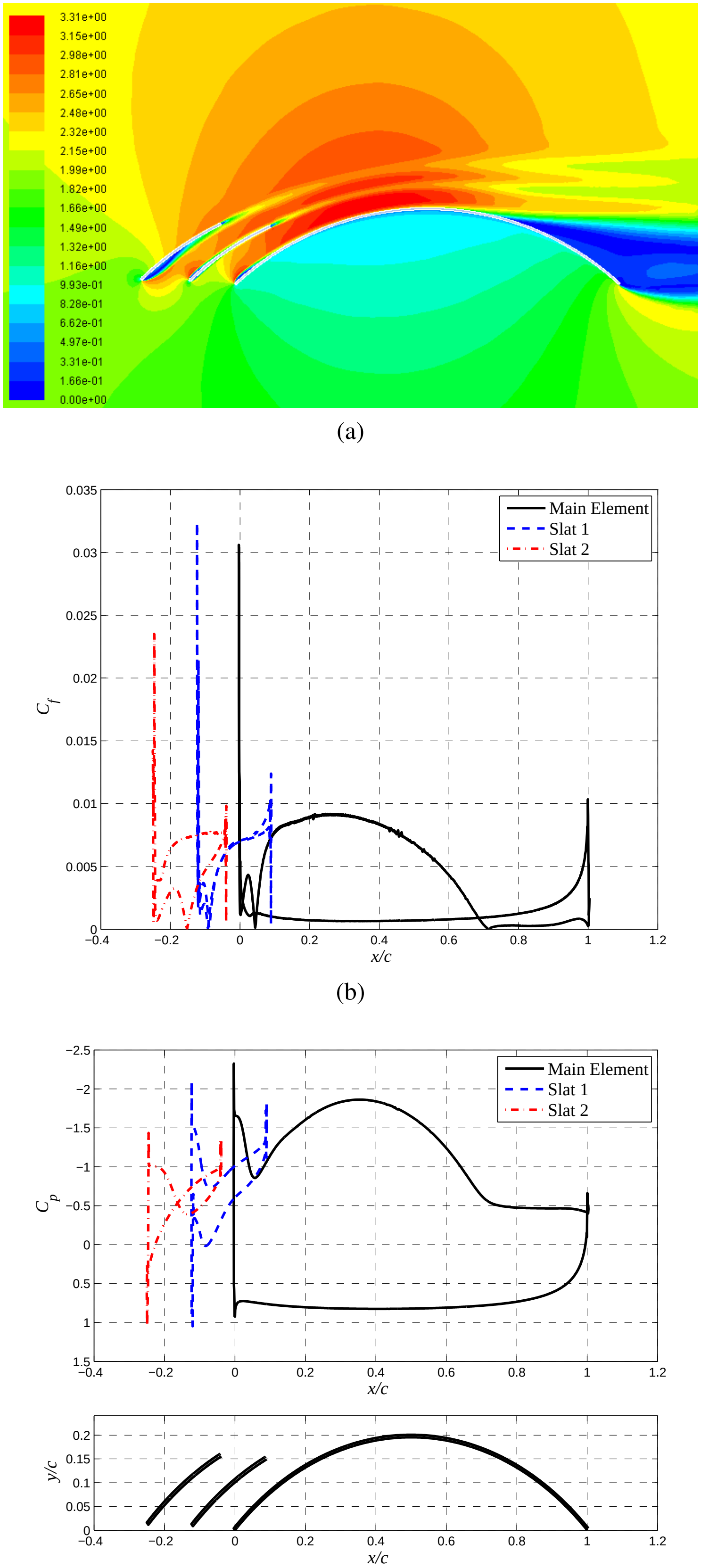

(a)

(b)

(c)

Figure 3.25: F11 trawl-door characteristics at $V_\infty = 2m/s$, $Re_c = 2 \times 10^6$, angle of attack $\alpha = 10^\circ$. a) Velocity contour, b) Skin friction coefficient (C_f), c) Pressure coefficient (C_p)

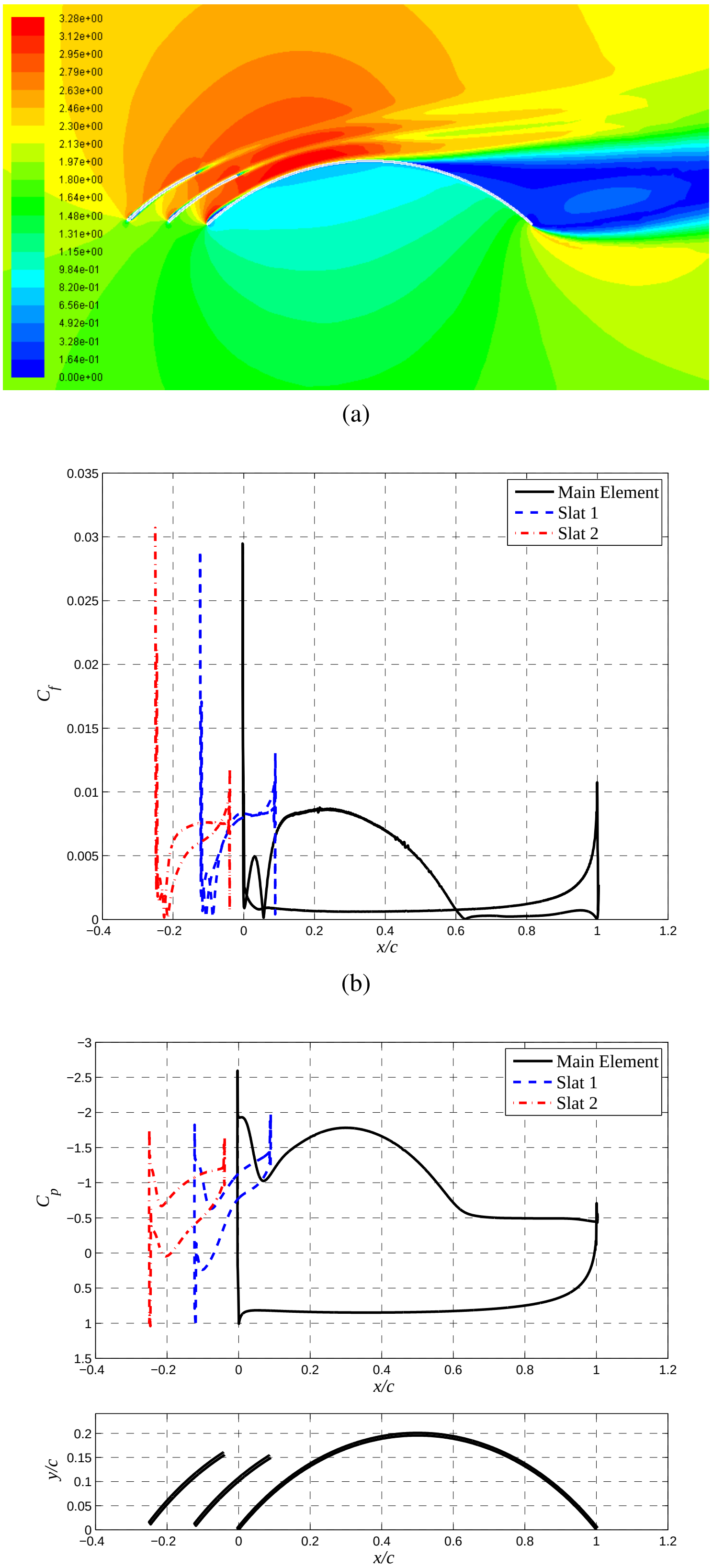

(a)

(b)

(c)

Figure 3.26: F11 trawl-door characteristics at $V_\infty = 2m/s$, $Re_c = 2 \times 10^6$, angle of attack $\alpha = 15°$. a) Velocity contour, b) Skin friction coefficient (C_f), c) Pressure coefficient (C_p)

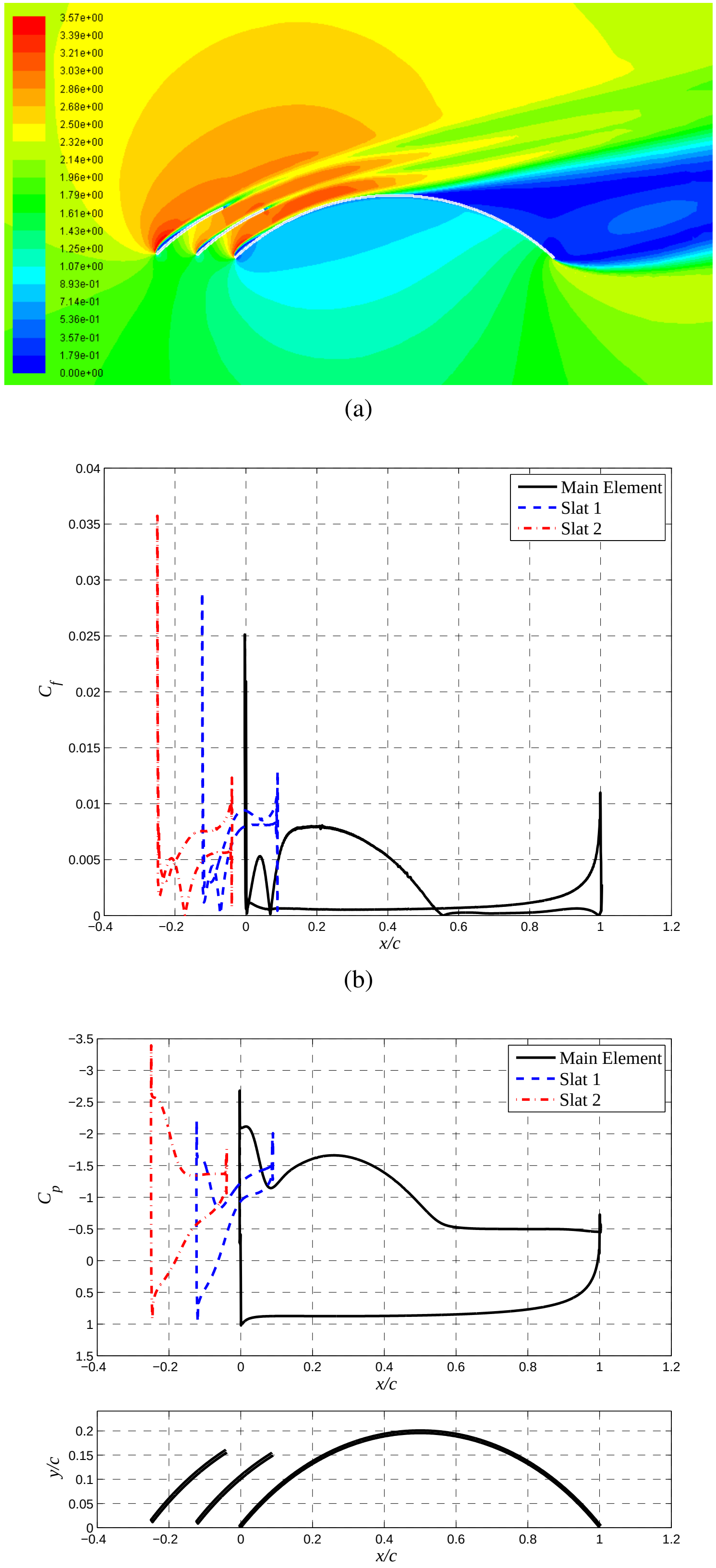

(a)

(b)

(c)

Figure 3.27: F11 trawl-door characteristics at $V_\infty = 2m/s$, $Re_c = 2 \times 10^6$, angle of attack $\alpha = 20°$. a) Velocity contour, b) Skin friction coefficient (C_f), c) Pressure coefficient (C_p)

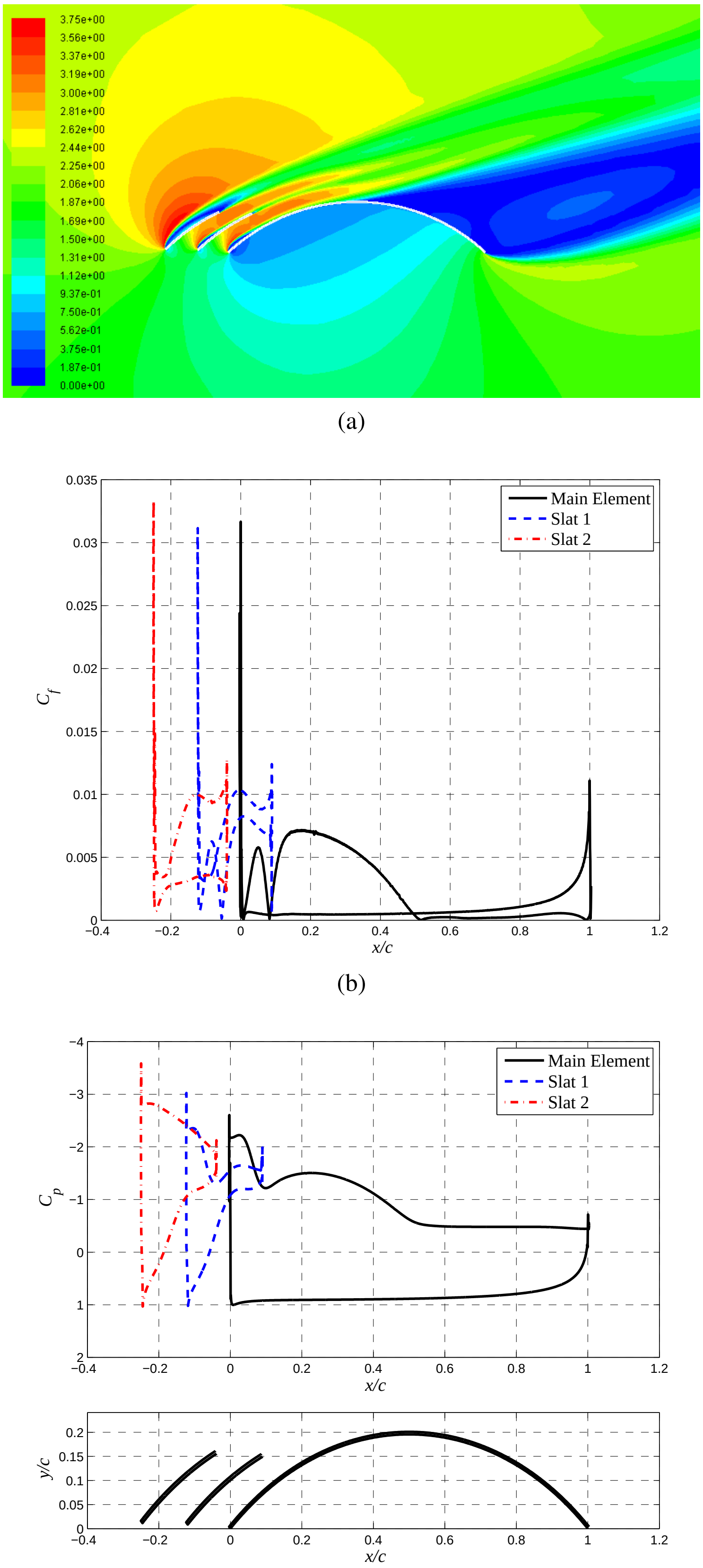

(a)

(b)

(c)

Figure 3.28: F11 trawl-door characteristics at $V_\infty = 2m/s$, $Re_c = 2 \times 10^6$, angle of attack $\alpha = 25°$. a) Velocity contour, b) Skin friction coefficient (C_f), c) Pressure coefficient (C_p)

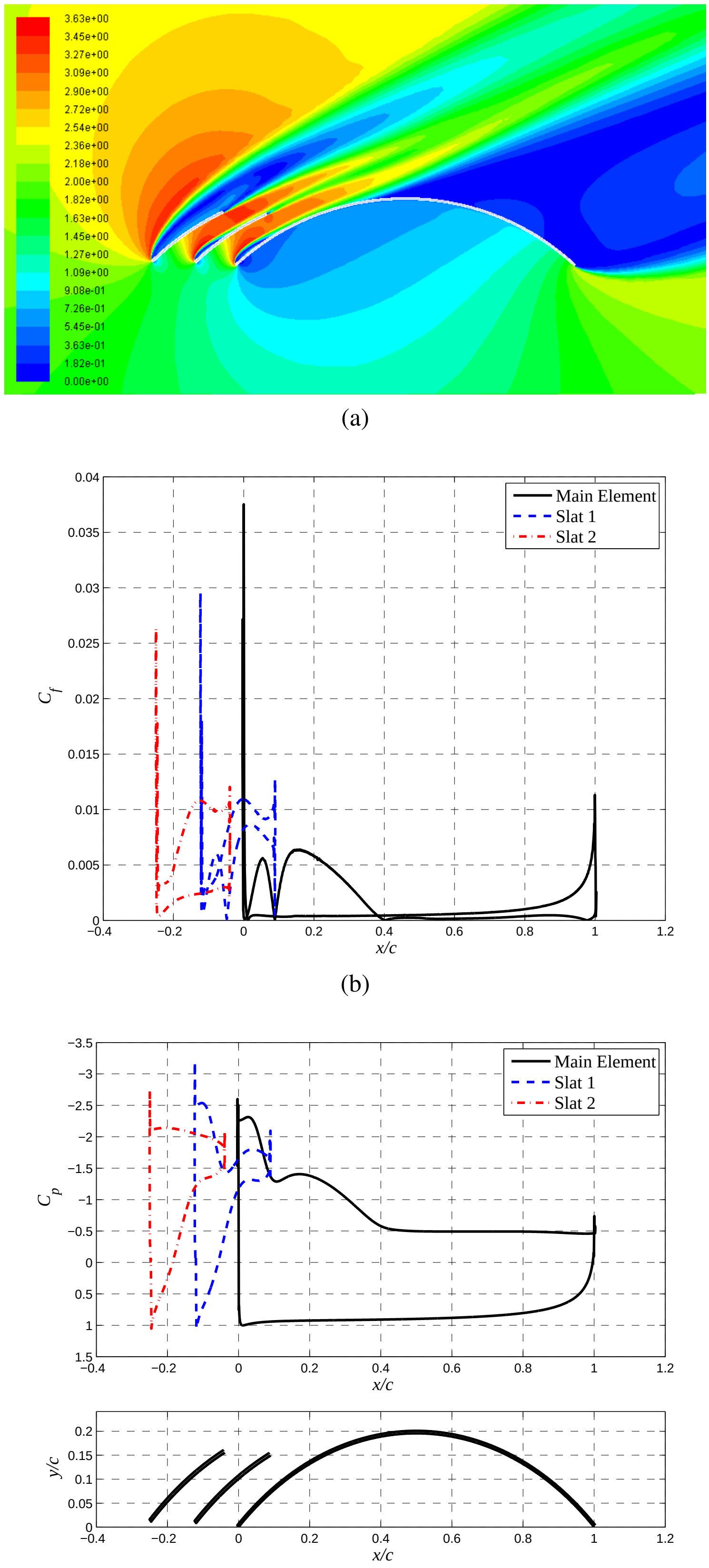

(a)

(b)

(c)

Figure 3.29: F11 trawl-door characteristics at $V_\infty = 2m/s$, $Re_c = 2 \times 10^6$, angle of attack $\alpha = 30°$. a) Velocity contour, b) Skin friction coefficient (C_f), c) Pressure coefficient (C_p)

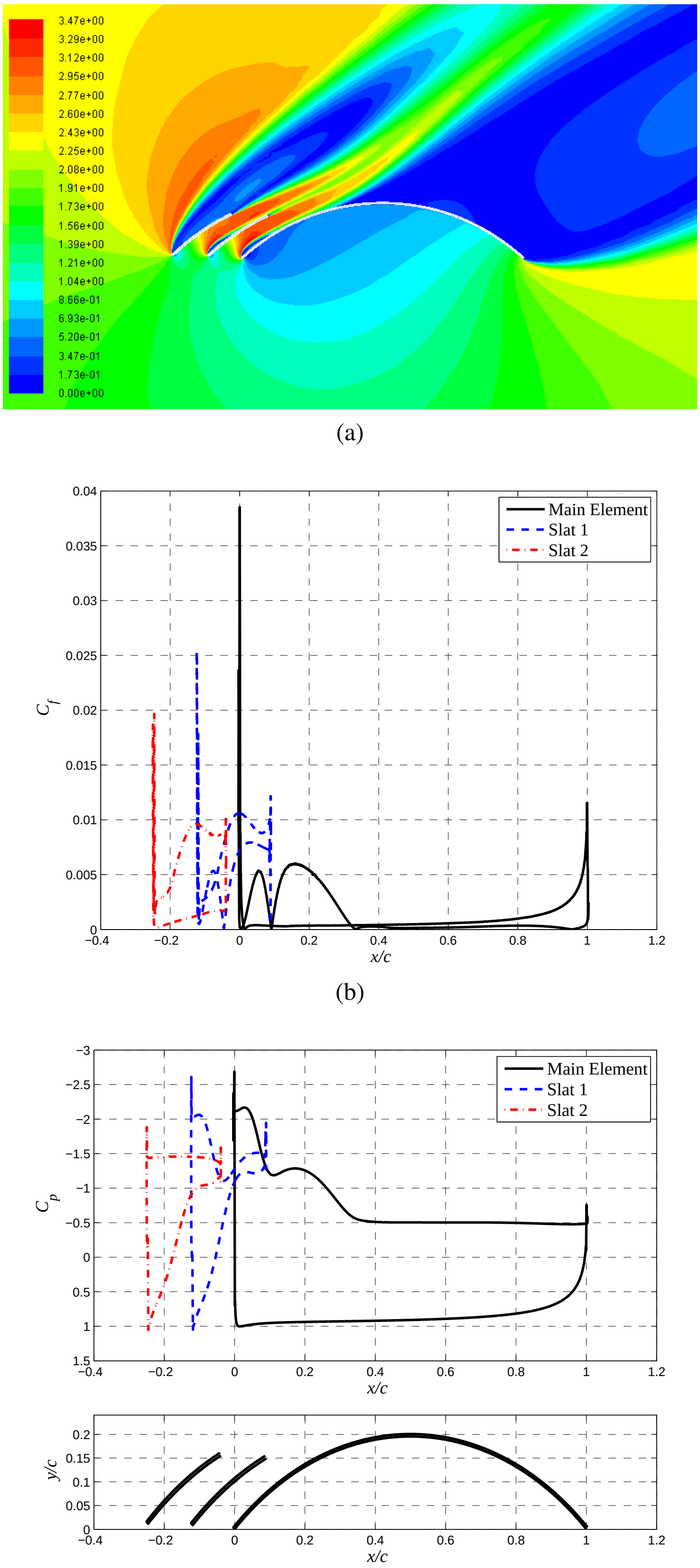

(a)

(b)

(c)

Figure 3.30: F11 trawl-door characteristics at $V_\infty = 2m/s$, $Re_c = 2 \times 10^6$, angle of attack $\alpha = 35°$. a) Velocity contour, b) Skin friction coefficient (C_f), c) Pressure coefficient (C_p)

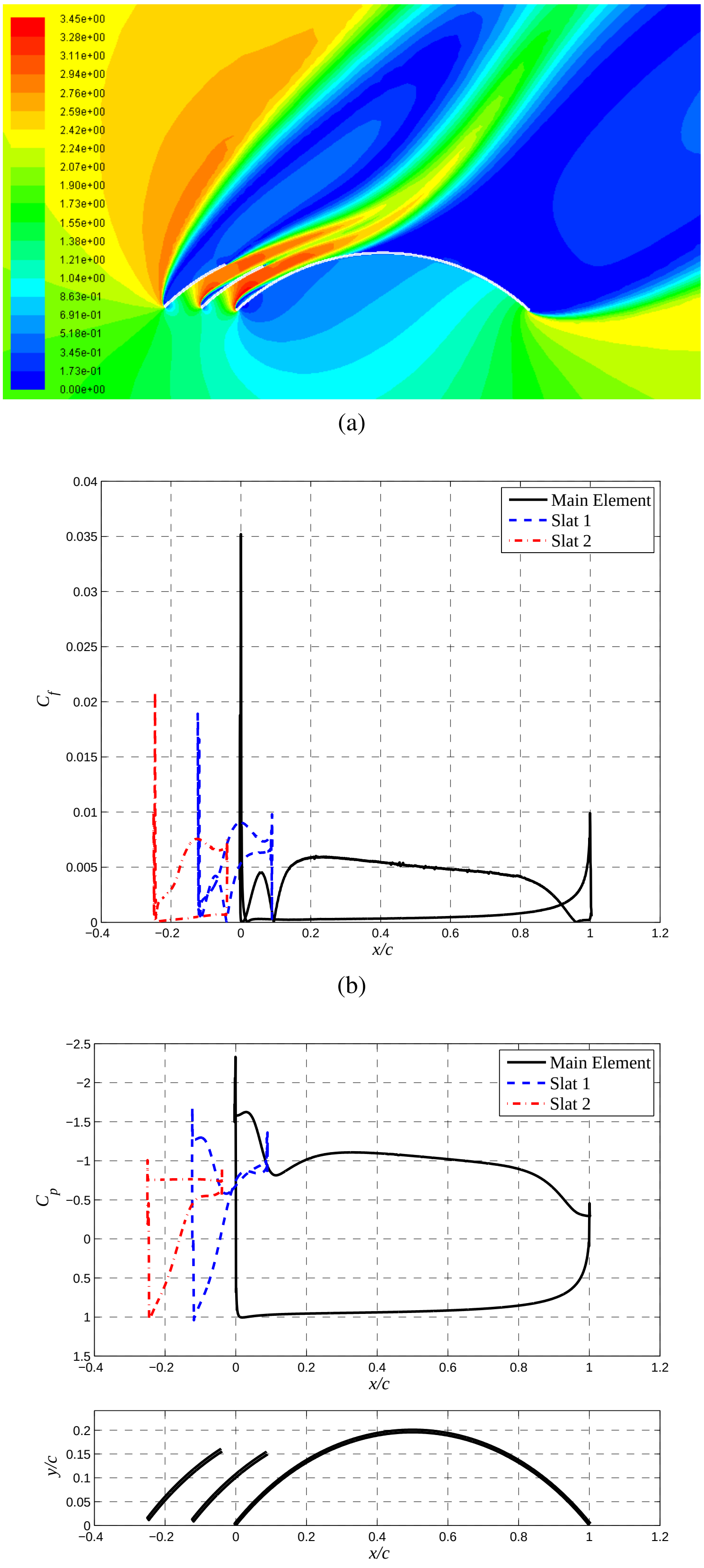

(a)

(b)

(c)

Figure 3.31: F11 trawl-door characteristics at $V_\infty = 2m/s$, $Re_c = 2 \times 10^6$, angle of attack $\alpha = 40°$. a) Velocity contour, b) Skin friction coefficient (C_f), c) Pressure coefficient (C_p)

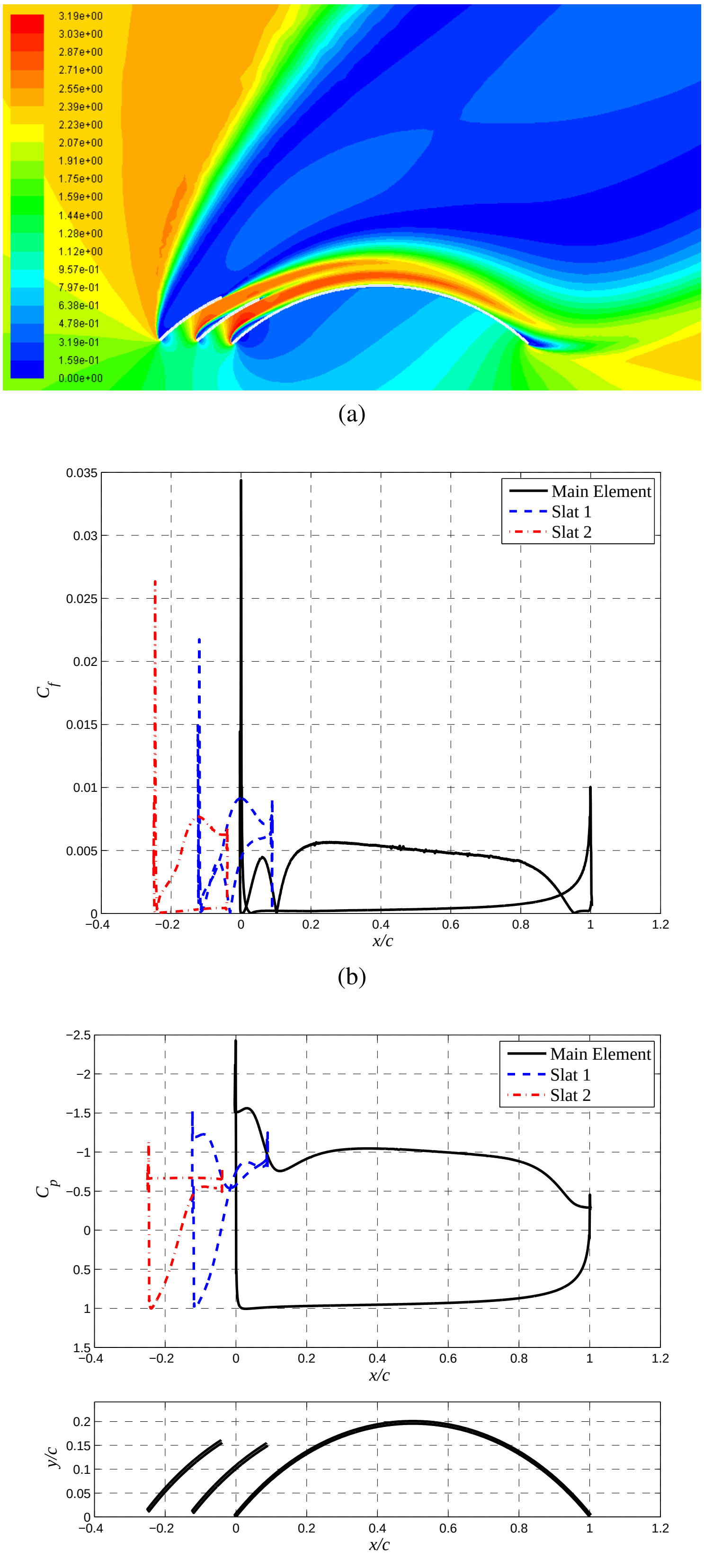

(a)

(b)

(c)

Figure 3.32: F11 trawl-door characteristics at $V_\infty = 2m/s$, $Re_c = 2 \times 10^6$, angle of attack $\alpha = 45°$. a) Velocity contour, b) Skin friction coefficient (C_f), c) Pressure coefficient (C_p)

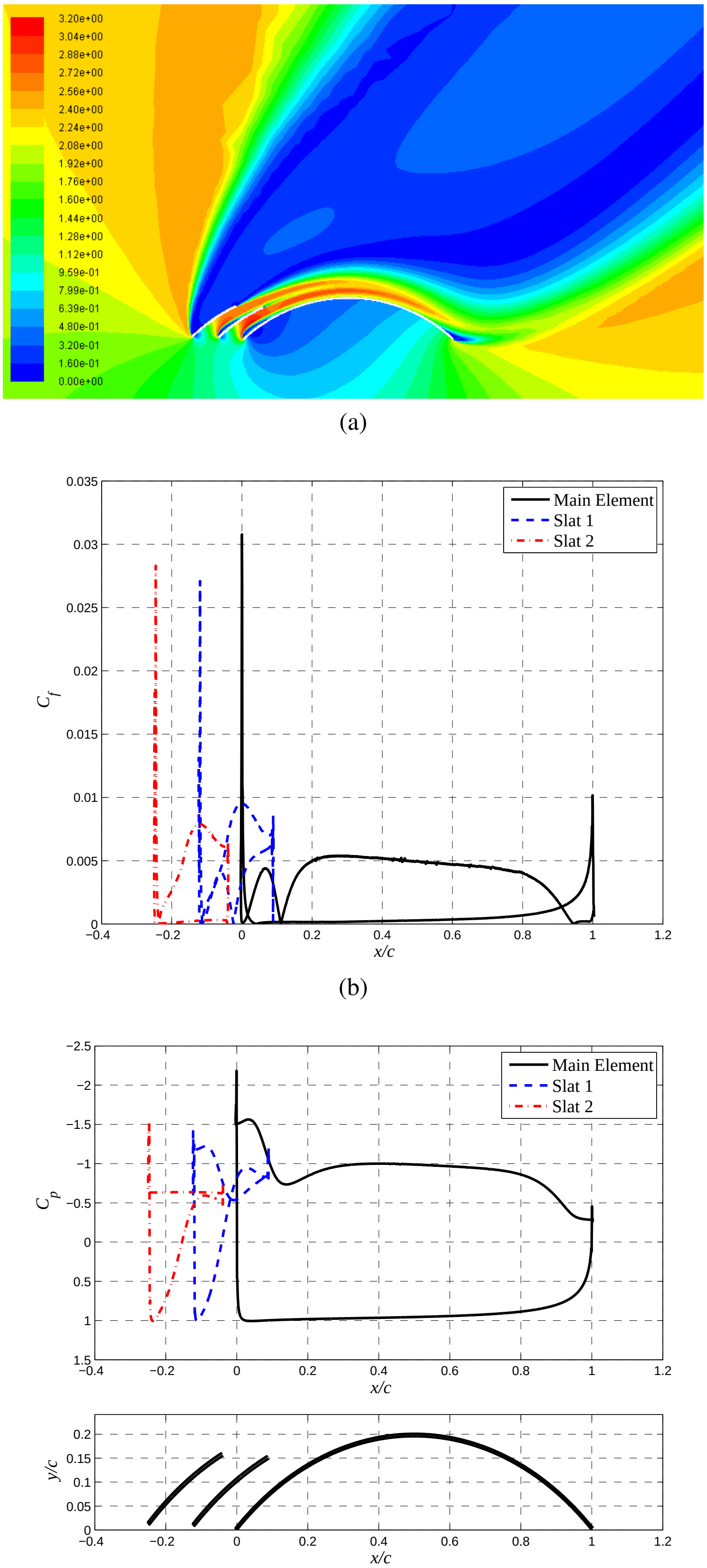

(a)

(b)

(c)

Figure 3.33: F11 trawl-door characteristics at $V_\infty = 2m/s$, $Re_c = 2 \times 10^6$, angle of attack $\alpha = 50°$. a) Velocity contour, b) Skin friction coefficient (C_f), c) Pressure coefficient (C_p)

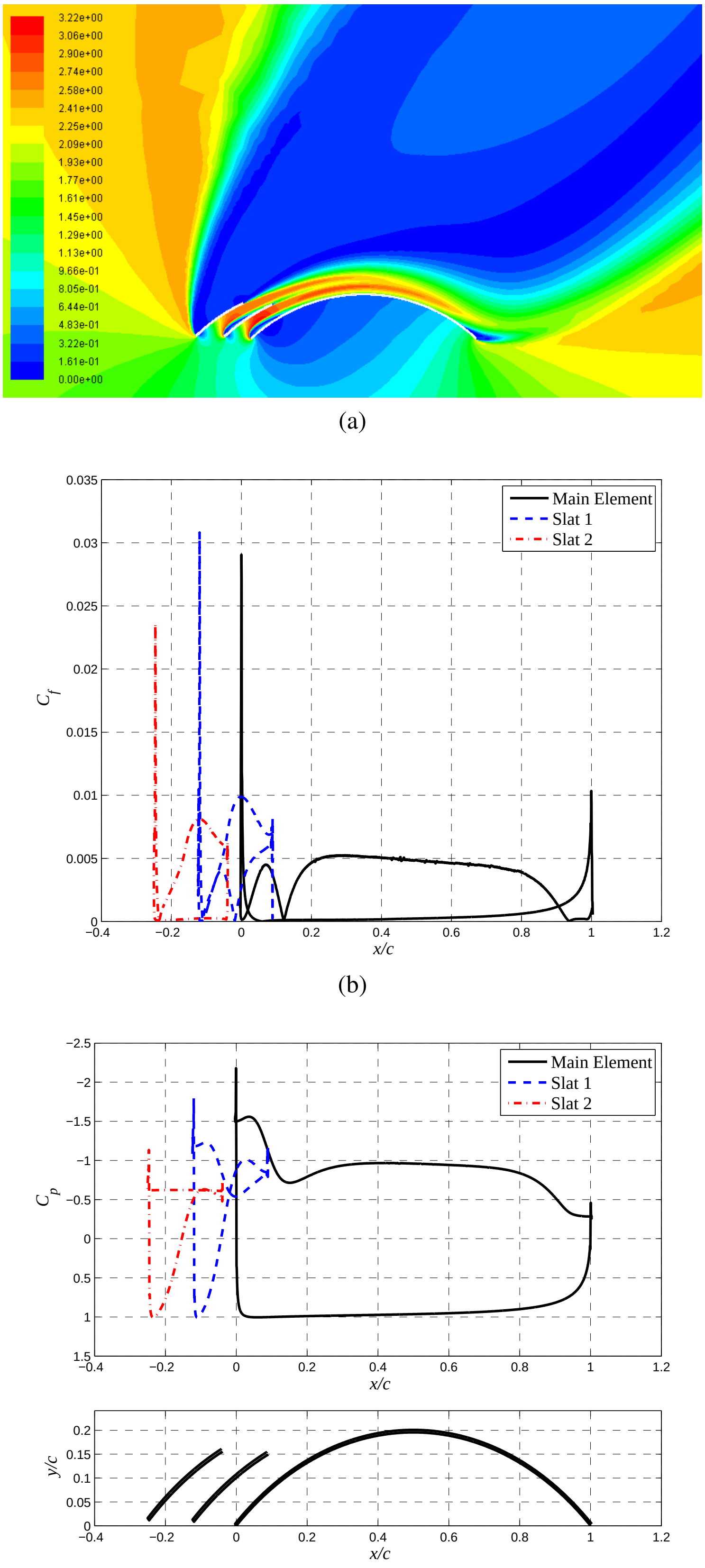

(a)

(b)

(c)

Figure 3.34: F11 trawl-door characteristics at $V_\infty = 2m/s$, $Re_c = 2 \times 10^6$, angle of attack $\alpha = 55°$. a) Velocity contour, b) Skin friction coefficient (C_f), c) Pressure coefficient (C_p)

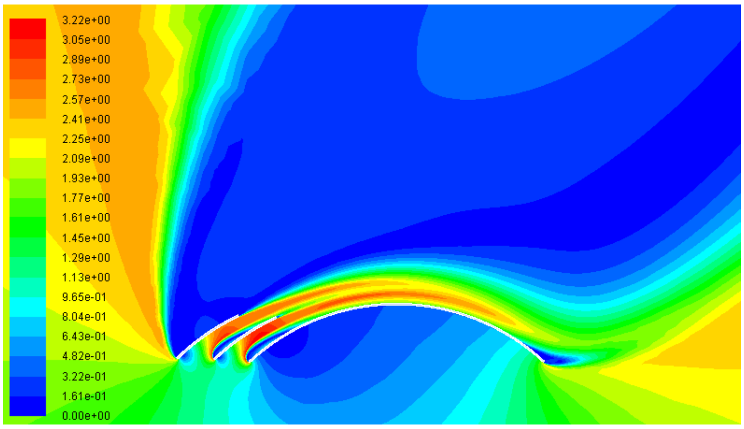

(a)

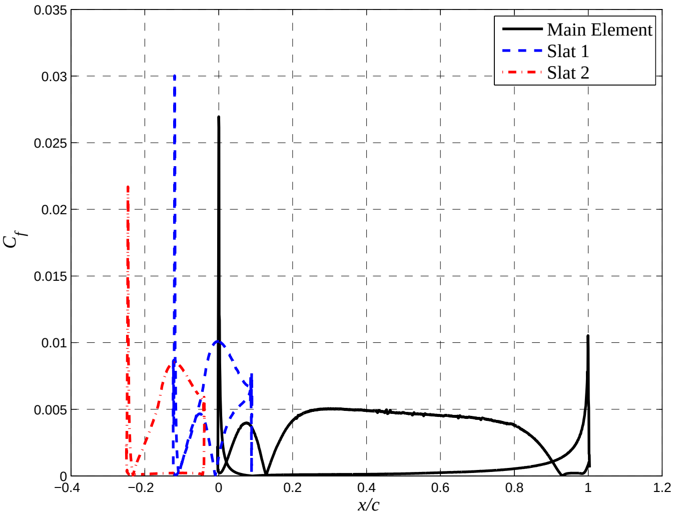

(b)

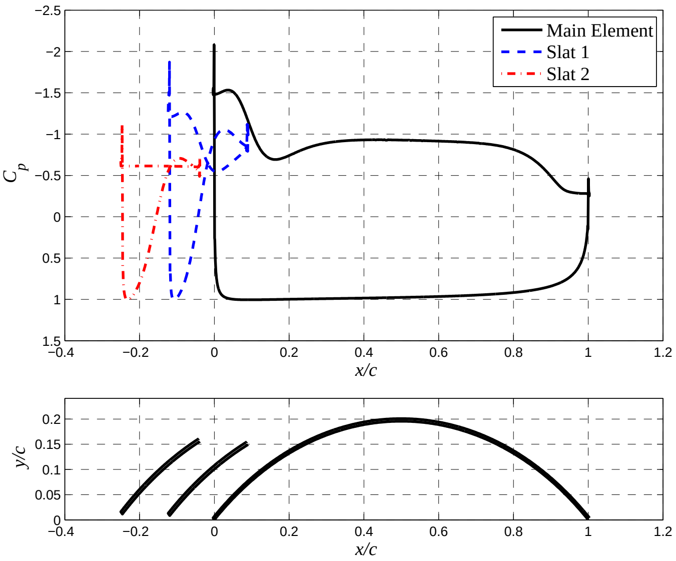

(c)

Figure 3.35: F11 trawl-door characteristics at $V_\infty = 2m/s$, $Re_c = 2 \times 10^6$, angle of attack $\alpha = 60°$. a) Velocity contour, b) Skin friction coefficient (C_f), c) Pressure coefficient (C_p)

3.3.2 Numerical noise

In order for the optimization to perform as expected the robustness of both high-fidelity and the low-fidelity have to be tested. The low-fidelity model is described in Section 3.4.2. As noticed during the performance analysis a steady-state analysis of high angle of attack may be difficult to obtain, in terms of a converged or a stable solution. The problem is highly transient for high angles of attack. Numerical noise can become a dominant factor in the solution when solver simply does not converge and oscillation exists in the steady state solution.

In order to check high- and low-fidelity models for numerical noise we simply choose two designs, $\mathbf{x}_1$ and $\mathbf{x}_2$ that are close to each other and vary linearly the design variables between these two designs and investigate their response or characteristics ($\mathbf{x} = [x/c, y/c, \theta, \alpha]^T$, see Section 3.4.1 for definition). The intermediate designs are defined as

$$\mathbf{x} = \zeta \mathbf{x}_1 + (1-\zeta)\mathbf{x}_2, \tag{3.3.1}$$

where ζ is a number between 0 and 1. Using a sequence of different values of ζ, a number of different intermediate designs can be tested. Selecting sufficiently many points between the two designs the intermediate responses should change linearly only if numerical noise is none. If noise is present in one or both models high- or low-fidelity model, the responses will not be linear and problems can arise during optimization process. With noise in the low-fidelity model and a consistent high-fidelity the low-fidelity model will not be a good representation of the high-fidelity model since it does not follow the same trend as the high-fidelity model. This can lead to the optimization algorithm not converging or possibly inaccurate solution. We note that any two points within the design space are valid for this kind of test since the high- and low-fidelity models should be consistent.

The proposed high- and low-fidelity models were tested for consistency and robustness. We select two designs

$$\mathbf{x}_1 = [-0.2515, -0.0299, 22.3649, 2.8059], \tag{3.3.2}$$

$$\mathbf{x}_2 = [-0.2495, -0.0289, 22.3649, 2.8059], \tag{3.3.3}$$

at $V_\infty = 2m/s, Re = 2 \times 10^6$ and varying ζ 10 times or from, $\zeta = [0, 0.1, \ldots, 0.9, 1]$, resulting in total 11 tests. As show in Fig. 3.36 there is an obvious noise or oscillation in the low-fidelity response for both lift and drag. Linearity or consistency in response is much better in terms of the high-fidelity model except for one point at $\zeta = 0.8$. These results suggest that the low-fidelity model is noisy with change in lift and drag being obvious.

Oscillation around some mean response value is evident. This will mean that if an initial design or any design is close to an optimum, and the drag response change is small between designs, the optimization algorithm will get stuck and yield no improvement. The response must be smaller than the amplitude of the oscillation. Again, this means that any design that is close to an optimum may never reach the optimum due to this inconsistency in responses of the fine model and coarse model when geometry is varied slightly. Optimization algorithm will get stuck and yield no improved solution. Despite of this, improved designs may still be found globally if the difference in lift and drag coefficients response is at least larger than the noise or the amplitude of the oscillation around its mean value in the low-fidelity model.

3.3.3 Conclusion

Performance analysis of the three cases presented above reveals important knowledge about the F11 trawl-door design. By removing slats from the F11 one after another and performing the same analysis gives also important information about the improvements the slats add to the F11 design. Slats effect extends lift coefficient curve, where α_{stall} occurs at a higher angle of attack, hence $C_{l,\max}$ increases. Drag can also be seen increasing abruptly when stall occurs. The F11 trawl-door lacks smooth leading edges and aerodynamic shape as can seen in velocity contour plots, skin friction and pressure coefficient plots where separation bubbles form and pressure drops. This is a typical behaviour of a thin airfoil, see Appendix B.6. At some point between $\alpha = 40 - 45°$ the flow seems to reattach to the main element. This, however, is of little effect as pressure plot reveals and lift continues to decrease with higher angle of attack.

Numerical noise and oscillation in response is present as shown above. It is evident based on the discussion above that the resulting flow is difficult for steady state analysis since it is highly transient due to a massive flow separation, vortex shedding even at low angles of attack and numerical noise. It is therefore recommended that a transient analysis is performed for this type of problem at high angles of attack.

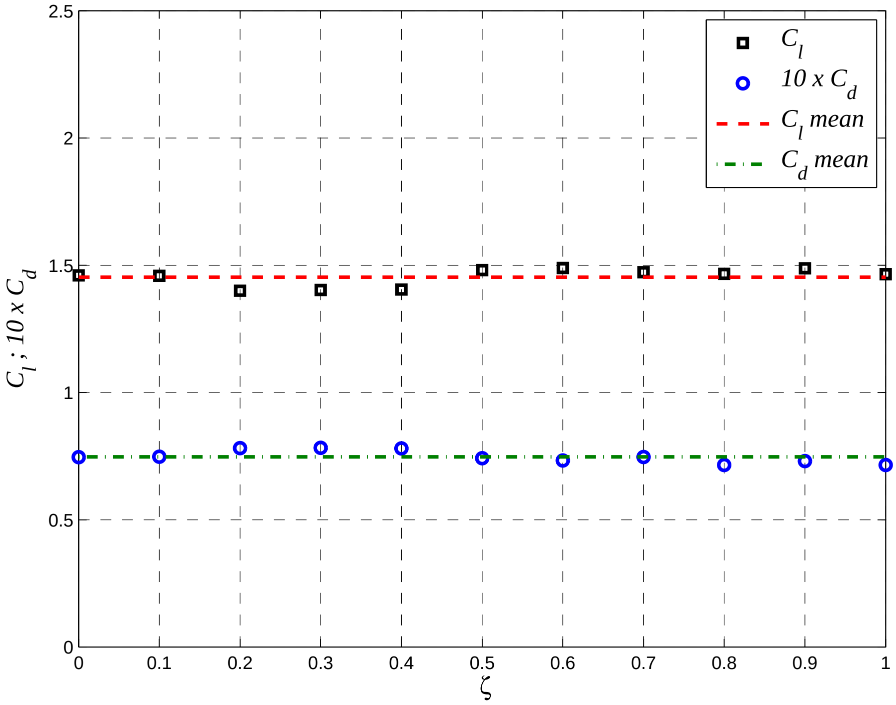

(a)

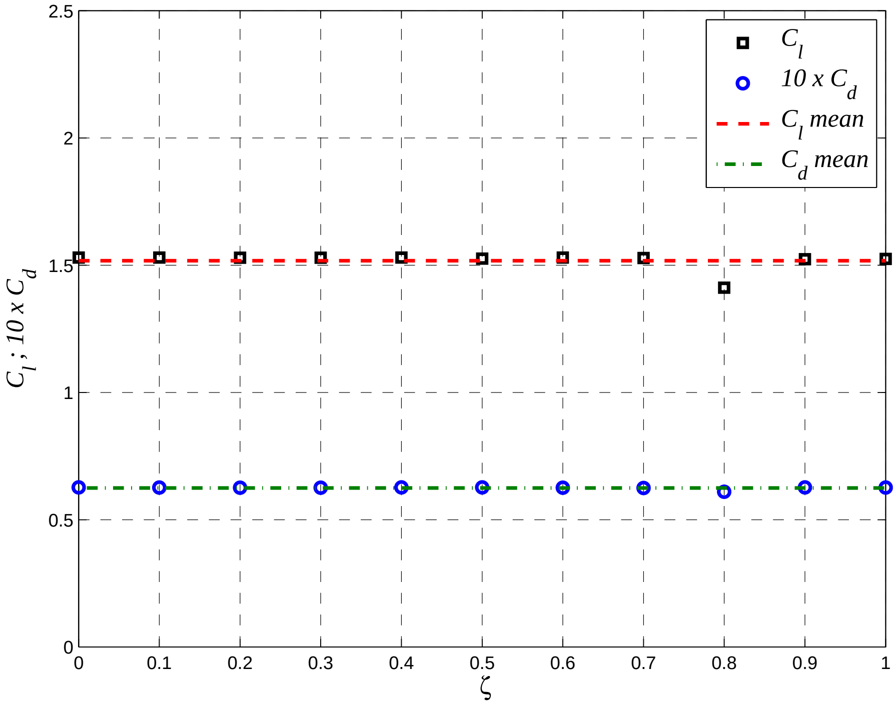

(b)

Figure 3.36: Linear validation between two designs $\mathbf{x}_1 = [-0.2515, -0.0299, 22.3649, 2.8059]$ and $\mathbf{x}_2 = [-0.2495, -0.0289, 22.3649, 2.8059]$. Validation is done at $V_\infty = 2m/s, Re = 2 \times 10^6$ at angle of attack $\alpha = 2.8059°$ a) Low-fidelity model response. Noise due to transient flow effects or the solver not able to converge are visible for the low-fidelity model. Obvious oscillation of lift and drag, (squares and circles, respectively) around mean response values for lift (- -) and drag (.-.). b) High-fidelity model response. Model shows consistency in lift and drag except for one design.

3.4 Design Optimization of the Trawl-door

We proceed with a low angle of attack steady-state analysis where we try to work in the range where separation is limited, thus, avoiding strong transient effects. The goal is to optimize the location of one slat design to match or exceed the performance of F11 trawl-door. Formulation of the problem and optimization is first given, followed by a description of the low-fidelity model construction.

We consider a drag minimization case where we carry out the optimization of the trawl-door, using direct optimization and in more computationally efficient manner follow the space mapping (SM) methodology presented in Section 2.4.

3.4.1 Formulation

To simplify the geometry and the case study, the slat furthest upstream of the F11 design is removed and we consider only the remaining geometry for optimization as shown in Fig. 3.37. The trawl-door shape is parametrized such that design variables considered in this work include the location of the slat $(x_{S1}/c_{ME}, y_{S1}/c_{ME}) = (x/c, y/c)$, the slat orientation $\theta_{S1} = \theta$ and the angle of attack α of the flow. This is shown in Fig. 3.4. The design vector is written as $\mathbf{x} = [x/c, y/c, \theta, \alpha]^T$. Other variables are kept constant such as the radius and thickness of either element and can be found in Table 3.1.

The objective is to minimize the drag coefficient $C_{d,f}$ subject to constrain on the lift coefficient $C_{l,f} \geq C_{l,\min}$. Here we select $C_{l,\min} = 1.5$. Additional constrain include validity check. Geometry of the proposed design must be validated. Design validity is checked at every iteration such that the optimizer rejects designs if slat and main cross, that is share the same points in space, or violate the minimum gap, $Gap \geq Gap_{\min}$, or maximum overlap, $Overlap \leq Overlap_{\max}$, between elements. The minimum gap between elements is defined as the minimum distance from any point on the main element to any point on the slat. Maximum overlap is defined as the distance x/c which the trailing edge of the slat overlaps the leading edge of the main element. Definition of gap and overlap are shown in Fig. 3.38.

Lower and upper bounds are specified for each of the design variables $(x/c, y/c, \theta, \alpha)$. Due to the noise problem presented in the Section 3.3.2 we begin the optimization with large design space, summarizing the starting conditions and constrains of the problem

$$\mathbf{x}^* = \arg\min_{\mathbf{x}} C_d, \tag{3.4.1}$$

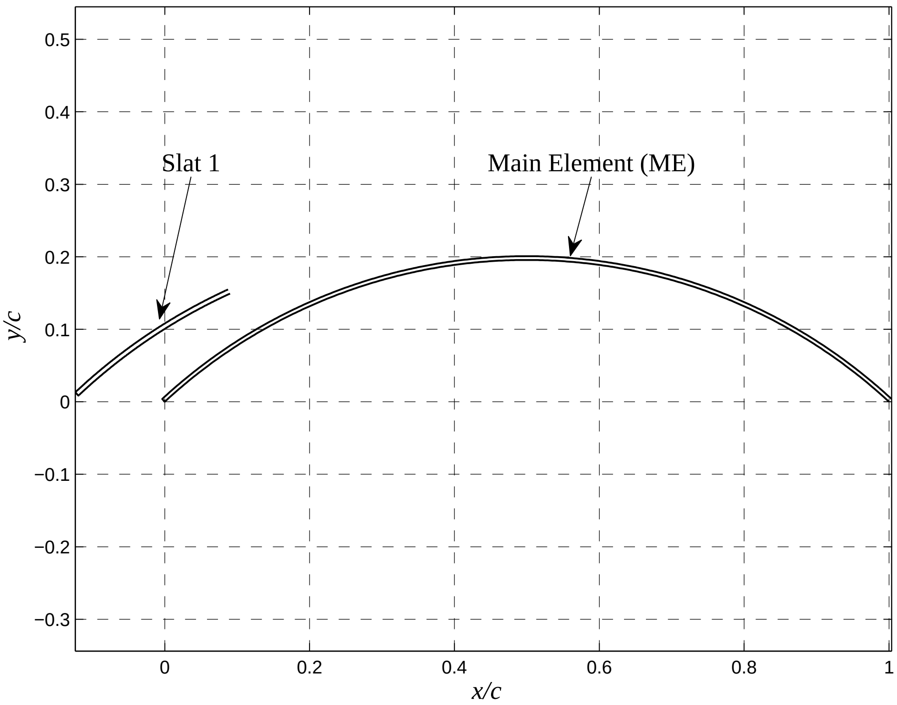

Figure 3.37: Modified design of the F11 trawl-door where two element assembly, main element and one slat, is considered as an initial design for optimization process.

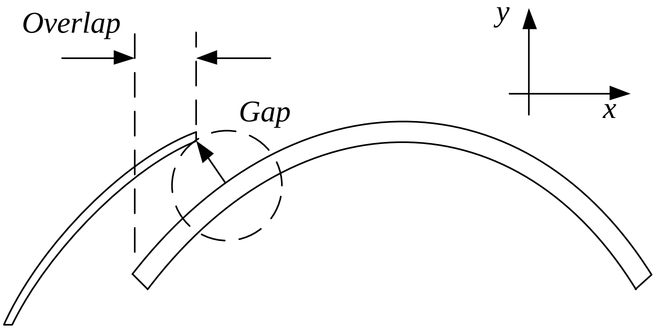

Figure 3.38: Definitions of gap and overlap.

subject to

$$\begin{aligned} C_{l,f} \geq C_{l,\min} &= 1.5, \\ Gap \geq Gap_{\min} &= 0.05, \\ Overlap \leq Overlap_{\max} &= 0.1, \end{aligned} \tag{3.4.2}$$

with the following design variable bounds

$$\begin{aligned} -0.3 \leq\, & x/c \leq 0.2, \\ -0.3 \leq\, & y/c \leq 0.2, \\ 20 \leq\, & \theta \leq 50, \\ 5 \leq\, & \alpha \leq 50. \end{aligned} \tag{3.4.3}$$

Termination condition for the optimization algorithms is set to $\|\mathbf{x}^{(i)} - \mathbf{x}^{(i-1)}\| < 10^{-3}$.

3.4.2 Low-Fidelity CFD Model

The general underlying low-fidelity model c used for all cases is constructed in the same way as the high-fidelity model f but with a coarser grid discretization and with a relaxed convergence criteria. Referring back to the grid study carried out in Section 3.2.5 and inspecting Fig. 3.9, we make our selection for the coarse low-fidelity model. Based on time and accuracy with respect of lift and drag we select the grid parameters that represent the fourth point from the right, giving 16,160 elements. Time necessary to evaluate the low-fidelity model is 2.3 minutes on four Intel-i7-2600 processors in parallel. Inspecting further the lift and drag convergence plot for the low-fidelity model Fig. 3.39 we note that the solution has converged after 150-200 iterations. However maximum number of iterations for the low-fidelity model is set to three times that, or 700 iterations, due to the nature of problem and different geometry to be optimized that used to perform the grid convergence study. This reduces the overall simulation time to 1.6 minutes. The ratio of simulation times of the high- and low- fidelity model in this case is high/low = 16/1.6 = 10. This is based on the solver uses all 700 iterations in the low-fidelity model to obtain a solution. As mentioned in 2.4, it is possible that space mapping (SM) will not perform much better than direct optimization and reduce computational cost for such a small ratio.

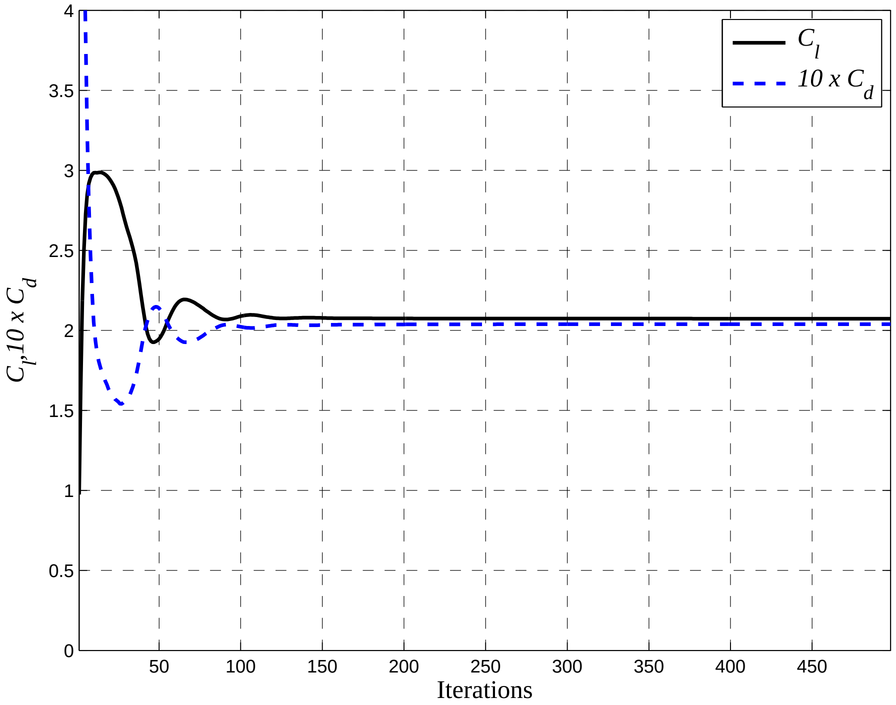

Figure 3.39: Lift and Drag coefficient convergence plot for low-fidelity model obtained in grid convergence study simulation for NACA 0012 at Reynolds number $Re = 2 \times 10^6$ and angle of attack $\alpha = 3°$.

3.4.3 Direct Optimization Results

Using direct optimization the low-fidelity model is first optimized, using its optimum as an initial design for the fine high-fidelity model which is then optimized.

Low-Fidelity Model Optimization

An attempt was made to create and use a Kriging model [11] as the coarse model, based on the low-fidelity model described in Section 3.4.2. Kriging model training data was obtained by uniform sampling the design space given in Eq. (3.4.3) with density of 5 for each design variable resulting in $5^4 = 625$ sample points. These points are however not all valid because of the geometric validity check. The number of valid points turns out to be 220. The coarse model is evaluated at all points and the Kriging model is trained using the 220 point responses of the low-fidelity model. The Kriging model however turns out to be unusable and a poor representation of the low-fidelity model. This is likely a consequence of the noise in the low-fidelity model since Kriging interpolates between training point responses which in this case include a heavy noise. The obtained Kriging model therefore can add even more error and inaccuracy to the response than the low-

Table 3.3: Numerical results of direct optimization, using random-search and pattern-search optimizing the low-fidelity model and pattern-search optimizing high-fidelity model. Shown are initial design, low-fidelity model optimum design (coarse) and the high-fidelity optimum design parameters (fine).

Variable	**Initial**	**Coarse Optimum**	Δ	**Fine Optimum**	Δ
x/c	-0.1192	-0.2611	-	-0.2515	-
y/c	0.0085	0.0098	-	-0.0298	-
θ [deg]	33.9	20.2289	-	22.3648	-
α [deg]	30.0	5.0151	-	2.8058	-
C_l	1.7925	1.3462	-25%	1.5634	-13%
C_d	0.5875	0.1289	-78%	0.0613	-90%
C_l/C_d	3.0511	10.4438	+242%	25.5041	+736%
N_c	-	300	-	-	
N_f	-	-	-	150	

fidelity model, resulting in a poor representation of the high-fidelity model. Design space is also relatively large and adding more training points may be considered to improve the model response but due to the noise Kriging model is altogether dropped.

We proceed without using the Kriging model by optimizing directly the low-fidelity model which is globally optimized using random-search and locally using pattern-search [21]. Numerical results for low-fidelity optimum is shown in Table 3.3.

Inspecting Table 3.3 we note that drag is reduced by -78% and lift to drag efficiency is increased by +242% compared to the initial design. Optimizer is however not able to keep lift above the constraint $C_l \geq C_{l,\min}$ where it is violated by 11%. This could be of previous mentioned noise where the optimizer gets stuck and terminates. Also investigating the coarse model optimum design values, we note that they are close to the boundaries of the design space presented in Eq. (3.4.3). Coarse optimum was obtained using $N_c = 300$ low-fidelity function evaluations.

High-Fidelity Model Optimization

In general, assuming that the low-fidelity model is a good representation of the high-fidelity model, the low-fidelity optimum should give a good idea of where the global optimum for the high-fidelity model is. Before proceeding with optimizing the high-fidelity model we change the side constraints of the design variables were we shrink the design space and try to center around the coarse model optimum. New side constraints

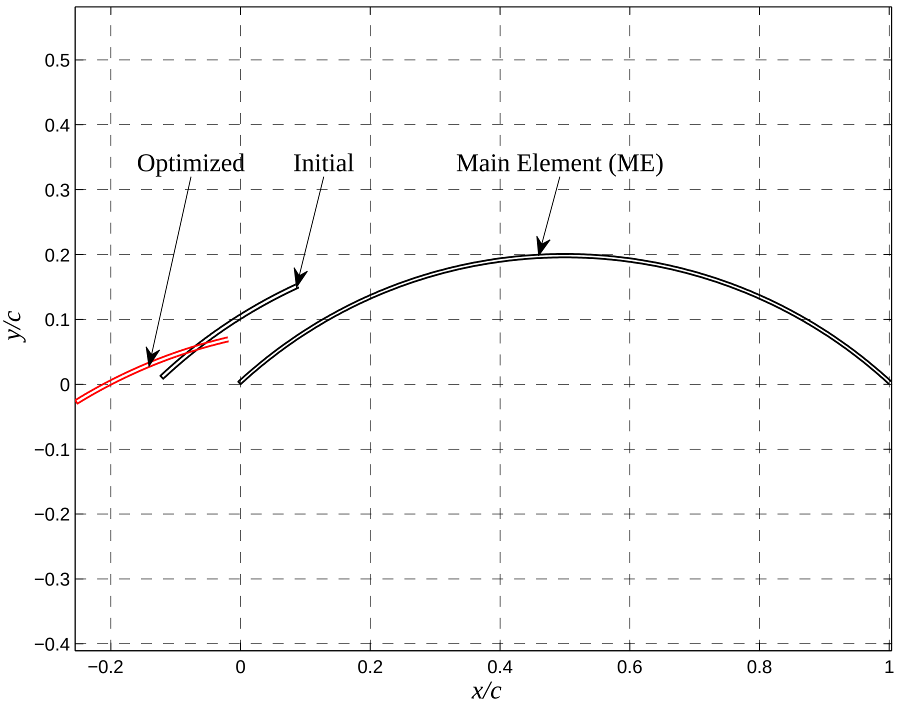

Figure 3.40: High-fidelity optimum design geometry obtained using direct optimization with the initial design shown as well.

chosen are

$$\begin{aligned} -0.30 \leq\, & x/c \leq -0.22, \\ -0.04 \leq\, & y/c \leq 0.06, \\ 17 \leq\, & \theta \leq 27, \\ 2 \leq\, & \alpha \leq 8. \end{aligned} \tag{3.4.4}$$

The initial design is set at the center of the new design space which is close to be the low-fidelity model optimum or $\mathbf{x}^{(0)} = [-0.26, 0.01, 22, 5]$ and is now optimize using patter-search [21]. The high-fidelity design optimum is shown in Fig. 3.40 and numerical results shown in Table 3.3. We note that the drag has been reduced by -90% and the lift to drag ration has increased by +736% compared to the initial design. Lift is close to the constraint as expected. Fine optimum was obtained using $N_f = 150$ high-fidelity function evaluations.

To give a fair comparison we compare the direct optimization results of the high-fidelity model to the F11 trawl-door at the same lift coefficient value $C_l = 1.5634$. Using the results from performance analysis study presented in Section 3.3 by reading Fig. 3.18 we note that to obtain such lift, angle of attack is $\alpha = 1.9246°$. Using this angle of attack $\alpha = 1.9246°$ we read off results for drag and lift to drag ratio from Fig. 3.19 and

Table 3.4: High-fidelity optimum design compared to interpolated results obtained from Fig. 3.18 to Fig. 3.21 for the F11 trawl-door design at lift $C_l = 1.5634$.

Variable	**F11 design**	**Fine Optimum**	Δ
α [deg]	1.9246	2.8058	+45%
C_d	0.1059	0.0613	-42%
C_l/C_d	14.7619	25.5041	+73%

Fig. 3.21, respectively. We summarize characteristics of the F11 trawl-door if operated at $C_l = 1.5634$ in Table 3.4.

Inspecting Table 3.4 we note that by comparing the optimized design and F11 trawl-door at same lift performance $C_l = 1.5634$ the drag is reduced by -42% and lift to drag ratio is increased by +73%.

By inspecting further the velocity contour, skin friction and pressure coefficient plots for the optimal design shown in Fig. 3.41a to Fig. 3.41c respectively, we note that separation is small and flow remains attacked over most of the upper surface on the main element. Skin friction and pressure plot confirm this result although flow is reversed and circulates at the lower surface of both elements.

An attempt was made to fix the angle of attack at $\alpha = 30°$ and $\alpha = 45°$ and optimize these two cases with the objective of minimizing drag. The optimization setup, initial conditions and procedure is the same as described above with the only difference of design variables are reduced to three $x/c, y/c, \theta$ and angle of attack α is kept fixed. These values are a typical operation value for trawl-door of this type. However, due to the highly transient nature of the problem at such high-angles of attack it was noted during the direct optimization that the solver had convergence problems and noise were substantial at some iteration steps. Although the optimization process minimized drag by finding better designs the accuracy of theses solution are questioned and not presented here.

3.4.4 Space Mapping Optimization Results

We exploit the space mapping methodology as described in Section 2.4 to carry out a computationally efficient optimization. Using the knowledge and low-fidelity optimum from direct optimization here, another attempt is made to create a Kriging model [11], using slightly modified and smaller design space. Based on the optimum design obtained by direct optimization in Table 3.3 we make small adjustments on the design space boundaries.

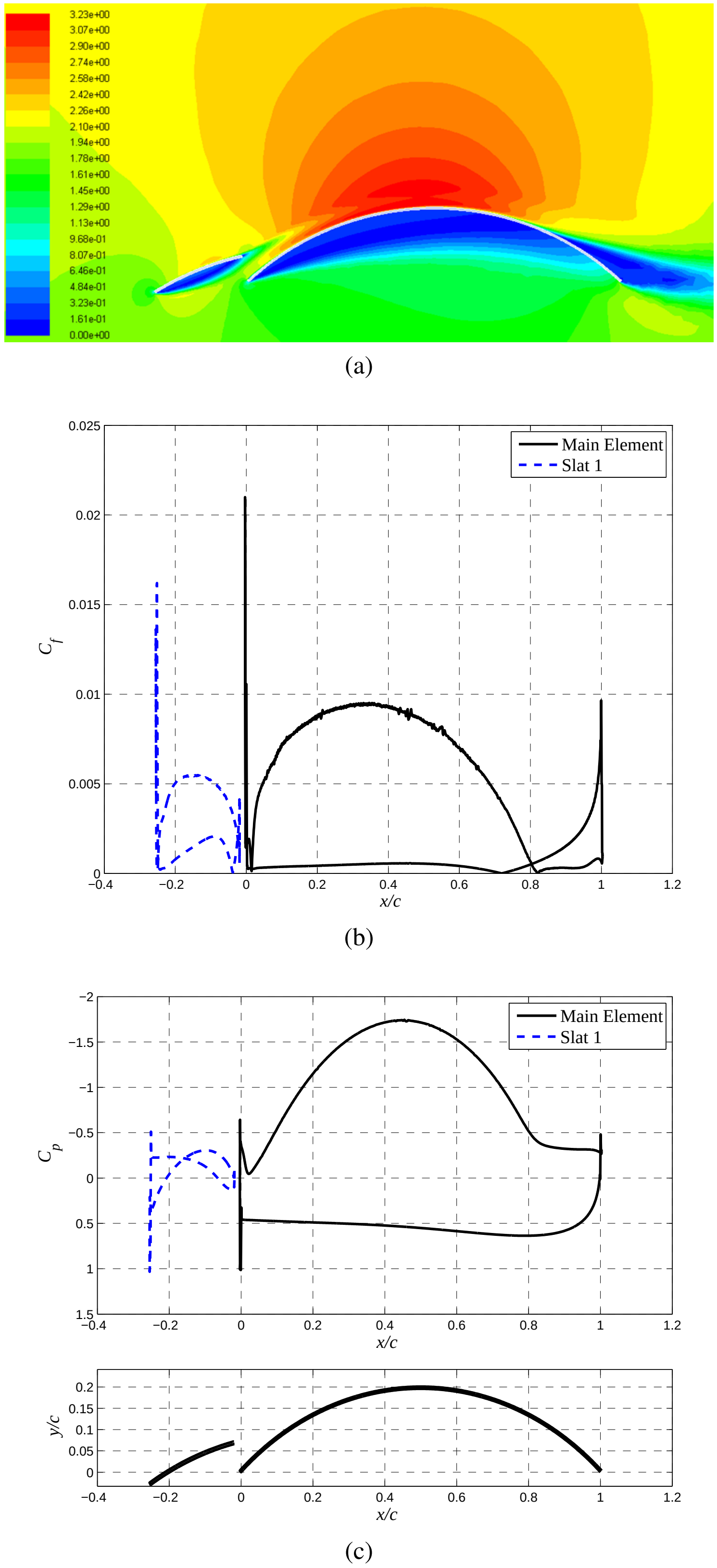

Figure 3.41: Direct optimization results $V_\infty = 2m/s, Re_c = 2 \times 10^6$. Optimized design characteristics at angle of attack $\alpha = 2.8058°$. a) Velocity contour, b) Skin friction coefficient (C_f), c) Pressure coefficient (C_p)

The new side constrains are;

$$\begin{aligned} -0.28 \leq x/c &\leq -0.22, \\ -0.05 \leq y/c &\leq -0.01, \\ 20 \leq \theta &\leq 30, \\ 2 \leq \alpha &\leq 8. \end{aligned} \tag{3.4.5}$$

The Kriging model is trained using 440 training samples from the low-fidelity model. However, due to numerical noise as described for direct optimization above the model turned out to be unusable where tested data showed inconsistency between the Kriging model and the low-fidelity model. Surrogate based optimization algorithms are sensitive to noise and high- and low-fidelity models must show similar trends.

To try to overcome the numerical noise issue within the low-fidelity model a second order polynomial approximation model is constructed [13] using 41 training points that where randomly sampled from the low-fidelity model. As for the Kriging model attempt we use Eq. (3.4.5) as the design space. The idea is to use relatively few points to construct the approximation model. The benefit is while Kriging interpolates between training data which includes numerical noise, the second order polynomial approximates the low-fidelity data response data. Polynomial regression [13] is used to fit the approximation model to the training data. In addition, second order polynomial model has nice analytical properties such as smoothness and convexity. This second order approximation model is used as the low-fidelity model c or the coarse model in this work.

Initial design is set as $\mathbf{x}^{(0)} = [-0.26, 0.01, 22, 5]$ for this SM optimization. Optimum design and numerical results are show in Fig. 3.42 and Table 3.5, respectively. Results using the proposed SM method are compared to the initial design of the modified F11 geometry design (two elements, main element and one slat), and the direct optimization of that design. We note that the drag is substantially decreased or by 90% and lift to drag ratio is increased by 668%. These are similar results as obtained with direct optimization. Lift constraint is however slightly violated by less than 5%. Direct and SM optimum designs agree quite well although SM results seem to hit the design value boundaries. Here, the approximation model most likely over-predicts the lift response compared to the high-fidelity model response where is does not violate the constrain resulting in the algorithm terminates. The proposed method requires less than 31 high-fidelity model evaluations, 250 surrogate and 5 high-fidelity which is considerably lower than if direct optimization is applied which required 180 high-fidelity model evaluations.

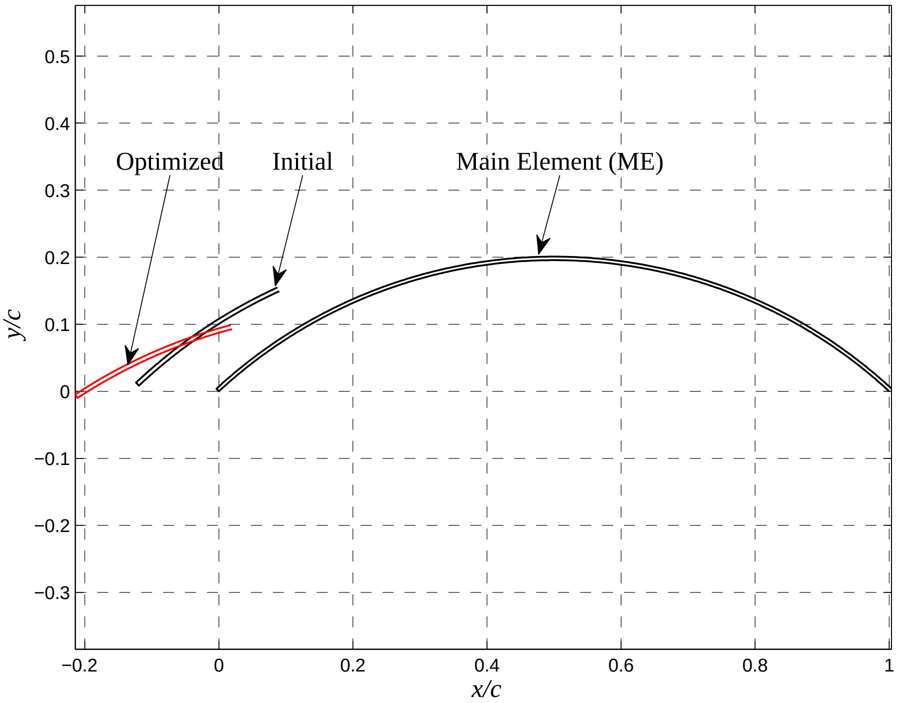

Figure 3.42: Optimum design geometry obtained using space mapping with the initial design shown as well.

Table 3.5: Numerical results initial, direct and surrogate based optimization using space mapping. The ratio of the high-fidelity model evaluation time to the low-fidelity is 10.

Variable	**Initial**	**Direct**	**This work (SM)**	Δ
x/c	-0.1192	-0.2515	-0.2107	-
y/c	0.0085	-0.0298	-0.0100	-
θ [deg]	33.9	22.3648	24.0113	-
α [deg]	30.0	2.8058	2.0000	-
C_l	1.7925	1.5634	1.4382	-20%
C_d	0.5875	0.0613	0.0614	-90%
C_l/C_d	3.0511	25.5041	23.4235	+668%
N_c	-	300	250	
N_f	-	150	6	
Total Cost	-	180	< 31	

Table 3.6: Space mapping optimum design compared to interpolated results obtained from Fig. 3.18 to Fig. 3.21 for the F11 trawl-door design at lift $C_l = 1.4382$.

Variable	**F11 design**	**This work (SM)**	Δ
α [deg]	0.7076	2.0000	+182%
C_d	0.1029	0.0614	-40%
C_l/C_d	13.9808	23.4235	+68%

As for direct optimization, the proposed algorithm is able to optimize the design such it improves performance substantially as presented in Table 3.5. Further we compare the F11 trawl-door at the same lift value as obtained with SM where $C_l = 1.4382$. Using the results from performance analysis study presented in Section 3.3 by reading Fig. 3.18 we note that to obtain such lift angle of attack is $\alpha = 0.7076°$. Using this angle of attack $\alpha = 0.7076°$ we read off results for drag and lift to drag ratio from Fig. 3.19 and Fig. 3.21, respectively. We summarize characteristics of the F11 trawl-door if operated at $C_l = 1.4382$ in Table 3.6.

Inspecting Table 3.6 we note that by comparing the SM optimized design and F11 trawl-door at same lift performance $C_l = 1.4382$ the drag is reduced by -40% and lift to drag ratio is increased by +68%.

The optimization history is shown in Fig. 3.43. One can observe the evolution of the objective function Fig. 3.43a, convergence plot Fig. 3.43b and evolution of lift and drag Fig. 3.43c and Fig. 3.43d respectively. It is observed that the algorithm shows a good convergence although it does not reach the 10^3 stopping criterion. The algorithm forces the lift to its constrain at $C_l \geq 1.5$ where the constrain is violated slightly while minimizing the drag.

Velocity contour, skin friction and pressure plots are shown in Fig. 3.44. Similarly as for the direct optimization flow separation is reduced. This is evident on the pressure plot where we can see that there is no sudden increase in pressure at the upper surface and the flow stays attached for longer time.

A successful attempt was made to improve and refine the approximation model response in order to yield better optimum results using the proposed method. Previously, the optimization process hit the boundaries and got terminated. Here, a second order approximation model is constructed without using the mixed terms. The design space is made smaller where the previously found optimum design $\mathbf{x} = [-0.2107, -0.0100, 24.0113, 2]$

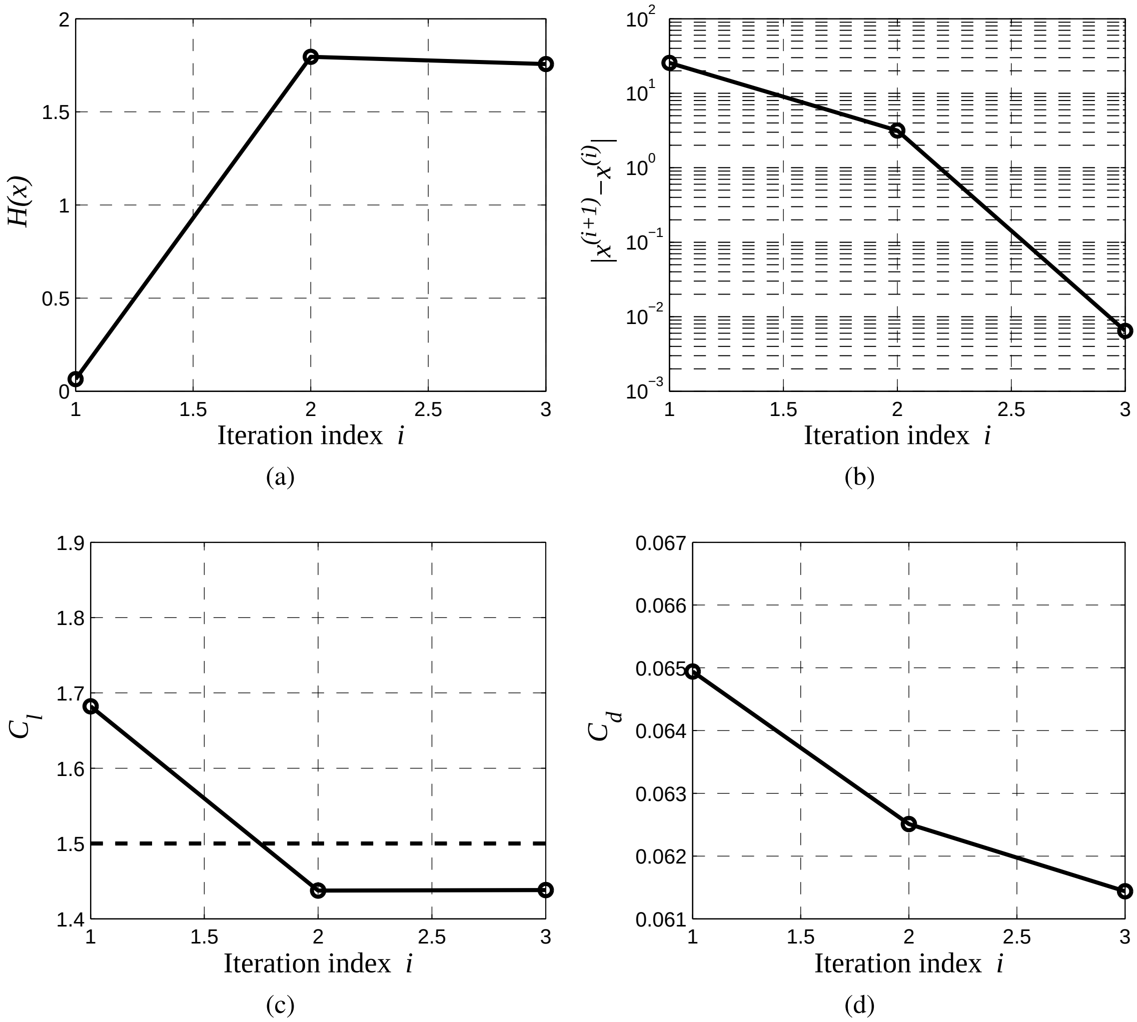

Figure 3.43: Optimization history using the proposed SM methodology. a) Evolution of the objective function; b) convergence Plot; c) evolution of lift coefficient where dash line (- -) is the lift constrain and; d) evolution of drag coefficient

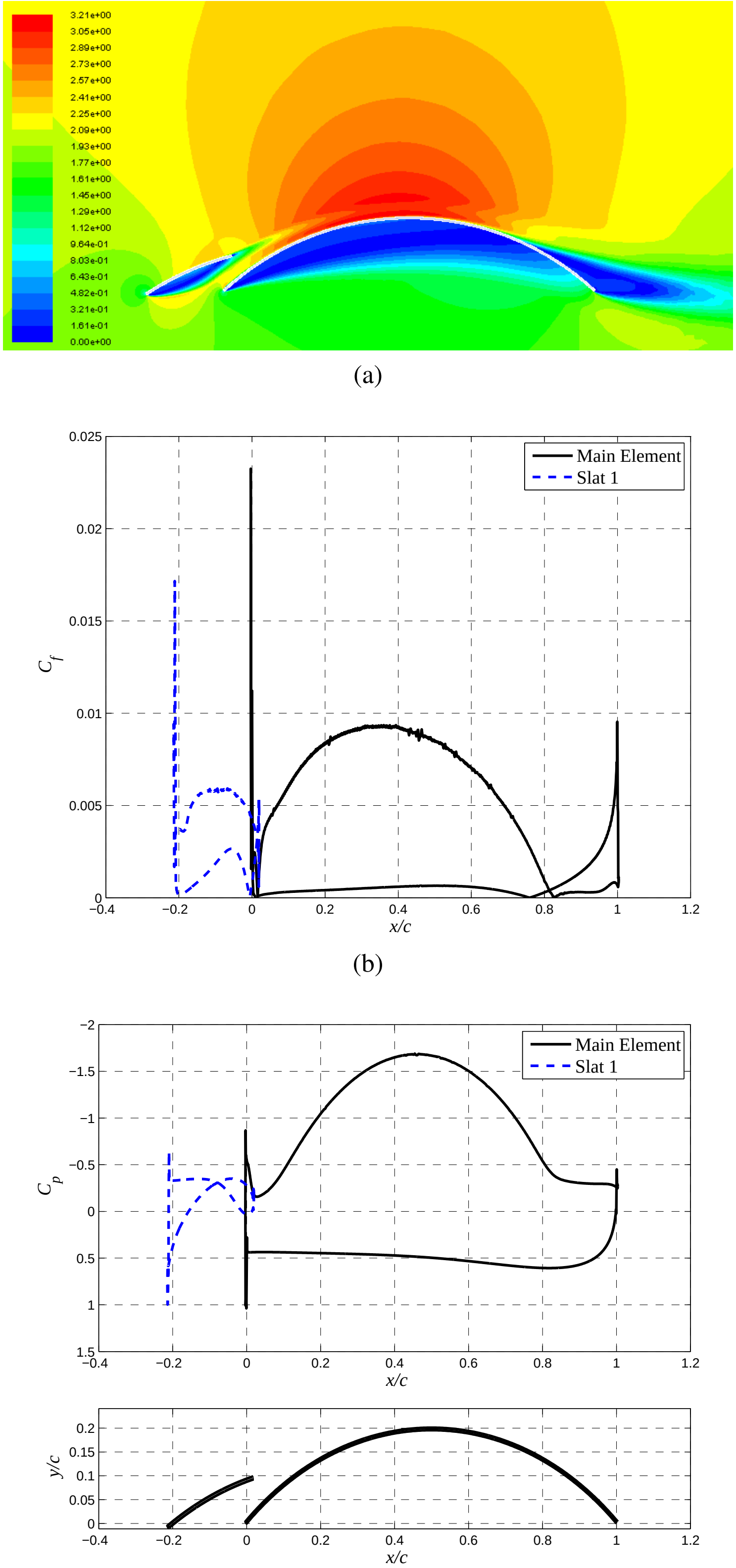

(a)

(b)

(c)

Figure 3.44: Space Mapping optimization results $V_\infty = 2m/s$, $Re_c = 2 \times 10^6$. Optimized design characteristics at angle of attack $\alpha = 2°$. a) Velocity contour, b) Skin friction coefficient (C_f), c) Pressure coefficient (C_p)

is at the center. New design boundaries are

$$\begin{aligned} -0.2307 \leq x/c &\leq -0.1907, \\ -0.0150 \leq y/c &\leq -0.0050, \\ 22.0113 \leq \theta &\leq 26.0113, \\ 1 \leq \alpha &\leq 3. \end{aligned} \tag{3.4.6}$$

The approximation model is trained using 9 high-fidelity data points sampled at design space boundaries in Eq. (3.4.6) (total of eight points) and at the center of the design space $\mathbf{x} = [-0.2107, -0.0100, 24.0113, 2]$ (one point). Using the center as a intial design the proposed method using the improved approximation model reaches minimum in 2 iterations where the optimum design is $x^* = [-0.21444, -0.01278, 23.2191, 2.9375]$ which is similar to previously found optimum as shown in Table 3.5.

3.5 Summary

Optimization of the modified F11 trawl-door geometry presented here turned out to be a challenging task. Operating at a high angle of attack obtaining a steady-state solution was difficult since the flow over the trawl-door geometry is highly transient where separation is huge. Therefore the optimization is done for relatively low angle of attacks. In addition the low-fidelity model presented here includes substantial noise. Despite of that a direct optimization yielded a optimized design with drag reduction of 43% compared to the F11 design.

As described, the surrogate based optimization method is sensitive for numerical noise in both low- and high-fidelity models. Low- and high-fidelity grids and flow solver methodologies must be redesigned and redone in such way a linear design variation will not yield different lift and drag responses as observed here. This task is however quite challenging. Designing grids is a true art and transient flow solver solutions adds overhead to the optimization process.

Results obtained with the proposed computationally efficient optimization methodology, space mapping shows that the algorithm can be applied to such problem and yield accurate results. The proposed method was able to reduce drag substantially or by 40% compared to the F11 design. The proposed method requires less than 31 high-fidelity model evaluations, 250 surrogate and 5 high-fidelity which is considerably lower than if direct optimization is applies which required 180 high-fidelity model evaluations. The optimization method used here therefore brings over -80% reduction in high-fidelity model evaluations.

Chapter 4

Transonic Wing Optimization

In this chapter, the proposed surrogate based optimization methodology is applied to a three dimensional rectangular wing design at a transonic flow condition. The goal is to optimize its geometry in order to maximize its lift. First we introduce the high-fidelity model where we define the governing equations of the flow, wing geometry, computational grid, solver setup and boundary conditions. A grid convergence study is then performed in order to verify the computational grid. The high-fidelity model is validated using a ONERA M6 wing geometry, where CFD simulation data is compared to experimental data from an ONERA M6 wing experiment. The design optimization formulation is presented defining the objective and constraints used in this optimization. The low-fidelity model is constructed followed by presenting the optimization results using the method introduced in 2.4. This chapter concludes with a summary.

4.1 Problem Definition

The wing is the most important component of an aircraft, affecting, the overall performance significantly. As the wing provides lift, it is at the same time the main source of drag, responsible for about 2/3 of the total drag of the aircraft [38]. Reducing this wing drag by a better design, hence minimizing cost, is therefore often the primary objective of modern aircraft design. Yet another important perspective is to maximize lift, but keep drag within constraints thereby increasing its lift to drag ratio, or the efficiency.

An aircraft wing is a three dimensional aerodynamic surface. Schematic of a trapezoidal transonic wing planform is shown in Fig. 4.1. At each spanstation (numbered 1 through 7) the cross-section is defined by an airfoil shape. An airfoil is a streamlined aerody-

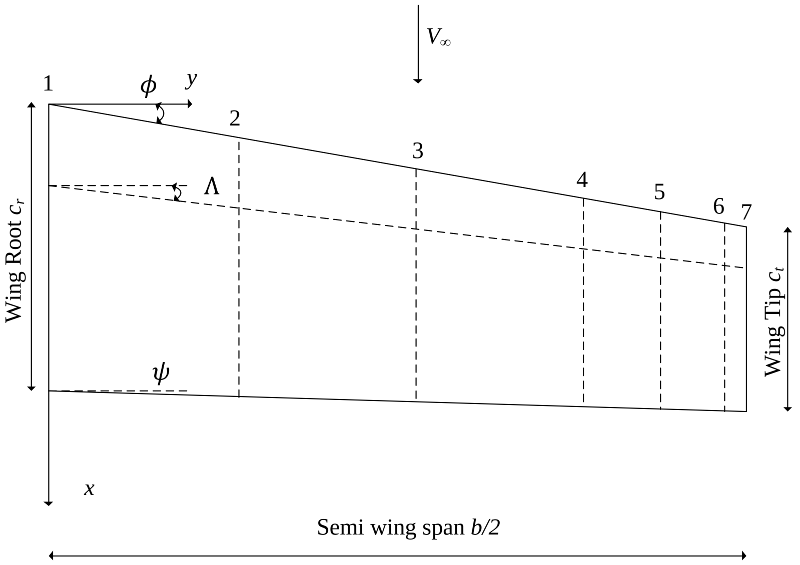

Figure 4.1: Planform view of a trapezoidal wing of a semi-span $b/2$ and quarter chord sweep angle Λ. Spanstations are marked 1 through 7 and freestream velocity is V_∞. Leading edge and trailing edge angles are ϕ and ψ is also shown. Other design parameters are not shown.

namic surface which describes the shape of a wing as seen in cross-section such as one in Fig. 4.2. The chord, denoted by c, is the distance from the leading edge (LE) to the trailing edge (TE) of the body. The chord line, is the line connecting the LE and TE. The LE is normally rounded and the TE is usually sharp either closed or open but can also be blunt (closed). The mean camber line is the locus of points halfway between the upper and lower surface. The curvature, called camber, is the distance from the chord line to the mean chamber line measured perpendicular to the chord line. The thickness, denoted by t, is the distance between the upper and lower surface measured also perpendicular to the chord line [35].

Number of spanstation on a wing can be larger or fewer than shown here and depend on the wing design. A straight line wrap is assumed between spanstations. Spanstations are mainly used for two purposes, to define different types of airfoils than the adjacent ones or simply defined as an interesting locations on the wing to observe pressure distributions and skin friction. Design parameters controlling the planform shape include the wing semi-span $b/2$, the quarter chord wing sweep angle Λ, thickness-to-chord ratio t/c at each spanstation, the wing taper ratio λ and twist distribution γ_θ. The number of design variables can therefore be much larger than for the two dimensional case. Lift and drag coefficients for a three dimensional surface are defined as

$$C_L = \frac{L}{q_\infty S}, \tag{4.1.1}$$

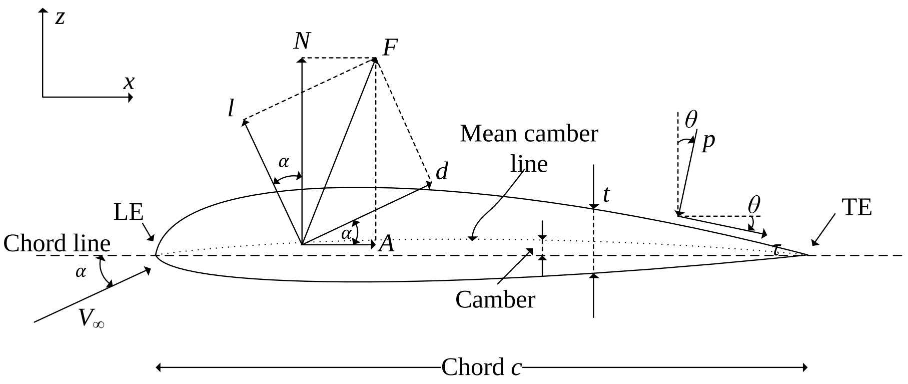

Figure 4.2: Airfoil wing cross-section (solid line) of thickness t and chord length c. V_∞ is the freestream velocity and is at an angle of attack α relative to the x-axis. F is the resulting aerodynamic force where l is the lift force, perpendicular to V_∞ and d is the drag force, parallel to V_∞. p is the pressure acting normal to a surface element ds. τ is the viscous wall shear stress acting parallel to the surface element. θ is the angle that p and τ make relative to the z and x-axis, respectively where positive angle is clockwise.

$$C_D = \frac{D}{q_\infty S}, \tag{4.1.2}$$

where S is usually chosen as the planform area, L and D is the magnitude of the total lift and drag forces respectively. The dynamic pressure q_∞ is defined as

$$q_\infty = \frac{1}{2}\rho_\infty V_\infty, \tag{4.1.3}$$

where ρ_∞ is the freestream density and V_∞ is the magnitude of the freestream velocity.

In this study, we will consider a simple rectangular wing geometry consisting of two airfoils, one at wing tip and one at wing root, at transonic flow conditions. The goal of this study is to maximize its lift C_L for a given drag constraint $C_D \leq C_{D,\max}$, by optimizing the airfoil shape at the wing tip while keeping other wing variables fixed.

4.2 High-Fidelity CFD Model

In this section, we present the high-fidelity CFD model. We start by describing the governing equations of the fluid flow. Following that, the wing geometry, computational grid, solver setting and boundary conditions are presented. The section concludes with a grid convergence study and high-fidelity model validation study performed on the ONERA M6 wing.

4.2.1 Governing Equations

Commercial aircraft operates at high speeds in the transonic flow regime where the flow is highly compressible. We assume that the fluid is air and is modelled by the ideal gas law and use the Sutherland law for dynamic viscosity μ. The flow is further assumed to be steady, viscous, and without body forces, mass-diffusion, chemical reactions or external heat addition. We apply and solve the RANS equations with the one equation Spalart-Allmaras turbulence model. See Appendix A.1 for the full Navier-Stokes equation matrices, RANS equations and turbulence model description.

4.2.2 Wing Geometry

Here, we present the methods used in this work to construct and parametrize a wing geometry. Generally, a wing consist of number of airfoil cross-sections. One needs to be able to describe these airfoil cross-sections numerically in order to in order to control the wing geometry. Several methods exists describing airfoil geometry numerically, each method with its own benefit and drawbacks. Number of design parameters are often closely related to the method selected to describe the geometry. In general there are two different approaches describing the airfoil geometry numerically, either the airfoil shape is parametrized or given an initial airfoil shape the deformation is parametrized. We consider only airfoil parametrization. Numerous airfoil parametrization methods have been developed. Non-Uniform Rational B-Spline (NURBS) and Bézier curves (special case of NURBS) are the methods that are commonly used today. These methods use a set of control points that describe the airfoil geometry and are general enough to be able to create almost any airfoil shape [39]. One can vary the number of control points depending on how accurately the airfoil geometry is to be controlled and in general, more points will give greater control of the upper and lower surface of the airfoil. These methods however come with a price. In aerodynamic shape optimization the afore mentioned control point are a part of the design variables of a given problem. The more the design variables, the more computational demanding the optimization will be. NURBS requires as few as thirteen control points to represent a large family of airfoils [39]. Other parametrization methods exists that require fewer control points.

For the sake of simplicity and having a small number of design variables, the NACA - 4 digit method is used to construct a wing geometry. It is one of the most studied and researched airfoils where developed by the National Advisory Committee for Aeronautics (NACA), the forefunner of NASA. The NACA four digit series was developed in the 1930s and is based on the results of a number of wind tunnel experiments. Shapes generated by this method is therefore limited to those investigations. However due to its simplicity requiring only three design parameters, NACA four digit parametrization method can be used for constructing a relatively complex three dimensional wing body with few design parameters making it computationally a feasible choice.

The rectangular wing consists of two NACA 4 digit airfoils one at the wing root and one at the wing tip with a straight line wrap assumed between airfoils. The formulation of the NACA 4 digit method is given here. The NACA 4 digit airfoil are denoted by convention as NACA $mpxx$ where:

m : the maximum ordinate of the mean camberline as a percent of the chord.
p : the chordwise position in tens of percents of the maximum ordinate
xx : the thickness-to-chord ratio in percents of chord t/c

The NACA airfoils are constructed by combining a thickness function $z_t(x)$ with a mean chamber line function $z_c(x)$ [35]. The x and z coordinates are

$$x_{u,l} = x \mp z_t \sin\theta, \tag{4.2.1}$$

$$z_{u,l} = z_c \pm z_t \cos\theta, \tag{4.2.2}$$

where u and l are the upper and lower surfaces, respectively, and

$$\theta = \tan^{-1}\left(\frac{dz_c}{dx}\right), \tag{4.2.3}$$

is the mean camber line slope. The NACA four digit thickness distribution is given by

$$z_t = t\left(a_0 x^{1/2} - a_1 x a_2 x^2 + a_3 x^3 - a_4 x^4\right), \tag{4.2.4}$$

where $a_0 = 1.4845, a_1 = 0.6300, a_2 = 1.7580, a_3 = 1.4215, a_4 = 0.5075$, and t is the maximum thickness. The mean chamber line is given by

$$z_c = \left\{ \begin{array}{ll} \frac{m}{p^2}\left(2px - x^2\right) & x < p \\ \frac{m}{(1-p)^2}\left(1 - 2p + 2px - x^2\right) & x \geq p \end{array} \right., \tag{4.2.5}$$

Examples of a airfoils generated with NACA four digit method are shown in Fig. 4.3. A finite wing can then be described by number of airfoils where each airfoil represents the wings cross-section at a given spanstation as shown in Fig. 4.4. This offers great scalability since each airfoil shape is free to change and can have different geometric angle of attack and aerodynamic angle of attack.

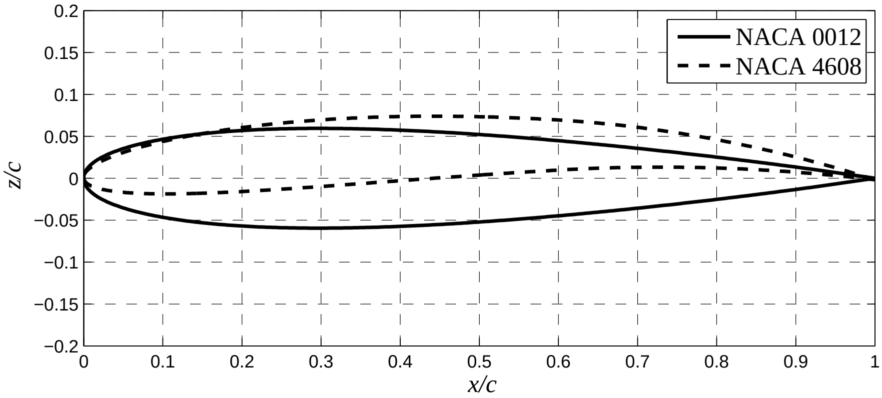

Figure 4.3: Examples of two airfoils sections generated with the NACA four digit method. NACA 0012 $m = 0, p = 0, t/c = 0.12$ is shown by solid line (–) and is a symmetric airfoil. NACA 0012 $m = 0.04, p = 0.6, t/c = 0.08$ is shown by dash line (- -).

In this work a simple constant chord wing, or a rectangular wing geometry is used. It consists of two NACA four digit airfoils, one at wing root and the second at wing tip as shown in Fig. 4.4a. A CAD drawing of the wing is shown in Fig. 4.4b. The method developed in this work, using the NACA four digit method, is very flexible and not limited to constant chord wings consisting of two airfoils only. By introducing sweep as a design variable one can generate a more complex wing geometries. An example of more complex wing is a conventional transport wing as shown in Fig. 4.5 where three airfoils and sweep make up the wing geometry.

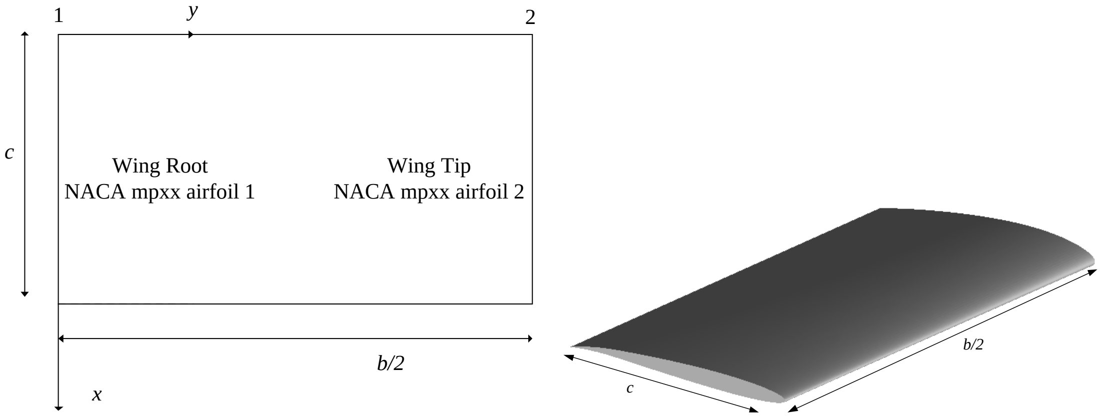
1
y
2
c
Wing Root
NACA mpxx airfoil 1
Wing Tip
NACA mpxx airfoil 2
b/2
x
c
b/2

(a) Planform view (b) CAD drawing

Figure 4.4: Planform view of a constant chord wing used in this work. The rectangular wing consisting of two NACA airfoils, shown at spanstations 1 the wing root and 2 wing tip. Each airfoil has its own set of design parameters, $m, c, t/c$, describing the airfoil cross-section.

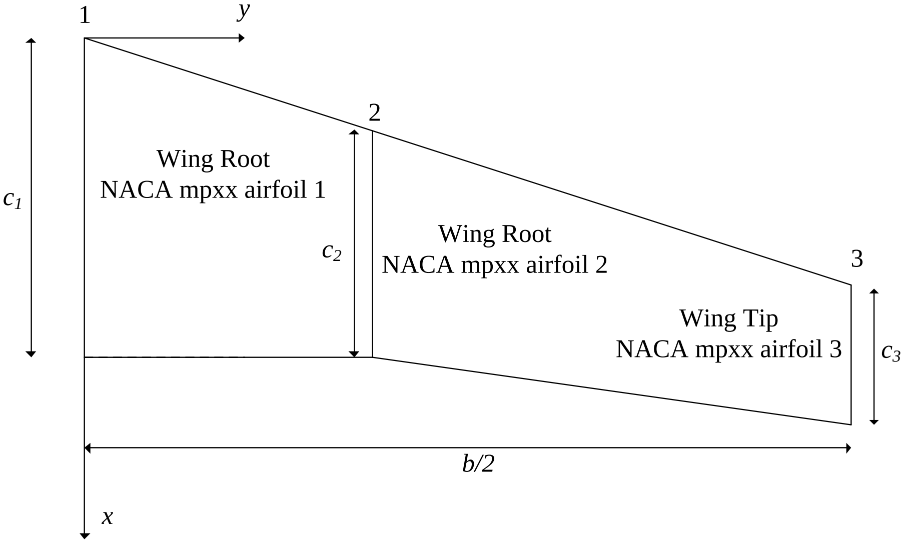
1
y
2
Wing Root
NACA mpxx airfoil 1
c_1
c_2
Wing Root
NACA mpxx airfoil 2
3
Wing Tip
NACA mpxx airfoil 3
c_3
b/2
x

Figure 4.5: Planform view of a conventional transport wing consisting of 3 NACA 4 digit airfoils where sweep has been introduced. Each spanstation $1 - 3$ is an airfoil which has its own set of design parameters $m, c, t/c$.

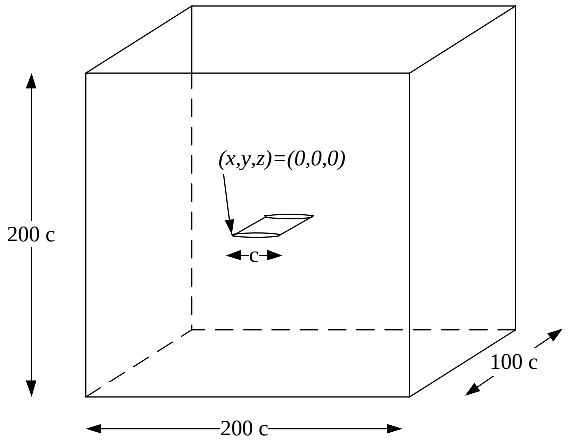

Figure 4.6: Farfield configured as a box topology. The leading edge of the wing root airfoil is placed at $(x, y, z) = (0, 0, 0)$.

4.2.3 Computational Grid

Working with three dimensional body, choosing the appropriate grid method and strategy becomes very important since element count depend heavily on the method used. Here, we give a description of the parameters used for the high-fidelity CFD grid. The grid parameter values representing the fine model are acquired through a grid convergence study which is considered in Section 4.2.5. Modelling and acquiring accurate drag prediction is a difficult task especially in three dimensions. The objective is to obtain a grid that can be adapted in the sense that cell count can be refined in an efficient manner without affecting its global topology. We follow the guidelines and procedures presented by the Drag Prediction Workshop series in this work [40]. Developing an error free grid turned out to be a formidable task. It must be noted that the grid strategy used here is only one of many that were employed and tested although their details are not presented here.

An unstructured tri/tetra shell grid is created on all surfaces. The shell grid from the wing is then extruded into the volume where the volume is flooded with tri/tetra elements. The grid is made dense close to the wing where it then gradually grows in size as moving away from the wing surfaces. To capture the viscous boundary layer an inflation layer or a prism layer is created on the wing surfaces as well.

The farfield is set up as a box where the wing root is place in the center of the symmetry plane with its leading edge placed at the origin $(x, y, z) = (0, 0, 0)$ as shown in Fig. 4.6. The farfield extends 100 chord lengths, $100c$, in all directions from the wing, upstream, above, below and aft of the wing where the maximum element size in the flow domain is 11 chord lengths or $11c$. Resulting farfield shell grid is shown in Fig. 4.7e.

The wing is discretized x and y direction, namely the stream-wise and span-wise direction, respectively. In stream-wise direction number of elements on the wing is set to 100 on both upper and lower surface. The bi-geometric bunching law with growth ratio of 1.2 is also employed in the stream-wise direction over the wing to obtain a more dense element distribution at the leading edge and the trailing edge. This is done in order to capture the high pressure gradient at the leading edge and the separation at the trailing edge. Resulting element density is sufficiently dense to capture the shock appearing on the upper surface. The minimum element size which is located at the leading and trailing edge of the wing in the stream-wise direction is set to 0.1% of the chord length, $0.1\%c$. In span-wise direction number of elements are set to 100 and they are distributed uniformly over the semi-span. Resulting grid is shown in Fig. 4.7a to Fig. 4.7c.

A prism layer is used to capture the viscous boundary layer. This layer consists of number of structured elements that grow in size normal to the wing surface into the domain volume. The initial element height from the surface is usually orders of magnitude smaller than the wing chord length. In this work the initial layer has the height of $5 \times 10^{-6}c$ where it is grown 20 layers into the volume using a exponential law with ratio of 1.2. The initial layer height is chosen such that $y^+ < 1$ (see Appendix A.1.3) at all nodes on the wing and is shown in Fig. 4.7d.

The resulting volume grid is shown in Fig. 4.8a to Fig. 4.8c. The high-fidelity grid is generated with the computer code ANSYS ICEM CFD [34]. The resulting high-fidelity grid has roughly 1.6 million elements. We summarize here the grid properties and parameters;

- **General Parameters**
  - Farfield extends 100 chord lengths, $100c$, from the origin $(x, y, z) = (0, 0, 0)$ in all directions, see Fig. 4.6.
  - Maximum element size in the flow domain is 11 chord lengths or $11c$, see Fig. 4.7e.
- **Wing Parameters**
  - Number of stream-wise nodes are 100, distributed using bigeometric bunching law, see Fig. 4.7a.
    - Growth ratio 1.2
    - Minimum element size stream-wise is 0.1% of the chord length $0.001c$.
  - Number of nodes on span-wise direction are 100, distributed uniformly

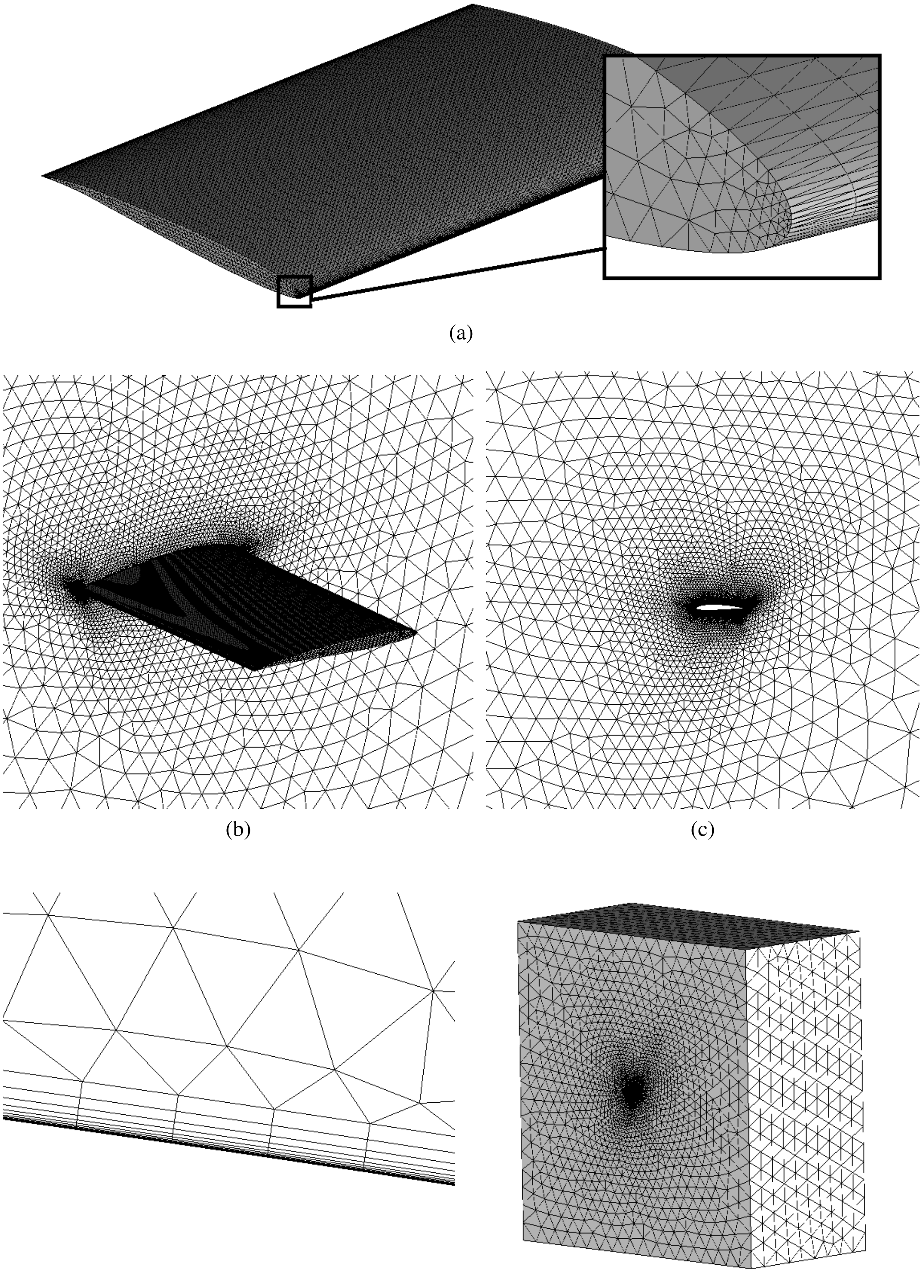

(a)

(b)

(c)

(d)

(e)

Figure 4.7: Shell grid shown for all surfaces. a) wing shell grid; b-c) symmetry plane where the wing placed; d) prism layer applied close to the wing surface to capture the viscous boundary layer; e) farfield volume

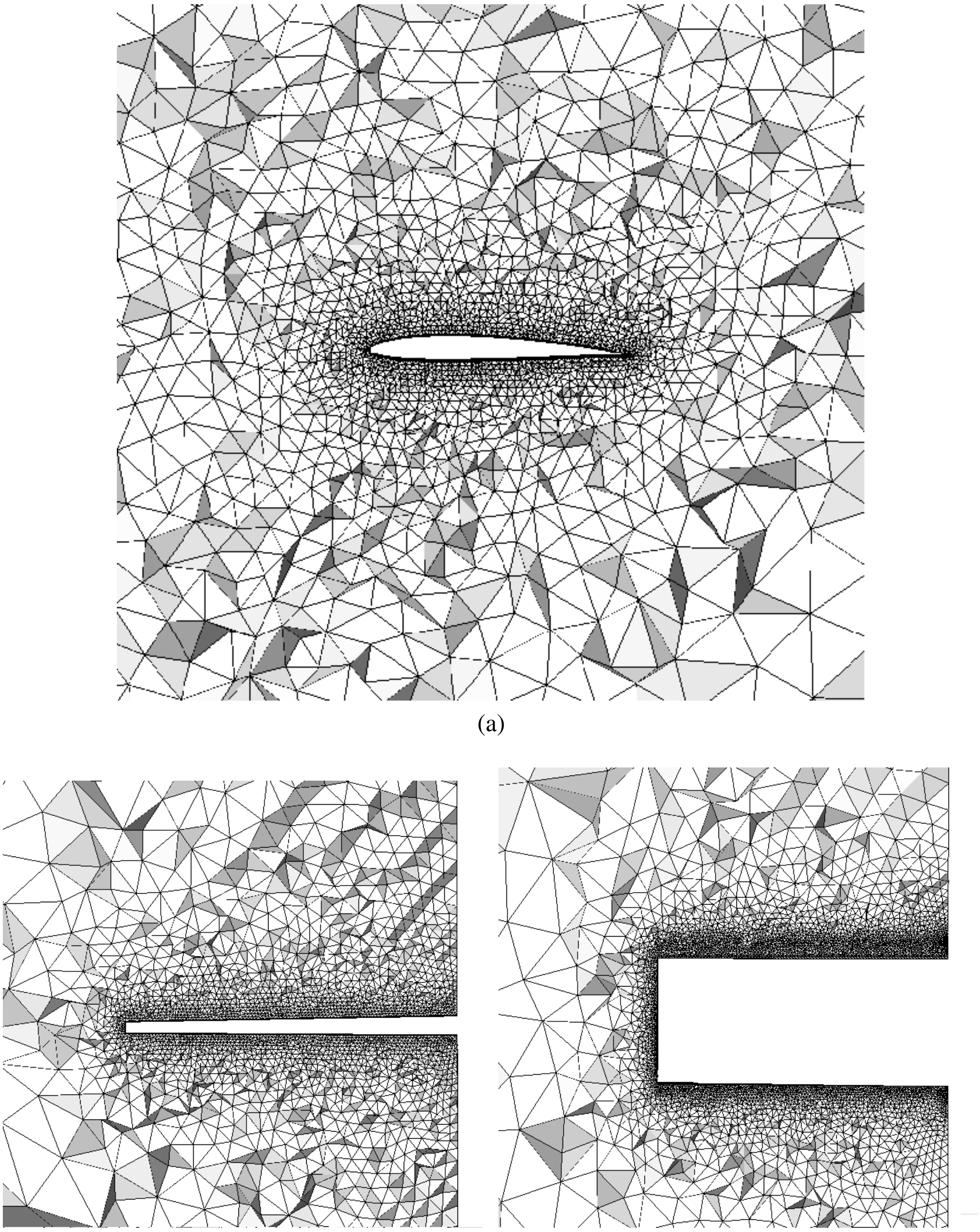

(a)

(b) (c)

Figure 4.8: Volume grid a) looking in span-wise direction y-axis; b) looking in stream-wise direction x-axis; c) looking from below along z-axis. We note how the elements are dense close to the surface and gradually grow into the volume.

- **Boundary Layer**
  - Initial layer height is $5 \times 10^{-6}c$.
  - Exponential growth ration is set 1.2.
  - Number of prism layers are set to 20, see Fig. 4.8b.
  - Above properties yield $y^{+} < 1$ at any point on the wing surfaces.

4.2.4 Boundary Conditions and Solver Setup

Numerical fluid flow simulations are performed using the computer code ANSYS FLUENT [32]. Here, the implicit density-based solver is applied using the Roe-FDS flux type. Spatial discretization schemes are set to second order consistency for all variables and gradient information is found using the Green-Gauss node based method. The residuals, which are the sum of the L^2 norm of all governing equations in each cell, are monitored and checked for convergence. The convergence criterion for the high-fidelity model is such that a solution is considered to be converged if the residuals have dropped by six orders of magnitude, 10^{-6}, or the total number of iterations has reached 10^3. Also the lift and drag coefficients are monitored for convergence.

To reflect the compressible nature of this problem two types of boundaries are used. Pressure-farfield is set as the boundary on all surfaces except one where the wing penetrates which is set as a symmetry boundary. A breakout of the boundary types is show in Fig. 4.9.

Air is the working fluid at compressible transonic conditions. Free-stream Reynolds number $Re_{\infty,S} = 11.72 \times 10^6$, where S is the reference area, which in this case is planform area. Mach number is set to $M_\infty = 0.8395$ and the angle of attack is set to $\alpha = 0°$. We assume that the flow is calm at its boundaries and turbulent viscosity ratio set to $\mu_t/\mu_\infty = 1$. Further, boundary pressure and temperature is set to $p_\infty = 80507.2Pa$ and $T_\infty = 255.6K$. Other fluid properties and boundary condition are summarized in Table 4.1. The values shown here are part of an experimental setup which found and calculated in Section 4.2.6.

4.2.5 Grid Convergence Study - ONERA M6

A grid convergence study is conducted. The idea of this grid convergence study is to acquire fine enough grid that resolves the physics properly and yields an accurate enough

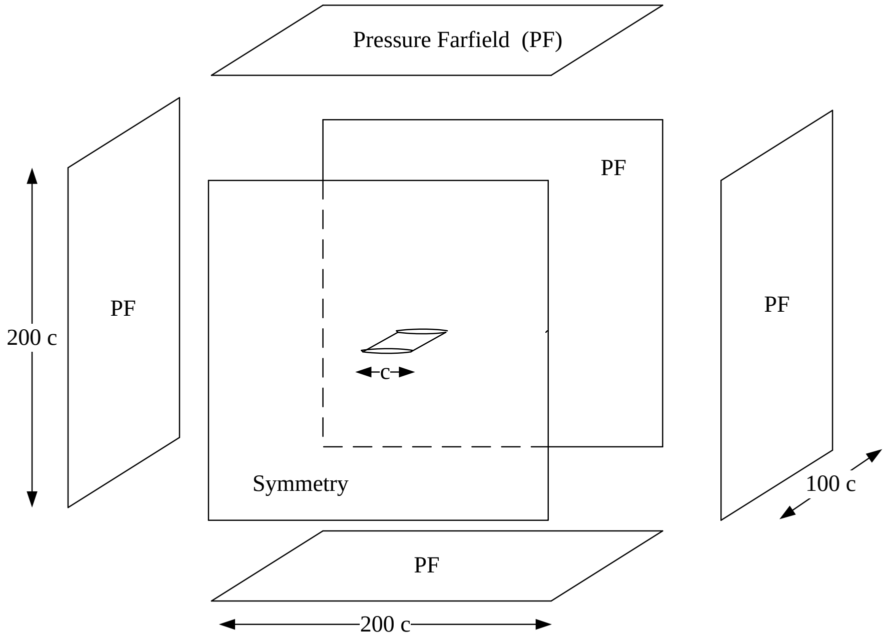

Figure 4.9: Breakout of the boundary types used. All boundaries are set as pressure-farfield (PF) except one the wing penetrates which is a symmetry boundary.

Table 4.1: Air properties and boundary conditions for pressure-farfield.

Fluid Properties	**Value**	**Units**
Density ρ_∞	Ideal gas	-
Specific Heat Capacity c_p	1003.06	$J/kg\,K$
Thermal Conductivity k	0.0242	$W/m\,K$
Viscosity μ_∞	Sutherland	$kg/m\,s$
Molecular Mass	28.966	$kg/kgmol$

Boundary Conditions	**Value**	**Units**
Reynolds number $Re_{\infty,S}$	11.72×10^6	-
Mach M_∞	0.8395	-
Turbulent viscosity ratio μ_t/μ_∞	1	-
Gauge Pressure p_∞	80507.2	Pa
Temperature T	255.6	K

aerodynamic result. The study is performed using the ONEARA M6 wing [41]. Details of geometry is presented in Section 4.2.6.

Convergence Study Setup

The ONERA M6 wing is simulated at various grid resolution at $M_\infty = 0.8395$ and angle of attack $\alpha = 3.06^\circ$. The flow conditions are selected to match experimental flow conditions of an ONERA M6 wing experiment 2308 conducted by Schmitt, V. and F. Charpin [5], see Section 4.2.6. Other flow and boundary conditions are the same as presented in Table 4.1.

Convergence Study Results

The grid convergence study shown in Fig. 4.10a revealed that 1,576,413 cells are needed for convergence in lift. The drag, however, can still be improved as evident from Fig. 4.10a where convergence has not been reached. This could be done by refining the grid further and adding density region in the wake. However, due to limitations in the computational resources we proceed with this grid as the high-fidelity model grid.

The overall simulation time needed for one high-fidelity CFD simulation was around 223 minutes, as shown in Fig. 4.10b, executed on four Intel-i7-2600 processors in parallel. This execution time is based on 10^3 solver iterations where the solver terminated due to the maximum number of iterations limit. The grid parameter details obtained through this study where previously presented and summarized in 4.2.3 above.

4.2.6 CFD Model Validation - ONERA M6

The ONERA M6 wing is a commonly used CFD validation case for external flows because of its simple geometry combined with complexities of transonic flow, i.e., local supersonic flow, shocks, and turbulent boundary layers separation. Here, we consider the ONERA M6 wing as a validation case for the high-fidelity CFD model presented in Section 4.2.

ONERA M6 Geometry

The ONERA M6 wing is a swept, semi-span wing with no twist and then symmetrical ONERA D airfoil section [5]. The numerical coordinates of the airfoil section at the

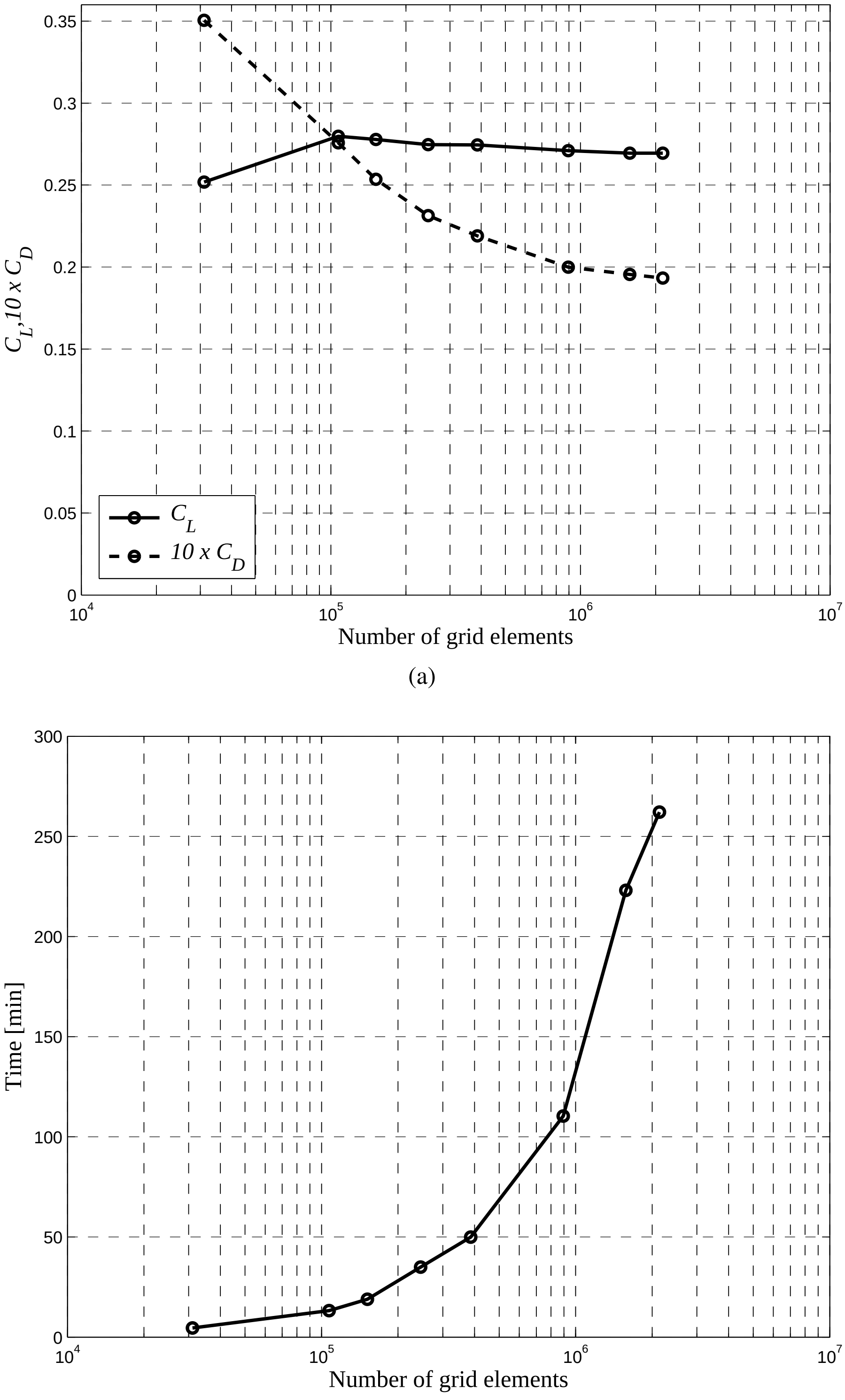

(a)

(b)

Figure 4.10: Grid convergence study using the ONERA M6 wing at $M_\infty = 0.8395$ and angle of attack $\alpha = 3.06°$. a) Lift (C_L) and drag (C_D) coefficient versus number of grid elements, b) simulation time versus number of grid elements.

Table 4.2: Geometry properties of the ONERA M6 wing.

Variable	**Value**	**Unit**
Chord length at wing root c	0.8059	m
Mean Aerodynamic Chord Length c_{mac}	0.64607	m
Semi-span $b/2$	1.1963	m
Aspect Ratio AR	3.8	-
Taper Ratio λ	0.562	-
Leading Edge Sweep ϕ	30	deg
Trailing Edge Sweep ψ	15.8	deg
Reference Area S	0.7530	m^2

Table 4.3: Flow condition of the ONERA M6 experiment 2308 conducted by Schmitt, V. and F. Charpin [5].

Variable	**Value**	**Unit**
Reynolds Number $Re_{\infty,c_{mac}}$	11.72×10^6	-
Mach M_∞	0.8395	-
Freestream Temperature T_∞	255.6	K
Angle of attack α	3.06	deg

$y/(b/2) = 0$ are obtained from NASA [41]. The coordinates indicate that there is a finite thickness to the trailing edge. In this work, we use a zero trailing edge thickness. The airfoil coordinates are linearly scaled near the trailing edge so that the trailing edge thickness is zero. Geometric properties of the ONERA M6 wing is found in Table 4.2.

Validation Setup

To validate the high-fidelity grid we need experimental data for comparison. We use experimental data from a ONEARA M6 wing wind tunnel experiment 2308 conducted by Schmitt, V. and F. Charpin [5]. The experimental flow conditions are listed in Table 4.3

In order to perform a CFD simulation, we need to calculate other flow properties and boundary conditions such as the freestream pressure p_∞. The free-stream speed of sound a_∞ for a perfect gas depends on temperature only and is defined and is found to be

$$a_\infty = \sqrt{\gamma R T_\infty} = \sqrt{1.401 \times 287 \times 255.6} = 320.5\, m/s, \tag{4.2.6}$$

where $\gamma = 1.401$ is the ratio of specific heats for air and $R = 287 J/kg\, K$ is the gas constant for dry air [42]. Using the definition of Mach number we find the flow velocity

$$V_\infty = Ma_\infty = 0.8395 \times 320.5 = 269.1\, m/s, \tag{4.2.7}$$

Using the freestream temperature we find the viscosity for air using Sutherland's Law [42]

$$\mu_\infty = \mu_0 \left(\frac{T_\infty}{T_0}\right)^{3/2} \left(\frac{T_0 + S}{T_\infty + S}\right) = 1.62 \times 10^{-5}\, kg/m\, s, \tag{4.2.8}$$

where at standard sea level $S = 110$, $\mu_0 = 1.7894 \times 10^{-5} Kg/m\, s$ and $T_0 = 288.16K$. Now using Reynolds number definition $Re_{c_{mac}} = \rho_\infty V_\infty c_{mac}/\mu_\infty$ and the ideal gas law $p_\infty = \rho_\infty R T_\infty$ solving the equations together we obtain the freestream static pressure

$$p_\infty = \frac{Re_{c_{mac}} \mu_\infty R T_\infty}{V_\infty c_{mac}} = 80507.2\, Pa. \tag{4.2.9}$$

Specific heat capacity is then found to be

$$c_p = \frac{\gamma R}{\gamma - 1} = 1003.06\, J/Kg\, k. \tag{4.2.10}$$

The above boundary conditions and fluid properties where previously presented and summarized in Section 4.2.4 Table 4.1, respectively.

Validation Result

The available experimental data obtained by Schmitt and Charpin, consists of pressure coefficients (C_p) values at seven cross-sections along the span of the wing where the cross-section are at $y/(b/2)$ = 0.2, 0.44, 0.65, 0.8, 0.9, 0.95, 0.99. We simulate the ONERA M6 geometry using the flow and boundary conditions presented above, extract pressure data and compare the CFD data to the Schmitt and Charpin experimental data [5]. Results are presented in Fig. 4.11 to Fig. 4.17. Inspecting the result we see that the correlation between CFD data and experimental data is excellent although at $y/(b/2)$ = 0.99, shown in Fig. 4.17 there appears to be notable difference at the trailing edge upper surface. We are able to resolve the steep pressure gradient at the leading edge as well as capture the double shock with its distinctive "lambda" pattern appearing on the upper surface of the wing as show in Fig. 4.18.

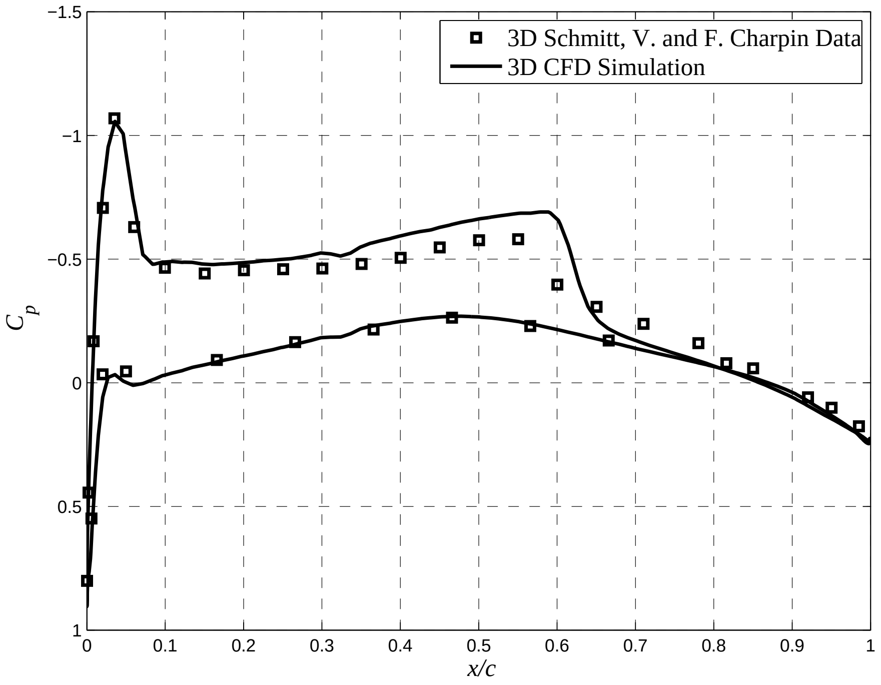

Figure 4.11: Pressure coefficient (C_p) at $y/(b/2) = 0.2$ of ONERA M6 wing at $M_\infty = 0.8395$ and angle of attack $\alpha = 3.06°$. CFD results shown with solid line (-). Wind tunnel experiment 2308 conducted by Schmitt, V. and F. Charpin [5] shown with square markers.

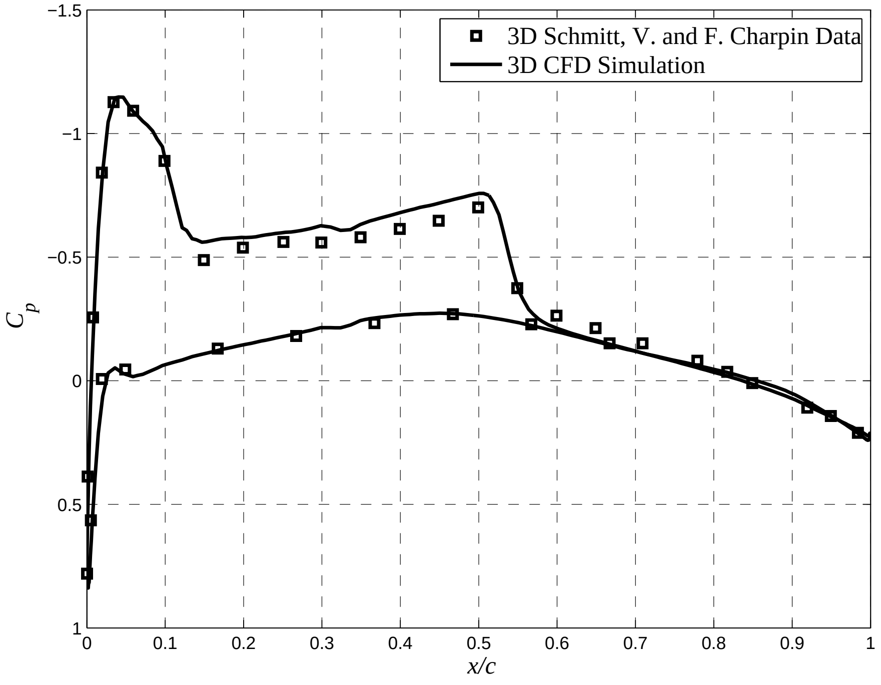

Figure 4.12: Pressure coefficient (C_p) at $y/(b/2) = 0.44$ of ONERA M6 wing at $M_\infty = 0.8395$ and angle of attack $\alpha = 3.06°$. CFD results shown with solid line (-). Wind tunnel experiment 2308 conducted by Schmitt, V. and F. Charpin [5] shown with square markers.

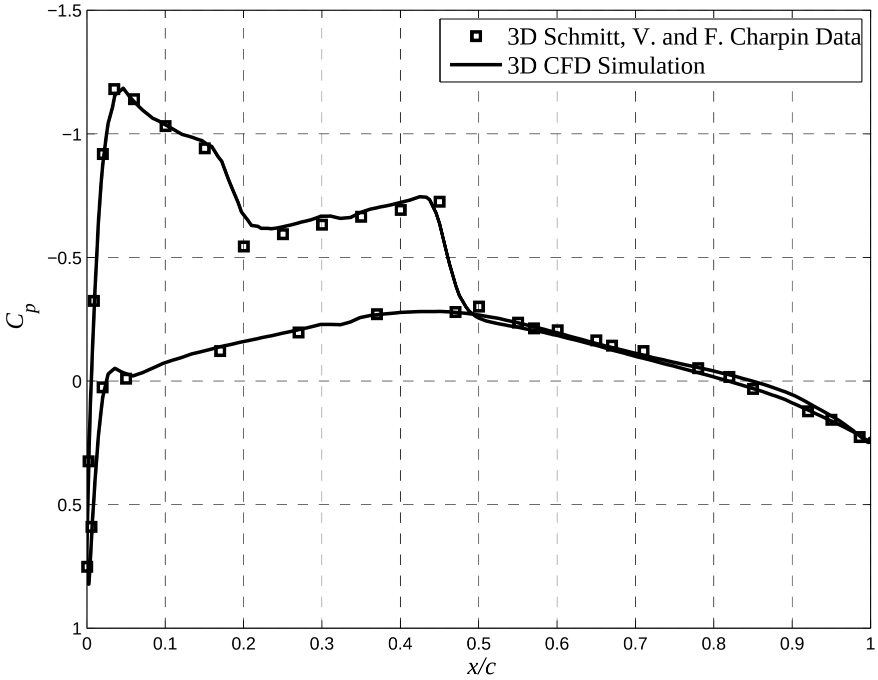

Figure 4.13: Pressure coefficient (C_p) at $y/(b/2) = 0.65$ of ONERA M6 wing at $M_\infty = 0.8395$ and angle of attack $\alpha = 3.06°$. CFD results shown with solid line (-). Wind tunnel experiment 2308 conducted by Schmitt, V. and F. Charpin [5] shown with square markers.

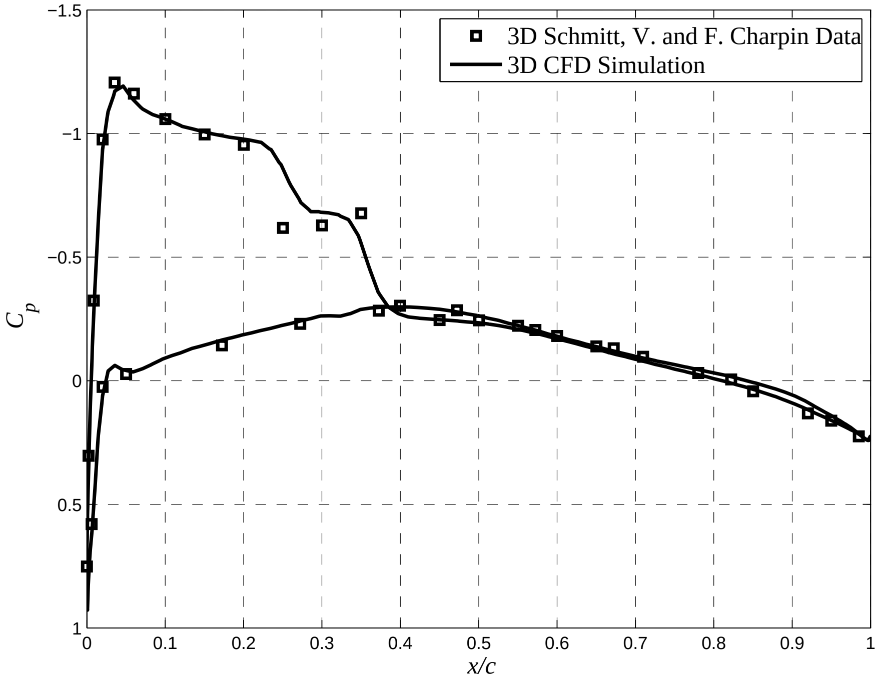

Figure 4.14: Pressure coefficient (C_p) at $y/(b/2) = 0.8$ of ONERA M6 wing at $M_\infty = 0.8395$ and angle of attack $\alpha = 3.06°$. CFD results shown with solid line (-). Wind tunnel experiment 2308 conducted by Schmitt, V. and F. Charpin [5] shown with square markers.

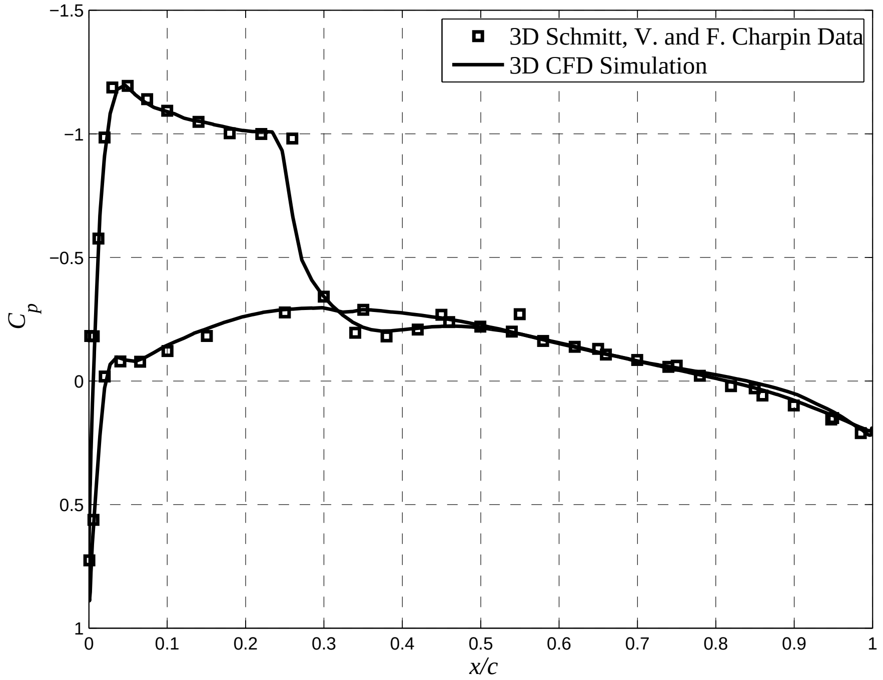

Figure 4.15: Pressure coefficient (C_p) at $y/(b/2) = 0.9$ of ONERA M6 wing at $M_\infty = 0.8395$ and angle of attack $\alpha = 3.06°$. CFD results shown with solid line (-). Wind tunnel experiment 2308 conducted by Schmitt, V. and F. Charpin [5] shown with square markers.

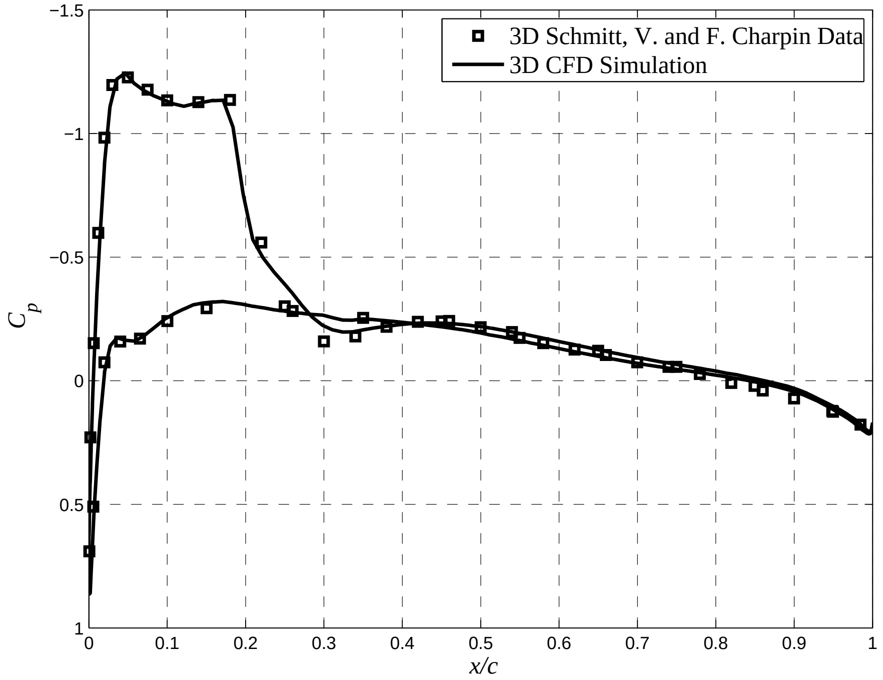

Figure 4.16: Pressure coefficient (C_p) at $y/(b/2) = 0.95$ of ONERA M6 wing at $M_\infty = 0.8395$ and angle of attack $\alpha = 3.06°$. CFD results shown with solid line (-). Wind tunnel experiment 2308 conducted by Schmitt, V. and F. Charpin [5] shown with square markers.

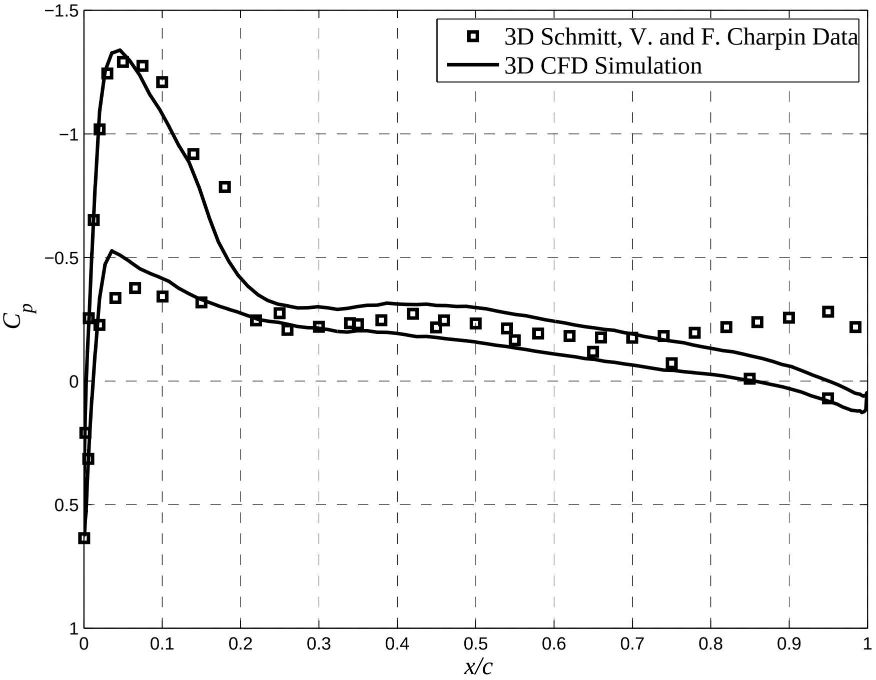

Figure 4.17: Pressure coefficient (C_p) at $y/(b/2) = 0.99$ of ONERA M6 wing at $M_\infty = 0.8395$ and angle of attack $\alpha = 3.06°$. CFD results shown with solid line (-). Wind tunnel experiment 2308 conducted by Schmitt, V. and F. Charpin [5] shown with square markers.

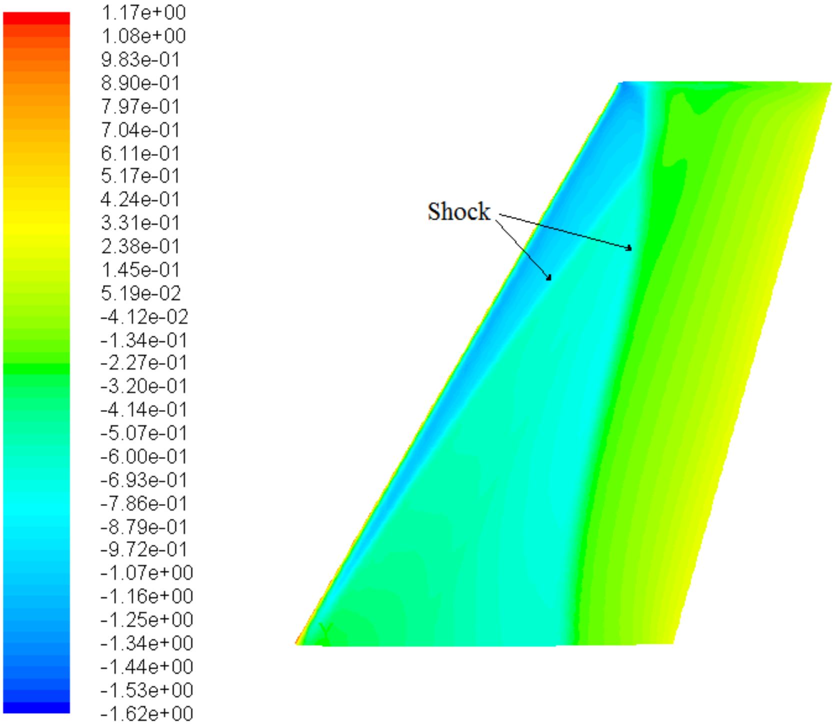

Figure 4.18: Upper surface, pressure coefficient (C_p) contour plot of ONERA M6 wing at $M_\infty = 0.8395$ and angle of attack $\alpha = 3.06°$. Note the double shock on the surface, one at the leading edge and one at mid wing, where they then merge close to the wing tip.

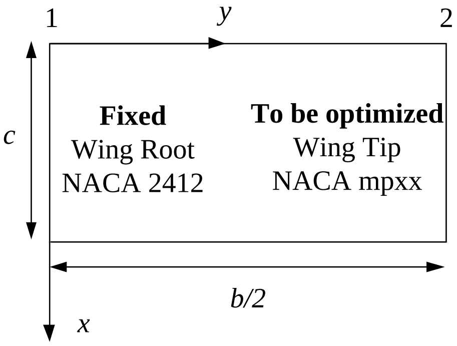

Figure 4.19: Rectangular wing planform view. $b/2$ is the normalized wingspan and c is the normalized wing chord length.

4.3 Wing Design Optimization at Transonic Flow Conditions

In this study, we consider a lift maximization case of a rectangular wing at transonic conditions where we carry out the optimization, using the space mapping methodology presented in Section 2.4. No direct optimization of the problem will be done simply due to the heavy computational cost of the high-fidelity model. Using a simple rectangular wing consisting of two NACA 4 digit airfoils at wing root and wing tip. We want to design the wing shape by optimizing only the wing tip airfoil, and keeping all other geometric parameters fixed.

Formulation of the problem is given first, followed by a presentation on the low-fidelity model construction used in this work. The section concludes by presenting the space mapping optimization results.

4.3.1 Formulation

For the sake of simplicity, we consider a simple unswept and untwisted rectangular wing as an illustration case for the proposed optimization algorithm. Planform view of the wing is shown in Fig. 4.19.

The wing consists of two normalized NACA 4 digit airfoils with a normalized chord length $c = 1$ and a straight line wrap between airfoils. The wing shape is parametrized such that design variables considered in this work include only the wing tip NACA airfoil parameters $(m, p, t/c)$. A NACA 2412 airfoil is chosen as the wing root airfoil and kept fixed. The initial design $\mathrm{x}^{(0)}$ for the wing tip is chosen at random. The normalized semi-wingspan is set as twice the wing chord length c as $(b/2) = 2c$. The wing aspect ratio is found to be;

$$AR = \frac{b^2}{A} = \frac{b^2}{b \times c} = \frac{b}{c} = \frac{4c}{c} = 4, \tag{4.3.1}$$

which is a low aspect ratio wing. With such low aspect ratio, induced drag effects from downwash or vortexes at the wing tip affect the wing performance even more than it would for a high aspect ratio wing. All other wing parameters are fixed during the optimization. The design vector for optimizing the wing can be written as $\mathbf{x} = [m, p, t/c]^T$ where the variables represent the wing tip NACA airfoil parameters.

The objective is to maximize the lift coefficient $C_{L,f}$ subject to constraints on the drag coefficient $C_{D,f} \leq C_{D,\max}$ where $C_{D,\max} = 0.03$. Additionally, we set constraints on the structure of the wing by setting a constraint on the wing tip normalized cross-sectional area such that $A \geq A_{\min}$. Initially the area constraints was selected as $A_{\min} = 0.06$. This turned out to be too high where the proposed algorithm could not improve the design since the cross-sectional area was already at its constraint boundary. The area constraint was therefore reduced to $A_{\min} = 0.01$ to alleviate the problem. Lower and upper bounds are specified for each of the design variables $\mathbf{x} = [m, p, t/c]$. The side constraints on the design variables are $0 \leq m \leq 0.03$, $0.4 \leq p \leq 0.8$ and $0.07 \leq t/c \leq 0.12$.

We summarize the optimization setup of the problem for convenience

$$\mathbf{x}^* = \arg\max_{\mathbf{x}} C_L, \tag{4.3.2}$$

subject to

$$\begin{aligned} C_{D,f} \leq C_{D,\max} &= 0.03, \\ A \geq A_{\min} &= 0.01, \end{aligned} \tag{4.3.3}$$

with the following design variable bounds

$$\begin{aligned} 0 \leq\, & m \leq 0.03, \\ 0.4 \leq\, & p \leq 0.8, \\ 0.07 \leq\, & t/c \leq 0.12. \end{aligned} \tag{4.3.4}$$

Terminating condition for the optimization algorithm is set to $||\mathbf{x}^{(i)} - \mathbf{x}^{(i-1)}|| < 10^{-3}$.

4.3.2 Low-Fidelity CFD Model

The low-fidelity model c is constructed in the same way as the high-fidelity model f but with a coarser grid discretization and with a relaxed convergence criteria. Referring back to the grid study made in Section 4.2.5 inspecting Fig. 4.10a we make our selection

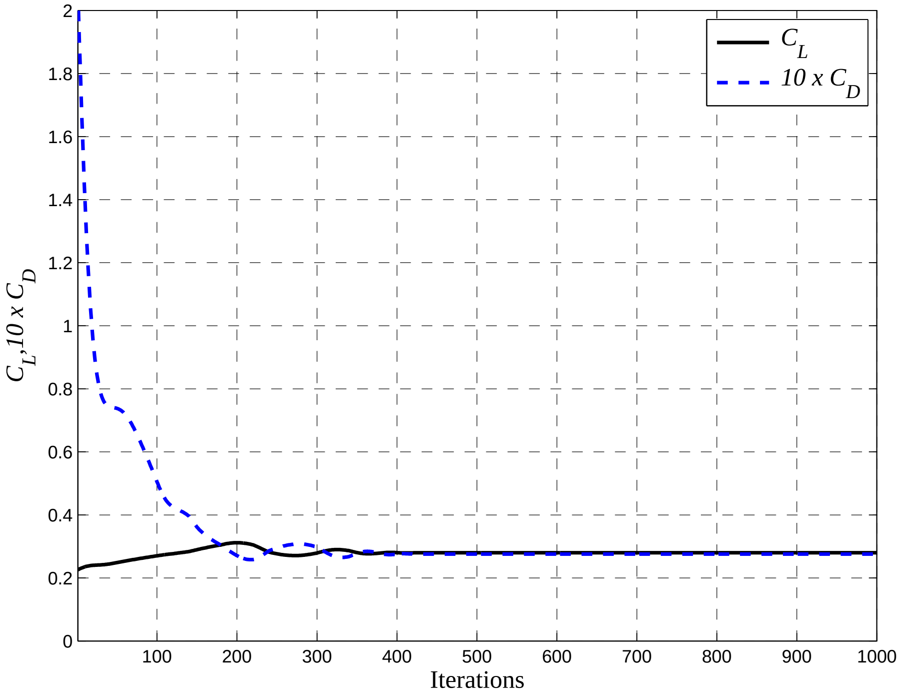

Figure 4.20: Lift and Drag coefficient convergence plot for low-fidelity model obtained in grid convergence study simulation using ONERA M6 wing at Mach number $M_\infty = 0.8395$ and angle of attack $\alpha = 3.06°$.

for the coarse low-fidelity model. Based on time and accuracy with respect of lift and drag we select the grid parameters that represent the second point from left, giving a 107,054 elements. The time taken to evaluate the low-fidelity model is 13.2 minutes on four Intel-i7-2600 processors in parallel. Inspecting further the lift and drag convergence plot for the low-fidelity model Fig. 4.20 we note that the solution has converged after 400-500 iterations. Maximum number of iterations for the low-fidelity model is set to 500 iterations. This reduces the overall simulation time to 6.6 minutes. The ratio of simulation times of the high- and low- fidelity model in this case is high/low = $223/6.6 \approxeq 34$. This is based on the solver uses all 500 iterations in the low-fidelity model to obtain a solution.

4.3.3 Space Mapping Optimization Results

We exploit the space mapping methodology as described in Section 2.4 to carry out a computationally efficient optimization.

An attempt was made to construct and use a Kriging model [11] as the coarse model, based on the low-fidelity model described in Section 4.3.2. Kriging model training data was obtained by uniform sampling the design space given in Eq. (4.3.4) with density of 5 for each design variable resulting in $5^3 = 125$ sample points. Kriging model was tested with 20 additional training points sampled using Latin Hypercube Sampling (LHS) [7] from the same design space as given in Eq. (4.3.4).

The Kriging model, however, turns out to be unusable and a poor representation of the low-fidelity model. This is likely a consequence of the noise in the low-fidelity model. Kriging model assumes the data is an accurate response and interpolates between training point responses which in this case include a heavy noise. The Kriging model therefore can add even more error and inaccuracy to the response than the low-fidelity model, resulting in a poor representation of the high-fidelity model. Design space is also relatively large and adding more training points may be considered to improve the model response but due to the noise the Kriging approach is altogether dropped.

In order to alleviate the problem and to try to overcome the numerical noise issue present in the low-fidelity model, a second order polynomial approximation model is constructed [13] using 50 training points sampled using LHS from the low-fidelity model. These points are sampled from a smaller design space where we update the design space boundaries:

$$\begin{aligned} 0.02 \leq\, & m \leq 0.03, \\ 0.7 \leq\, & p \leq 0.9, \\ 0.06 \leq\, & t/c \leq 0.08. \end{aligned} \tag{4.3.5}$$

As before the idea is to use relatively few points to construct the approximation model. The benefit is while Kriging interpolates the training data, which includes numerical noise, the second order polynomial approximates the low-fidelity data response data. Polynomial regression [13] is used to fit the approximation model to the training data. In addition, second order polynomial model has nice analytical properties such as smoothness and convexity. This second order approximation model is used as the low-fidelity model c or the coarse model in this work. The surrogate approximation model is optimized using pattern-search [21] during the optimization.

The proposed method was executed twice with different initial designs that where chosen at random within the design space presented in Eq. (4.3.5). Optimum numerical results obtained by the proposed method for both runs are presented in the following sections.

Results for Run 1

For run number 1 the initial design is $\mathbf{x}^{(0)} = [0.0200, 0.7000, 0.0628]$ for this SM optimization run. Optimum numerical results obtained by the proposed method are shown in Table 4.4, where they are compared to the initial design. Inspecting the table we see that the proposed method is able to increase lift by +10%. The drag is pushed above its limit at $C_{D,\max} = 0.03$, where the optimized drag coefficient $C_D = 0.0311$ increases by +29% and violates the constraint slightly, or by +4%, which is within the 5% constraint band tolerance. The lift to drag ratio is decreased by 14%. The proposed method requires less than 10 high-fidelity model evaluations, 50 low-fidelity model evaluations used to create the approximation model and 8 high-fidelity model evaluations.

The optimized wing tip NACA airfoil section is shown in Fig. 4.21. It is evident that the optimized wing tip airfoil is thicker. The normalized cross-sectional area is increased by +26%, and the increased drag can be related to the increment in area. No change is in the camber m but the location of the maximum camber p is moved slightly aft.

The optimization history for Run 1 is shown in Fig. 4.22. One can observe the evolution of the objective function Fig. 4.22a, convergence plot Fig. 4.22b and evolution of lift and drag Fig. 4.22c and Fig. 4.22d respectively. It is observed that the algorithm shows a good convergence reaching the 10^3 stopping criterion. The algorithm is able to increase lift while it forces the drag to its constraint at $C_D \leq 0.03$ where the constraint is slightly violated. To underline the algorithm robustness, during the optimization, at iteration 3 the flow solver crashed during a high-fidelity model evaluation due to a grid error resulting in large negative values for lift and drag. However, the algorithm is able to recover.

Pressure coefficient plots comparison between the initial design and optimized designs are given for airfoil cross-section at $y/(b/2)$ = 0.2, 0.44, 0.65, 0.8, 0.9, 0.95, 0.99, and are shown in Fig. 4.23 to Fig. 4.29. Further, a planform pressure coefficient contour plots of the initial and optimized designs are shown in Fig. 4.30 and Fig. 4.31, respectively. Both upper and lower surfaces are shown and compared. It is clear from the plots that by moving the camber aft the pressure distribution opens up a little bit along the wing-span but also induces another shock close to the trailing edge and the wing tip. The shock gets stronger when moving along the span. The effect from this shock increases the lift but also increases the drag.

Mach number contour plots comparing initial and optimized design for airfoil cross-section at $y/(b/2)$ = 0.2, 0.44, 0.65, 0.8, 0.9, 0.95, 0.99 are shown in Fig. 4.32 to Fig. 4.38.

Table 4.4: Optimum numerical results for Run 1 compared to initial design $\mathbf{x}^{(0)} = [0.0200, 0.7000, 0.0628]$. The ratio of the high-fidelity model evaluation time to the low-fidelity is 34.

Variable	**Initial**	**This work (SM)**	Δ
m	0.0200	0.0200	-
p	0.7000	0.8725	-
t/c	0.0628	0.0793	-
C_L	0.2759	0.3047	+10%
C_D	0.0241	0.0311	+29%
C_L/C_D	11.4481	9.7974	-14%
A	0.0422	0.0534	+26%
N_c	-	50	
N_f	-	8	
Total Cost	-	< 10	

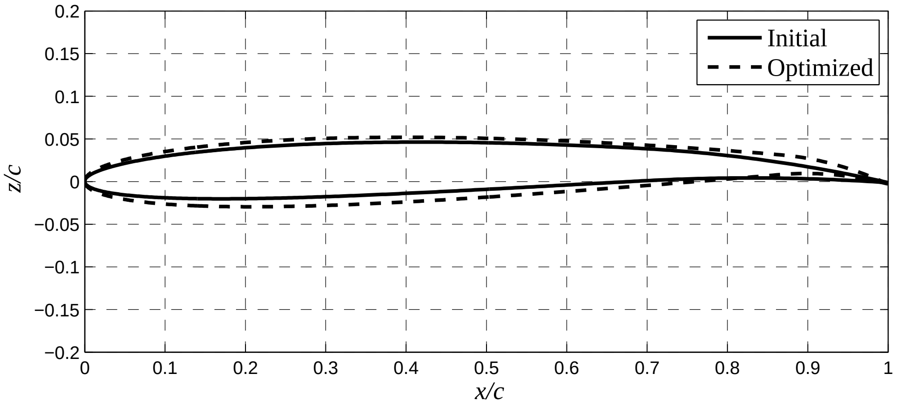

Figure 4.21: Run 1 optimum design geometry of the NACA airfoil obtained using space mapping algorithm shown with dashed line (- -). Initial design shown with solid line (–).

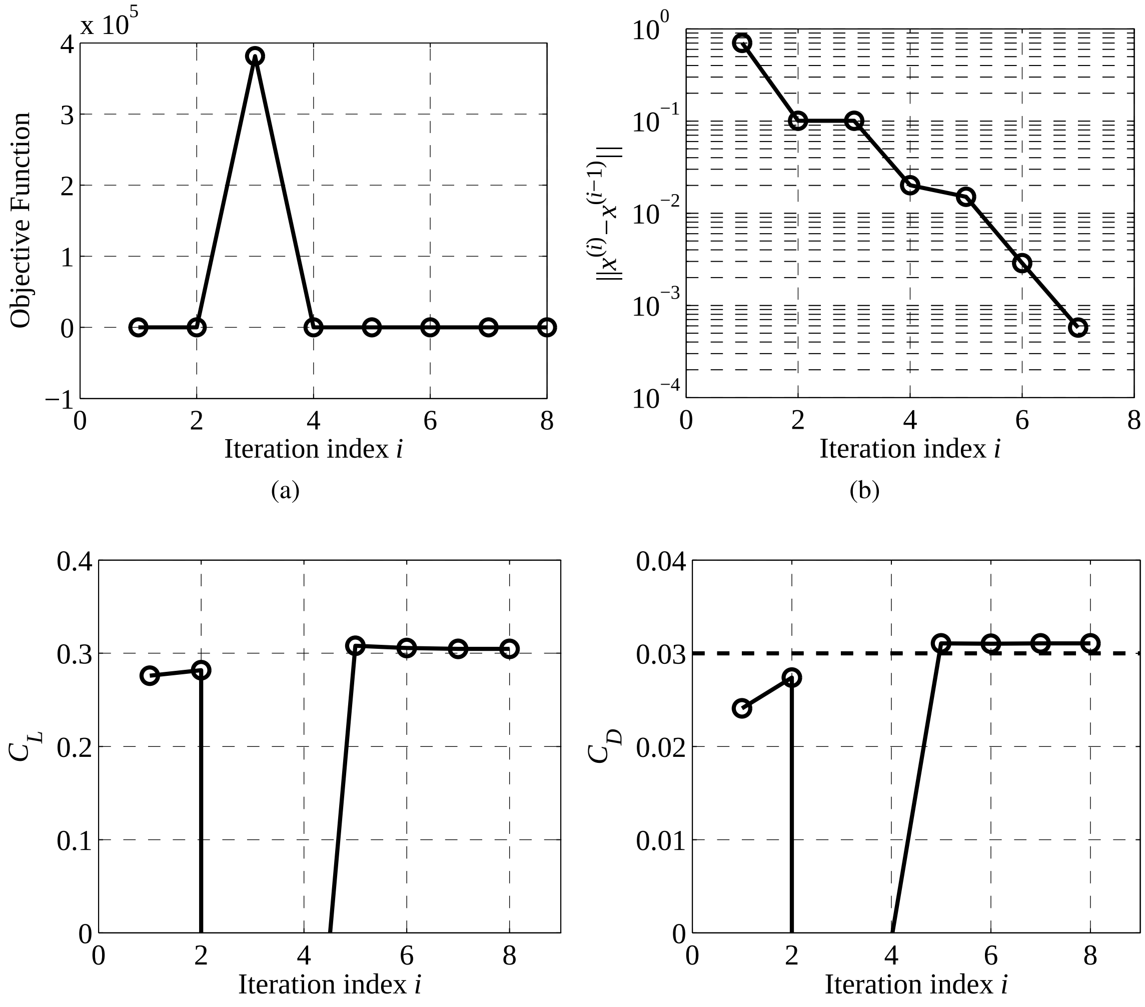

(a) (b)

(c) (d)

Figure 4.22: Optimization history using the proposed SM methodology. a) Evolution of the objective function; b) convergence Plot; c) evolution of lift coefficient and; d) evolution of drag coefficient where dash line (- -) is the drag constraint. At iteration 3 flow solver crashes due to grid error.

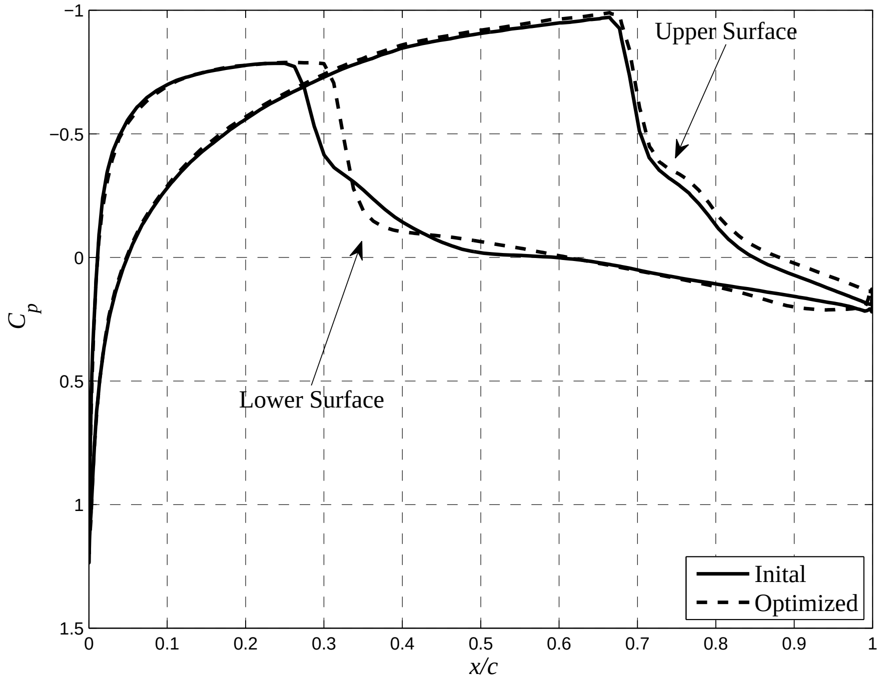

Figure 4.23: Run 1 pressure coefficient (C_p) at $y/(b/2) = 0.2$ where $M_\infty = 0.8395$ and angle of attack $\alpha = 0°$. Initial design shown with solid line (–). Optimum design shown with dashed line (- -).

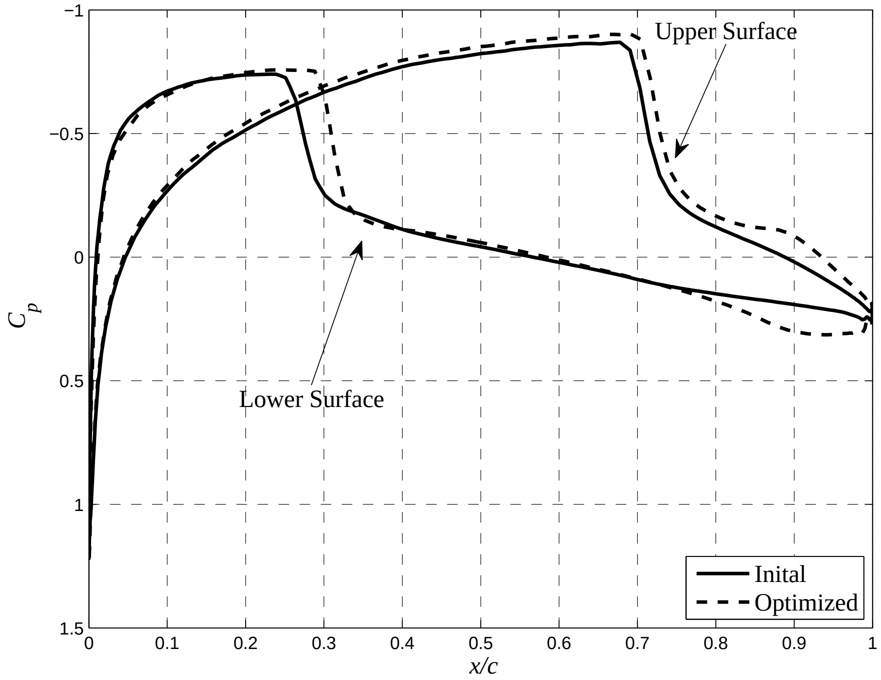

Figure 4.24: Run 1 pressure coefficient (C_p) at $y/(b/2) = 0.44$ where $M_\infty = 0.8395$ and angle of attack $\alpha = 0°$. Initial design shown with solid line (–). Optimum design shown with dashed line (- -).

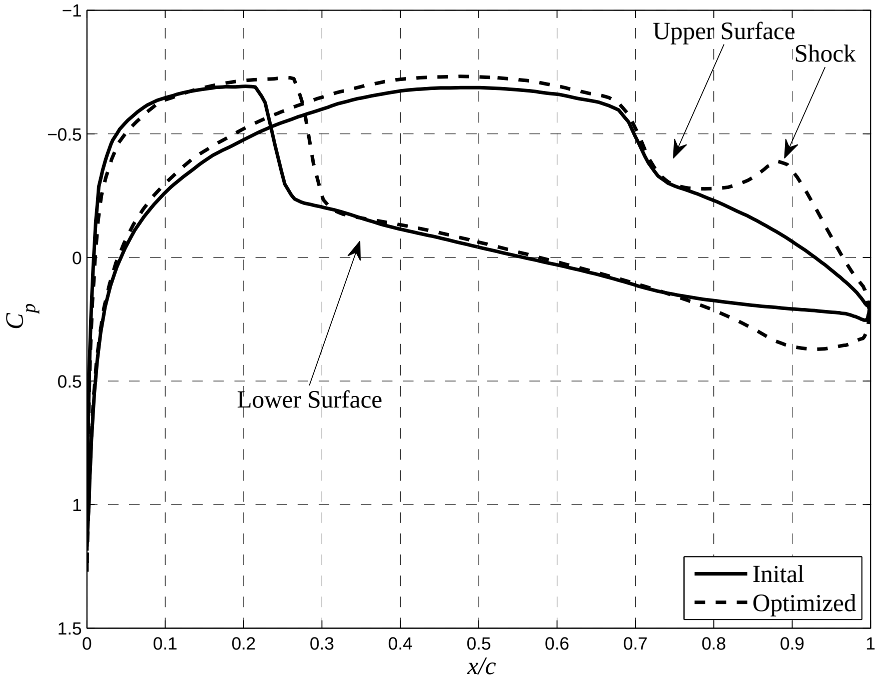

Figure 4.25: Run 1 pressure coefficient (C_p) at $y/(b/2) = 0.65$ where $M_\infty = 0.8395$ and angle of attack $\alpha = 0°$. Initial design shown with solid line (–). Optimum design shown with dashed line (- -). Notice the shock close to the trailing edge.

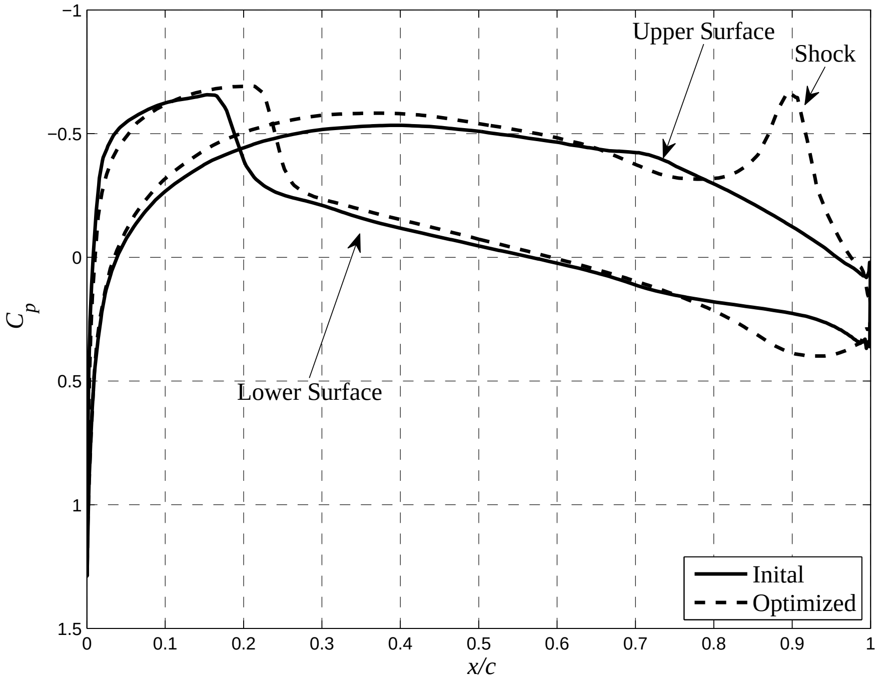

Figure 4.26: Run 1 pressure coefficient (C_p) at $y/(b/2) = 0.8$ where $M_\infty = 0.8395$ and angle of attack $\alpha = 0°$. Initial design shown with solid line (–). Optimum design shown with dashed line (- -). Notice the shock close to the trailing edge.

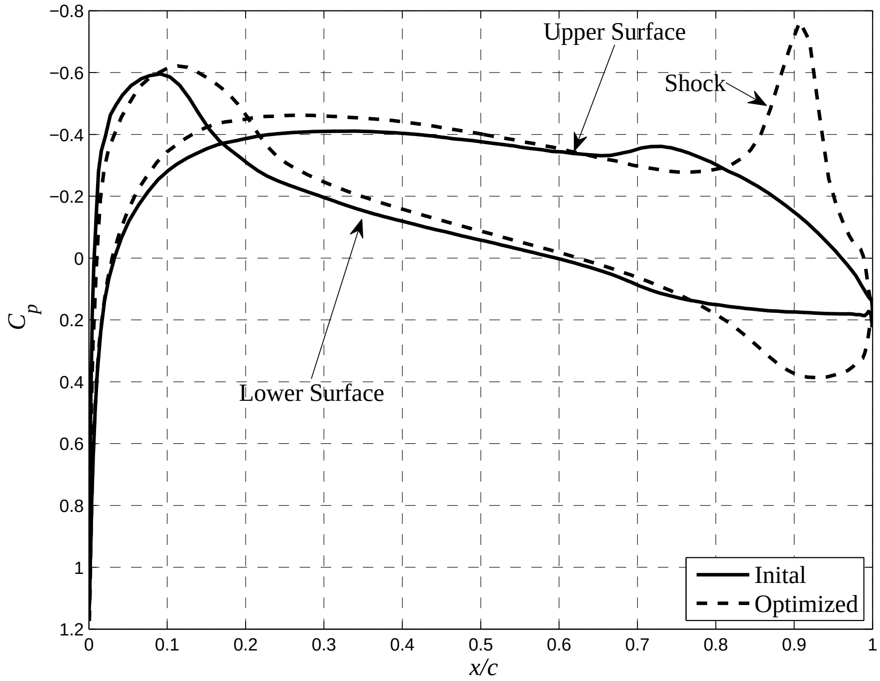

Figure 4.27: Run 1 pressure coefficient (C_p) at $y/(b/2) = 0.9$ where $M_\infty = 0.8395$ and angle of attack $\alpha = 0°$. Initial design shown with solid line (–). Optimum design shown with dashed line (- -). Notice the shock close to the trailing edge.

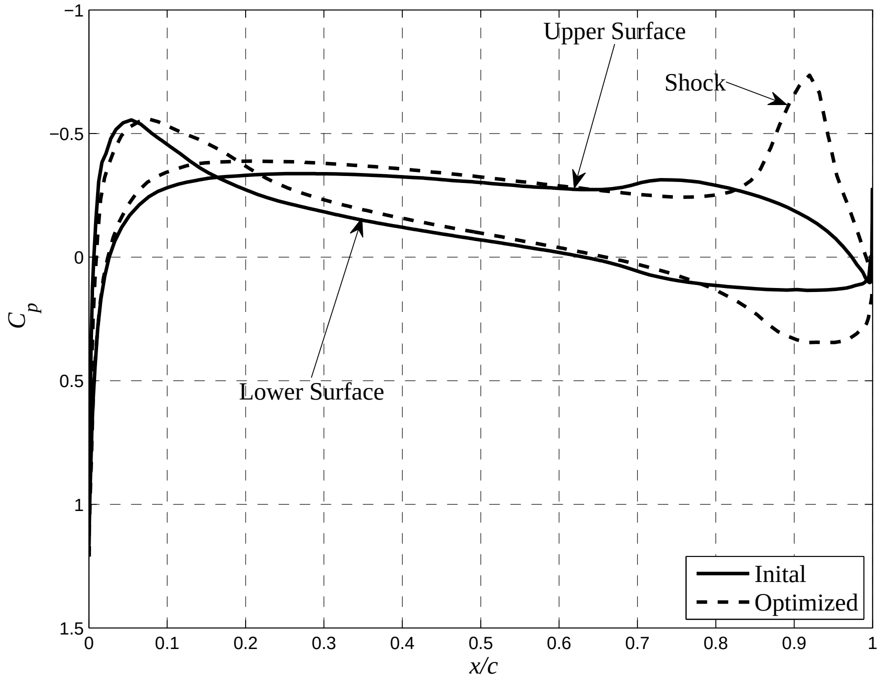

Figure 4.28: Run 1 pressure coefficient (C_p) at $y/(b/2) = 0.95$ where $M_\infty = 0.8395$ and angle of attack $\alpha = 0°$. Initial design shown with solid line (–). Optimum design shown with dashed line (- -). Notice the shock close to the trailing edge.

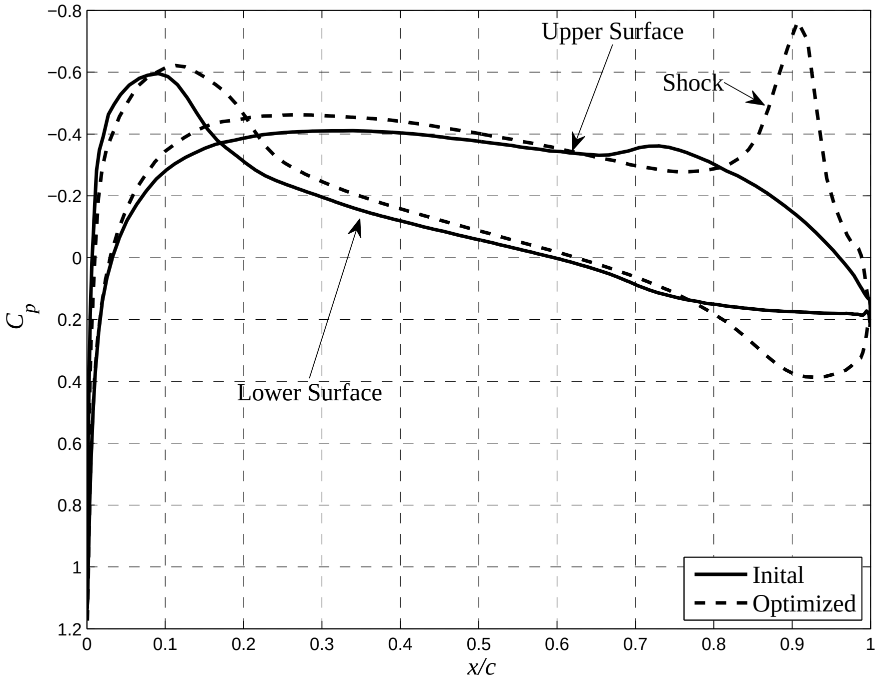

Figure 4.29: Run 1 pressure coefficient (C_p) at $y/(b/2) = 0.99$ where $M_\infty = 0.8395$ and angle of attack $\alpha = 0°$. Initial design shown with solid line (–). Optimum design shown with dashed line (- -). Notice the shock close to the trailing edge.

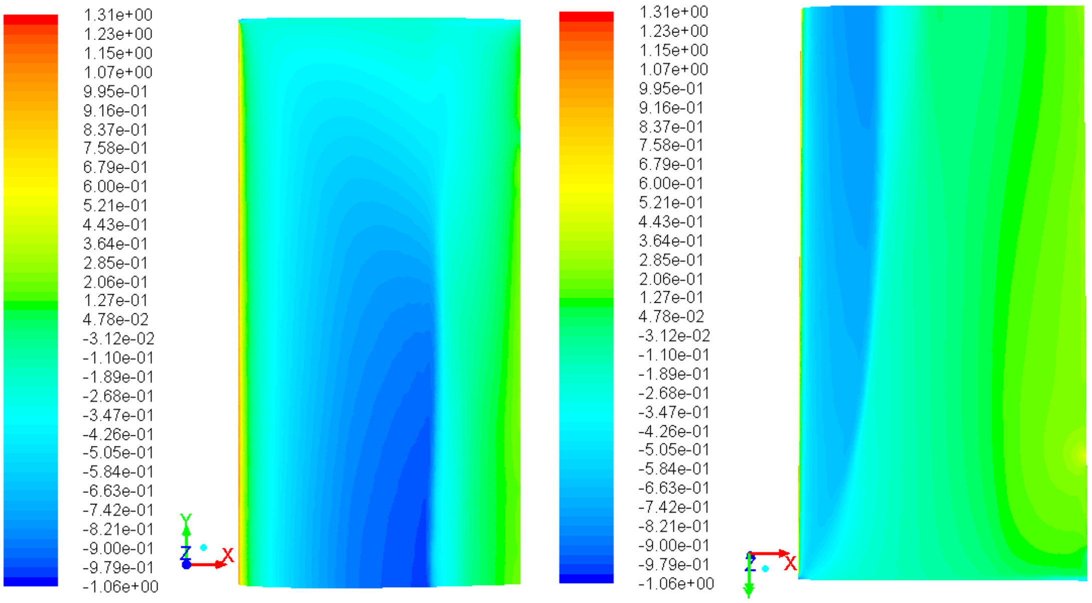

(a) Upper surface (b) Lower surface

Figure 4.30: Run 1 planform pressure coefficient contour plots of the initial design geometry. a) The upper surface shows a shocks at mid section of the wing. b) The lower surface shows one shock at the leading edge.

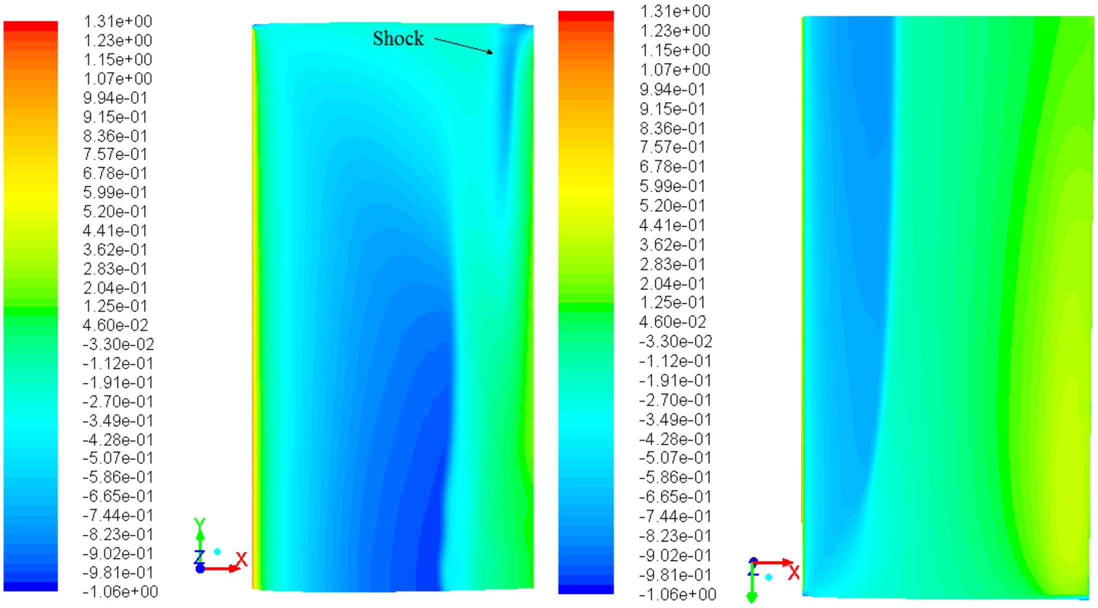

(a) Upper surface (b) Lower surface

Figure 4.31: Run 1 planform pressure coefficient contour plots of the optimized design geometry. a) The upper surface shows two shocks, one at mid section of the wing and one close to the wing tip at the trailing edge. b) The lower surface shows one shock at the leading edge.

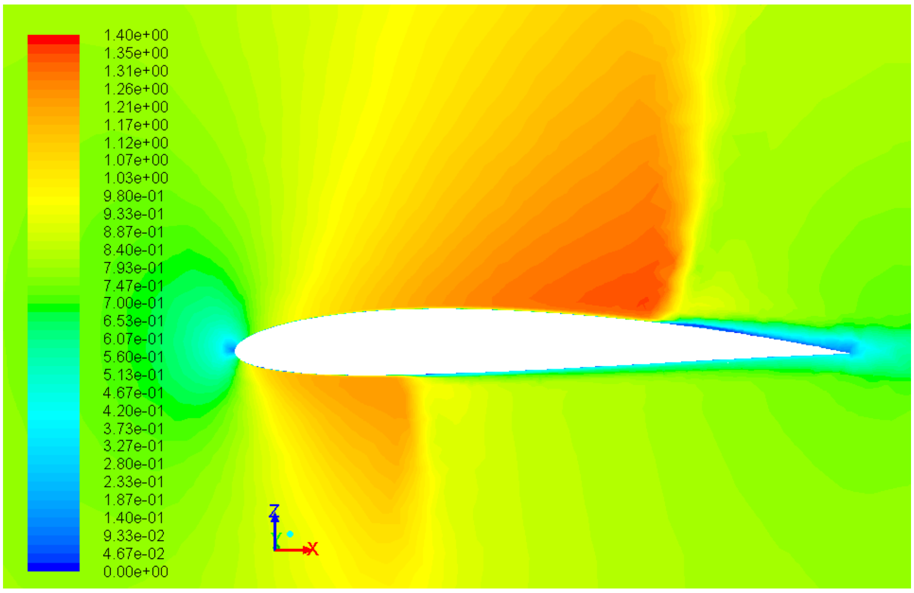

(a) Initial

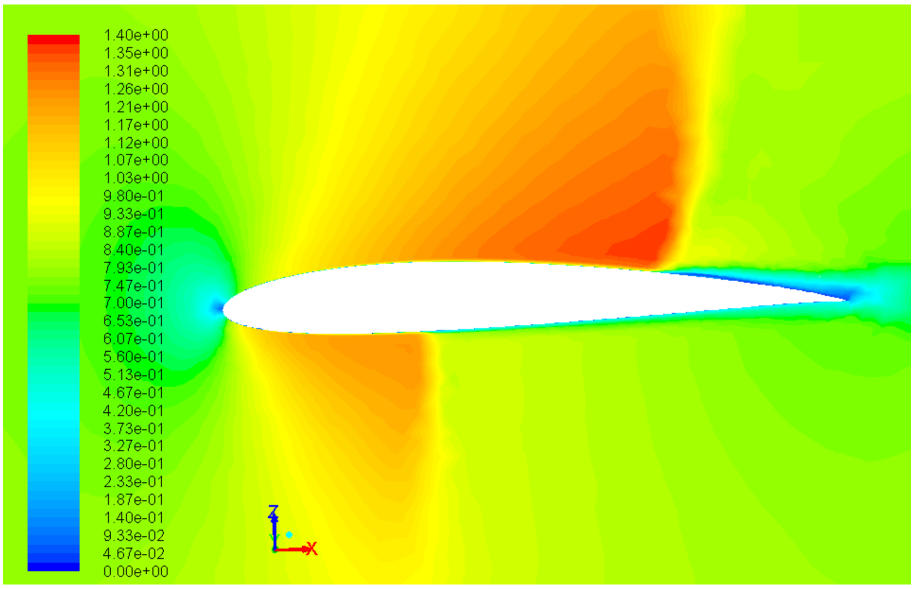

(b) Optimized

Figure 4.32: Run 1 Mach number contour plot (M) at $y/(b/2) = 0.2$ where $M_\infty = 0.8395$ and angle of attack $\alpha = 0°$. a) Shows the initial design; b) Shows the optimized design.

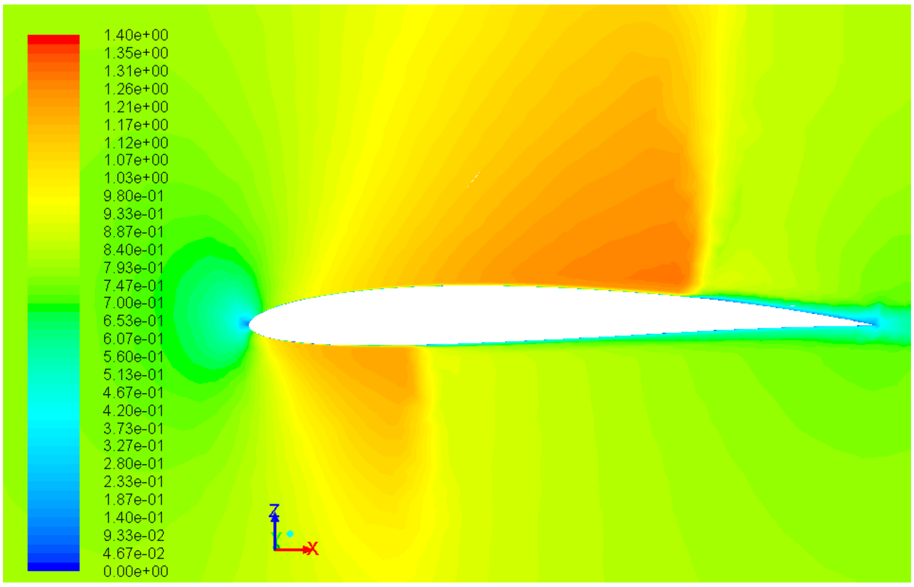

(a) Initial

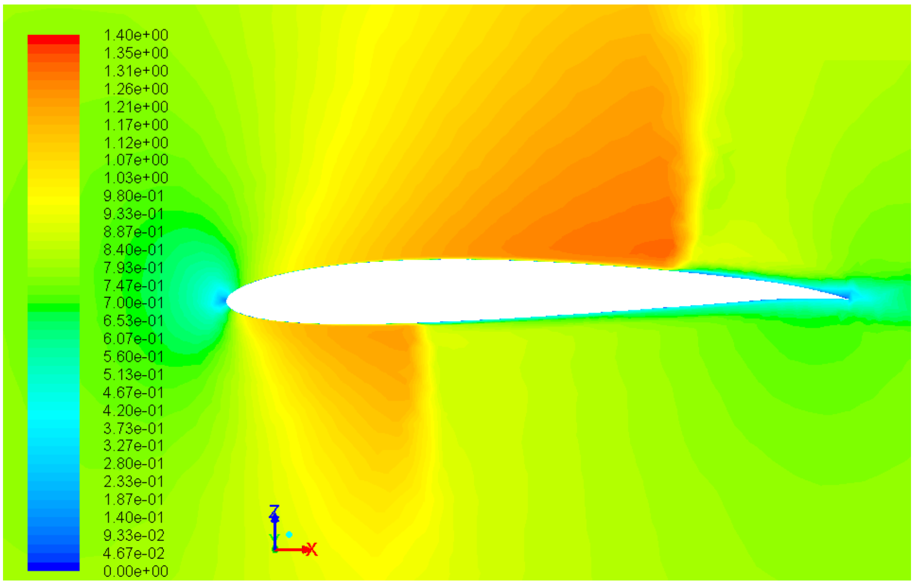

(b) Optimized

Figure 4.33: Run 1 Mach number contour plot (M) at $y/(b/2) = 0.44$ where $M_\infty = 0.8395$ and angle of attack $\alpha = 0°$. a) Shows the initial design; b) Shows the optimized design.

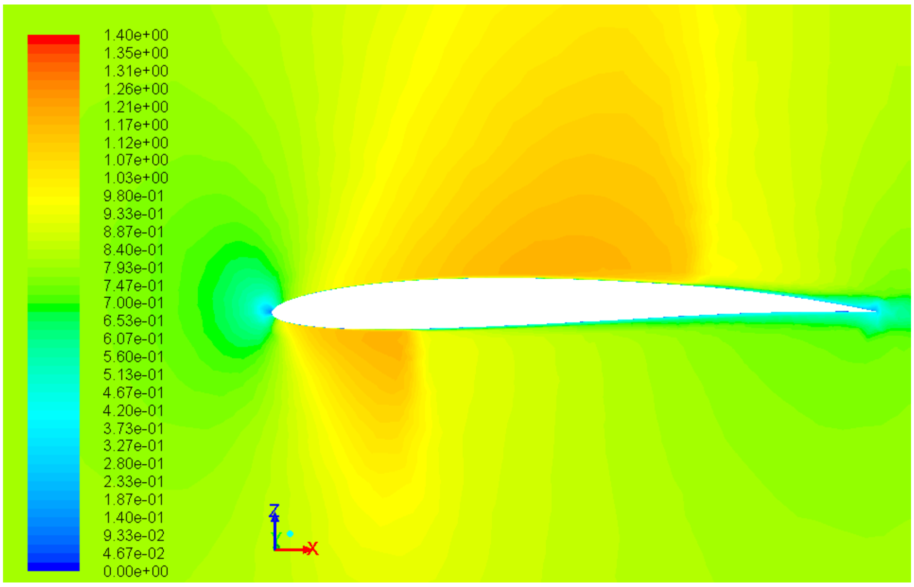

(a) Initial

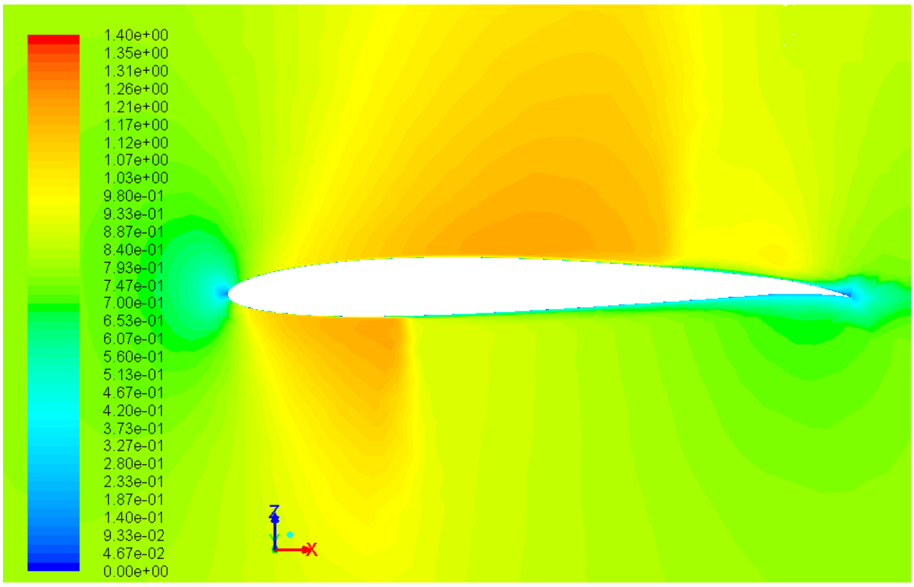

(b) Optimized

Figure 4.34: Run 1 Mach number contour plot (M) at $y/(b/2) = 0.65$ where $M_\infty = 0.8395$ and angle of attack $\alpha = 0°$. a) Shows the initial design; b) Shows the optimized design.

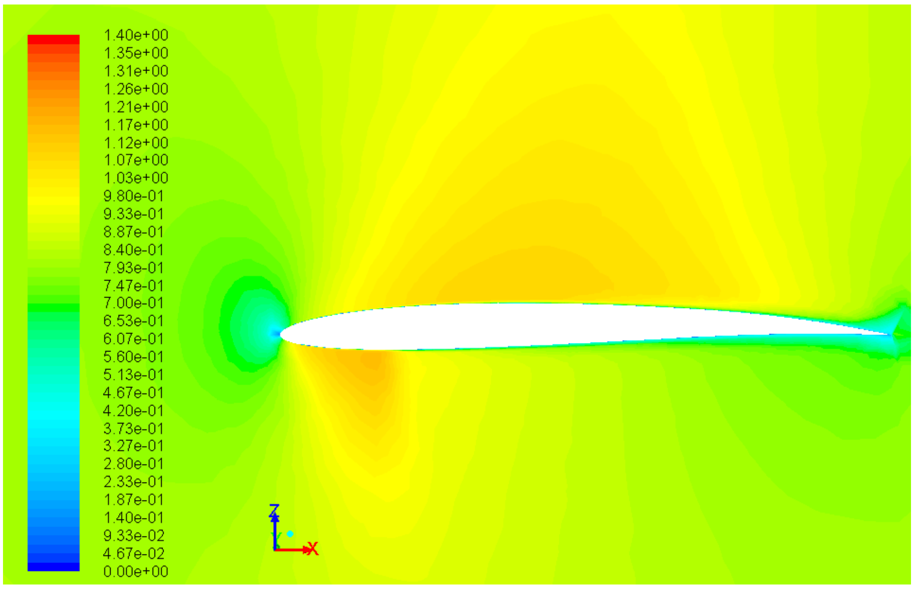

(a) Initial

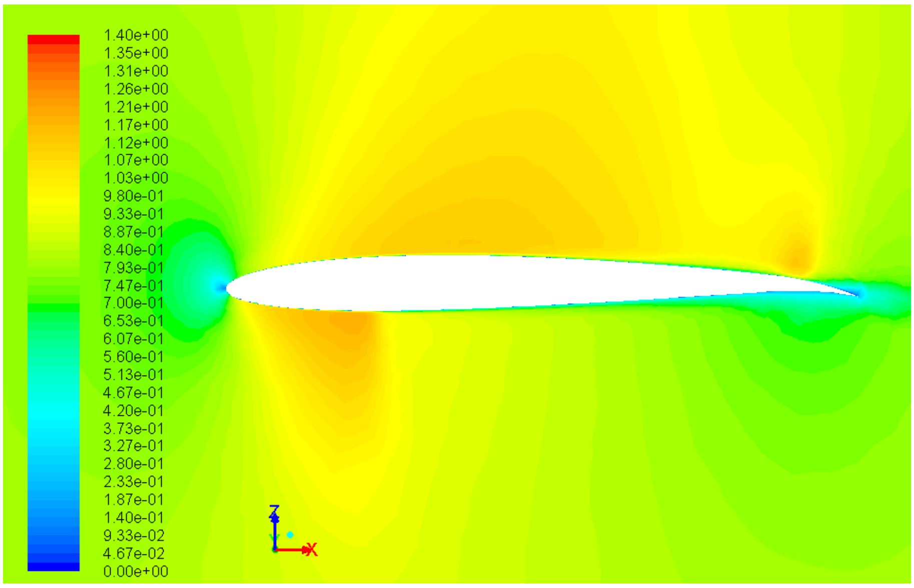

(b) Optimized

Figure 4.35: Run 1 Mach number contour plot (M) at $y/(b/2) = 0.8$ where $M_\infty = 0.8395$ and angle of attack $\alpha = 0°$. a) Shows the initial design; b) Shows the optimized design. Notice the shock at the trailing edge.

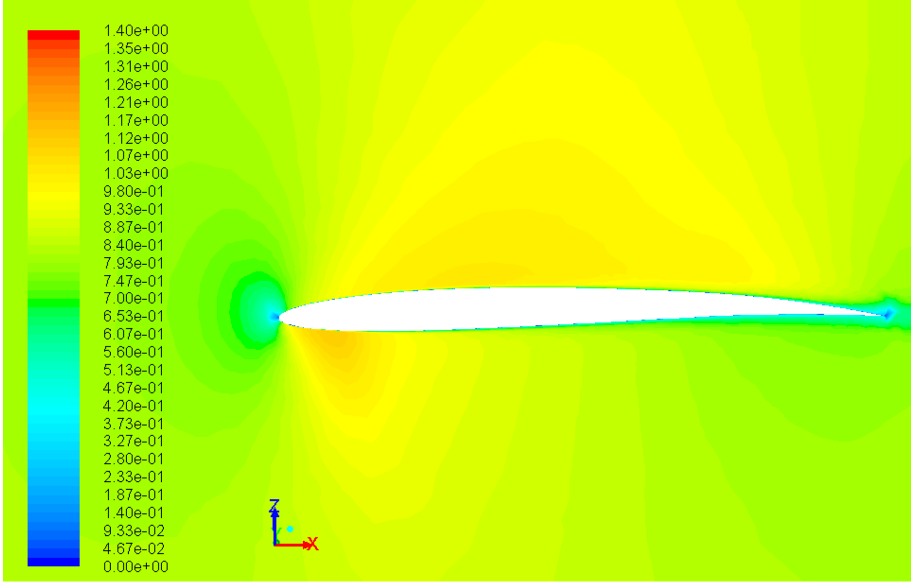

(a) Initial

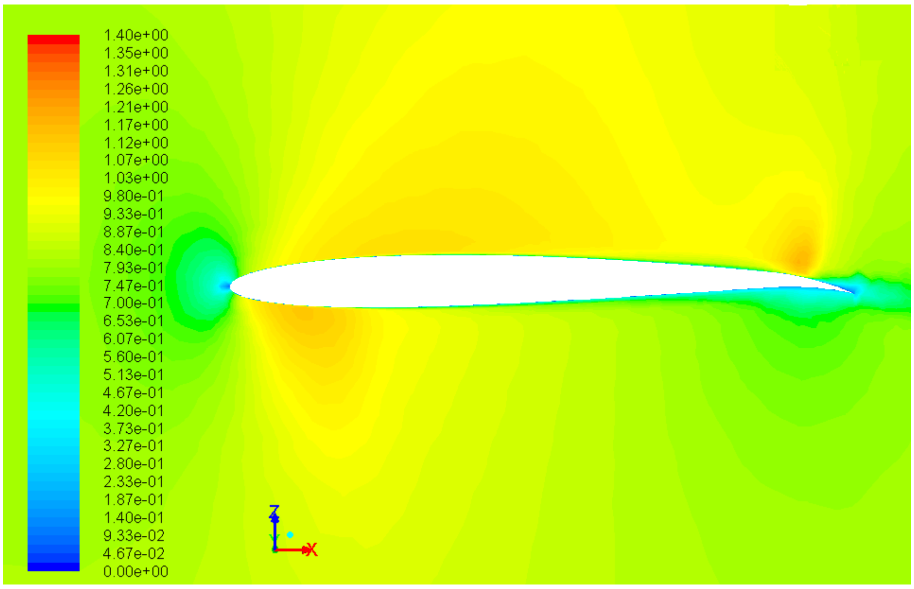

(b) Optimized

Figure 4.36: Run 1 Mach number contour plot (M) at $y/(b/2) = 0.9$ where $M_\infty = 0.8395$ and angle of attack $\alpha = 0°$. a) Shows the initial design; b) Shows the optimized design. Notice the shock at the trailing edge.

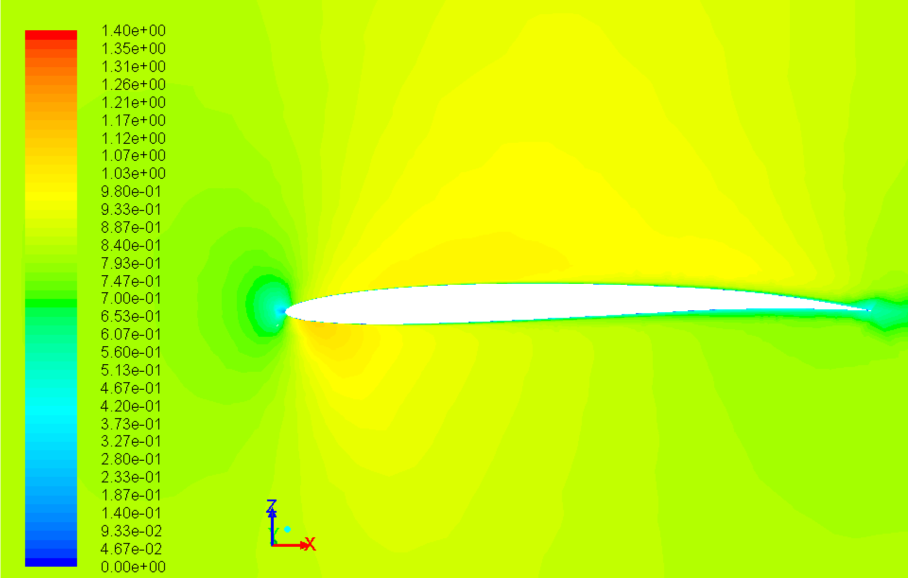

(a) Initial

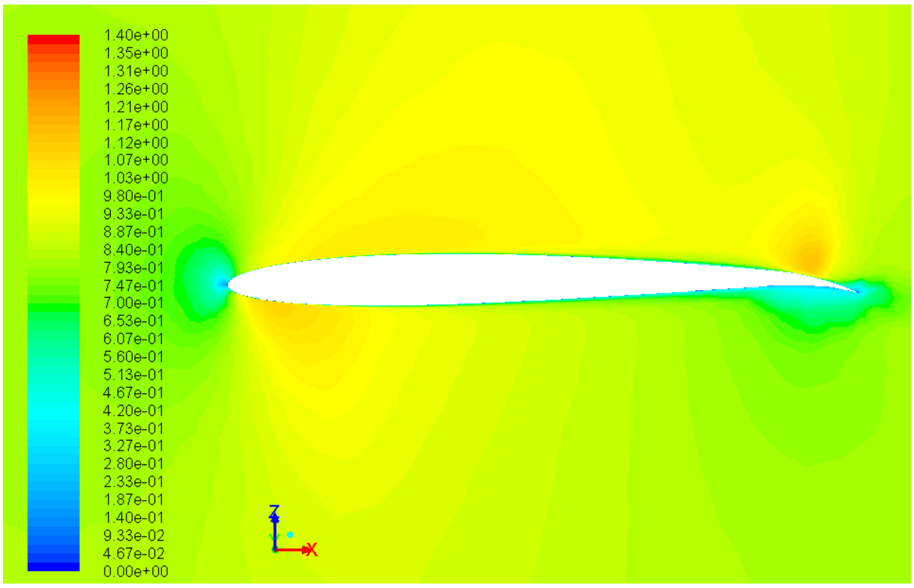

(b) Optimized

Figure 4.37: Run 1 Mach number contour plot (M) at $y/(b/2) = 0.95$ where $M_\infty = 0.8395$ and angle of attack $\alpha = 0°$. a) Shows the initial design; b) Shows the optimized design. Notice the shock at the trailing edge.

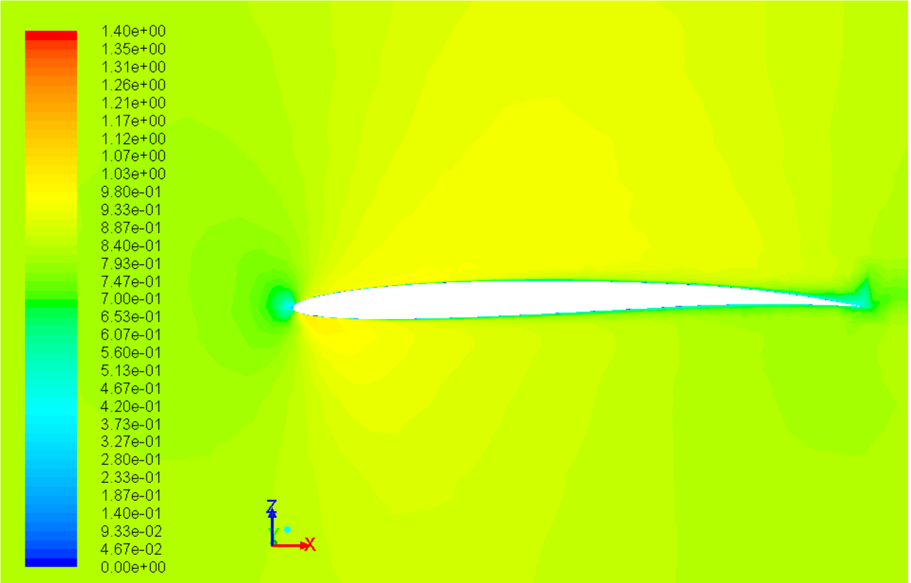

(a) Initial

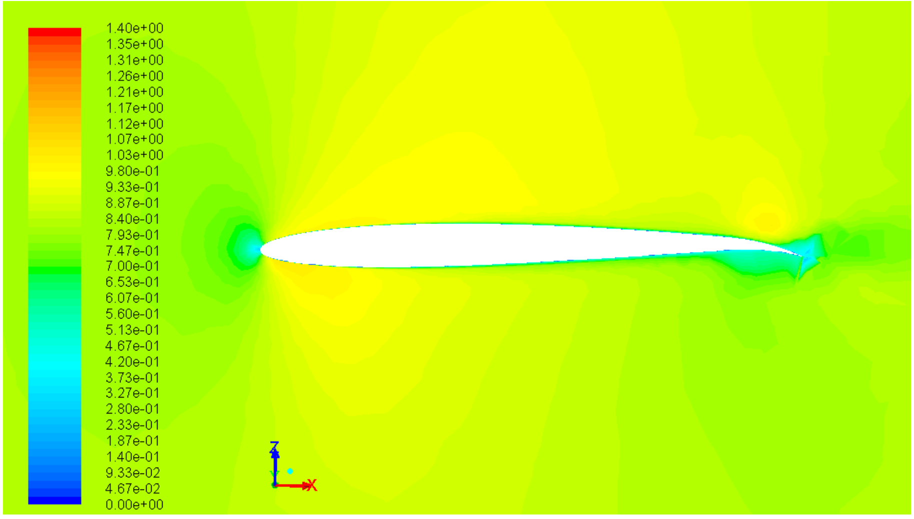

(b) Optimized

Figure 4.38: Run 1 Mach number contour plot (M) at $y/(b/2) = 0.99$ where $M_\infty = 0.8395$ and angle of attack $\alpha = 0°$. a) Shows the initial design; b) Shows the optimized design.

Results for Run 2

For the second run the initial design is $\mathbf{x}^{(0)} = [0.0232, 0.8550, 0.0600]$. Optimum numerical results obtained by the proposed method are shown, in Table 4.5, where they are compared to the initial design. Inspecting the initial design response we note that we already have high lift but the drag constraint is violated. The proposed algorithm is able to push the drag to its constraint limit, $C_{D,\max} = 0.03$, where the optimized drag coefficient $C_D = 0.0307$ slightly violates the constraint by +2%, which is within the 5% constraint band tolerance. Lift coefficient however only drops by -1% while the drag coefficient is decreased by -11%. As a result the lift to drag ratio is increased by +11%. We see that although the objective is to maximize lift, the proposed method is able to maintain the initial design lift although the drag constrain is heavily violated at the initial design. The proposed method requires less than 9 high-fidelity model evaluations, 50 low-fidelity model evaluations used to create the approximation model and 7 high-fidelity model evaluations.

The optimized wing tip NACA airfoil section is shown in Fig. 4.39. The optimized wing tip airfoil is thinner than the initial design as indicated by t/c. The normalized cross-sectional area is reduced by -20%, where the decreased drag can be related to the decrease in area. Camber m is slightly changed and maximum camber location p do not change much.

The optimization history for Run 2 is shown in Fig. 4.40. One can observe the evolution of the objective function Fig. 4.40a, convergence plot Fig. 4.40b and evolution of lift and drag Fig. 4.40c and Fig. 4.40d respectively. It is observed that the algorithm shows a good convergence reaching the 10^3 stopping criterion. The algorithm forces the drag to its constraint at $C_D \leq 0.03$ where the constraint is violated slightly but within design.

Planform pressure coefficient contour plot, comparing initial design and optimum design is shown in Fig. 4.41. The left figure shows the upper surface where two shocks appear, one at mid section of the wing and another close to the wing tip at the trailing edge. The right figure shows the lower surface shows one shock between the leading edge and mid section of the wing.

Table 4.5: Optimum numerical results for Run 2 compared to initial design $\mathbf{x}^{(0)} = [0.0232, 0.8550, 0.0600]$. The ratio of the high-fidelity model evaluation time to the low-fidelity is 34.

Variable	**Initial**	**This work (SM)**	Δ
m	0.0259	0.0232	-
p	0.8531	0.8550	-
t/c	0.0750	0.0600	-
C_L	0.3426	0.3388	-1%
C_D	0.0344	0.0307	-11%
C_L/C_D	9.9593	11.0358	+11%
A	0.0505	0.0404	-20%
N_c	-	50	
N_f	-	7	
Total Cost	-	< 9	

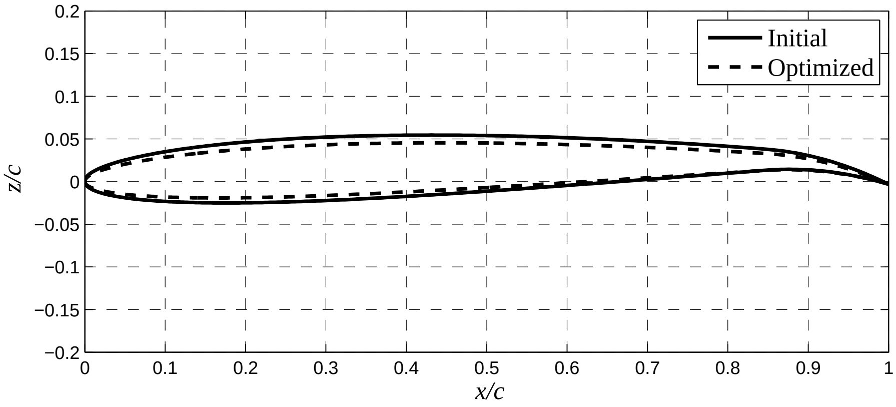

Figure 4.39: Run 2 optimum design geometry of the NACA airfoil obtained using space mapping algorithm shown with dashed line (- -). Initial design shown with solid line (- -).

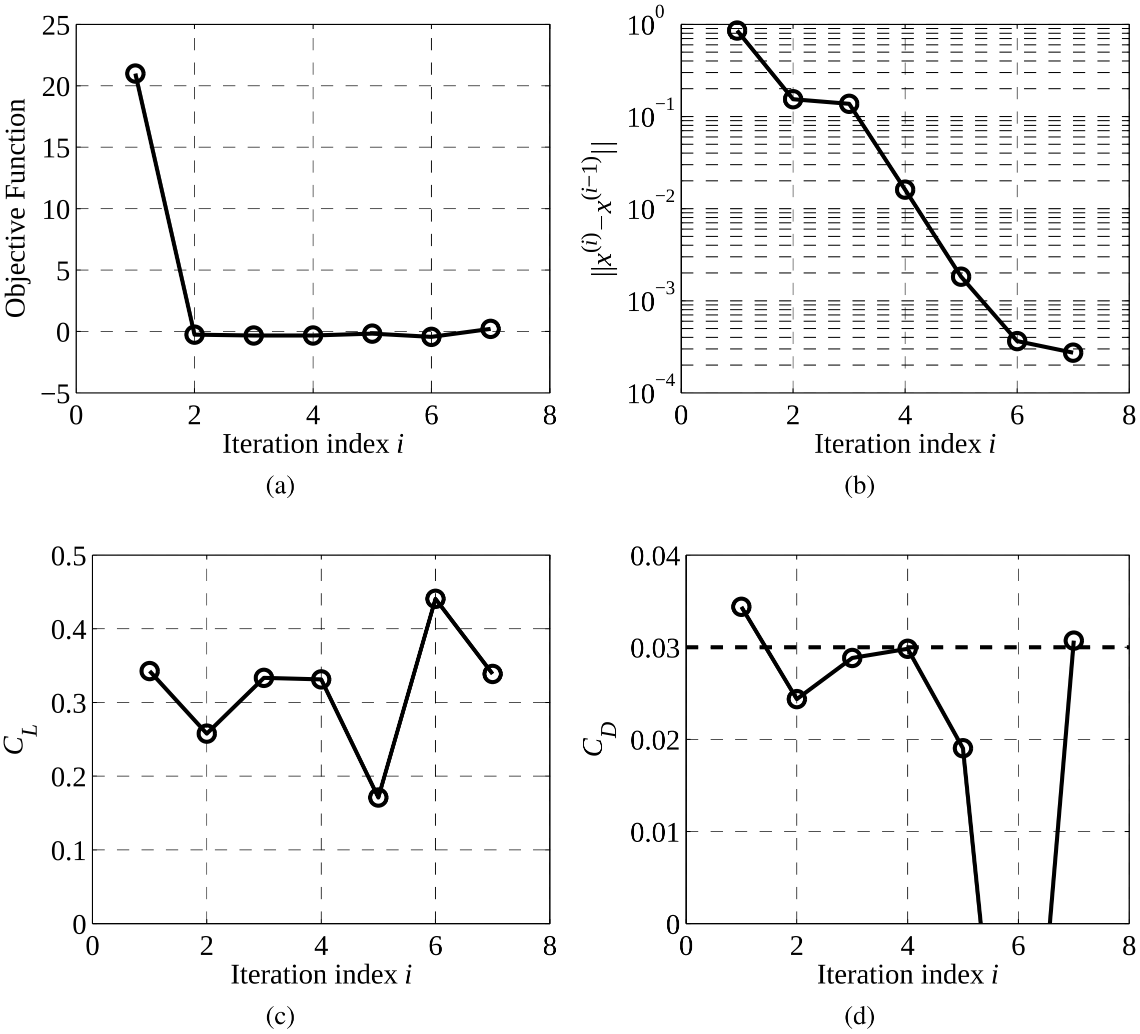

(a) (b)

(c) (d)

Figure 4.40: Optimization history using the proposed SM methodology. a) Evolution of the objective function; b) convergence Plot; c) evolution of lift coefficient and; d) evolution of drag coefficient where dash line (- -) is the lift constraint. At iteration 6 the flow solver crashes due to grid error.

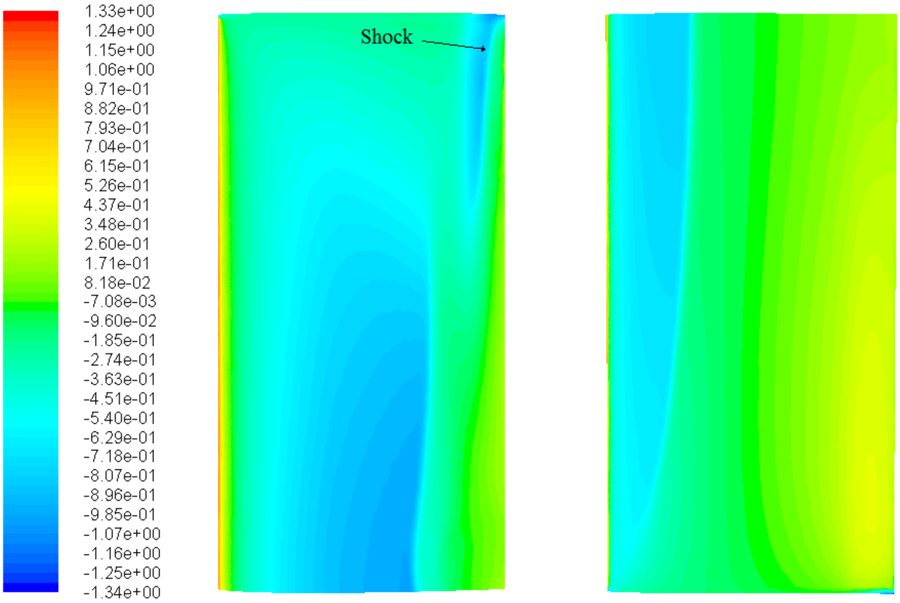

Figure 4.41: Run 2 pressure contour plot of the optimum design geometry obtained using space mapping. Left) The upper surface shows two shocks one at mid section of the wing and another close to the wing tip at the trailing edge. Right) The lower surface shows one shock between the leading edge and mid section of the wing.

Table 4.6: Numerical comparison of Run 1 and Run 2, initial and optimized designs. The ratio of the high-fidelity model evaluation time to the low-fidelity is 34.

	Initial		Optimized	
Variable	**Run 1**	**Run 2**	**Run 1**	**Run 2**
m	0.0200	0.0259	0.0200	0.0232
p	0.7000	0.8531	0.8725	0.8550
t/c	0.0628	0.0750	0.0793	0.0600
C_L	0.2759	0.3426	0.3047	0.3388
C_D	0.0241	0.0344	0.0311	0.0307
C_L/C_D	11.4481	9.9593	9.7974	11.0358
A	0.0422	0.0505	0.0534	0.0404
N_c	-	-	50	50
N_f	-	-	8	7
Total Cost	-	-	< 10	< 9

Results Comparison

The results from Run 1 and Run 2 are compared and shown in Table 4.6. Further initial airfoil cross-sections and optimized airfoil cross-sections are show in Fig. 4.42a and Fig. 4.42b, respectively. We note that although starting from different initial designs in Run 1 and Run 2, the optimized designs show similarities in two of three design variables, the maximum camber m and maximum camber location p. The third, the airfoil thickness t/c differs. This is due to initial violation of the drag constraint in Run 2. We also note that the difference in optimized lift between runs is 11% higher for optimum design found in Run 2 although drag is similar and at constraints boundaries. The reason here is most likely due to two different local minimums found in the design space. Optimum design is obtain in less than 10 high-fidelity model evaluation for Run 1 and Run 2.

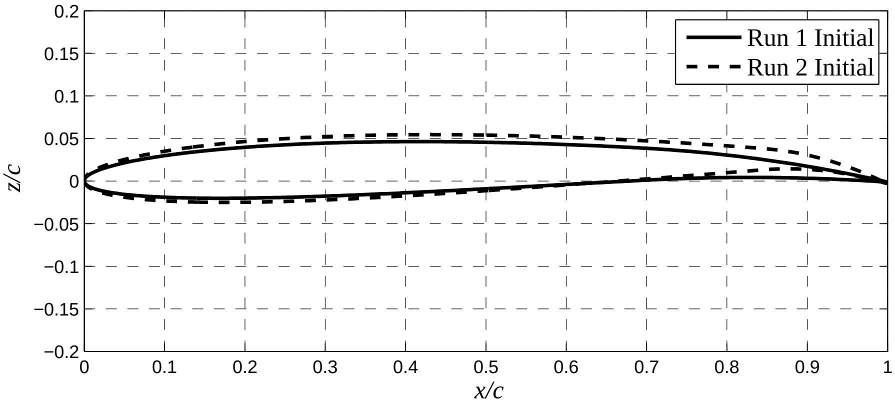

(a) Initial

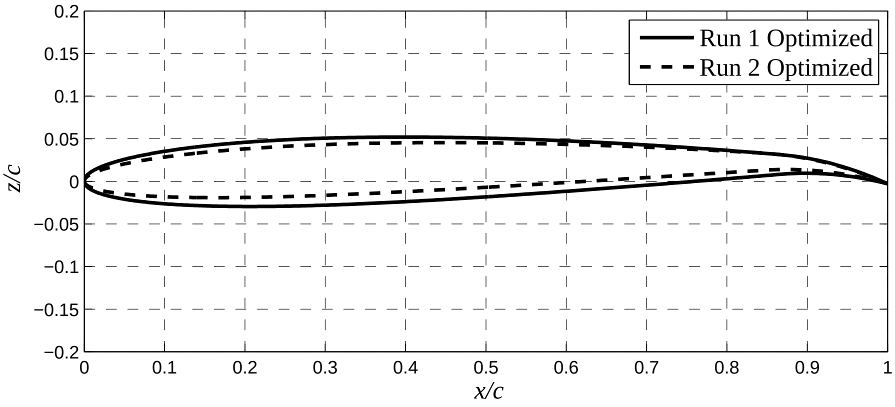

(b) Optimized

Figure 4.42: Graphical comparison of Run 1 and Run 2, initial and optimized designs. a) Initial design comparison b) Optimized comparison. Run 1 is shown with a solid lines (–), and Run 2 with dashed lines (- -)

4.4 Summary

Optimization of the transonic wing turned out to be a difficult task. Number of different grid strategies where tested and as it turns out it is difficult to create robust, error free, grid routine. Due to numerical noise in the low-fidelity model and after attempts creating a Kriging model based on the low-fidelity CFD model a second order approximation model was constructed.

The proposed algorithm turned out to be robust method. A simple rectangular wing geometry, consisting of two NACA 4 digit airfoils was considered where only the wing tip airfoil was to be optimized while other parameters where kept fixed. The objective was to maximize lift with constraint on drag. Starting from random initial airfoil design the proposed method was able to increase lift by +10% during Run 1. At Run 2, starting from a drag violation, the proposed method was able to decrease the drag by -11% while still maintaining lift where the lift coefficient value decreased by only -1%. The optimized designs are obtained using less than 10 high-fidelity model evaluations.

Chapter 5

Conclusion and Future Work

Let us summarize what we have discussed and accomplished in this work. A robust and computationally efficient methodology for designing aerodynamic shapes is presented. The method exploits a computationally cheap, physics-based low-fidelity CFD model which is corrected using the space mapping technique. The surrogate optimized is able to predict an approximate optimum design solution to the computationally expensive high-fidelity CFD model. The space mapping correction is applied both to the objectives and constraints. Using output space mapping with addition and multiplication, we are able to perform the parameter extraction analytically ensuring zero-order consistency and a perfect alignment between the surrogate and the high-fidelity model. Numerical noise in the low-fidelity models used in both applications turned out to be a big problem for the optimization algorithm. Attempts to create Kriging models failed but using a second-order approximation model turned out to be successful.

The proposed method is applied to two different aerodynamic applications. In the first application, we considered a constrained, high-lift, trawl-door drag minimization problem in a two-dimensional viscous low-speed flow where we optimize the location of one slat relative to the main element of the trawl-door. In the second application, we considered a simple three-dimensional rectangular wing at viscous transonic flow conditions where a constrained lift maximization optimization is performed by optimizing wing tip airfoil shape. In both cases, the optimized designs are obtained at a low number of high-fidelity model evaluations, reducing computational cost by more then 80% compared to a direct optimization, as shown in the trawl-door application. It is evident from the considered applications that the proposed optimizations methodology is a computationally cheap and efficient method that can be used in aerodynamic shape optimizations problems to obtain improved designs at a low computational cost.

In order to further validate and verify the computational efficiency of the proposed methods the high-fidelity model of the presented applications, trawl-door and wing need to be optimized using optimization method such as Kriging with updates rather than direct optimization.

In order to use variable-resolution low-fidelity models more successfully and without approximation models, more work needs to be done. Future work should include analysis such as, when the coarse model breaks down, meaning when does the grid stop to represent the geometry under consideration. What is the coarsest model one can use, what are the assumption we can make about the grid and when do the responses from the high-fidelity model and low-fidelity more differ too much ? Using adaptive grid codes that refine grids during flow solving may also be considered. In order to alleviate the numerical noise present in the low-fidelity model one can use a simplified physics low-fidelity model instead or in conjunction with a variable-resolution model. When dealing with low-speed flow, numerous analytical methods exist and panel methods could be used [42]. For high-speed transonic flow, the Euler, potential or transonic small-disturbance equations could be applied as the governing flow equations [42]. Further, the scalability in terms of computational cost needs to be studied in terms of increasing the number of design variables.

Bibliography

[1] John Garner. *Botnvarpan og bunadur hennar*. Fiskifelag Islands, 1967.

[2] C. LADSON. Effects of independent variation of mach and reynolds numbers on the low-speed aerodynamic characteristics of the naca 0012 airfoil section. 1988.

[3] N. Gregory, CL O'reilly, and Aeronautical Research Council (Great Britain). *Low-speed aerodynamic characteristics of NACA 0012 aerofoil section, including the effects of upper-surface roughness simulating hoar frost*. National Physical Laboratory England, 1970.

[4] C. LADSON, A. HILL, W. JOHNSON, and JR A M G. Pressure distributions from high reynolds number transonic tests of an naca 0012 airfoil in the langley 0. 3-meter transonic cryogenic tunnel. 1987.

[5] V. Schmitt and F. Charpin. Pressure distributions on the onera-m6-wing at transonic mach numbers. *Experimental Data Base for Computer Program Assessment*, Report of the Fluid Dynamics Panel Working Group 04, AGARD AR 138, May 1979, 1979.

[6] N.M. Alexandrov, R.M. Lewis, C.R. Gumbert, L.L. Green, and P.A. Newman. Optimization with variable-fidelity models applied to wing design. In *38th Aerospace Science Meeting & Exibit*, 2000.

[7] A.J. Keane and P.B. Nair. Computational approaches for aerospace design. *John Wiley&Sons, Ltd, West Sussex*, page 582, 2005.

[8] Hicks R.M. and Henne P.A. Wing design by numerical optimization. *Journal of Aircraft*, Vol. 15(No. 7):407–412, 1978.

[9] K. Leoviriyakit, S. Kim, and A. Jameson. Viscous aerodynamic shape optimization of wings including planform variables. In *21st AIAA Applied Aerodynamics Conference*, volume AIAA Paper AIAA-2003-3791, Orlando FL, 2003.

[10] S. J.J. Alonso Kim and A. Jameson. Two-dimensional high-lift aerodynamic optimization using the continuous adjoint methods. In *8th AiAA/ASAF/NASA/ISSMO*

Symposium on Multidisciplinary Analisys and Optimization, volume AIAA Paper AIAA-2000-4741, Long Beach, 2000.

[11] A.I.J. Forrester and A.J. Keane. Recent advances in surrogate-based optimization. *Progress in Aerospace Sciences*, 45(1-3):50–79, 2009.

[12] N.V. Queipo, R.T. Haftka, W. Shyy, T. Goel, R. Vaidyanathan, and P. Kevin Tucker. Surrogate-based analysis and optimization. *Progress in Aerospace Sciences*, 41(1):1–28, 2005.

[13] S. Koziel, D. E. Ciaurri, and L. Leifsson. Surrogate-based methods. In *Computational optimization and applications in engineering and industry*, volume 359. Springer, 2011.

[14] L. Leifsson and S. Koziel. Multi-fidelity design optimization of transonic airfoils using shape-preserving response prediction. *Procedia Computer Science*, 1(1):1311–1320, 2010.

[15] J.W. Bandler, Q.S. Cheng, S.A. Dakroury, A.S. Mohamed, M.H. Bakr, K. Madsen, and J. Sondergaard. Space mapping: the state of the art. *Microwave Theory and Techniques, IEEE Transactions on*, 52(1):337–361, 2004.

[16] N.M. Alexandrov and R.M. Lewis. An overview of first-order model management for engineering optimization. *Optimization and Engineering*, 2(4):413–430, 2001.

[17] L. Leifsson and S. Koziel. Airfoil shape optimization using variable-fidelity modeling and shape-preserving response prediction. In *Computational Optimization, Methods and Algorithms*, volume 356. Springer, 2011.

[18] S. Koziel and L. Leifsson. Knowlegde-based airfoil shape optimization using space mapping. 2012.

[19] L. Leifsson and S. Koziel. Variable-fidelity aerodynamic shape optimization. In *Computational Optimization, Methods and Algorithms*, volume 356. Springer, 2011.

[20] R.M. Hicks and P.A. Henne. Wing design by numerical optimization. *Journal of Aircraft*, 15(7):407–412, 1977.

[21] T.G. Kolda, R.M. Lewis, and V. Torczon. Optimization by direct search: New perspectives on some classical and modern methods. *SIAM review*, pages 385–482, 2003.

[22] J.A. Nelder and R. Mead. A simplex method for function minimization. *The computer journal*, 7(4):308–313, 1965.

[23] D.E. Goldberg. *Genetic algorithms in search, optimization, and machine learning*. Addison-wesley, 1989.

[24] Z. Michalewicz. *Genetic algorithms+ data structures*. Springer, 1996.

[25] M. Clerc and J. Kennedy. The particle swarm-explosion, stability, and convergence in a multidimensional complex space. *Evolutionary Computation, IEEE Transactions on*, 6(1):58–73, 2002.

[26] J. Kennedy and R. Eberhart. Particle swarm optimization. In *Neural Networks, 1995. Proceedings., IEEE International Conference on*, volume 4, pages 1942–1948. IEEE, 1995.

[27] T.W. Simpson, JD Poplinski, P.N. Koch, and J.K. Allen. Metamodels for computer-based engineering design: survey and recommendations. *Engineering with computers*, 17(2):129–150, July 2001.

[28] A.J. Booker, J.E. Dennis, P.D. Frank, D.B. Serafini, V. Torczon, and M.W. Trosset. A rigorous framework for optimization of expensive functions by surrogates. *Structural and Multidisciplinary Optimization*, 17(1):1–13, 1999.

[29] S. Koziel, J.W. Bandler, and K. Madsen. A space-mapping framework for engineering optimization&# 8212; theory and implementation. *Microwave Theory and Techniques, IEEE Transactions on*, 54(10):3721–3730, 2006.

[30] J. Zhu, J.W. Bandler, N.K. Nikolova, and S. Koziel. Antenna optimization through space mapping. *Antennas and Propagation, IEEE Transactions on*, 55(3):651–658, 2007.

[31] PK Kundu and IM Cohen. *Fluid Mechanics. 2004*. Elsevier Academic Press, 2008.

[32] ANSYS. *ANSYS FLUENT Theory Guide*. ANSYS, Southpointe 275 Thecnology Drive Canonburg PA 15317, release 13.0 edition, November 2010.

[33] J.C. Tannehill, D.A. Anderson, and R.H. Pletcher. *Computational fluid mechanics and heat transfer*. Taylor & Francis Group, 1997.

[34] ANSYS. *ANSYS ICEM CFD*. ANSYS, Southpointe 275 Thecnology Drive Canonburg PA 15317, release 13.0 edition, November 2010.

[35] I.H. Abbott and A.E. Von Doenhoff. *Theory of wing sections: including a summary of airfoil data*. Dover Pubns, 1959.

[36] C.L. Rumsey, B.R. Smith, and G.P. Huang. Description of a website resource for turbulence modeling verification and validation. *AIAA Paper*, 4742, 2010.

[37] W.H. Mason. *High-Lift Aerodynamics*, chapter 8, pages 1–22. April 18, 2012.

[38] D.P. Raymer. *Aircraft design: a conceptual approach*. American Institute of Aeronautics and Astronautics, 2006.

[39] J. Lépine, F. Guibault, J.Y. Trepanier, and F. Pépin. Optimized nonuniform rational b-spline geometrical representation for aerodynamic design of wings. *AIAA journal*, 39(11):2033–2041, 2001.

[40] D.J. Mavriplis, J.C. Vassberg, E.N. Tinoco, M. Mani, O.P. Brodersen, B. Eisfeld, R.A. Wahls, J.H. Morrison, T. Zickuhr, D. Levy, et al. Grid quality and resolution issues from the drag prediction workshop series. *AIAA Paper*, 930:2008, 2008.

[41] NASA. Onera-m6-wing validation case. In *http://www.grc.nasa.gov/WWW/wind/valid/m6wing/m6wing.html*, 2008.

[42] John David Anderson. *Fundamentals of Aerodynamics*. McGraw-Hill, 5th edition edition, 2010.

[43] C. Hirsch. *Numerical Computations of Internal and External Flows*. Butterworth-Heinemann, 2nd edition edition, 2007.

Appendix A

Computational Fluid Dynamic Modeling

Computational fluid dynamics (CFD) is the methodology that enables us to get numerical solutions of a fluid flow with the use of a computer by solving the governing equations of a given fluid flow. Effective use of CFD is becoming the key ingredient in a successful design a modern aerodynamic design. CFD simulation and modeling can be divided into components and these components make up this chapter. In this chapter we introducing the mathematical model defining the equations governing of the flow and setting up a hierarchy defining the level of approximations to reality that are commonly used in external aerodynamic design. Next, the numerical modelling procedure is introduced. The numerical model can be further divided into, defining the geometry, discretizing the flow domain and the governing equations, selecting the appropriate numerical scheme for flow solution.

A.1 Governing Equations

A.1.1 Navier Stokes Equations

The fundamental equations of fluid dynamics are based on three universal laws of conservation; the conservation of mass, momentum and energy. For a Newtonian fluid, the nonlinear compressible viscous Navier-Stokes equations in three dimensional Cartesian coordinates without body forces, mass diffusion, finite-rate chemical reactions or external heat addition are commonly written in a vector form as Eq. (A.1.1) [33]

$$\frac{\partial \mathbf{U}}{\partial t} + \frac{\partial \mathbf{E}}{\partial x} + \frac{\partial \mathbf{F}}{\partial y} + \frac{\partial \mathbf{G}}{\partial z} = 0 \tag{A.1.1}$$

where $\mathbf{U}, \mathbf{E}, \mathbf{F}$ and $\mathbf{G}$ are vectors given by

$$\mathbf{U} = \begin{bmatrix} \rho \\ \rho u \\ \rho v \\ \rho w \\ E_t \end{bmatrix} \tag{A.1.2a}$$

$$\mathbf{E} = \begin{bmatrix} \rho u \\ \rho u^2 + p - \tau_{xx} \\ \rho uv - \tau_{xy} \\ \rho uw - \tau_{xz} \\ (E_t + p)u - u\tau_{xx} - v\tau_{xy} - w\tau_{xz} + q_x \end{bmatrix} \tag{A.1.2b}$$

$$\mathbf{F} = \begin{bmatrix} \rho v \\ \rho uv - \tau_{xy} \\ \rho v^2 + p - \tau_{yy} \\ \rho vw - \tau_{yz} \\ (E_t + p)v - u\tau_{xy} - v\tau_{yy} - w\tau_{yz} + q_y \end{bmatrix} \tag{A.1.2c}$$

$$\mathbf{G} = \begin{bmatrix} \rho w \\ \rho uw - \tau_{xz} \\ \rho vw - \tau_{yz} \\ \rho w^2 + p - \tau_{zz} \\ (E_t + p)w - u\tau_{xz} - v\tau_{yz} - w\tau_{zz} + q_z \end{bmatrix} \tag{A.1.2d}$$

Fluid density is denoted by ρ, the fluid velocity components are denoted, u, v, w for x, y, z direction respectively, p is the static pressure, $E_t = \rho\left(e + \frac{V^2}{2}\right)$ is the total energy per unit volume, e is the internal energy per unit mass, $V^2/2$ is the kinetic energy and τ_{ij} is the viscous shear stress tensor given in summation notation [33]

$$\tau_{ij} = \mu\left[\left(\frac{\partial u_i}{\partial x_j} + \frac{\partial u_j}{\partial x_i}\right) - \frac{2}{3}\delta_{ij}\frac{\partial u_k}{\partial x_k}\right] \quad i, j, k = 1, 2, 3 \tag{A.1.3}$$

where μ is the dynamic viscosity, δ is the Kronecker delta function. First row in each vector in Eq. (A.1.2) is the continuity equation, second, third and fourth are the momentum equations and the last is the energy equation. Strictly speaking the term Navier-Stokes equation refers only to the components of the momentum equation. It is however customary to include the continuity and energy equations in the set of equations referred to as the Navier-Stokes equation [33]. These scalar equations form a system of five, fully coupled, time dependant, partial differential equations containing seven unknowns namely (ρ, p, e, T, u, v, w). Here we assume that the μ, k the dynamic viscosity and thermal conductivity can be related to the thermodynamic properties in the list of unknowns [33]. Two equations are needed to close the system and they can be obtained by relating thermodynamic variables. According to the *state principle* of thermodynamics the local thermodynamic state is fixed by any two independent thermodynamic variables. Thus choosing the internal energy e and density ρ as the independent variables the equations of state

$$p = p(e, \rho) \quad T = T(e, \rho) \tag{A.1.4}$$

are necessary [33]. For most problems in gas dynamics it is sufficient to assume perfect gas model, where perfect gas is defined as a gas where intermolecular forces are negligible. Perfect gas obeys the perfect gas equation of state

$$p = \rho R T \tag{A.1.5}$$

where R is the gas constant per unit mass defined and is equal to the universal gas constant divided by the molecular mass of the fluid [33] closing our set of equations.

Solving the set of afore mentioned equations numerically can be quite challenging even for a simple laminar flow. Most real flow situations occurring in nature are however turbulent complicating things further. Fluid flow will transition from a laminar flow to a turbulent flow above a critical value of the Reynolds number,

$$Re_L = \frac{\rho V L}{\mu} = \frac{V L}{\nu}, \tag{A.1.6}$$

where, V, μ, ν, L are the velocity, dynamic viscosity, kinematic viscosity, geometric length scales respectively.

This form of instability is a consequence of the nonlinear convective terms. This instability generated in the turbulent regime can characterized by the presence of statistical fluctuation of all flow quantities. These fluctuations are superimposed on a mean or an average value and can attain in many situations 10% of the mean value. [43]. Clearly a numerical description of the turbulent fluctuations is a formidable task demanding extreme amount of computing resources. Direct Numerical Simulation (DNS) has the objective to simulate the whole range of the turbulent statistical fluctuations from the smallest eddies to the order of the physical dimension of the problem. Total computational effort for

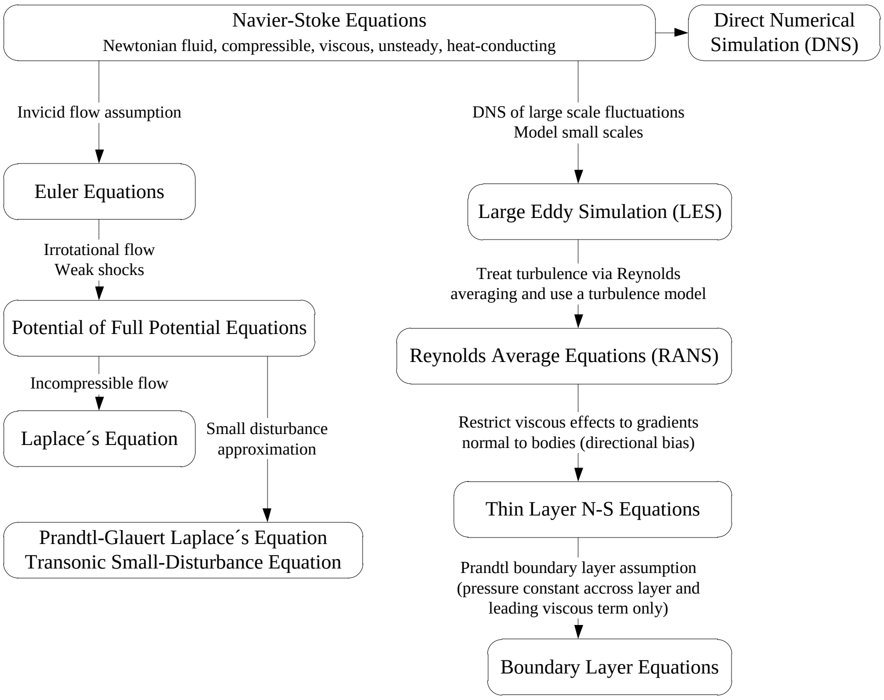
Navier-Stoke Equations
Newtonian fluid, compressible, viscous, unsteady, heat-conducting
Direct Numerical Simulation (DNS)
Invicid flow assumption
Euler Equations
Irrotational flow
Weak shocks
Potential of Full Potential Equations
Incompressible flow
Laplace´s Equation
Small disturbance approximation
Prandtl-Glauert Laplace´s Equation
Transonic Small-Disturbance Equation
DNS of large scale fluctuations
Model small scales
Large Eddy Simulation (LES)
Treat turbulence via Reynolds averaging and use a turbulence model
Reynolds Average Equations (RANS)
Restrict viscous effects to gradients normal to bodies (directional bias)
Thin Layer N-S Equations
Prandtl boundary layer assumption (pressure constant accross layer and leading viscous term only)
Boundary Layer Equations

Figure A.1: A hierarchy of the governing equation along with approximations and associated assumptions

DNS simulations is proportional to Re^3 for a homogeneous turbulence [43]. This means by increasing the Reynolds number by a factor of 10 requires a computational increase in at least a factor 1000. DNS simulations are therefore not a realistic option for an external flow application where its not uncommon to have a Reynolds number in the range of $10^5 - 10^7$.

By making appropriate assumptions about the fluid flow one can simplify the governing equations enabling the numerical description of turbulence in acceptable CPU time. Figure A.1 shows the hierarchy of equations and assumptions. Large eddy simulations (LES) is the highest approximation and is similar to DNS. Its objective is to simulate directly the turbulence fluctuations, but restrict to the larger scales and use models to account for the smaller ones. This method is still very computationally expensive and is proportional to $Re^{9/4}$ [43]. The Reynolds Average Navier-Stoke (RANS) equations are the most widely applied approximations in CFD today and is covered in the next section.

A.1.2 RANS equations

Variables of the instantaneous Navier-Stokes equations are decomposed into mean or time-averaged and fluctuating components. For velocity

$$u_i = \bar{u}_i + u_i' \tag{A.1.7}$$

where u_i and u_i' (i=1,2,3) are the mean and the fluctuating components [32]. Substituting into the continuity and momentum equations and taking a time average and dropping the over bar in the mean velocity $\bar{u}_i$ yields the ensemble-averaged momentum equations. They can be written in Cartesian tensor form as:

$$\frac{\partial \rho}{\partial t} + \frac{\partial}{\partial x_i}(\rho u_i) = 0 \tag{A.1.8}$$

$$\frac{\partial}{\partial t}(\rho u_i) + \frac{\partial}{\partial x_j}(\rho u_i u_j) = -\frac{\partial p}{\partial x_i} + \frac{\partial}{\partial x_j}\left[\mu\left(\frac{\partial u_i}{\partial x_j} + \frac{\partial u_j}{\partial x_i} - \frac{2}{3}\delta_{ij}\frac{\partial u_l}{\partial x_l}\right)\right] + \frac{\partial}{\partial x_j}\left(-\rho\overline{u_i' u_j'}\right) \tag{A.1.9}$$

where δ_{ij} is the Kronecker delta [32]. This gives rise to a new term the Reynolds stress tensor $-\rho\overline{u_i' u_j'}$, which can be interpreted as apparent stress gradients and heat flux quantities associated with the turbulent motion [33]. This requires the RANS equations to be supplemented with turbulence models for the Reynolds stresses. As a result, a loss in accuracy of the solution is introduced since the turbulence models have limitations and are usually designed and developed for limited operating range. By using these model the RANS approach retains the viscous effect in the fluid flow but at the same time reduces the computational effort since there is no need resolving all turbulent scales as done in DNS and LES.

A.1.3 Turbulence Models

As previously noted, none of the available turbulence models available today are universal. Many turbulence models exists all having its own limitations. When using turbulence models one must verify the validity of the solution by comparing results to experimental data. Two turbulence models will be used in this work and a brief description of each will be given here. The most common turbulence models used today in simulation past airfoils and wings are the Spalart-Allmaras one-equation and the $k-\omega-SST$ two equation turbulence models [33].

Spalart-Allmaras Model

The Spalart-Allmaras mode is a one-equation model designed specifically for aerospace applications involving wall-bounded flows and has proven to give good results for boundary layers subjected to adverse pressure gradients [32]. In its original form Spalart-Allmaras model is effectively at low Reynolds-number model, requiring the viscosity affected region of the boundary layer to be solved properly where $y^+ \sim 1$ and is defined as

$$y^+ = \frac{\rho u_\tau y}{\mu} \tag{A.1.10}$$

where ρ is the density, μ is the dynamic viscosity, y is the distance from the wall and u_τ is the friction velocity and is defined as

$$u_\tau = \sqrt{\frac{\tau_w}{\rho}} \tag{A.1.11}$$

where τ_w is the wall shear stress.

For the Spalart-Allmaras model it has been shown to produce consistent results for wall function resolution $y^* > 15$ and for fine meshes $y^* < 3$ [32]. Good numerical results for the wall boundary layer can only be obtained if the overall resolution of the mesh is sufficient [32]. Capturing the boundary layers successfully with good accuracy can be achieved with approximately 20 prism cells in the normal direction of the wall. The thickness of the prism layer should be designed so that around 15 cells fully cover the boundary layer leaving the rest to act as a buffer in the design. The design thickness can be checked after a solution is obtained, by looking at the turbulent viscosity which should have its maximum in the middle of the boundary layer. Twice this thickness should give an indication of where the boundary layer edge is and how thick the prism layers need to be. It must be stressed that the prism layers must cover all the boundary layer plus some extra layers for safety otherwise there is a danger that the prism layers confine the growth of the boundary layer [32].

k-ω - SST Model

The shear-stress transport (SST) $k-\omega$ is a two equation model that has gained popularity recently mainly because the model do not contain terms which are undefined at the wall. It is computationally more expensive than Spalart-Allmaras and has proven to be robust for a wide range of boundary layer flows with pressure gradient and complex geometries. This model is widely used in aerodynamic applications. [33, 32]

A.2 Numerical Modeling

In the following section the method used to construct all numerical models in this thesis will be explained. The process of constructing a numerical model to be simulated and optimized for a given problem can be split into several components as shown in Fig. A.2. These components are, constructing the geometry to be analysed, generating mesh appropriate to capture the physics properly, obtain numerical solution of the governing equations extracting relevant information from the solution and finally calculate the objective function and evaluating constrains.

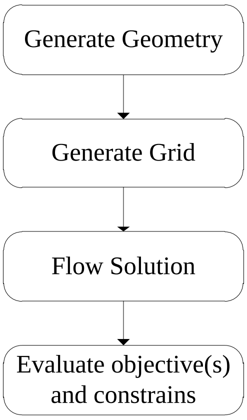

Figure A.2: Basic flow diagram of a single CFD simulation in numerical wing shape optimization

A.2.1 Geometry

Aerodynamic considerations of wings can be split into two parts, study of a section of a wing or an airfoil, and the modification of airfoils properties to account for the complete finite wing. Experiments on airfoils are performed in wind tunnels where a constant chord wing spans the entire test section from one sidewall to the other. This is considered an infinite wing where the flow see the wing without wing tips. Because the airfoil section is the same at any spanwise location, the properties of an airfoil and an infinite wing are the same. Several methods exists describing airfoils geometry numerically, each method with its own benefit and drawbacks. Number of design parameters are often closely related to the method selected to describe the geometry. In general there are two different approaches describing the airfoil geometry numerically, either the airfoil shape is parametrized or given an initial airfoil shape the deformation is parametrized. Here we consider only airfoil parametrization. Numerous airfoil parametrization methods have been developed. Non-Uniform Rational B-Spline (NURBS) and Bézier curves (special case of NURBS) are the methods that are commonly used today. These methods use a set of control points that describe the airfoil geometry and are general enough to be able to create almost any airfoil shape [39]. One can vary the number of control points depending on how accurately the airfoil geometry is to be controlled and in general, more points will give greater control of the upper and lower surface of the airfoil. These methods however come with a price. In aerodynamic shape optimization the afore mentioned control point are a part of the design variables of a given problem. The more the design variables, the more computational demanding the optimization will be. NURBS requires as few as thirteen control points to represent a large family of airfoils [39]. Other parametrization methods exists that require fewer control points. In this thesis the NACA 4 digit method is defined in 4.2.2.

A.2.2 Computational Grid

Grid generation is a major component in CFD simulations and has a crucial role the CFD process. It is the necessary step, since no simulation can be started without having defined the mesh and its parameters. Tools have been developed to aid users to generate meshes in as efficient and sophisticated way as possible. The importance of the mesh cannot be emphasized enough since it plays essential role in overall quality and accuracy of the CFD simulation. The governing equations are solved on a computational grid. The grid needs to resolve the entire solution domain, as well as the detailed geometry. Further-more, the grid needs to be sufficiently fine to capture the flow physics accurately. Too coarse mesh gives bad or incorrect solution as very fine mesh take too much time to compute a solution [43] For example, a fine grid resolution is necessary near the airfoil surface, especially near the LE where the flow gradients are large. Also due to viscous effects the grid needs to be fine near the entire airfoil surface. The grid can be much coarser several chord lengths away from the geometry and in the far-field. The meshing process is therefore often considered a true art. Software methods in support of the grid generators are complex and difficult to make for any geometry. Many grid generators exist both free and commercial but the free ones often tend to lack support and are poorly updated for bug fixes. ANSYS ICEM CFD [34] is a commercial grid generator is widely used software. It supports a number of advanced CAD/geometry readers and repair tools to allow the user to quickly progress to a variety of geometry-tolerant meshers and produce high-quality volume or surface meshes with minimal effort. ANSYS ICEM CFD then also support number of CFD solvers.

Generally grids can be classified into two types **structured** and **unstructured** whereas the former is composed of families of intersecting lines, one for each dimension, where each point in the grid is located at the intersection of one line, and only one line of each family. Unstructured meshes on the other hand refer to a arbitrary distribution of mesh points connecting for example triangles in 2D and polyhedrals in 3D. In the upcoming subsections the basics of both mesh types will be covered briefly to give the reader insight into the properties of each type [43]. For a detailed discussion on grid generation the reader is referred to [33, 43].

In this thesis all grids will be hybrid, where far-field and volume will be unstructured with triangles or polyhedral and prism layers are applied to capture the boundary layer at the surface of the aerodynamic geometry. These prisms are constructed of either structured quad or hex elements.

Structured Mesh

Structured mesh can be considered as most natural for flow problems as the flow is generally aligned with the solid body and the mesh often looks somewhat like streamlines in some sense. The ideal mesh would be when all points are equidistant from each other, or $\Delta x = \Delta y = \Delta z$ in Cartesian coordinate system. This type of mesh will generally lead to the highest accuracy [43]. However when the geometry include curved solid surfaces it is not possible to work with the ideal meshes. **Body-fitted** meshes or curvilinear mesh are then used instead to try to fit the mesh lines to the solid surface. Depending on the orientation of the grid lines various configurations exist indicated by a letter to which they resemble the most. To name few H-type, C-type, O-type and various configurations of their combination [43].

H-Mesh Mesh lines are curvilinear, approaching a set of horizontal and vertical lines in a pseudo-orthogonal configuration with a topology that can be associated to the letter H.

C-Mesh Mesh lines are curvilinear, surrounding the geometry resembling to the letter C on the leading edge but remaining open at the trailing edge.

O-Mesh Mesh lines are like the C-Mesh but surrounds the at the trailing edge as well.

The drawback of structured grids comes clear when adding a point locally it implies adding lines through that point which affect the whole domain. Several ways exist to counter these constrains. One is to define multi-block meshes where each block cover a subset the computational domain with it own structured mesh. Another is to have a overlapping meshes where independent generated mesh around a fixed or moving solid surface is made to overlap with a background fixed mesh. This method has however limitations in 3D and becomes extremely challenging [43].

Structured grids, compared to unstructured grids often tend to take less CPU time and memory and in CFD point of view be more efficient and accurate. However the time taken to generate a good quality structured mesh can often take weeks or months, hence commercial companies in today's competitive environment tend to lean towards the automatically generated unstructured meshes [43].

Unstructured Mesh

As mentioned earlier unstructured meshes have become the dominating approach to commercial CFD due to the impossibility to generate automatically block-structured meshes on arbitrary geometries. However unstructured meshes tend to have lower accuracy than corresponding structured meshes [43]. Unstructured mesh on the other hand has a clear advantage when performing local refinement in a certain region without affecting mesh point distribution in the whole domain. This is normally referred as **mesh adaptation**. Grid adaptation is based on adding mesh points in order to increase the accuracy in regions of large flow variations and remove mesh points where solution is already acceptable.

Unstructured mesh contains and is formed by, **triangular/tetrahedral** elements, **hybrid** elements involving combinations of tetrahedral, pyramids and prisms and **quadrilaterals** and **hexahedra** elements [43].

Triangle/Tetrahedra Cells Various methods exists generating triangle/tetrahedral mesh for arbitrary solids. Most mesh generators require a initial surface mesh which has to be generated prior to the volume mesh.

Quadrilaterals/Hexahedra Cells Often offers advantages compared to tetrahedral cell in terms of memory usage and accuracy [43].

Hybrid Mesh One of triangle/tetrahedral meshes is that they do not capture the boundary layer well enough in high Reynolds number flows. This is due to the grid density in the normal direction has to be adapted to the boundary layer velocity profiles.

Ration of mesh size should be optimally close to $\Delta x/\Delta y \sim \sqrt{Re}$, where δx and δy are the representative mesh sizes in the streamwise and normal directions, respectively. This shows that larger the ratios of $\Delta x/\Delta y$ will lead to a poorly configured triangles with a large height to base ratio, consequently, a significant loss in accuracy. To counter this problem hybrid grids are used where layers of quadrilaterals or prisms are generated in the near-wall by form of extrusion process out from the triangular surface mesh [43].

A.2.3 Flow solution

Commercial numerical solvers like FLUENT that will be used in this thesis are based on the Finite Volume Method (FVM). FVM takes its name from the technique witch the integral formulation of the conservation laws is discretized directly in the physical space. FVM is based on cell-averaged values which appear as a most fundamental quantity in CFD. The strength of FVM is its direct connection to the physical flow properties. This distinguishes FVM from other methods such as Finite Difference (FDM) or Finite Element Method (FEM) where numerical quantities are local function values at the mesh point [32]. The grid is subdivided into finite volumes one control volume being associated to each mesh point. To each local finite volume or a control volume the integral conservation laws, mass, momentum and energy are applies to these finite volume.

The result is a set of linear algebraic equations one for each control volume. This set of equations is then solved simultaneously and the solution then iterated. The iterative solution is usually performed with relaxation factors to prevent a numerical oscillation of the solution that can lead to no solution or errors. Solution is considered to be converged if the difference in two subsequent iteration is smaller than a specified value. This value is usually kept small and ranges from $10^{-3} - 10^{-6}$. The number of iterations needed for a solution to converge is problem dependent.

Lift and drag coefficient are frequently used to determine convergence. Further reading on FVM is found in [33, 32]. For illustration purposes results for a typical 2D flow using $k - \omega$ turbulence model convergence plot for the residuals and lift and drag coefficients is shown in Fig. A.3.

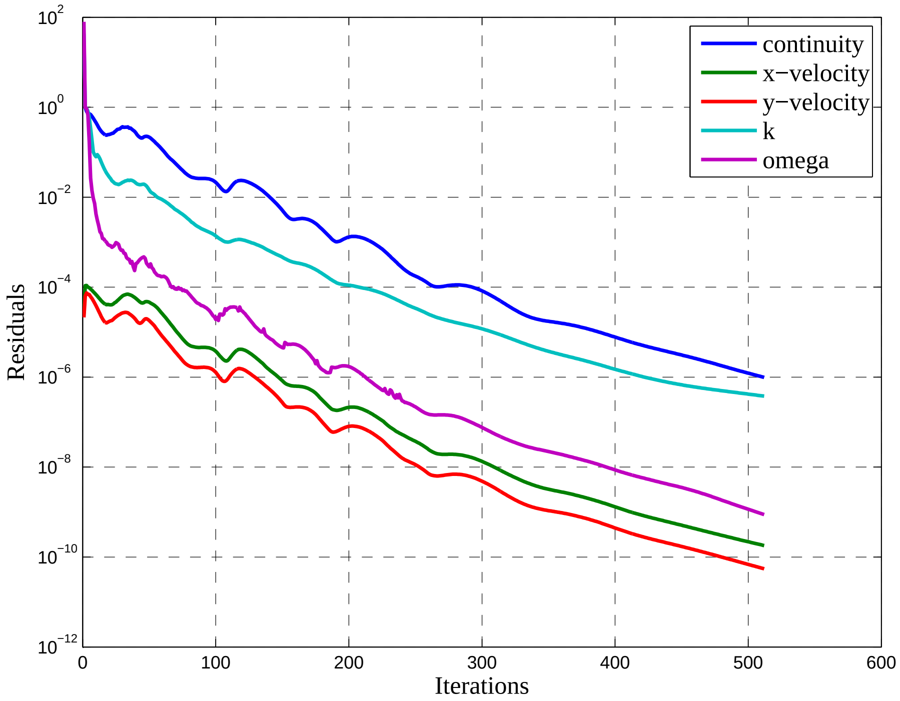

(a)

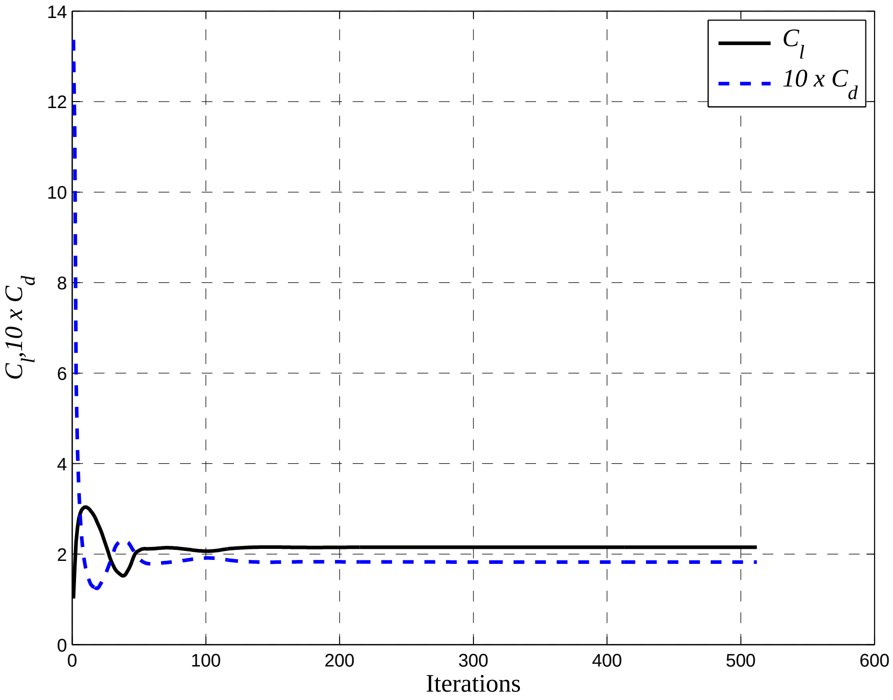

(b)

Figure A.3: Convergence history of a typical simulation. a) Residual convergence history b) lift and drag history

Appendix B

Aerodynamics

Here fundamental aerodynamics topics will be covered. First aerodynamic forces

B.1 Airfoil geometry

An airfoil is a streamlined aerodynamic surface which describes the shape of a wing as seen in cross-section such as one in Fig. B.1. The *chord*, denoted as c, is the distance from the *leading edge* (LE) to the *trailing edge* (TR) of the body. The *chord line* is the line connecting the LE and TE. The LE is normally rounded and the TE is usually sharp either closed or open but can also be blunt (closed). The *mean camber line* is the locus

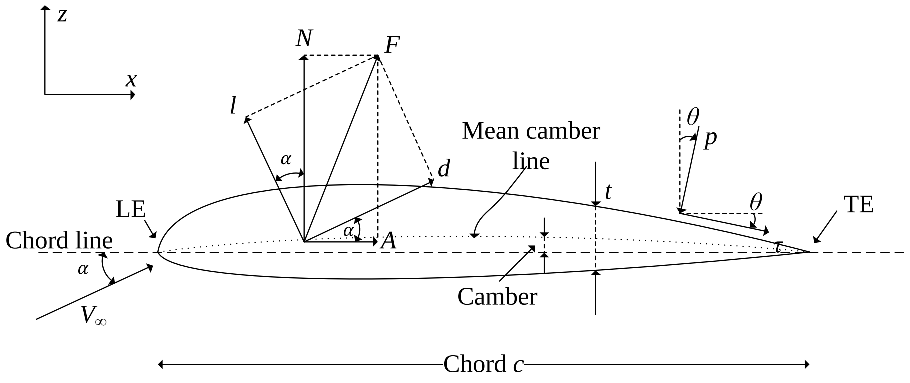

Figure B.1: Airfoil a wing cross-section (solid line) of thickness t and chord length c. V_∞ is the freestream velocity and is at an angle of attack α relative to the x-axis. F is the resulting aerodynamic force where L is the lift force, perpendicular to $\mathbf{V}_\infty$ and D is the drag force, parallel to V_∞. p is the pressure acting normal to a surface element ds. τ is the viscous wall shear stress acting parallel to the surface element. θ is the angle that p and τ make relative to the z and x-axis, respectively where positive angle is clockwise.

of points halfway between the upper and lower surface. The curvature is called *camber* is the distance from the chord line to the mean chamber line measured perpendicular to the chord line. The *thickness*, denoted as t, is the distance between the upper and lower surface measured also perpendicular to the chord line [35].

Forces for a two and three dimensional bodies such as airfoils and wings can be written in non-dimensional form as lift and drag coefficients. By convention aerodynamic coefficients and forces are denoted by lowercase letters for two dimensional bodies. The lift and drag coefficients are defined as

$$C_l = \frac{l}{q_\infty S} \tag{B.1.1}$$

$$C_d = \frac{d}{q_\infty S} \tag{B.1.2}$$

where l is the magnitude of the lift force, d the magnitude of the drag force, S is the reference surface (usually is $S = c$ for an airfoil). The dynamic pressure q_∞ is defined as

$$q_\infty = \frac{1}{2}\rho_\infty V_\infty \tag{B.1.3}$$

where ρ_∞ is the freestream density and V_∞ is the magnitude of the freestream velocity.

B.2 Wing geometry

An aircraft wing or a turbine blade is a three dimensional aerodynamic surface. Schematics of a typical wing planform is shown in Fig. B.2. At each spanstation (numbered 1 through 7) the cross-section is defined by an airfoil shape. Number of spanstation can be larger or fewer than shown here and depend on wing design. Between spanstations is a straight line wrap. Spanstations are mainly used for two purposes, to define different types of airfoils than the adjacent ones or simply defined as an interesting locations on the wing to observe pressure distributions and skin friction. Design parameters controlling the planform shape include the wing semi-span $b/2$, the quarter chord wing sweep angle Λ, thickness-to-chord ratio at each spanstation, the wing taper ratio and twist distribution. Number of design variables is therefore much larger than for an two dimensional case such as an airfoil (single spanstation). Equivalently the lift and drag coefficients for a three dimensional surface are defined as

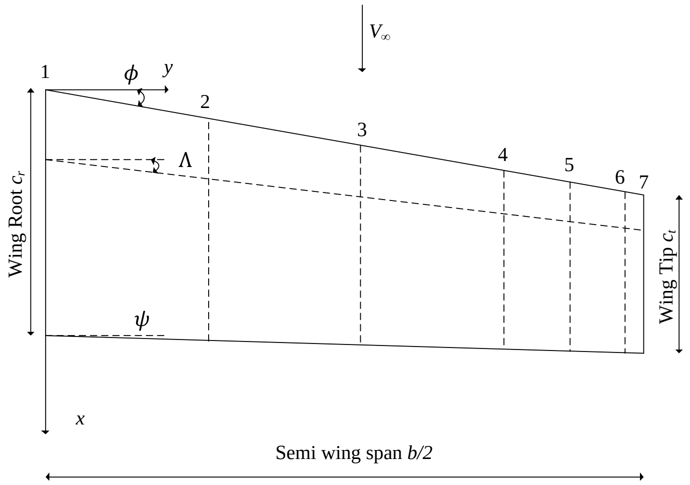

Figure B.2: Schematic of a wing planform of a semi-span $b/2$ and quarter chord sweep angle Λ. Spanstations are marked 1 through 7 and freestream velocity is V_∞. Leading edge and trailing edge angles are ϕ and ψ is also shown. Other design parameters are not shown.

$$C_L = \frac{L}{q_\infty S} \tag{B.2.1}$$

$$C_D = \frac{D}{q_\infty S} \tag{B.2.2}$$

where S is usually the planform area, L and D is the magnitude of the total lift and drag force respectively. These forces are usually determined experimentally or computationally.

B.3 Aerodynamic forces

An airfoil generates lift by forcing a change in velocity of the air passing over and under the airfoil. The airfoil angle of attack or the camber causes the fluid to travel faster over the upper surface of the wing than the lower surface. For subsonic flow Bernoulli's equation

$$p_0 = \frac{1}{2}\rho_\infty V_\infty^2 + p_\infty \tag{B.3.1}$$

where $\rho_\infty, V_\infty, p_\infty$ is the free-stream density, velocity and pressure, respectively, states that total pressure p_0 along a subsonic streamline remains constant. If the local air velocity increases, the dynamic pressure $1/2\rho_\infty V_\infty^2$ has increased so the static pressure p_∞ must decrease. Similarly a decrease in local velocity the static pressure must increase. This shows that higher velocities produces lower pressure. The integrated difference in pressure between the top and bottom surface generates a net force upward [38]. A typical

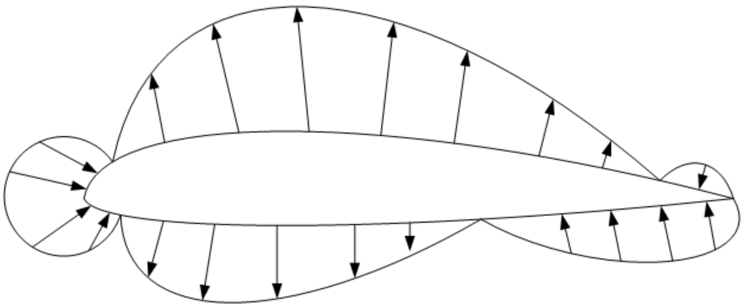

Figure B.3: Typical airfoil or wing pressure distribution

pressure distribution for upper and lower surface of an airfoil at subsonic speeds is shown in Fig. B.3.

Aerodynamic forces such as lift and drag acting on an airfoil or a wing need to be quantified. The airfoil main function is to generate lift force ***l*** at a range of operating conditions, freestream velocities V_∞ (Mach numbers M_∞) and angle of attacks α. The angle of attack α is defined as the angle between c and V_∞. Hence, α is also the angle between lift force l and N and between the drag force d and A, where N is the normal force and A is the axial force. Geometric relations between these two sets of components is

$$l = N\cos\alpha - A\sin\alpha \tag{B.3.2}$$

$$d = N\sin\alpha + A\cos\alpha \tag{B.3.3}$$

These forces are due to two basic sources, the pressure distribution p and the shear stress τ distribution acting normal and parallel to the body surface respectively. At a given point the pressure is normal to the surface and oriented at an angle θ relative to perpendicular. Shear stress is tangent and oriented at the same angle θ relative to the horizontal. Sign convention for θ is positive when measured clockwise. The net effect of the p and τ distributions integrated over the surface is a resultant aerodynamic force ***F***. The pressure and skin friction coefficients are defined as

$$C_p = \frac{p - p_\infty}{q_\infty} \tag{B.3.4}$$

$$C_f = \frac{\tau}{q_\infty} \tag{B.3.5}$$

respectively, where q_∞ is the dynamic pressure defined in Eq. (B.1.3). The normal and axial forces for a two dimensional airfoil with unit span can be found by integrating over the whole surface making use of the pressure and skin friction coefficient.

$$C_n = \frac{1}{c}\left[\int_0^c (C_{p,l} - C_{p,u})\,dx + \int_0^c \left(C_{f,u}\frac{dz_u}{dx} - C_{f,l}\frac{dz_l}{dx}\right)dx\right] \tag{B.3.6}$$

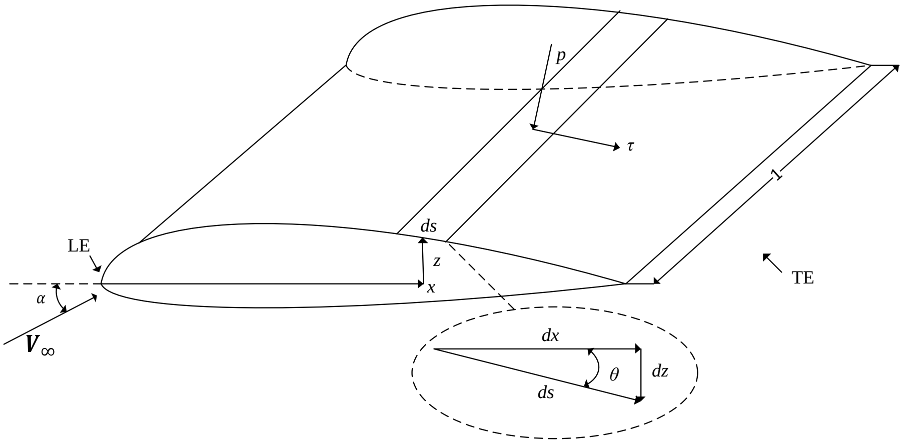

Figure B.4: Aerodynamic forces on an element of the body surface.

$$C_a = \frac{1}{c}\left[\int_0^c \left(C_{p,u}\frac{dz_u}{dx} - C_{p,l}\frac{dz_l}{dx}\right)dx + \int_0^c \left(C_{f,u} - C_{f,l}\right)dx\right] \tag{B.3.7}$$

where u and l denote upper and lower surface respectively. This is shown in Fig. B.4 for a unit span where ds is the length of the surface element, hence $dx = ds\cos\theta$ and $dz = -ds\sin\theta$. Similarly as in Eq. (B.3.3) the lift and drag coefficients can be written as

$$C_l = C_n\cos\alpha - C_a\sin\alpha = \frac{l}{q_\infty S} \tag{B.3.8}$$

$$C_d = C_n\sin\alpha + C_a\cos\alpha = \frac{d}{q_\infty S} \tag{B.3.9}$$

B.4 Lift Coefficient

Typical variation on lift coefficient with angle of attack for airfoils and wings is shown in Fig. B.5a. At low angles C_l varies linearly with α and the slope is called *lift slope* defined as

$$a_0 = \frac{dC_l}{d\alpha} \tag{B.4.1}$$

In this region the flow remains attached to most of the surface of the airfoil. At certain point as α becomes larger the flow tends to separate from the top surface creating a large wake aft of the airfoil. In this region the flow is recirculating and part of the flow is reversed. This is due to viscous effects. As a result the airfoil looses lift and the airfoil is staid to *stall* [42]. The maximum lift just before stall is denoted by $C_{l,max}$ and is an important parameter since it determines the stall speed of the aircraft, as the higher the $C_{l,max}$ the lower the stalling speed. Stalling speed for a three dimensional body is defined

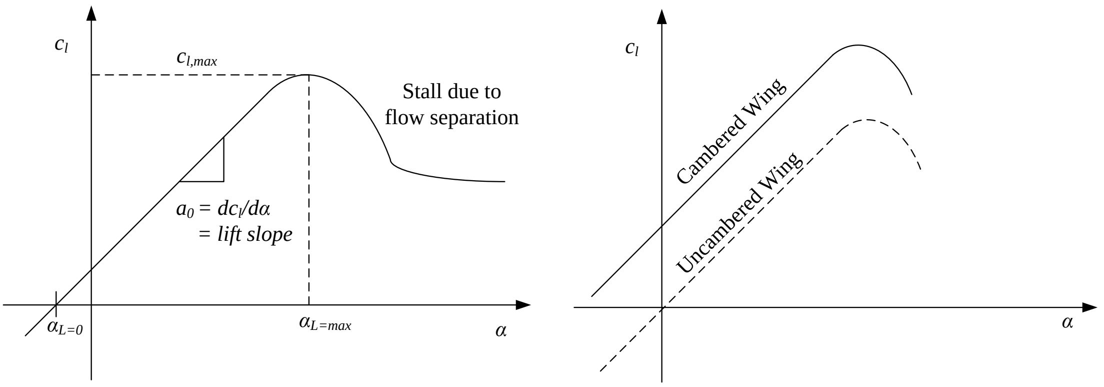

(a) Schematic of lift-coefficient variation with angle of attack for an airfoil or a wing.

(b) Effects on lift-coefficient variation with angle of attack for an cambered airfoil or a wing.

Figure B.5: Effects on lift coefficient by varying angle of attack and camber.

as

$$V_{stall} = \sqrt{\frac{2W}{\rho_\infty S C_{L,max}}} \tag{B.4.2}$$

where W is the weight of the body. Increasing $C_{l,max}$ is therefore often of primary interest in modern aircraft design [42]. Examining Fig. B.5a further we see as α passes $C_{l,max}$ the airfoil stalls. The value when lift is zero is called *zero-lift angle of attack* and is denoted by $\alpha_{L=0}$ [42]. The symmetric (uncambered) wing has no lift where $\alpha_{L=0} = 0$ and cambered wings have positive lift at zero angle of attack [38]. This is illustrated in Fig. B.5b.

B.4.1 Subsonic Lift-Curve slope

For 2D airfoil or an infinite-aspect ratio wing the theoretical subsonic is $a_0 = 2\pi$. Actual airfoils have 90-100$\%$ of the theoretical value and this percentage is referred to as airfoil efficiency defined as η [38]. Semi-empirical formula exists for a complete wing lift-curve slope and is valid up to drag-divergence Mach number.

$$C_{L\alpha} = \frac{2\pi AR}{2 + \sqrt{4 + \frac{AR^2\beta^2}{\eta^2}\left(1 + \frac{\tan^2(\Lambda_{\max t})}{\beta^2}\right)}} \left(\frac{S_{exposed}}{S_{ref}}\right)(F) \tag{B.4.3}$$

where

$$\beta^2 = 1 - M^2 \tag{B.4.4}$$

$$\eta = \frac{C_{l\alpha}}{2\pi/\beta} \tag{B.4.5}$$

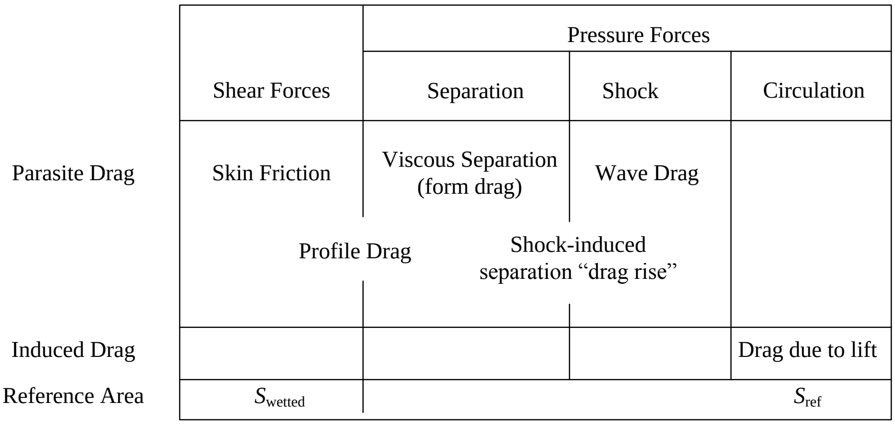

		Pressure Forces		
	Shear Forces	Separation	Shock	Circulation
Parasite Drag	Skin Friction	Viscous Separation (form drag)	Wave Drag	
	Profile Drag	Shock-induced separation “drag rise”		
Induced Drag				Drag due to lift
Reference Area	S_{wetted}			S_{ref}

Figure B.6: Various sources of drag and the drag terminology

where $\Lambda_{\max t}$ is the sweep of the wing at the chord length where the wing thickness is the most, $S_{exposed}$ is the exposed wing planform area. This is the reference area S_{ref} minus the area that the fuselage covers. F is the fuselage lift factor

$$F = 1.07(1 + d/b)^2 \tag{B.4.6}$$

where d is the fuselage diameter and b the span.

B.5 Drag Coefficient

As mentioned above are all drag forces due to only two sources, pressure and shear forces. However many classification schemes exist. Here we will cover the most common sources of drag although more exists. A drag terminology matrix show in B.6 summarizes the commonly used drag terms based on the origin of the drag source (shear of pressure) and how strongly related to lift the force is [38]. We will give a brief description below.

B.5.1 Parasite Drag

Drag forces not strongly related to lift are usually known as parasite drag. Drag can be divided into *pressure drag* and *skin friction*

Skin friction For an aircraft in a subsonic cruise the parasite drag is mostly skin friction drag which is related to the wetted area of the aircraft. Shear forces are strongly related to Reynolds number.

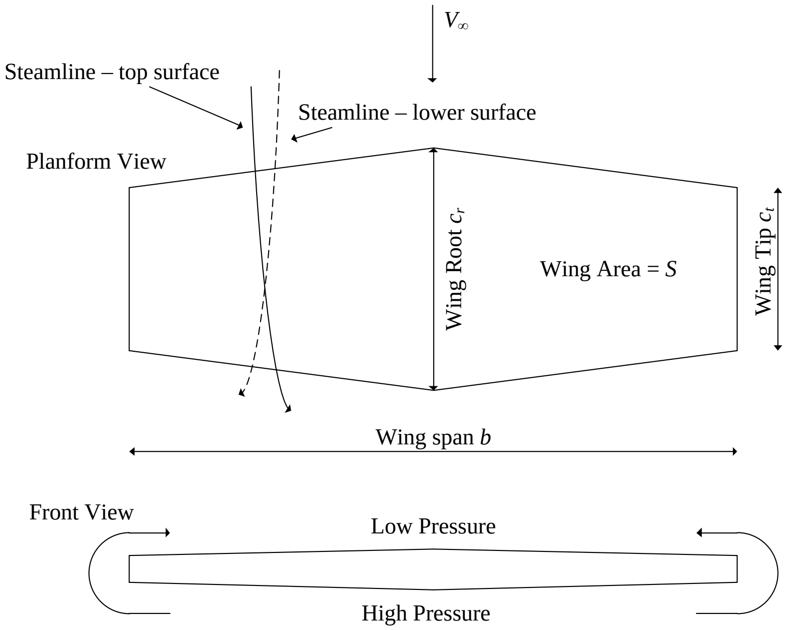

Figure B.7: Finite wing. Streamlines over the top and bottom surface shows that there exists a component of flow in spanwise direction.

Viscous separation drag is also called *form drag*. For a blunt body most of the drag is pressure drag. For a streamlined body most of the drag is skin friction drag. This depends upon the location of the separation point of the body. This effect is covered in detail in Appendix B.6. Separation points depends largely on the curvature of the body and also the amount of energy in the flow. Turbulent flow has higher energy than laminar so the turbulent boundary layer tends to delay separation.

Wave Drag is the drag caused by the formation of shock at subsonic or supersonic speeds. At high subsonic speeds the shock first appears on the upper surface of the wing and can appear on the lower as well.

Drag due to viscous separation and skin friction is commonly called *profile drag*. [42, 38].

B.5.2 Induced drag

Yet another form of pressure drag is the *induced drag* which is related to the lift of the wing and is produced at the wingtip due to the pressure difference above and below the wing. As a result there is generally a spanwise component of flow from the tip towards the root causing streamlines on the surface to bend towards the root as shown in B.7. Similarly the streamlines bend towards the tip on the lower surface. As fluid below the wing is drawn onto the top near the wing tips it establishes a swirling flow or vortices

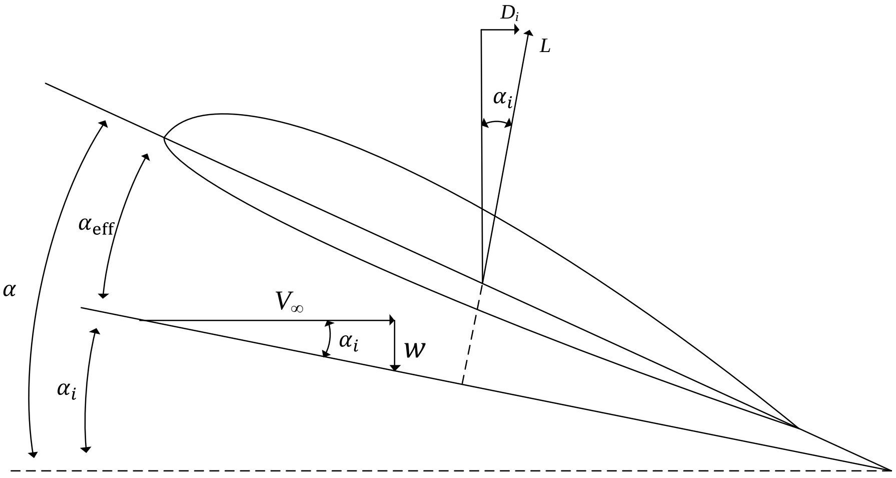

Figure B.8: Effect of downwash on the local flow over local airfoil section of wing.

trailing from the wing tips. The vortices drag surrounding fluid and generate a downward velocity component w called *downwash* on the wing. The downwash adds to the local freestream velocity creating a new fluid flow direction. The angle between the freestream and new flow is denoted by α_i, or the induced angle of attack. This behaviour changes the angle of attack actually seen by the local airfoil. This is called effective angle of attack denoted $\alpha_{\text{eff}} = \alpha - \alpha_i$. This behaviour "induces" a drag force D_i on the wing as shown in B.8 [42].

B.5.3 Total drag

The total drag is the sum of induced drag D_i, wave drag D_w, the skin friction drag D_f and the pressure drag D_p due to flow separation, latter two being viscous drag where the sum is usually called profile drag. For low speed subsonic flow, profile drag coefficient is usually obtained from airfoil theory and can be defined as

$$C_d = \frac{D_f - D_p}{q_\infty S} \tag{B.5.1}$$

and the induced drag coefficient as

$$C_{D,i} = \frac{D_i}{q_\infty S} = \frac{C_L^2}{\pi e AR} \tag{B.5.2}$$

where e is the span efficiency factor, AR the aspect ratio defined as $AR = b^2/S$. For low speed subsonic flow the total drag coefficient then defined as

$$C_D = C_d + C_{D,i} \tag{B.5.3}$$

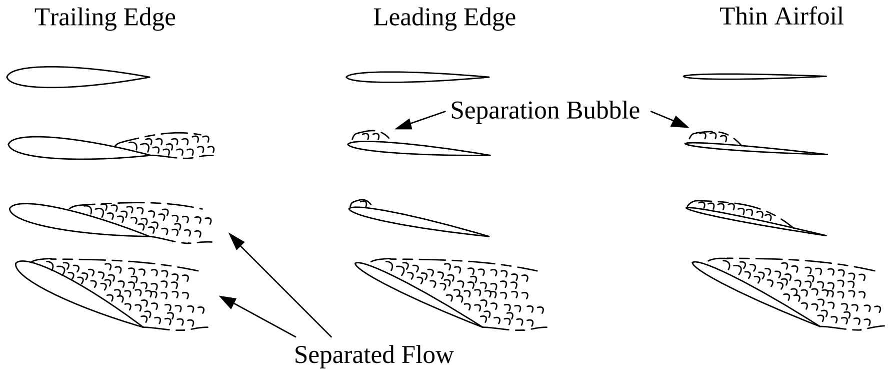

Figure B.9: Types of stall

B.6 Flow Separation and Stall

As mentioned above when wing looses lift the wing has entered the stall region and flow separation is extensive. Some airfoils exhibit a gradual reduction in lift while others experience quite violent loss in lift. These difference reflects the existence of three types of airfoil stall where each type is associated with the airfoil thickness [38].

Trailing edge stall occurs for airfoils that have a round leading edge and t/c greater than 14% where loss in lift occur gradually. Turbulent boundary layer increases with α and starts to separate around 10 degrees [38].

Leading edge stall appears for thin airfoils. If thickness is moderate, t/c is about 6-14%, the flow separates from the leading edge at small α but reattaches immediately so little effect is felt. This is called a separation bubble. At moderate α the flow fails to reattach which almost immediately stalls the entire airfoil [38].

Very thin airfoil stall has the same characteristics as previous type for low α. Separation bubble is formed and the flow reattaches. However for a very thin airfoil the bubble continues to grow towards the trailing edge. At maximum α the bubble is stretched from the leading edge all the way to trailing edge. Increasing α further results in a stall and the flow is separated from the whole airfoil. The loss in lift is gradual [38].

The three cases above are summarized in Fig. B.9. Stall characteristics for thinner airfoils can be improved with high-lift devices such as slats. High lift devices will be covered in Appendix B.7. Wing stall is directly related to airfoil stall only for high-aspect-ratio unswept wings. For low-aspect-ratio wings the 3D effect dominated the stall characteristics.

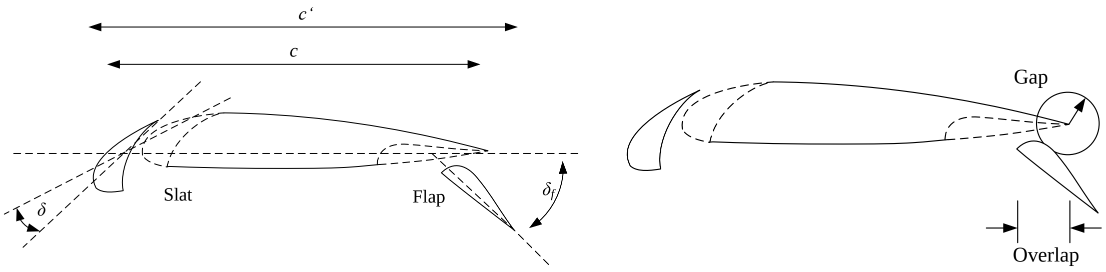

(a) Examples of slat and slotted fowler flap when deployed. c' is the modified chord length when high lift devices are deployed (solid lines) compared to c when retracted (dotted line). δ and δ_f are the deflection angles for slat and flat respectively

(b) Gap is the abolute distance between the main element and a flap or a slat. The overlap is the distance in x which the flap or slat overlaps the main element

Figure B.10: High lift devices nomenclature

B.7 High-Lift Devices

For transonic transport aircraft's the high-lift system design is a critical part design due to the functional requirements in the design. For cruise efficiency a wing should have a little camber as for takeoff and landing a wing should have high lift as well as lot of camber. For such requirements high-lift devices such as flaps and slats are applied [38]. Different configurations of high-lift devices exist and Fig. B.10 shows the geometry of a commonly used high-lift system, a slotted fowler flat and a slotted leading edge flap or a slat. When high-lift devices are deployed c' is the modified chord length (solid lines) compared to c when retracted (dotted line). δ and δ_f are the deflection angles for slat and flat respectively [37].

When calculating the lift coefficient $C_L = L/q_\infty S$ it is referenced to the original reference area $S = c$ hence the angle of attack for $C_{L,\max}$ remains the same but lift has increased. [37, 38].

B.7.1 Flap Effect

Flap chord length can typically be around 30 % of the airfoil chord length c. For a typical airfoil the maximum lift occurs when flap deflection is close to 40-45 degrees [38]. Typical flap increases the lift by increasing the camber of the airfoil.

Effect of deploying typical plain flat and a slotted fowler flap is shown in Fig. B.11. When deploying non-extending flap or a plain flap the angle of attack for $C_{L,\max}$ is in fact reduced but lift is increased. The lift curve moves to the left and up and lift slope is unaffected.

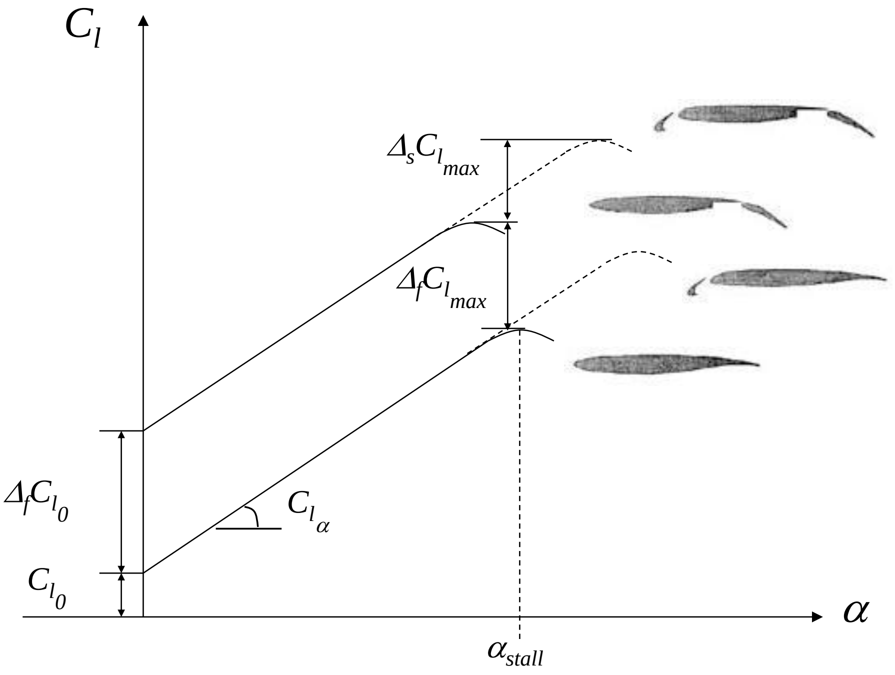

Figure B.11: The effects of high lift devices. Adding slat extends the lift slope hence increases $C_{l\,\max}$ and stall is experienced ad higher angle of attack (α_{stall}). Adding flap shifts the lift curve up and aft, increasing $C_{l\,\max}$ but stall occurs at lower angle of attack (α_{stall}).

By extending the flap aft introducing a slot between the wing and flap permits high-pressure air from the lower surface to exit through the slot and flow over the upper surface on the flap. This referred as *fresh boundary layer effect* and reduces separation from the upper surface, hence it increases the lift and reduces drag [38]. By using a fowler flap one benefits from the increased camber as well as increased area or the chord length c'. The lift slope is increased by approximately the ratio of the total extended wing area to the original wing area. Flaps do not increase the angle of stall. To increase stall angle slats are required.

B.7.2 Slats Effect

Leading edge slats are intended to hinder separation from the leading edge. Therefore they are only needed for high angle of attacks where flow separation starts to appear. They simply allow high-pressure fluid from lower surface to flow over the upper surface delaying the separation and stall They also provide increased camber and increase the area which will increase lift as shown in Fig. B.11. $C_{L,\max}$ is increased as well as the stall angle of attack [37, 38].

B.8 Types of flow

In this study we consider viscous flow over bodies

B.8.1 Incompressible versus Compressible Flow

Flow is considered incompressible when the density ρ of the fluid is kept constant. In contrast where the density is retained as a variable the flow is considered compressible. In flows of homogeneous liquids one can assume that $\rho = constant$. For the flow of gases at low Mach number is also essentially incompressible and for $M < 0.3$ it is always safe to assume thant $\rho = constant$ [42].

B.8.2 Mach Number and Flow Regimes

Distinction of flow in aerodynamics is base on the non-dimensional parameter, the Mach number defined as

$$M_\infty = \frac{V_\infty}{a_\infty} \tag{B.8.1}$$

where V_∞ and a_∞ are the free-stream velocity and speed of sound, respectively [42]. The Mach number is one of the most important parameters in aerodynamics. If M is the local Mach number at an arbitrary point in the flow field then the flow is locally,

Subsonic if $M < 1$

Sonic if $M = 1$

Supersonic if $M > 1$

By analysing the flow whole field simultaneously four different speed regimes can be identified using the Mach number criterion, subsonic, transonic, supersonic and hypersonic flow. Here we briefly cover subsonic and transonic regimes since they are of primary interest.

B.8.3 Subsonic Flow

In subsonic flow $M < 1$ at any point in the flow field of interest. Subsonic flow can be characterized by smooth streamlines over the body as show in Fig. B.12. Mach number less than 1 however does not guarantee a subsonic flow over a body. As fluid expands over the aerodynamic body the flow velocity can be greater than the free-stream Mach

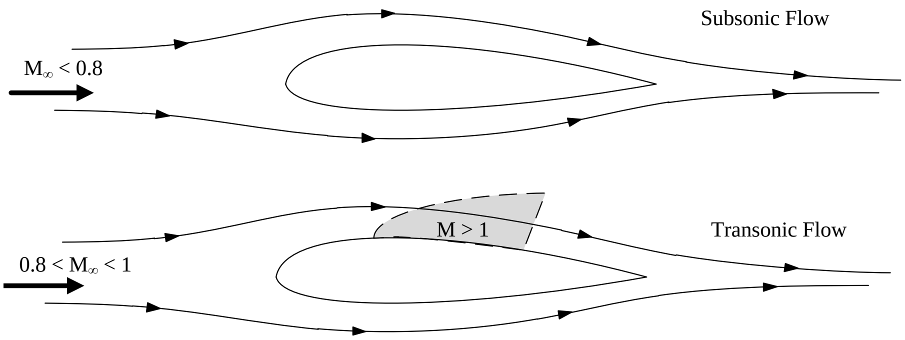

Figure B.12: Different regimes of flow

number. If M_∞ is close to 1 the local Mach number may become supersonic. This leads to a rule of thumb where $M_\infty < 0.8$ for subsonic flow over aerodynamic body. [42]

B.8.4 Transonic Flow

The transonic region is where subsonic flow and supersonic flow exist at the same time. This means that $M < 1$ and $M > 1$. If M_∞ is close to 1 the flow can become locally supersonic. This is shown in Fig. B.12. The figure shows a pocket of supersonic flow over the top surface terminated by a shock wave behind which the flow becomes subsonic again. Weak shock waves are usually terminated at the trailing edge and as the Mach number increases the shock moves further aft and becomes stronger [42]. This shock affects drag substantially and leads to a rapid increase in drag referred to as wave drag.

School of Science and Engineering
Reykjavík University
Menntavegur 1
101 Reykjavík, Iceland
Tel. +354 599 6200
Fax +354 599 6201
www.reykjavikuniversity.is
ISSN 1670-8539